Spring 1989

High resolution inelastic electron scattering from lead-208

James Patrick Connelly
University of New Hampshire, Durham

Order Number 8921932

High resolution inelastic electron scattering from ^{208}Pb

Connelly, James Patrick, Ph.D.

University of New Hampshire, 1989

U·M·I
300 N. Zeeb Rd.
Ann Arbor, MI 48106

HIGH RESOLUTION INELASTIC ELECTRON SCATTERING FROM ^{208}Pb

by

James Patrick Connelly
B.S., Morgan State University, 1981
B.A., Saint Mary's College of Maryland, 1975

A DISSERTATION

Submitted to the University of New Hampshire
in Partial Fulfillment of
the Requirements for the Degree of

Doctor of Philosophy
in
Physics

May, 1989

This dissertation has been examined and approved.

Dissertation director, Jochen Heisenberg
Professor of Physics

David Forrest
Assistant Professor of Physics

F. William Hersman
Associate Professor of Physics

Lyman Mower
Professor of Physics

John Wright
Professor of Physics

April 20, 1989
Date

ABSTRACT

HIGH RESOLUTION INELASTIC ELECTRON SCATTERING FROM ^{208}Pb

by

JAMES P. CONNELLY

University of New Hampshire, May, 1989

Inclusive electron scattering differential cross sections from ^{208}Pb have been measured with energy resolutions better than 20 keV for over 120 discrete states with excitation energies less than 7.3 MeV. The momentum–transfer dependence of these cross sections has been mapped over a range of 0.5 to 2.8 fm^{-1} in the forward direction and 1.0 to 2.9 fm^{-1} in the backward scattering direction. Over fifty excitations have been analyzed in the Distorted Wave Born Approximation to yield transition charge, current and magnetization densities. The nuclear structure of discrete excitations are interpreted in the framework of 1p–1h transitions. The nuclear structure of levels in the excitation region below 4.8 MeV is studied in detail. Above 4.8 MeV, multiplets from single particle–hole configurations coupling to high spin states ($J \geq 7$) are investigated. Experimental transition densities are compared to Tamm-Dancoff calculations from a correlated ground state.

to Winnie and Jan and Judi

Acknowledgements

This dissertation is the end result of many years of effort, not only by the author, but also by those people who provided their time, energy and expertise to this endeavor. It is my pleasure to offer my gratitude and best wishes to everyone who supplied the knowledge, material assistance and emotional support that made this work a reality.

First, my most profound thanks to Professor Jochen Heisenberg. A true gentleman, Dr. Heisenberg conceived the experiment and guided the work to completion. His ability to articulate the physics, balanced with his concern for both the success of the experiment and the well–being of his graduate student, was deeply appreciated.

Professor William Hersman, whose energy and enthusiasm kept us going in the wee hours at Bates, was instrumental in attaining the high resolution required by this experiment. His expertise on ELSSY and innovative approaches to focal plane corrections was invaluable.

Thanks also to Profesor Costas Papanicolas for many informative and inspirational discussions regarding the physics of ^{208}Pb and to the several University of Illinois graduate students that participated in the experiment.

Many thanks to Lymon Stinson and the staff at Bates for providing the resources that made this experiment possible. Thanks (and apologies) to the chief operators for giving us excellent beam while enduring my midnight harangues.

The entire University of New Hampshire Nuclear Physics Group were really the backbone in the data acquisition. Dr. John Wise and Dr. Woo Young Kim were literally always availiable with unfailing good humor and determination.

Two fellow graduate students deserve special recognition for both their contribution to the experiment and as friends. Dr. Tom Milliman gently initiated me into the mysteries of data analysis and kept us both laughing at the same time. Mark Leuschner, my office–mate and erstwhile maid–of–honor, unravelled both the complexities of the Q–system and the Red Sox batting averages, the former

with slightly more success.

My friends from both New Hampshire and Baltimore are treasured for reasons beyond ennumeration. In particular, Colleen Gibbons and Bob Thornton were the instigators and inspiration to embark upon the path which has led to this point. Alphonse Sterling and Parameswaran Sreekumar helped make the journey along that path pleasant and rewarding. Jack Williams, Kirby Woodward and Carole Diamond did their best to divert me from the path, for which I am eternally grateful.

My mother and father have shown extreme patience, faith and love as they watched their youngest flap his wings helplessly. My two brothers, Mike and Bob, and my sister Chris were always supportive, materially and emotionally, and I love them all.

To my wife Judi, your smile has been the source of my strength, your love the anchor for all that I do.

Table of Contents

Table Captions

Figure Captions

Chapter 1

Introduction

The ^{208}Pb nucleus is the largest doubly closed shell nucleus available for experimental study. In the shell model picture of the nucleus, protons and neutrons occupy distinct sets of single particle orbitals with good radial, angular momentum and spin quantum numbers. In the simplest approximation, nucleons are considered to be non-interacting fermions in the presence of an external central potential known as the mean field. This mean field is intended to approximate the average potential felt by a given nucleon from the actual nucleon–nucleon many body interactions. Including a strong spin–orbit term in the potential leads to the familiar shell structure of nucleon orbitals. Nuclear mean field structure calculations employ these single particle wave functions as a complete basis set upon which the theory attempts to expand the true nuclear wave function.

The theoretical importance of ^{208}Pb as a laboratory for mean field calculations comes both from the shell closure of the proton (82) and neutron (126) shells, and the relatively large number of nucleons considered, which lends more validity to the notion of an average mean field potential than in the case of lighter doubly closed shell nuclei such as ^{16}O or ^{48}Ca. Experimentally observed quantities from the ^{208}Pb nucleus provide the most stringent tests of mean field theoretical predictions for both ground state and dynamic nuclear observables.

Inelastic electron scattering at intermediate energies from atomic nuclei supplies a wealth of nuclear structure information with a degree of precision which is unique to this probe. The interaction of the electron with the nucleus is primarily electromagnetic and thus well described within the framework of Quantum Electro–Dynamics. Nuclear transition densities can be model independently decoupled from the reaction mechanism with a precision that challenges theoretical endeavors. Since the electromagnetic coupling constant is relatively small, nuclear interactions with intermediate energy electrons are just as likely to occur

in the interior of the nucleus as at the surface, unlike hadronic probes which test primarily the surface. Details on nuclear transitions from inelastic electron scattering measurements provide a stringent test for microscopic nuclear structure calculations.

The fundamental experimental quantities obtained in this experiment are the differential cross sections $d\sigma/d\Omega$ for the ground state and a host of discrete states with an excitation energy below 7.3 MeV. The formalism which relates these cross sections to electromagnetic transition densities is outlined in Chapter 2.

Electromagnetic transitions in nuclei will be either electric (natural parity) or magnetic (unnatural parity). The exchange of a virtual photon by the incident electron to the nucleus permits a sampling of both the longitudinal component of the transition, arising from charge scattering, and the transverse component, which is due to scattering from the current and magnetization distributions. Magnetic states will be purely transverse while electric states will in general display both longitudinal and transverse components in the cross section.

The energy level spectrum of ^{208}Pb below 7.5 MeV is characterized by an extremely high level density. Nuclear Data Sheets (1986)[1] lists over two hundred levels between 2.5 MeV and 7.5 MeV excitation energy. Many of these states are weakly excited by electron scattering and will not appear in (e, e') measurements with any appreciable cross section. In this experiment, evidence for approximately 120 levels were seen in this energy regime.

^{208}Pb has been the subject of intense experimental interest. In addition to electron scattering, other reactions such as proton scattering, stripping and pickup reactions, and radiative photon experiments have been performed. These experiments provide complimentary nuclear structure information. For example, electron scattering cannot unambiguously determine the spin and parity of a given excitation. However, angular distributions from proton scattering can quite reliably determine the spin, while transfer reactions provide spectroscopic factors of particle–hole transitions which participate in an excitation and the parity of the excitation. Measurements of radiative photons as the nucleus de-excites gives a

much more precise determination of the excitation energy of discrete transitions than can be obtained in high resolution electron and proton scattering experiments. In order to make sense out of the multitude of information measured in this experiment, results from other experiments on ^{208}Pb were incorporated as much as possible.

Previous electron scattering experiments, while restricted to strongly excited or well separated states, have determined charge and current densities with an unprecedented accuracy. The ground state charge density[2] is known to within $\pm 1\%$ and the transition charge density from the first excited state at 2.615 MeV[3] to within a few percent. Other low-lying excitations, such as the first two 5^- states at 3.198 MeV and 3.709 MeV[4], and the positive parity band of states 2^+ (4.085 MeV), 4^+ (4.323 MeV), 6^+ (4.424 MeV) and the 8^+ (4.610 MeV)[5] have also been well determined.

The primary experimental difficulty in studying the less strongly excited levels in ^{208}Pb, has been in obtaining the energy resolution neccesary to untangle these states. Lichtenstadt[6], in an electron scattering experiment on the high resolution spectrometer at MIT–Bates, was able to obtain energy resolutions of 40–60 keV. Electromagnetic form factors were measured for high spin states, including the 14^- stretched state at 6.74 MeV, 12^- states at 6.43 MeV and 7.06 MeV, for which quenching of calculated single particle–hole strengths were first observed.

The improvement of the resolution capabilities on the Energy Loss Spectrometer at MIT–Bates to $\delta p/p \leq 6 \times 10^{-5}$ was the spur for this experiment. The energy resolutions for the data presented in this work ranged from 12–24 keV. A discussion of the experimental techniques employed to optimize the resolution is presented in Chapter 3.

The excitations in ^{208}Pb may be loosely classified as either collective transitions, in which many mean field particle–hole configurations participate, and single particle states where one mean field configuration dominates the transition. Between these extremes there are states which display some collectivity but have one or two single particle–hole configurations with large amplitudes.

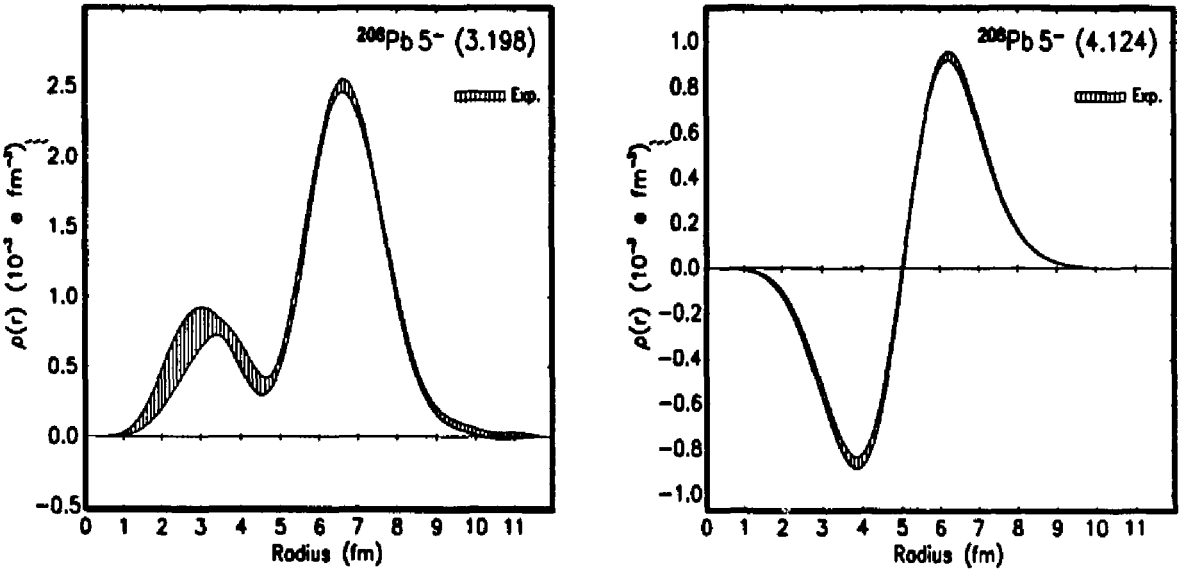

Fig.1.1 Transition charge densities from the 3.198 MeV 5^- state (left) and the 4.124 MeV 5^- state (right).

The differences between collective and single particle transitions is reflected in the transition charge densities. As seen in Figure 1.1, the highly collective 5^- 3.198 MeV state displays a strongly surface peaked charge density. Oscillations of the many 1p-1h configurations tend to cancel in the interior and build on the surface. In contrast, the transition charge density of the 5^- state at 4.124 MeV, which is primarily due to the $\pi(1h_{9/2}, 2d_{3/2}^{-1})$ configuration, shows that much of the transition is occuring within the interior of the nucleus. This is because the transition charge density in this case is essentially the product of the $1h_{9/2}$ wave function, which has no nodes, and the $2d_{3/2}$ wave function, which has one node. The transition charge density for this state reflects the interference between these single particle wave functions.

Collectivity tends to decrease with increasing multipolarity since the number of configurations which can couple to higher multipolarities is reduced. This phenomenon is most drastically seen in the very high spin states, 14^- and 12^+,

where only one mean field configuration can couple to either of these states. In these cases the transition may truly be considered a single particle–hole state.

Very collective states tend to be purely longitudinal. The transition charge densities will be enhanced by the sum of many particle–hole transitions, while the currents produced by individual nucleons will cancel to produce a small or neglible transition current densities. The octupole state at 2.615 MeV, the 5^- state at 3.198 MeV, and the 2^+, 4^+, 6^+ and 8^+ collective states display very strong longitudinal form factors and extremely small transverse form factors. As the collectivity decreases and one or more single particle–hole configurations begin to dominate the transition, the transition current density will increase and reflect in structure the dominant configurations.

The residual interaction, which in mean field theory mixes the single particle–hole configurations, is strongly attractive for natural parity transitions. However, for unnatural parity transitions the residual interaction is weak and slightly repulsive. Thus, magnetic states, unless there are contributing 1p–1h configurations with very close single particle–hole energies, will be dominated by one mean field configuration.

The doubly closed shell character of ^{208}Pb makes this nucleus especially suited for comparison to theoretical calculations which express discrete excitations as a linear sum of 1p–1h transitions, such as the Random Phase Approximation (RPA) or the Tamm–Dancoff Approximation (TDA). This should be compared to the case of open shell nuclei, where shell model calculations involving many particle–many hole transitions are needed. Several RPA calculations by Ring and Speth[7] , Knüpfer *et al.*[8] , Dechargé and Gogny[9] , and Heisenberg and Krewald[10] and others have been performed in the past with a variety of interactions in an attempt to predict the transition densities from collective states. In this work comparisons will be between experimental densities and predictions from preliminary results by Heisenberg[11] using TDA with ground state correlations explicitly included. A discussion of RPA and the correlated ground state TDA will be presented in Chapter 4.

The quenching of single particle–hole amplitudes observed by Lichtenstadt[12] and proton scattering experiments[13][14] have generated a great deal of theoretical interest. Several models have been presented by Hamamoto *et al.*[15] and by Suzuki *et al*[16] investigating the influence of core polarization effects, and by Krewald and Speth[17] demonstrating the fragmentation of 1p–1h strength through configuration mixing with 2p–2h transition. The analysis of single particle–hole states and comparison of results to other experiments and predictions will be reviewed in Chapter 5.7.

The overall objective of this experiment was to investigate the details of the electron scattering discrete state spectrum from ^{208}Pb by measuring inelastic (e, e') cross sections with an energy resolution better by a factor of two than previous electron scattering experiments. More specific goals were,

- to measure inelastic (e, e') cross sections from states previously studied and attempt to resolve these levels from nearby levels which have been acted as contaminants in other experiments.
- to extract transition densities from states for which the spin and parity have been determined by other reactions but have not been measured with electron scattering.
- to make assignments of spin and parity and extract transition densities where possible, in particular those states which result primarily from a single particle–hole configuration.
- to measure the amplitudes of relevant mean field configurations for states with only one or two dominant configurations. In particular to measure the quenching from the calculated single particle–hole strengths.
- to determine the excitation energies of transitions to within 5 keV.

In the analysis of the discrete state cross sections, we accepted the spin and

parity assignments as determined by other reactions, unless our data provided convincing evidence to the contrary. For many levels, no spin or parity has been firmly established. In some cases it was possible to make assignments based upon the criteria discussed in Chapter 5.

The analysis from over fifty states are presented in Chapter 5, although cross sections were measured for many more. Normalized cross sections for the states from which transition densities were extracted are given in Appendix A. The measured cross sections of states for which no analysis was performed are listed in Appendix B.

Chapter 2

Electron Scattering

Electron scattering experiments have played a prominent role in exploring the properties and structure of atomic nuclei. With the development of both particle accelerators and particle physics a variety of probes have become available to nuclear physicists. These probes are characterized by the energy with which they are incident upon the target nucleus and the nucleon–particle interaction which produces the scattering.

In nuclear structure investigations, the wave–like nature of the particle probing the nucleus is a crucial aspect. The distances over which the probe is sensitive is determined by the de Broglie wavelength of the particle and therefore of the incident energy. Wavelengths of highly relativistic particles is given by

$$\lambda = \frac{h}{p} \tag{2.1}$$

so that higher energies correspond to smaller wavelengths. Energies which correspond to the wavelength regime pertinent to nuclear structure effects are traditionally termed intermediate energies and are roughly bounded by wavelengths the size of the nucleus ($\sim 10fm$) to distances just beginning to probe the interior of the individual nucleons ($\sim .3fm$).

Nuclear constituents are hadrons and can participate in interactions involving any of the four forces of nature; gravity, the weak nuclear force, electromagnetism, and the strong nuclear force. Gravity, and to a large degree the weak force, are unattractive scatterers due to the smallness of their coupling constants. Using hadrons themselves as probes has two clear advantages; 1.) use of the strong force results in large interaction matrix elements and therefore shorter counting times, and 2.) the strong force is isospin invariant and is equally sensitive to proton and neutron distributions. These points are offset by the present uncertainty

of the hadron–hadron interaction within the nucleus. The interaction must be determined phenomenologically and models must be employed to decouple nuclear structure information from the reaction matrix elements.

Electronic probes are sensitive primarily to the electromagnetic fields produced by the charge and current densities of the nucleus. This interaction is well understood within the theoretical framework of quantum electrodynamics and hence the reaction matrix elements can be cleanly unfolded from the nuclear structure response functions. The theoretical basis through which electron scattering results may be understood has been described in numerous references [18] [19] [20] and we present only a sketch of the formalism in this work. Inclusive electron scattering cross sections and the fundamental nuclear structure densities will be introduced in Section 2.2 with a brief treatment of the one photon exchange approximation or Plane Wave Born Approximation (PWBA). Corrections resulting from radiative dispersion effects will be considered in Section 2.3. For heavy nuclei, higher order corrections must be considered due to the distortion of the electron wave function from the nuclear coulomb field. This leads to the Distorted Wave Born Approximation (DWBA) and will be discussed is Section 2.4. A synopsis of the DWBA calculations is presented in Section 2.5. We begin the review of electron scattering formalism by outlining the kinematics of electron–nucleus scattering.

2.1 Kinematics

In the Plane Wave Born Approximation (PWBA), relativistic electron plane waves are incident upon the electromagnetic fields of the nuclear charge, current and magnetization densities. To the lowest order in the electromagnetic coupling constant α ($\alpha = \frac{1}{137}$), a single virtual photon transfers a four momentum q_μ from the electron to the nuclear system, represented by the Feynman diagram in Figure 2.1.

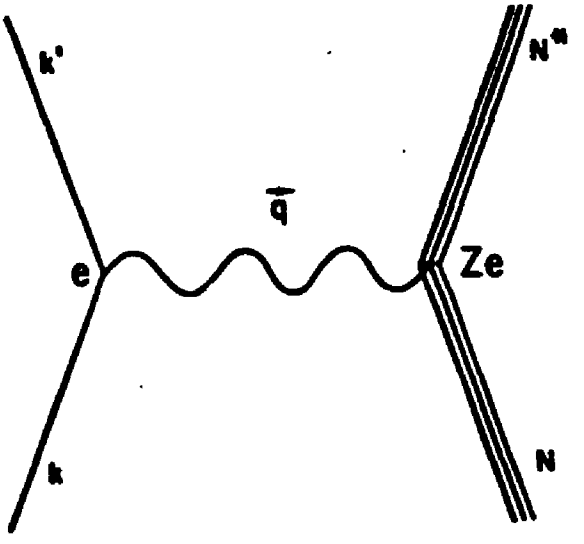

Fig.2.1 Lowest order electron–nucleus scattering diagram.

The initial and final four momenta are defined by the Lorentz invariant scalar products

$$\begin{aligned} k_\mu k^\mu &= m_e^2 c^2 - \vec{k}^{\,2} && \text{initial electron momentum} \\ k'_\mu k'^\mu &= m_e^2 c^2 - \vec{k}'^2 && \text{final electron momentum} \\ P_\mu P^\mu &= M^2 c^2 && \text{initial nuclear momentum} \\ P'_\mu P'^\mu &= M^2 c^2 - \vec{P}'^2 && \text{final nuclear momentum} \end{aligned} \tag{2.2}$$

where the nucleus is initially at rest in the laboratory reference frame.

The scalar product of the momentum transfer is

$$q_\mu q^\mu = (k'_\mu - k_\mu)(k'^\mu - k^\mu) \tag{2.3}$$

$$= \omega^2 - \vec{q}^{\,2} \tag{2.4}$$

Unlike photonuclear reactions, the virtual photon rest mass is not constrained to be zero, but must only be a positive quantity. This leads to a functional

dependence of the three momentum transfer upon the initial and final electron energies and the scattering angle. For highly relativistic electrons, the electron mass is negligible and the expression for $\vec{q}^{\,2}$ reduces to

$$\vec{q}^{\,2} = \frac{4E_i E_f}{\hbar^2 c^2} \, sin^2\left(\frac{\theta}{2}\right) \tag{2.5}$$

The presence of a finite nuclear rest mass has the effect of reducing the density of final electron states, due to nuclear recoil. Conservation of energy and momentum gives

$$E_f = \eta \left\{ E_i - \left(\omega + \frac{\hbar^2 \omega^2}{2Mc^2} \right) \right\} \tag{2.6}$$

where

$$\eta = \left[1 + \frac{2E_i}{Mc^2} sin^2\left(\frac{\theta}{2}\right) \right]^{-1} \tag{2.7}$$

is the nuclear recoil factor.

2.2 PWBA

Many references on PWBA are available (Walecka[20] , Lee[21] , *etc.*). An abbreviated description is supplied here, relating the matrix elements of electromagnetic operators connecting the nuclear initial and final states, to nuclear structure factors which may be determined directly from experiment. The notation will follow a review article by Heisenberg[22] .

In inclusive electron scattering (e, e'), the initial and final states of the electron are measured. Quantum electrodynamics provides a precise description of the electron wave functions and thus the associated electron charge and current. The interaction with the nucleus is given through the charge–charge and current–current interactions. The total interaction, therefore, is specified once the nuclear charge and current densities have been determined. The nuclear matrix elements

of the electromagnetic operators can be written in terms of reduced matrix elements by use of a multipole expansion and the Wigner–Ekhart theorem.

$$\langle \Psi_f | \rho^{op}(\vec{r}) | \Psi_i \rangle = \sum_{L,M} \langle J_i M_i L M | J_f M_f \rangle \; \rho_L(r_N) \, {Y_L}^{*M} \tag{2.8}$$

$$\begin{aligned} \langle \Psi_f | \vec{J}^{op}(\vec{r}) | \Psi_i \rangle = \sum_{L,M} & \langle J_i M_i L M | J_f M_f \rangle \times \\ & [J_{L,L-1}(r_N) \, \vec{Y}^*{}_{L,L-1}{}^M + J_{L,L}(r_N) \, \vec{Y}^*{}_{L,L}{}^M + \\ & J_{L,L+1}(r_N) \, \vec{Y}^*{}_{L,L+1}{}^M] \end{aligned} \tag{2.9}$$

The reduced matrix elements $\rho_L(r_N)$, $J_{L,L-1}(r_N)$, $J_{L,L+1}(r_N)$, and $J_{L,L}(r_N)$ represent transition densities associated with the nuclear charge, transverse electric currents and magnetization respectively. The transition charge and electric transition current densities are related through the continuity equation,

$$\begin{aligned} (2L+1)^{\frac{1}{2}} \, \frac{\omega}{c} \rho_L(r) = & L^{\frac{1}{2}} \Big(\frac{L-1}{r} - \frac{d}{dr} \Big) \, J_{L,L-1}(r) \\ & - (L+1)^{\frac{1}{2}} \Big(\frac{L+2}{r} - \frac{d}{dr} \Big) \, J_{L,L+1}(r) \end{aligned} \tag{2.10}$$

where $\hbar\,\omega$ is the excitation energy.

The PWBA cross section is given by

$$\begin{aligned} \frac{d\sigma}{d\Omega} = & \Big(\frac{d\sigma}{d\Omega} \Big)_{Mott} \eta \, Z^2 \Big\{ \sum_{L \geq 0} |F_L^C(q)|^2 + \Big(\frac{1}{2} + tan^2 \frac{\theta}{2} \Big) \times \\ & \sum_{L \geq 1} \Big[\, |F_L^E(q)|^2 + |F_L^M(q)|^2 \Big] \Big\} \end{aligned} \tag{2.11}$$

where

$$\eta = \text{nuclear recoil factor} \tag{2.12}$$

and

$$\Big(\frac{d\sigma}{d\Omega} \Big)_{Mott} = \frac{\pi \alpha^2}{E_i^2 sin^4 \left(\frac{\theta}{2} \right)} cos^2 \frac{\theta}{2} \tag{2.13}$$

is the cross section derived from electrons scattering off a point charge.

The nuclear structure information is entirely contained in the Coulomb (or longitudinal) form factor $F_L^C(q)$ and the transverse form factors F_L^E and F_L^M. Since the relative contribution of the transverse form factors to the total cross section has an angular dependence of $(\frac{1}{2} + tan^2\frac{\theta}{2})$, the transverse and longitudinal components may be separated by measuring the cross section at a variety of energies and scattering angles.

These nuclear structure factors are related to the transition charge and current densities through Fourier–Bessel transforms

$$F_L^C(q) = \left(\frac{\hat{J}_f}{\hat{J}_i}\right) \int_0^\infty \rho_L(r)\; j_L(qr) r^2 \; dr \tag{2.14}$$

$$F_L^M(q) = \left(\frac{\hat{J}_f}{\hat{J}_i}\right) \int_0^\infty J_{L,L}(r)\; j_L(qr) r^2 \; dr \tag{215}$$

$$\begin{aligned} F_L^E(q) = &\left(\frac{\hat{J}_f}{\hat{J}_i}\right)\Big[\int_0^\infty (L+1)^{\frac{1}{2}}\; J_{L,L-1}(r)\; j_{L-1}(qr) r^2 \; dr \\ &+ \int_0^\infty L^{\frac{1}{2}}\; J_{L,L+1}(r)\; j_{L+1}(qr) r^2 \; dr\Big] \end{aligned} \tag{2.16}$$

The dependence upon the spherical Bessel functions $j_L(qr)$ gives the form factors local maxima and minima, much like a diffraction pattern, when mapped in momentum space. The main effect on the nuclear densities is seen in the amplitudes and relative positions of the maxima and minima.

Coupling the continuity equation (2.10) with equations (2.14) and (2.16) reduces to two the number of independent densities which can be determined by a complete (e, e') electron scattering experiment, the charge density and one of the current densities. The third density is then specified by the continuity equation.

Selection rules due to time reversal invariance determine that the transition charge and transverse electric currents are non–zero only for natural parity transitions ($\Delta\pi = (-1)^L$), while the transverse magnetic current is non–zero only for unnatural parity transitions ($\Delta\pi = (-1)^{L+1}$).

In nuclei where the ground state angular momentum is zero, such as ^{208}Pb, only transitions with multipolarity constrained by $L = J_f$ may participate, and the sums in equation (2.11) reduces to single terms. Use of the time invariance and angular momentum selection rules and a separation of longitudinal and transverse form factors makes possible the extraction of experimental transition charge and current densities in an unambiguous way.

2.3 Radiative Corrections

Processes other than a simple one photon exchange influence the measured state of scattered electrons, and must be included in an analysis of electron scattering data[19] [22] [23]. Higher order corrections to the PWBA may in general be classified as being either static or dynamic effects. The dynamic effects, also known as dispersion corrections, arise from the excitation of the internal nuclear degrees of freedom through a multiple photon exchange. Effects due to the excitation of the nucleus into an intermediate state are considered small and are difficult to include in a calculation. Contributions to the cross section from these effects may be considered negligible and will be ignored in this work.

Static corrections, which do not excite the nucleus into an intermediate state, may be accounted for much more easily than dispersion effects. Static corrections are classified as Coulomb or radiative and are partially represented by the Feynman diagrams shown in Figure 2.2.

The Coulomb correction diagrams are those which involve an elastic interaction with the nucleus through the exchange of soft, low frequency photons and are responsible for the disortion of the electron wave function. These corrections are calculated in the Distorted Wave Born Approximation (DWBA), discussed in Section 2.4.

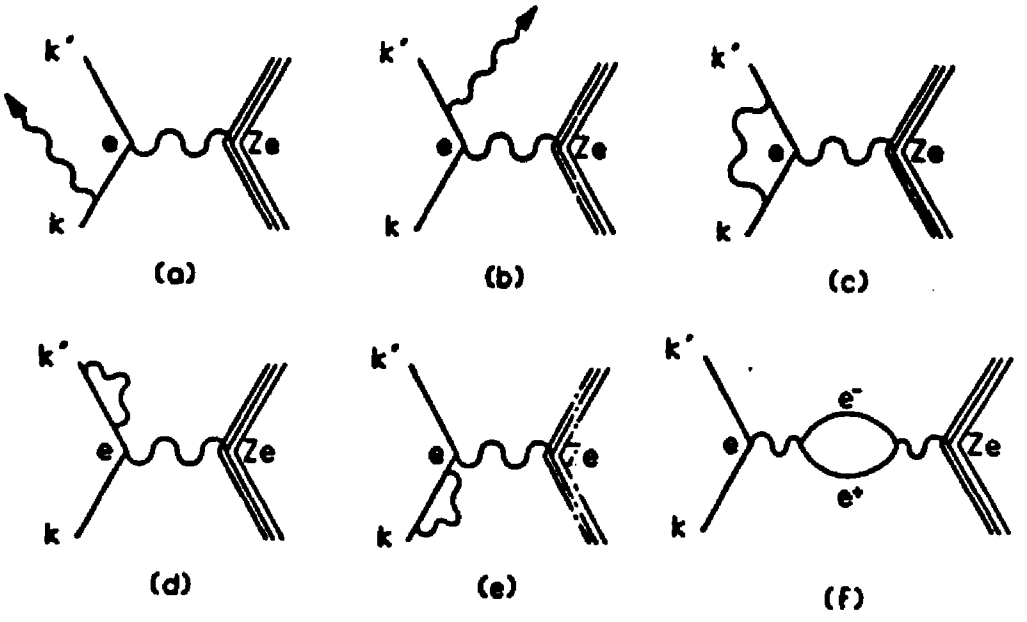

Fig.2.2 Diagrams representing radiative corrections.

Energy losses due to the electrons either interacting with their own radiation field or momentum changes from non–nuclear interactions between the electron and the target matter are termed radiative effects. Corrections arising from the electron's self–interaction lead to renormalizations of the electron's charge and mass and are proportional to the target thickness. Another type of correction to the same order is large angle Bremsstrahlung, involving the emission of hard photons near the primary scattering center. Higher order terms, proportional to the target thickness squared, come from processes outside of the main scattering region. Small angle bremsstrahlung and ionization losses from collisions with atomic electrons contribute to the energy loss tail of the scattered electrons and to the broadening of the measured energy resolution in the scattered electron spectrum.

Broadening effects, which come from statistical fluctuations in the amount of energy radiated, are important for a high resolution experiment such as this

one. Minimization of the effective target thickness is a practical implication of the target thickness dependence of the radiative corrections. The actual corrections to the experimental cross sections are made when performing the line–shape fitting to the energy loss spectrum using the fitting code ALLFIT(Sect 3.9).

2.4 DWBA

In the PWBA, plane wave electron wave functions interact with the nucleus at a point via a one photon exchange, and then scatter as spherical Bessel functions. This simple picture is useful in gaining a qualitative understanding of the relation between the underlying nuclear structure and inelastic electron scattering cross sections. For light nuclei the electromagnetic coupling constant ($Z\alpha = \frac{Z}{137}$) is small enough that a one photon exchange approximation is a viable first order approximation of the scattering process. For large Z nuclei such as ^{208}Pb, the distortion of the electron wave function from the coulomb field of the nucleus must be included in any realistic calculation. The Distorted Wave Born Approximation (DWBA), as calculated in the computer codes FOUBES1, FOUBES2 and FOUBES2A by Heisenberg, has been derived in several references [21] [22] [24] .

Although the electron interacts with the nuclear coulomb field through a multiple soft photon exchange, the basic assumption made in the DWBA is that only one photon is responsible for exciting the nucleus. The electron wave functions are solutions of the Dirac equation in a spherical coulomb potential. The distorted electron waves are represented through phase shifts from a partial wave expansion of the incoming and outgoing electron wave functions, the initial and final nuclear states and the interaction Green's function. From first order time dependent perturbation theory, the cross section for a transition of mulipolarity L is given by,

$$\frac{d\sigma_L}{d\Omega} = \frac{E_f^2}{(2\pi\hbar c)^2} \sum_{M,m,m'} \frac{1}{2J_i+1} |A_{if}(LMmm')|^2 \qquad (2.18)$$

where A_{if} is the nuclear matrix element between the initial and final nuclear states of the interaction Hamiltonian.

Unlike the PWBA, the relations between transition charge and current densities and the longitudinal and transverse cross sections are not decoupled in the DWBA. Inelastic electron scattering producing a transition in the charge density will have a transverse component in addition to the longitudinal component. In the DWBA, the fundamental nuclear structure quantities are the transition charge and current densities which must be unfolded from longitudinal and transverse form factors.

For the purpose of displaying the data, the experimental form factors are plotted as a function of q_{eff}, where,

$$q_{eff} = q\left(1+\frac{4}{3}\frac{Z\alpha\hbar c}{E_i R_{rms}}\right) \tag{2.19}$$

Through the use of q_{eff} one accounts approximately for the shift in the mean scattering energy which is given to first order by the incident electron energy plus the coulomb energy at the surface of the nucleus. This makes q_{eff} convenient for plotting purposes since it helps correct for the energy dependence of the form factor.

2.5 DWBA Calculations

Several programs have been developed by J. Heisenberg, based on the GBROW program and the work by Tuan, Wright and Ouley[24] , to determine transition densities from experimental cross sections. The nature of the transition, whether purely longitudinal or transverse or a combination of both components, and theoretical assumptions such as the application of mean field models, are input into one of the DWBA programs. Depending upon the initial assumptions, the codes perform a least squares fit to the data in coordinate space by varying parameters describing the radial transition densities.

The parametrization of nuclear densities in the DWBA codes may be chosen in one of three analytical models; a Fourier–Bessel expansion (FBE), a sum of Woods–Saxon single particle wave functions (SPM), or a Gaussian times a series

of polynomials (G–P). The choice of models is determined by the precision of the data and by assumptions concerning the nuclear structure of the transition.

In the case where data extends over a broad region of momentum transfer, the FBE provides an excellent means of describing densities as an expansion of spherical Bessel functions. A cut–off radius R_0, which for ^{208}Pb was taken to be 12.0 fm, is introduced to restrict non-zero values of the radial coordinate to $r \leq R_0$. In the FBE model, transition densities are taken to be a sum of fifteen expansion coefficients times the appropriate spherical Bessel function,

$$\rho_L(r) = \sum_{\mu=1}^{15} A_\mu q_\mu^{L-1} j_L(q_\mu^{L-1} r) \tag{2.20}$$

$$J_{L,L+1}(r) = \left(\frac{2l+1}{l+1}\right)^{\frac{1}{2}} \frac{\omega}{c} \sum_{\mu=1}^{15} B_\mu j_{L+1}(q_\mu^L r) \tag{2.21}$$

$$J_{L,L}(r) = \sum_{\mu=1}^{15} C_\mu j_L(q_\mu^L r) \tag{2.22}$$

where,

$$j_L(q_\mu^L R_0) = 0 \tag{2.23}$$

To construct transition densities model independently, data would have to extend over an infinite range of momentum transfer. As shown by Dreher and Rothhaas[26] reasonable results are obtained by inserting some model dependence in the DWBA fit at high momentum transfer. Although the expansion is truncated from a complete infinite set to 15 terms, the data often must be extended artificially in the region $q_{max} \leq q \leq q_{15}$, where q_{max} is the highest momentum transfer measured. A set of pseudodata is calculated which represent uncertainties to some exponential upper limit input into the program. Another source of model dependence enters from constraining the shape of the transition density at large r to an exponential tail in coordinate space. Both of these constraints contribute to uncertainty in the overall fit to the experimental data.

Radial densities for which data does not extend over a large enough range of momentum transfer to permit the use of a FBE least squares fit, may still be parametrized with a simple polynomial times gaussian line–shape (G-P). Up to the five coefficients A_n may be varied, as well as a radial scaling factor r_0. The charge density is expressed as,

$$\rho_L(r) = \sum_{n=1}^{5} A_n \left(\frac{r}{r_0}\right)^{2n+L} e^{-(r/r_0)^2} \tag{2.24}$$

The G-P expansion is useful for collective excitations which display strong gaussian shapes in the radial density at the surface. One also is spared the neccessity of including a tail bias and pseudodata in the fit as in the FBE, as it is implicitly contained in the choice of the model.

The DWBA programs may also employ a single particle model (SPM) to describe transition densities. If the assumption is made that the transition is due to a sum of particle–hole excitations in a mean field, the SPM will yield microscopic nuclear structure information. For the charge density, the form of the transition density is given by,

$$\rho_\lambda(r) = \sum_{a,b} \frac{1}{J_f} S_{ab,\lambda}\ \rho_\lambda^{ab}(r) \tag{2.25}$$

where the spectroscopic amplitude $S_{ab,\lambda}$ is the result of the Wigner–Eckart theorem to produce the reduced matrix elements as weighting factors,

$$S_{ab,\lambda} = \frac{J_f}{\lambda} \langle \psi_f || [a_a^\dagger \otimes a_b]_\lambda || \psi_i \rangle \tag{2.26}$$

The single particle orbitals involved in the excitation are denoted by a, b, and $a_a^\dagger$, a_b are creation and destruction operators. The form of the Wigner–Eckart theorem used in these calculations give $S_{ab,\lambda} = 1$ for pure single particle transitions. The single particle charge density is expressed in terms of the single particle wave functions $u_i(r)$, as,

$$\rho_\lambda^{ab}(r) = C_{ab,\lambda}\ u_a(r)\ u_b(r) \tag{2.27}$$

where $C_{ab,\lambda}$ is a geometrical factor involving Clebsch–Gordan coefficients.

The transition current densites are the result of both the nucleonic charge, or the convective current, and the magnetization of the nucleons. These densities are expressed in the SPM as,

$$J^{ab,C}_{\lambda,\lambda+1} = \frac{\hbar}{2mc} C_{ab,\lambda} \frac{1}{\sqrt{\lambda+1\lambda}} \Bigg\{ (\lambda+1) \left[\frac{du_a}{dr} u_b - u_a \frac{du_b}{dr} \right] + [l_b(l_b+1) - [l_a(l_a+1)] \frac{u_a u_b}{r} \Bigg\} \tag{2.28}$$

$$J^{ab,M}_{\lambda,\lambda+1} = \mu \frac{\hbar}{2mc} C_{ab,\lambda} \frac{1}{\sqrt{\lambda+1\lambda}} (\chi_b - \chi_a) \left(\frac{d}{dr} - \frac{\lambda}{r} \right) u_b u_a \tag{2.29}$$

$$J^{ab,C}_{\lambda,\lambda} = \frac{\hbar}{2mc} C_{ab,\lambda} \frac{1}{\sqrt{\lambda(\lambda+1)}} (\chi_a + \chi_b - \lambda)(\chi_a + \chi_b + \lambda + 1) u_a u_b \tag{2.39}$$

$$J^{ab,M}_{\lambda,\lambda} = \mu \frac{\hbar}{2mc} C_{ab,\lambda} \frac{1}{\sqrt{\lambda(\lambda+1)}} \left[\frac{\lambda(\lambda+1)}{r} + (\chi_a + \chi_b) \left(\frac{d}{dr} + \frac{1}{r} \right) \right] u_b u_a \tag{2.31}$$

$$J^{ab,C}_{\lambda,\lambda-1} = \frac{\hbar}{2mc} C_{ab,\lambda} \frac{1}{\sqrt{\lambda\lambda}} \Bigg\{ -\lambda \left[\frac{du_a}{dr} u_b - u_a \frac{du_b}{dr} \right] + [l_b(l_b+1) - [l_a(l_a+1)] \frac{u_a u_b}{r} \Bigg\} \tag{2.32}$$

$$J^{ab,M}_{\lambda,\lambda} = \mu \frac{\hbar}{2mc} C_{ab,\lambda} \frac{1}{\sqrt{\lambda\lambda}} (\chi_b - \chi_a) \left(\frac{d}{dr} - \frac{\lambda+1}{r} \right) u_b u_a \tag{2.33}$$

where $\chi = (l-j)(2j+1)$ and μ is the magnetic moment of the nucleon participating in the excitation.

The single particle wave functions u_n are calculated from either a Woods-Saxon potential with a spin-orbit coupling or a self-consistent Hartree-Fock potential. The adjustable parameters in the potential are the radius and well depth,

which are independent for each orbital, a spin–orbit coupling constant and the well diffuseness parameter, which are held fixed for all wave functions. An amplitude for each particle–hole excitation is varied in the least squares fit to the cross sections. The well depth for each orbit is taken to be the value which produces the correct experimentally observed separation energies. Hartree–Fock radial wave functions are expressed in terms of a Fourier–Bessel expansion, with no adjustable radial parameters.

To be compared to the experimental data, the densities given above must be corrected for the finite size of the nucleons. In momentum space, this means that the nucleon charge and magnetization form factors are multipiled by the particle–hole form factors. The proton charge form factor is taken from Simon *et al.*[26] . The magnitude of the neutron charge form factor is small enough to be ignored in these calculations.

The program FOUBES1 is used to determine either transition densities from data for which one assumes that only one density is contributing to the cross section. This is the case for excitations which are purely longitudinal and the $\rho_L(r)$ terms are calculated, or for magnetization densities from unnatural parity states from which the $J_{L,L}$ terms are determined. Any of the analytical modes described above may be used with FOUBES1.

The analysis of data with a non–negligible transverse electric form factor is done with FOUBES2 or FOUBES2A. The program FOUBES2 performs a simultaneous fit to the charge and transverse electric form factors employing the FBE method. FOUBES2A permits the use of the G–P and SPM expansions in the same manner.

Chapter 3

The Experiment

Data for this experiment were taken at the MIT Bates Linear Accelerator during three separate runs in 1985, 1986 and 1988. Electron beam energies ranging from 100 to 280 MeV were incident on isotopically enriched ^{208}Pb targets and detected via the 900 MeV Energy Loss Spectrometer (ELSSY) . Data was acquired and analyzed on–line with a PDP 11/45 computer for the 1985 and 1986 running periods and a MicroVax utilizing the Los Alamos Q-system for the 1988 runs.

3.1 The MIT Bates Linear Accelerator

The Bates Accelerator came on line in 1972 to meet the need for a high current/high duty factor electron accelerator capable of attaining the energy resolution neccessary to study the discrete level structure of atomic nuclei. The resolution first achieved at Bates on ELSSY improved resolution by a factor of 10 over the older generation of electron accelerators. The linac and the associated instrumentation has been described in previous publications[27][28] and countless theses.

The Bates LINAC is a pulsed electron accelerator driven by 10 4MW/65kM klystrons and is able to deliver electron energies ranging from 70 to 400 MeV for a single pass through the LINAC. A recirculator exists enabling the incident electron energy to be increased to over 800 MeV but was not used for this experiment. The maximum repetition rate used was 600 $\frac{pulses}{sec}$; the maximum pulse length is 15 μsec; and the maximum duty cycle is 5.6% for energies less than 200 MeV, 1.8% for energies greater than 200 MeV. Beam current was monitored by two independent torroids stationed near the scattering chamber accurate to within 1 part in a thousand. The information from the torroids were integrated and read into the data file at the end of a run to provide a measure of the incident electron flux on the target. Although average beam currents of up to 60 μA were available,

due to target considerations the above parameters were set so that the average current was kept below 25 μA.

Figure 3.1 is a schematic diagram of the steering magnets used to bring the beam from the accelerator, through the Beam Switch Yard (BSY) onto the target via beam line B, and out to the beam dump. The quadrupole magnet at Q0 optically decouples the beam in the BSY from the accelerator magnets. The system of quadrupoles Q1,Q2 and Q3 along with two 7° bending magnets form an achromatic transport system to the B3 bending magnet. At Q2 the beam is spread energetically in the horizontal direction where two titanium slits select an energy range typically at 0.3 % of the nominal electron energy.

The beam is refocused just upstream of the SB3 bending magnet and the SQ4 quadrupole, which function to image the object point focus at the target position, to disperse the beam monochromatically at the target, and to bend the beam an additional 23° into the North Hall Spectrometer Room. The beam is rotated 90° by a series of quadrupoles so that the energy dispersion is in the vertical direction to match the vertical geometry of ELSSY. The quadrupole Q7 acts as an adjustment to the beam dispersion so that the dispersion on target matches the dispersion of the spectrometer.

As the beam traverses the North Hall spectrometer room, it enters the target chamber. Scattered electrons enter the spectrometer, which bends scattered electrons down vertically into a detection area located 8 meters below the beam line. Most of the electron flux, however, passes through the target and into a large diameter pipe which carries the beam to the dump. At the dump the beam is deflected by the dump magnet to minimize background events.

3.2 The Energy Loss Spectometer (ELSSY)

The energy loss principle, described in detail by Bertozzi *et al.*[27] , offers the experimenter the advantage of using a broad electron energy range as defined by the energy slits S1 (Figure 3.1). These slits are usually kept approximately 10 inches apart, permitting an energy range of 0.3% to be incident on the target.

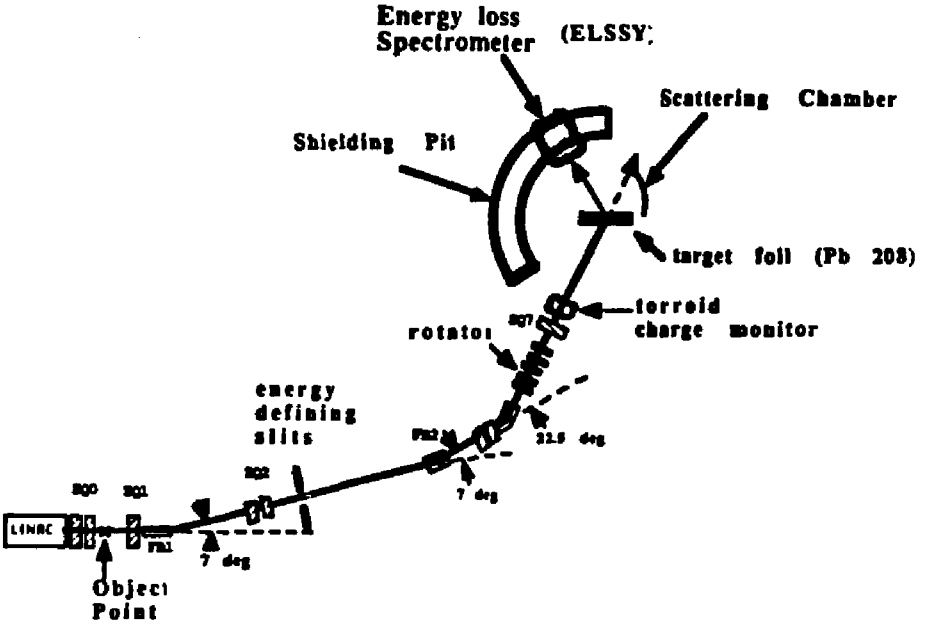

Fig 3.1 Beam Switchyard

Thus, the incident electron flux is much higher than in conventional systems where the beam must be kept as monochromatic as possible.

A schematic layout of ELSSY is shown in Figure 3.2. The spectrometer consists of a split pole magnet system with a 2.23 meter radius of curvature which act as the second half of an achromatic transport system. The magnetic field of the two dipole magnets are monitored continuously by two nuclear magnetic resonance probes accurate to within 0.001%. The spectrometer entrance is attached to the target chamber via a sliding seal mechanism which facilitates angle changes of the spectrometer. The entire spectrometer, along with the target chamber and the beam line are evacuated to 10^{-5} *torr*. Vertical and horizontal slits, defining the scattering aperture, are stationed inside the spectrometer and have a maximum solid angle acceptance of 3.33 *millisteradians*. Electrons are then bent ~90°, 8.1 meters into a concrete floor where a thin mylar exit flange separates the spectrometer from the open air and the detector system.

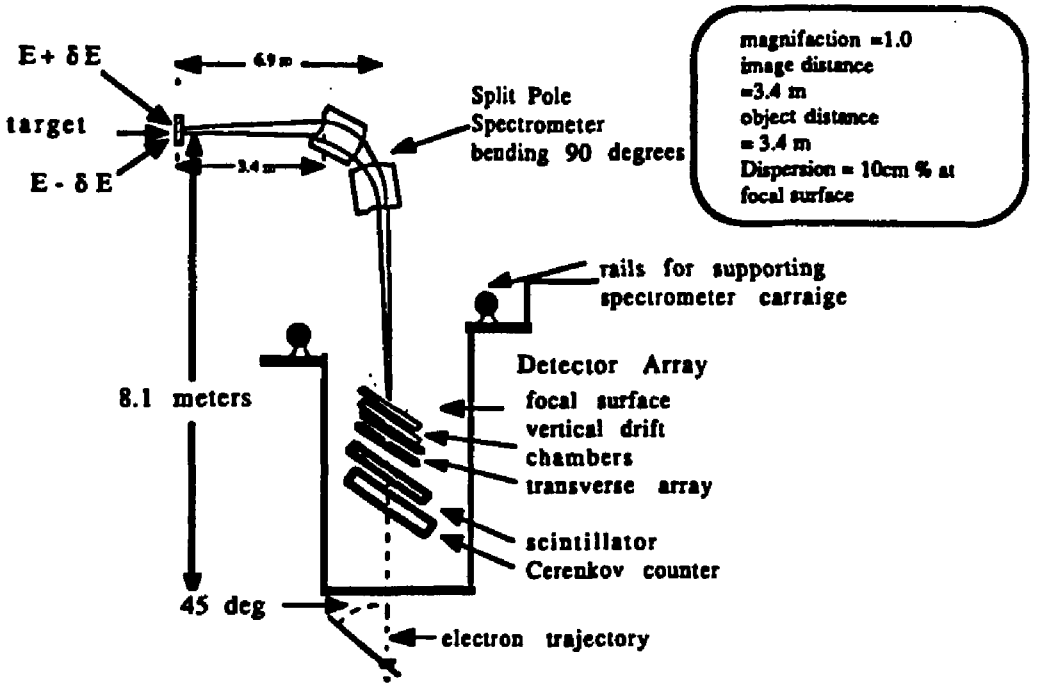

Fig 3.2 Energy Loss Spectrometer System

The spectrometer focuses scattered electrons according to the energy loss principle with approximately unit magnification, to a focal plane intersecting the detector array. However, magnetic field aberrations cause distortions in the focal plane surface. The spectrometer dipoles are constructed so that only third order field aberrations play a significant role, primarily curving the focal plane surface perpendicular to the momentum axis. A precise tracing of the electron trajectory from the detector to the focal plane surface must be performed to determine the electron momentum with a high degree of accuracy. The field geometry is such that electrons focused along the central ray pass through the focal plane at a 45° angle.

3.3 Targets

Twelve thin 99.86% isotopically enriched ^{208}Pb targets constructed by MicroMatter Inc. were used for this experiment. Target thicknesses ranged from 2.5 $\frac{mg}{cm^2}$ to

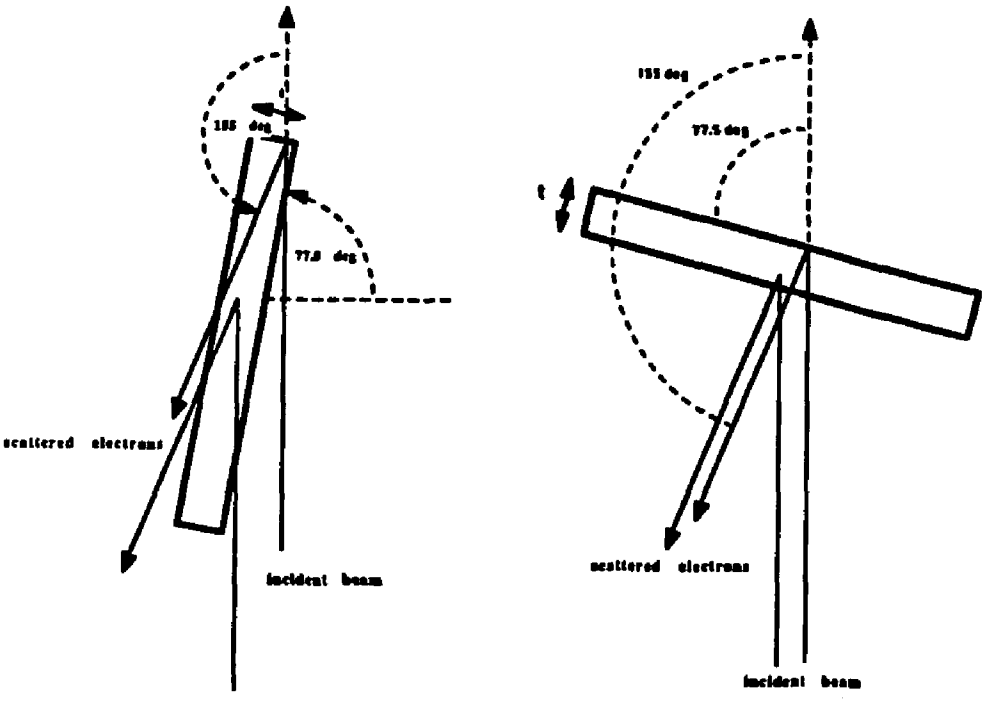

Fig 3.3 Target geometries – transmission mode (left), reflection mode (right)

4.0 $\frac{mg}{cm^2}$. The targets used in the April 1985 run were evaporated onto a collodion backing which evaporated when exposed to the beam. For the May 1986 and January 1988 runs, we used a 20.0 $\frac{\mu gm}{cm^2}$ carbon foil backing to provide support and to help dissipate heat.

The target was placed in transmission mode which required a target angle of $\theta/2$ relative to the the direction of the beam, where θ is the scattering angle. This insures that the average path the electron traverses in the target is independent of the depth in the target that the scattering takes place (Figure 3.3), reducing energy loss effects which are dependent upon the target thickness, but increasing the total effective target thickness. Hence, a nominal target thickness of 2.5 $\frac{mg}{cm^2}$ at 77.5° becomes an effective target thickness of ~11.55 $\frac{mg}{cm^2}$.

An alternative target geometry is the reflection mode. In this target alignment, the incident electron bisects the angle made by the scattering angle and the ray perpendicular to the face of the target. In this case, the effective target

thickness is not constant but a linear function of the actual target thickness, depending upon how far into the target the scattering occured. Reflection mode is not the optimal target geometry for high resolution experiments since energy losses due to the effective target thickness vary. In the electron scattering experiment on ^{208}Pb by Lichtenstadt[6], the reflection mode was used for data taken at 160° for the purpose of increasing the effective target surface seen by the incident beam. In this experiment, we took backward scattering angle data at 155°, both to increase the count rate and to use the transmission mode target geometry. In Lichtenstadt's experiment, the energy resolution of the backward angle data was 60 KeV, 20 keV worse than the forward angle resolution of 40 KeV. Using the transmission mode, the backward angle data (20 keV) was degraded by only 6 KeV from the forward angle data (14 keV).

3.4 Detector Array

The focal plane detector system, as shown in Figure 3.4, consists of two vertical drift chambers (VDCI and VDCII), two multiwire proportional chambers (MWPC) also known as the transverse array (TA), a plastic scintillator (S1), a Cerenkov counter (C1), and the associated readout electronics.

C1 is a lucite Cerenkov counter designed to emit signals when relativistic electrons traverse the medium. These signals, taken in coincidence with a signal from S1, provide a start for the readout of the position sensing chambers (VDCI, VDCII, and the TA). The start usually demands at least a two–fold coincidence between C1 and S1 and in some cases a three-fold coincidence is used including the TA signal.

The two MWPC which form the transverse array are offset from each other along the axis of measurement so that the sensing wires of one MWPC bisects the cells formed by the sensing wires of the other. Both MWPC are hardwired into the same readout electronics, doubling the precision of the TA. The transverse array functions to determine the position of the event along the direction perpendicular to the momentum axis.

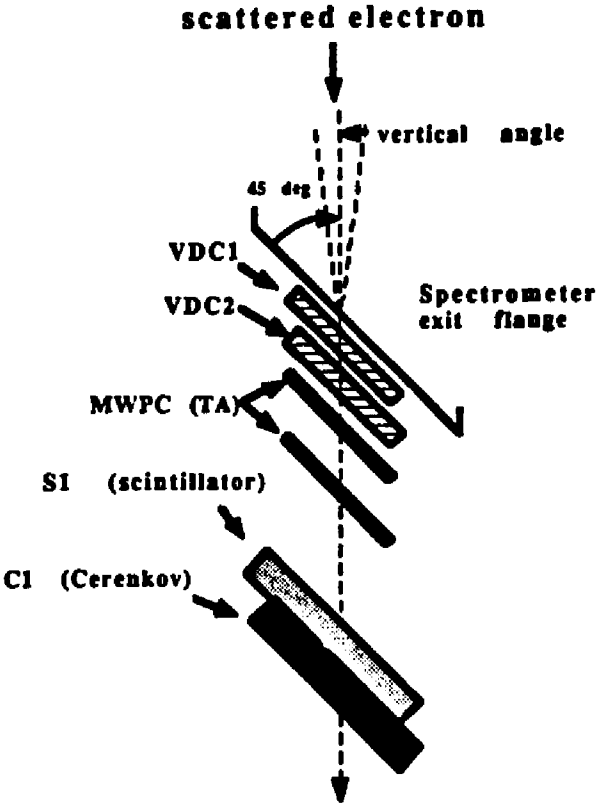

Fig 3.4 Detector System

The two vertical drift chambers determine the position of events along the momentum axis of VDCI and the angle at which the electron trajectory intersects the plane defined by the sensing wires of VDCI. As shown in Figure 3.4, the detector array is set at a 45° angle to the trajectory of the electron along the central ray of the spectrometer. This geometry approximately mimics that of the actual focal plane. The angle determined for each event is measured in terms of its deviation from the angle made by the central ray.

Bertozzi *et al.*[28] describe in detail the physical operation of the vertical drift chamber. The chambers are filled with an isobutane–argon gas mixture which is ionized by the passing relativistic electron. There are 99 sensing wires held at ground relative to two high voltage aluminum mylar planes on either side of the

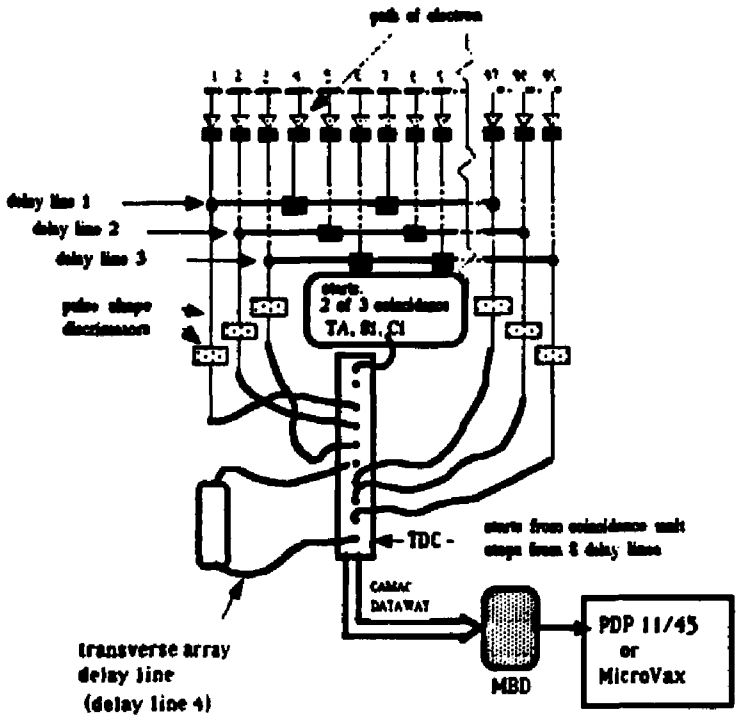

Fig 3.5 Delay line Readout

sensing plane. The electric field lines are nearly linear, and drift velocities for ionized particles are constant except very near the sensing wire. Thus the drift time can be correlated with the drift length and the region of ionization can be determined.

Every third sensing wire in the VDC is hardwired into one of three delay lines, which is described schematically in Figure 3.5. When a pulse from the sensing wire reaches a delay line, the pulse splits towards both ends of the delay line and provide stops for a time–to–digital converter (TDC) which was started by the C1 and S1 signals in coincidence. These times are then read by the CAMAC/MBD system into the computer for on-line analysis. Denoting these times from either end of a given delay line as t_r and t_l, the wire number n of the sensing wire and the drift time t_{drift} can be decoded from the following formulas

$$t_r - t_l = 33\tau + 2t_{drift}$$

$$t_r + t_l = 2n\tau - 33\tau$$

where 33 is the number of sensing wires connected into one delay line and τ is the intertap delay, nominally about $1.5nsec$.

The drift times from each of the three delay lines, along with the corresponding wire or channel number, allows the electron track to be deduced from three points along the trajectory. The addition of VDC2 improves the precision of the vertical angle (the deviation of the trajectory from 45°) by adding another point along this line, at a much larger relative distance from the three points given by VDC1. Since the vertical angle plays an important role in determining corrections due to focal plane aberrations, the addition of the second VDC is critical for any high resolution experiment on ELSSY, improving the resolution by as much as 25%.

3.5 High Resolution Considerations

'Tuning' the beam through the adjustment of the BSY magnets has a large effect on the energy resolution at the focal plane. Typically six to twelve hours of beam time were spent at each accelerator energy in this process. The upstream optics were adjusted first due to the dependence of Q2 upon Q0 and Q7 upon Q4, although in the interest of precision Q4 and Q7 were adjusted iteratively. During the beam tuning, the dispersion of the beam on the target is made to match the dispersion of the spectrometer. This means that the monochromatic components of the beam are dispersed spatially on the target in such a way that electrons will be focused at the focal plane as a function of their energy loss only, regardless of their incident energy. The separation of events with differing energy losses less than $\frac{\Delta E}{E} \sim 10^{-4}$ is possible even with an incident energy spread of $\frac{\Delta E}{E} \sim 3 \times 10^{-3}$.

A large contribution to the momentum resolution of the experiment comes from the target. As the electron passes through the target, it experiences an energy loss due to ionization collisions with atomic electrons. This effect roughly contributes to peak broadening at about 0.5 $\frac{kev-cm^2}{mg}$. However, for very thin

targets, irregularites in the target thickness is the more important effect and is difficult to quantify. However, peak resolution was a function of both beam current and the amount of time the target was exposed to the beam. For this reason, currents were generally constrained to be less than $20\mu A$. It was also necessary to move the spectrometer to forward angles periodically to check resolution.

3.6 Data Processing

The raw data are read from the TDC's and ADC's stationed in the CAMAC crate via the Multi-Branch Driver (MBD). The MBD is a programmed interface between the CAMAC dataway and the PDP11/45 or MicroVax. Entry into event processing routine of the MBD is accomplished by the reception of a Look–At–Me (LAM) generated by a start on the VDC1 readout TDC. Each event consisted of 24 words of information which were accumulated in a buffer and dumped to the computer for on–line analysis. All events were also written to tape for off–line analysis.

With the development of an off-line analysis code, it became possible to perform all of the pertinent software corrections off-line. This task was a major effort in the data replay .

The final energy loss spectrum output from the event analyzer is a 3072 channel fine spectrum. Corrections from several sources, notably focal plane aberrations, were applied to the energy loss spectrum.

3.7 Focal Plane Corrections

Each event detected by the vertical drift chambers is correlated with the delay line tap which has the smallest drift time for any given event. Using the drift times from adjacent detecting wires to reconstruct the trajectory of the scattered electron through VDC1, a fine spectrum is calculated. This spectrum is constructed assuming the focal plane is flat and the scattering aperture is point–like. In order to accommodate a finite scattering aperture and the curvature of the focal plane

along the direction transverse to the energy loss axis, along with higher order focal plane distortions, several corrections must be applied to the fine spectrum.

A correction to the energy loss due to nuclear recoil is assumed to be linear in the scattering angle θ, which corresponds to the channel measured by the transverse array. A correction as a linear function of the vertical angle is also applied as a first order correction to the curvature of the focal plane. The variation in these first order coefficients as a function of focal plane position is a measure of higher order distortions.

Second order or higher distortions in the focal plane are functions of the transverse angle (θ), the vertical angle (ϕ) and the coarse channel(C) along the momentum axis. In the on–line analysis code higher order corrections were performed through a Taylor series expansion of θ, ϕ and C. The Taylor series coefficients used in the on–line code were also used in the off-line analysis, but the resulting corrected fine spectrum still displayed deviations in the peak resolution depending upon C, θ and ϕ. Instead of attempting to correct the Taylor series coefficients, a more direct method was used.

High statistics data was taken in the event–by–event mode on a thin ($5.82\ \frac{mg}{cm^2}$) ^{92}Mo with the spectrometer magnets set such that the elastic peak appeared in six positions across the focal plane in six different runs. In the data replay, the events under the elastic peak were binned according to θ and ϕ, resulting in 96 sub–histograms of the ^{92}Mo elastic peak . Ideally, the centroid of each of these sub–peaks should be at the same focal plane position. The deviation from a mean centroid position was determined for each of the 96 sub–peaks and placed in a table accessed by the off–line code. This was done for each of the six spectrometer settings for a total of 576 focal plane offsets. During the ^{208}Pb replay, one of these offsets was added per event to the corrected fine spectrum depending on the transverse angle, vertical angle and coarse channel positions. Generally, this procedure had the effect of increasing the energy resolution of peaks detected away from the center of the focal plane. For levels near the center of the focal plane, higher order corrections appear to be less important, and the improvement

in resolution was not significant.

3.8 Data Reduction

The accumulated corrected fine energy loss spectra for each data point in the momentum transfer were summed to provide the final energy loss histograms for line shape fitting. The ALLFIT program, originally obtained from MIT, was used to subtract random background events, delineate the various peaks from the elastic and discrete state channels and to calculate raw cross sections.

ALLFIT performs a least squares fit to the data using a ten parameter chi-square space. A hypergaussian line shape with five free parameters was chosen to represent the centroid region of each peak and was matched on the left and right to decaying exponential functions. A theoretical model for the radiative tail was folded in on the energy loss side of the peak to account for non-nuclear energy losses such as bremsstrahlung and other effects discussed in Chapter 2. Parameters defining the radiative tail, peak resolution and left–right asymmetry were fit to a strong state and then held constant during the analysis of the entire spectrum.

The raw cross sections generated by the ALLFIT program were scaled by several factors before either a DWBA or a model dependent analysis could be reliably performed. Corrections for both experimental deadtime and an artificial deadtime imposed by software cuts are calculated explicitly. Other corrections which for various reasons must be applied are folded together in the normalization. All of these corrections are applied globally for each data point. For this reason, care must be used during both the running of the experiment and the event analysis to reject runs which may have local inefficiencies in the energy loss spectrum.

Hardware deadtime

Signals from the coincidence logic which indicate a valid event are not always processed by the event analyzer. If two coincidences occur within the trigger

timing envelope of 300 *ns*, both coincidences are registered as vetoes and the TDC's are cleared. A hardware deadtime correction can be calculated as

$$hardware\ deadtime(\mathrm{HDT}) = \frac{starts}{coincidences}$$

Unless the data rate is very high, the hardware deadtime correction is usually less than 1.0%.

Some ambiguity exists in the application of the HDT correction factor to the raw cross sections obtained from the line shape fitting program. The raw cross sections are reduced from an analysis of events which are totally good in the sense that they pass successfully the various software cuts. An assumption must be made that the number of totally good events not analyzed due to a hardware veto scales with the ratio of good events analyzed to the number of analyzer starts. This assumption is dependent upon the experimental conditions. If, for some reason, a large number of background events are interferring with hardware acceptance of valid events, the HDT correction will be spurious. Care must be taken during the running of the experiment and during the data analysis to not include data sets which have the characteristics of a high background rate.

Software deadtime

During the event analysis, a series of tests and cuts are administered to each start into the analyzer in an attempt to reduce the number of unphysical or poor quality events binned into the final energy loss spectrum. Due to inefficiences in the detectors, particularly the transverse array, and glitches in the electronics, not all events discarded in this manner should be thrown out. A software deadtime (SDT) correction factor must be calculated from the diagnostic histograms which contain events not accepted in the final energy loss spectrum, and applied to the raw cross sections. Two software correction factors are calculated, one for VDC1 and one for VDC2, and both are folded into the hardware deadtime before being applied to the raw cross sections. Milliman[29] describes in some detail the calculation of both the hardware and software deadtimes.

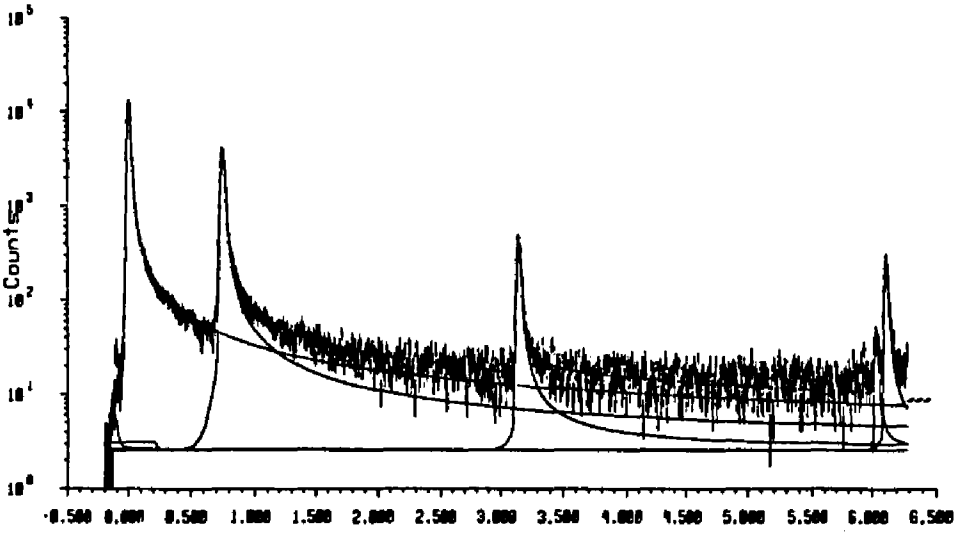

Fig 3.6 Energy Calibration Spectrum (BeO, E_i=250.0, $\theta = 40°$)

The total deadtime correction (TDTC) factor applied to the raw cross sections is given by

$$\text{TDTC} = \text{HDT} \times \text{SCDT1} \times \text{SCDT2}$$

Energy Calibration

During the course of the experiment, the energy of the beam is set to some nominal value by the beam operator as requested by the experimenter. The actual value of the energy can vary from the nominal value by several percent. It is neccessary therefore to perform an energy calibration by measuring the differential recoil between nuclei with different masses. The recoil factor is given by,

$$\eta = \left(1 + \frac{2E_i}{Mc^2} sin^2 \frac{\theta}{2}\right)^{-1}$$

By measuring the energy difference between measured levels with a well known energy (such as the elastic peak) of differing isotopes, it is possible to unfold the incident electron energy, provided the scattering angle is known. Figure 3.6 shows the energy differential provided by recoil between ^{16}O and ^{9}Be at a nominal energy of 250 MeV and a scattering angle of 40°.

While there exists a possible uncertainty in the scattering angle due to any deviations of the beam from 0° scattering angle, it is generally assumed that the measured scattering angle is correct to within 0.5 milliradians.

For $E_i << M_t c^2$, the recoil energy differential between elastic levels of nuclei with differing masses is given by

$$\delta_{12} \simeq 2q^2(E_i, \theta) \left| \frac{1}{M_1} - \frac{1}{M_2} \right|$$

If the nuclear masses, scattering angle and energy levels are known, the incident electron energy can be determined. Table 3.1 lists the energies, angles and momenta transfer for the set of data measured in this experiment.

Normalization

Absolute cross sections were not obtained from this experiment and the raw cross sections were scaled by a normalization factor. The need for normalization arose from several sources. Uncertainties and non–uniformites in the target thickness can lead to very large fluctuations in the observed cross sections. This was particularly true in the backward angle data, where long running times induced melting and holes in the target. Inefficiencies in the detectors, uncertainties in the measurement of the incident electron flux, and the solid angle readout were not quantified. These effects were corrected by an overall normalization applied to each data point.

The normalization of the data was accomplished using calculated cross sections derived from the results of previous (e, e') experiments. Elastic cross sections, along with several of the inelastic levels (3^-, 2^+, 4^+, 6^+, 8^+), were calculated at the kinematics measured in this experiment from the Fourier–Bessel coefficients given by Heisenberg *et al.*[30]

The ratio of the calculated cross section to the raw unfolded experimental cross section was determined for each of the states used in normalization. The uncertainty on these ratios includes only the statistical error given by line–shape fitting. An overall normalization for each of the kinematics was obtained by a

Energy (MeV)		Angle (deg)	q_{eff} (fm^{-1})
100.3	±1.5	155°	1.105
125.4	±0.7	155°	1.353
149.967	±0.4	155°	1.610
175.043	±1.9	155°	1.857
200.992	±2.3	155°	2.114
224.468	±0.3	155°	2.346
247.735	±0.1	155°	2.659
279.670	±0.95	155°	2.925
149.967	±0.4	42°	0.591
187.54	±0.8	40°	0.705
224.468	±0.3	41°	0.844
247.735	±0.1	40°	0.903
279.670	±0.95	40°	1.014
300.632	±0.53	40°	1.086
279.670	±0.95	50°	1.245
300.632	±0.53	55°	1.467
300.632	±0.53	65°	1.706
300.632	±0.53	75°	1.933
279.670	±0.95	100°	2.272
300.632	±0.53	110°	2.600

Tab 3.1 Data Set

least squares fit of a constant to the set of $(d\sigma/d\Omega_{calc})/(d\sigma/d\Omega_{exp})$. The uncertainty obtained from normalization was folded with the statistical error. Table 3.2 lists ratios of calculated to experimental cross section and the normalizations and errors obtained. Figures 3.7 to 3.12 presents the normalized data with the calculated form factors for the states used in normalization and the ratio of the normalized cross sections to calculated cross sections.

Kinematics	$\frac{d\sigma}{d\Omega}_{calc} / \frac{d\sigma}{d\Omega}_{exp}$						Normalization
	Elastic	3^- 2.615 MeV	2^+ 4.085 MeV	4^+ 4.323 MeV	6^+ 4.424 MeV	8^+ 4.610 MeV	used in experiment
150 MeV, 42°	1.492 ± 0.0025	1.478 ± 0.031	1.538 ± 0.060	1.522 ± 0.089			1.492 ± 0.005
187 MeV, 40°	0.955 ± 0.0016	1.004 ± 0.051	0.858 ± 0.039	1.117 ± 0.059	1.205 ± 0.160		0.945 ± 0.048
225 MeV, 41°	0.6889 ± 0.001	0.6916 ± 0.010	0.7471 ± 0.032	0.7541 ± 0.065			0.689 ± 0.015
225 MeV, 155°	1.035 ± 0.077						1.035 ± 0.150
250 MeV, 40°	0.6713 ± 0.0017	0.7183 ± 0.020	0.667 ± 0.030	0.658 ± 0.142	0.693 ± 0.042	0.688 ± 0.597	0.676 ± 0.091
280 MeV, 40°	1.138 ± 0.002	1.102 ± 0.020	1.165 ± 0.017	1.146 ± 0.036	1.094 ± 0.031	1.011 ± 0.098	1.116 ± 0.028
280 MeV, 50°	1.179 ± 0.021	1.179 ± 0.074	1.220 ± 0.050	1.099 ± 0.043	1.186 ± 0.023	1.124 ± 0.037	1.116 ± 0.078
280 MeV, 100°	1.525 ± 0.711				1.152 ± 0.481	1.237 ± 0.950	1.166 ± 0.200
280 MeV, 155°							1.166 ± 0.200
300 MeV, 40°	1.124 ± 0.010	1.051 ± 0.051	1.053 ± 0.057	1.098 ± 0.075	1.102 ± 0.058	1.149 ± 0.189	1.110 ± 0.044
300 MeV, 55°	1.044 ± 0.011	0.983 ± 0.092	1.114 ± 0.085	1.036 ± 0.070	1.132 ± 0.099	1.009 ± 0.071	1.110 ± 0.080
300 MeV, 65°	1.114 ± 0.018	1.255 ± 0.154	1.669 ± 0.558	1.178 ± 0.250	1.159 ± 0.121	1.263 ± 0.118	1.110 ± 0.098
300 MeV, 75°	1.371 ± 0.238			1.201 ± 0.126	1.137 ± 0.121	1.113 ± 0.0460	1.110 ± 0.110
300 MeV, 110°							1.110 ± 0.110
100 MeV, 155°		2.237 ± 0.057		2.345 ± 0.086	2.271 ± 0.170	2.344 ± 0.198	2.291 ± 0.053
125 MeV, 155°		1.033 ± 0.032		1.010 ± 0.075	1.083 ± 0.098	1.041 ± 0.048	1.050 ± 0.015
150 MeV, 155°	0.615 ± 0.013	0.638 ± 0.049		0.589 ± 0.075	0.650 ± 0.098	0.602 ± 0.048	0.619 ± 0.022
175 MeV, 155°	2.029 ± 0.020	2.478 ± 0.551		2.835 ± 0.638	2.120 ± 0.237	2.009 ± 0.942	2.029 ± 0.031
187 MeV, 155°	1.050 ± 0.033	1.265 ± 0.462	0.829 ± 0.927				1.050 ± 0.045
201 MeV, 155°	1.689 ± 0.021	1.251 ± 0.315				1.444 ± 0.885	1.689 ± 0.042
250 MeV, 155°	0.646 ± 0.100						0.646 ± 0.200

Tab 3.2 Ratios of calculated to experimental cross sections and normalizations obtained from least squares analysis. Forward angle data points with the same beam energy were analyzed together.

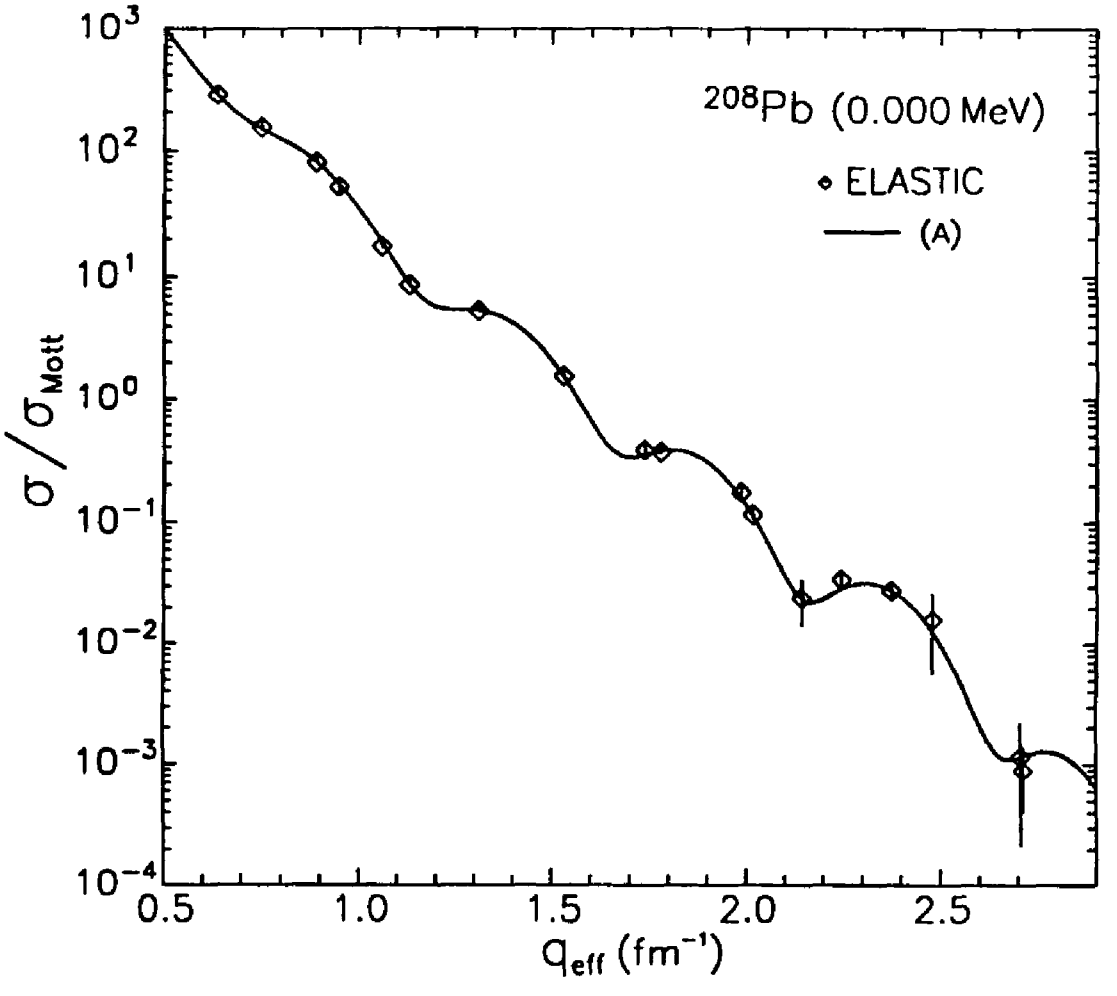

Fig 3.7 Normalized form factors from the elastic state with known form factor curve calculated from known (e, e') data.

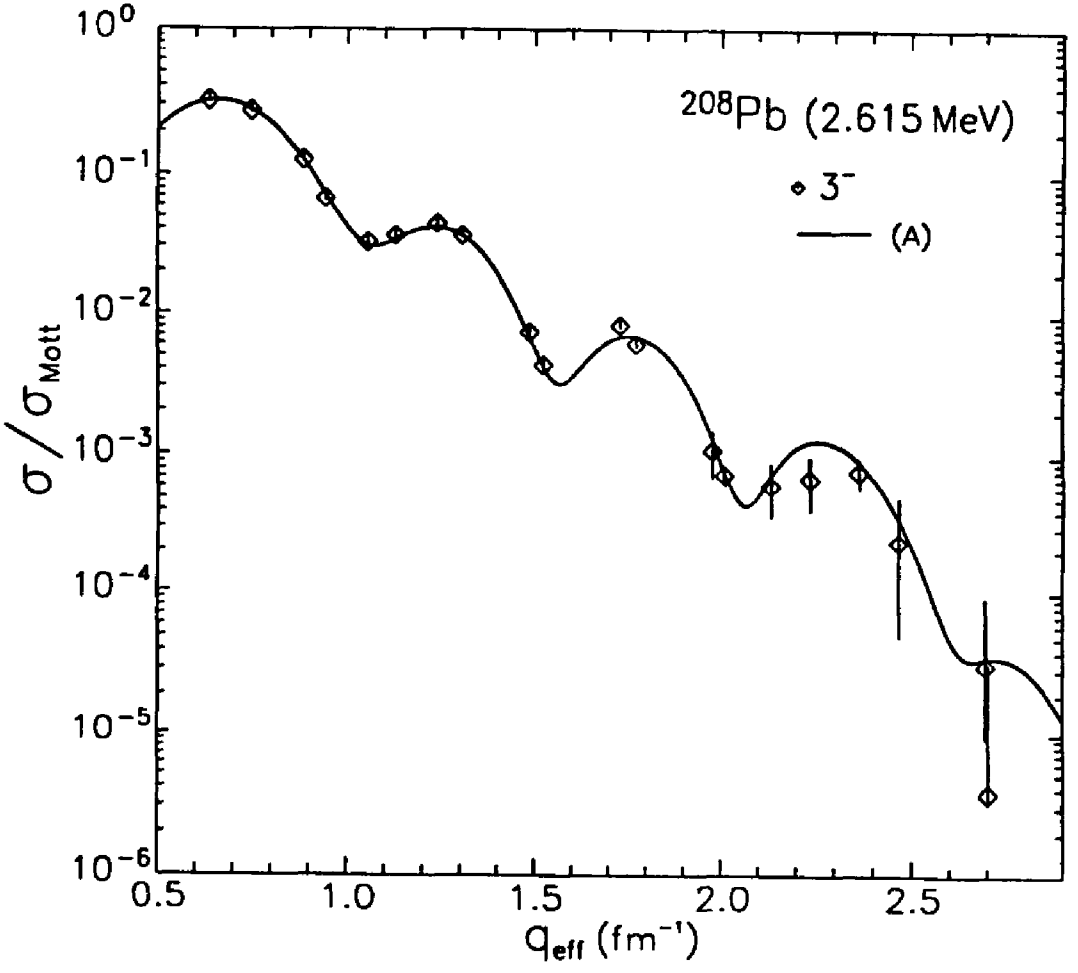

Fig 3.8 Normalized form factors from the 2.615 MeV 3^- state with known form factor curve calculated from known (e, e') data.

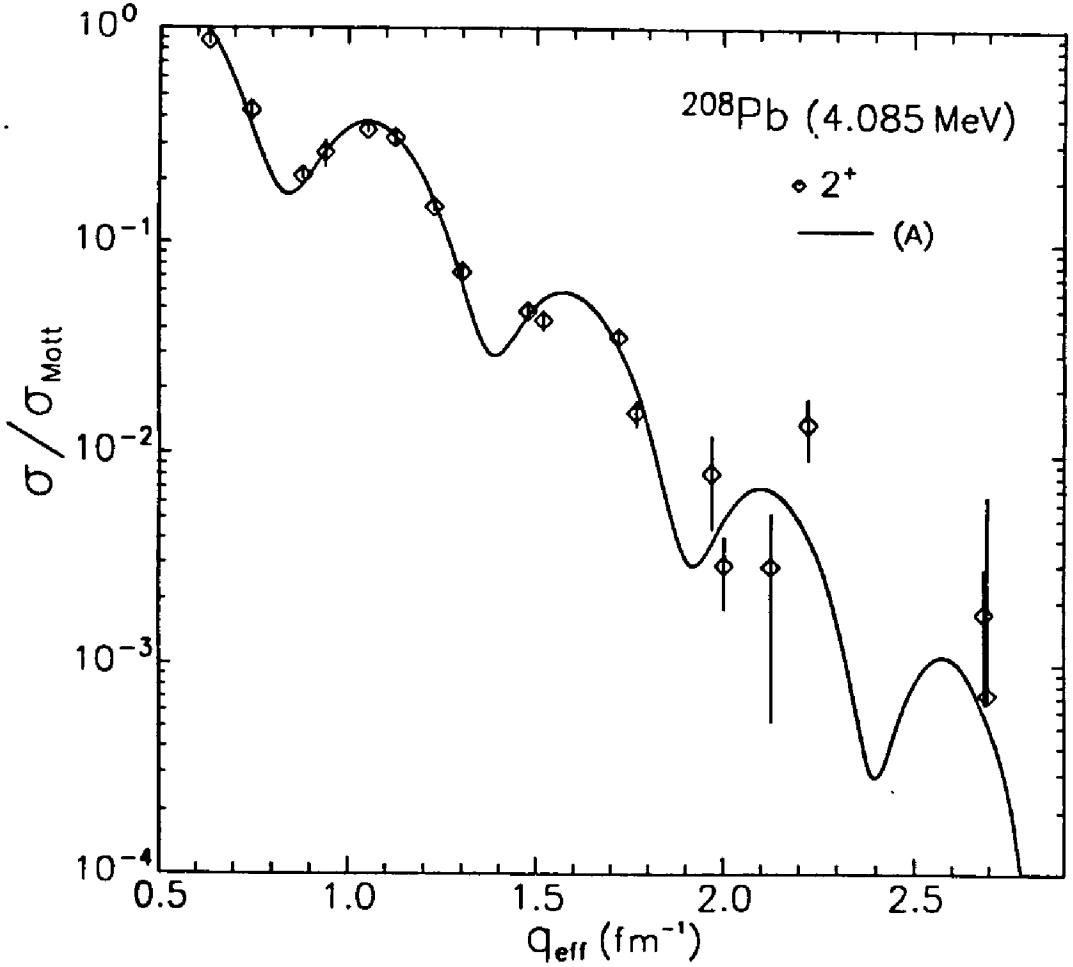

Fig 3.9 Normalized form factors from the 4.085 MeV 2^+ state with known form factor curve calculated from knwon (e, e') data.

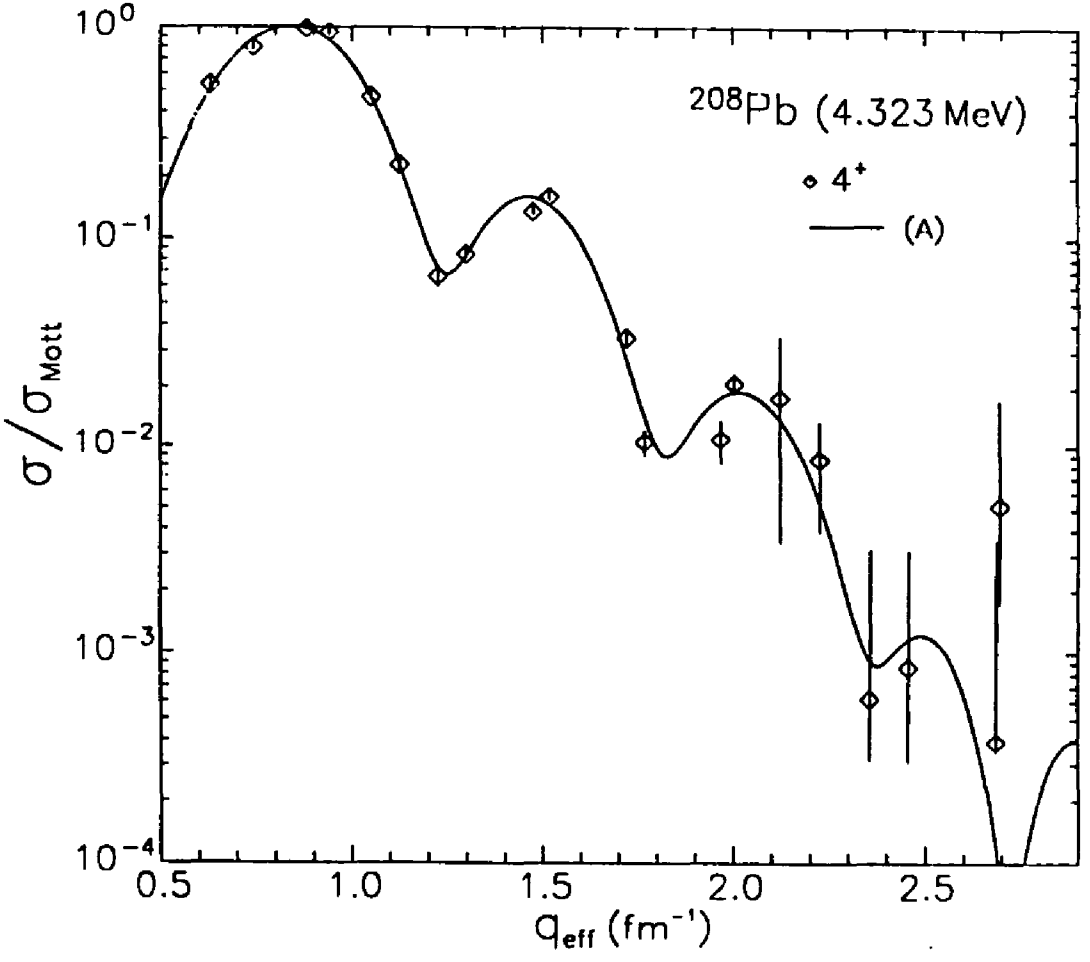

Fig 3.10 Normalized form factors from the 4.323 MeV 4^+ state with known form factor curve calculated from known (e, e') data.

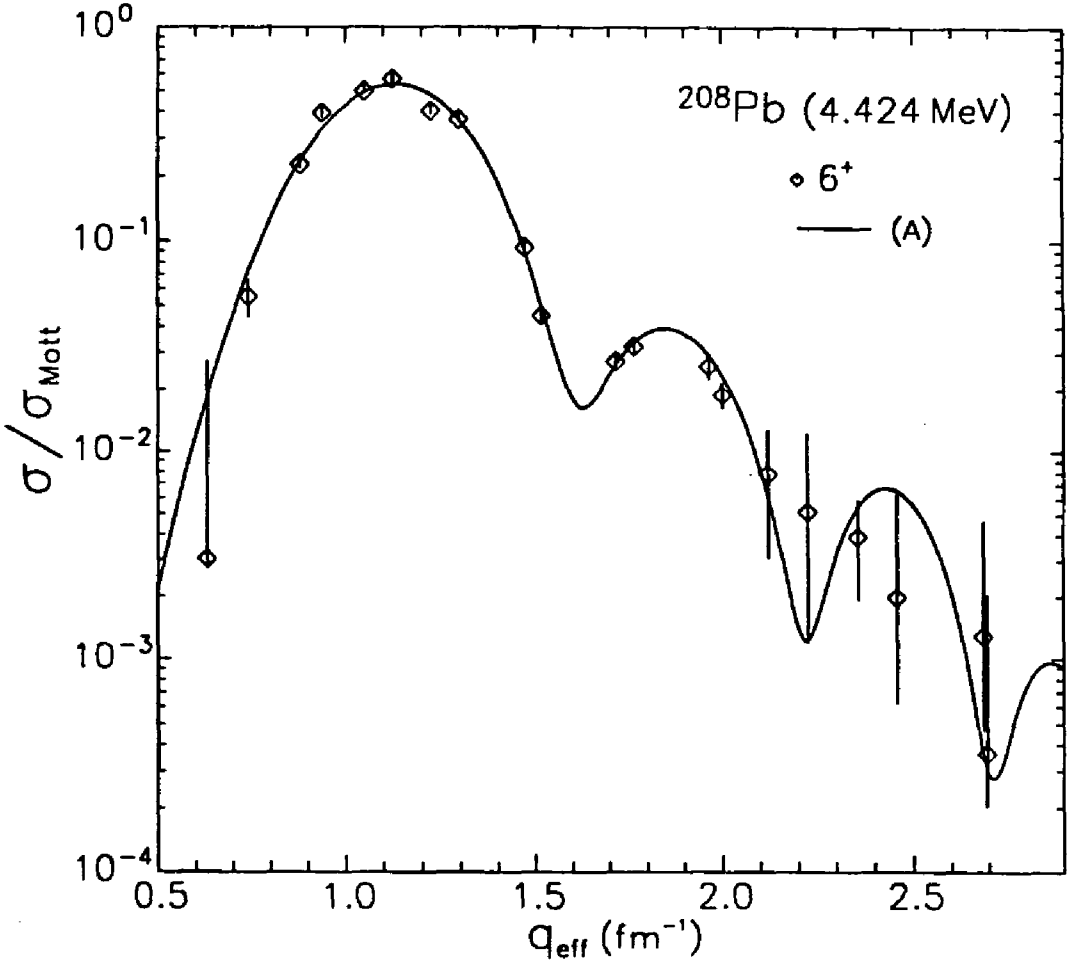

Fig 3.11 Normalized form factors from the 4.424 MeV 6^+ state with known form factor curve calculated from known (e, e') data.

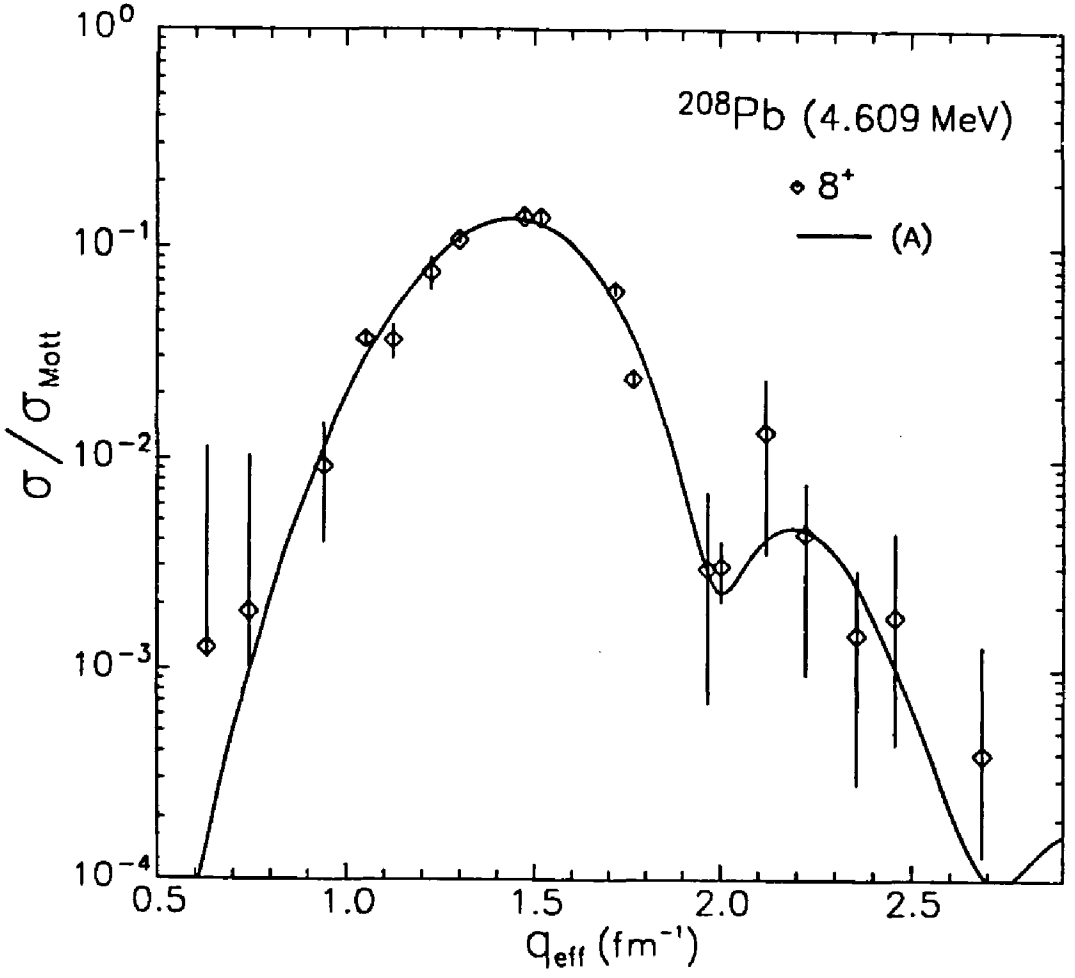

Fig 3.12 Normalized form factors from the 4.610 MeV 8^+ state with known form factor curve calculated from known (e, e') data.

Experimental uncertainty

In the reduction of raw electron scattering events to cross sections, uncertainties in experimental parameters and in the extracted measurements are sources of error and must be propagated throughout the analysis. The errors on all cross sections quoted in this work are the folded result of the various uncertainties, whether calculated or estimated.

Uncertainties in the experimental parameters introduces error which is not easily quantified. Errors in the target thickness, beam current integration, solid angle readout, scattering and target angles and inefficiencies in the detectors contribute to an uncertainty in the measured cross section. Of these, the largest contribution to the error is from the uncertainty in the target thickness. Very thin targets were used and the targets were often damaged during the course of the experiment. This is reflected in the large normalizations sometimes obtained for the high–q data, where the running times were long and changes in the target occured. The importance of using up to six well known levels to determine the normalization of the data is clear.

In the calculation of the incident beam energy, using the recoil method described earlier, an error was generated from the uncertainty in the peak postion of the calibration levels. This error was reflected in the normalization. By normalizing not only to the elastic level but also to inelastic levels which have a much different q–dependence, the uncertainty in the beam energy was directly correlated to the uncertainty in the normalization through the energy dependence of the momentum transfer.

The errors obtained through normalization were assumed to represent the uncertainties in the beam energy and current, target thickness and other possible experimental inefficiencies.

Statistical and relative uncertainty

In the reduction of the scattering events to differential cross sections, statistical and relative errors are generated by the fitting program ALLFIT. The sta-

tistical errors goes as $\sqrt{N}$, where N is the number of events in a given peak. The relative uncertainty is a measure of the correlation between neighboring peaks. In ^{208}Pb, the high level density increases the relative uncertainty, especially for data with low statistics. The statistical uncertainty is added in quadrature to the relative uncertainty and output with the raw cross sections before normalization.

Due to the large number of discrete states in ^{208}Pb and the uncertainties in many of the excitation energies, a reliable calibration of energy loss to channel was essential. Three calibration points per spectrum were selected to provide a quadratic channel function of the energy. In the low momentum transfer region the statistics of such well known peaks as the elastic, 3^- (2.615 MeV), and the 2^+ (4.085 MeV) states were sufficient to insure a reliable calibration. At higher momentum transfer however, the statistics decrease dramatically, and those states which are strong are usually the lesser known higher spin states producing some uncertainty in the energy to channel calibration.

The uncertainties on the energy assignments given in this work were obtained in the following manner. States for which a precise energy was not known were fitted by allowing the excitation energy of the state to change in a spectrum where the form factor for that state is large. Once the excitaion energy and the uncertainty is determined, that energy is used without adjustment in the final fitting for all spectra.

Error propagation through the DWBA analysis of the normalized cross sections leads to an uncertainty in the transition charge and current densities as a function of the radial coordinate. The derivation of the error band is due to the $\chi^2(r)$ from the fit to the cross sections folded with the uncertainty which arises from an incomplete knowledge of the behavior of the form factor across the complete range of momentum transfer (see Heisenberg[22]). In addition, a systematic error of 3% was imposed.

Chapter 4

Nuclear Structure Calculations

4.1 Independent Particle Model

The success of a shell model approach in the prediction of basic nuclear properties supports the initial assumption that nucleons move independently in an average potential produced by all the the nucleons. For spherical doubly closed nuclei such as ^{208}Pb, single particle wave functions deduced from mean field theories approximate the ground state charge distribution and nuclear binding energies[2][86]. Qualitative agreement is also seen between mean field single particle radial wave functions and those experimental transition charge densities where a single particle radial distribution may be easily deduced[12][13][14][86][87].

The Independent Particle Model (IPM) assumes a system of non–interacting fermions which fill energy eigenstates completely to a cut–off energy dictated by the number of nucleons. The simplest central potential which produces a qualitative picture of the shell structure of ^{208}Pb is a Harmonic Oscillator potential coupled to a strong spin–orbit force. The energy levels are degenerate to the degree 2j+1 in the orientation of the total spin $\vec{j}$ ($\vec{j} = \vec{l} + \vec{s}$), as shown in Figure 4.1 for ^{208}Pb.

In practice, more realistic potentials are used to generate single particle wave functions. The Woods–Saxon potential,

$$V_{WS}(r) = -V_0 \left[1 + \exp\left(\frac{r - R_0}{a}\right)\right]^{-1} \tag{4.1}$$

where,

$$R_0 = r_0 A^{1/3}; \;\; V_0 \sim 50 \text{ MeV}; \;\; a \sim 0.7 \; fm; \;\; r_0 \sim 1.2 \; fm$$

are parameters determined from experience, describes a mean field which goes to zero at large r and confines the microscopic wave functions primarily to the

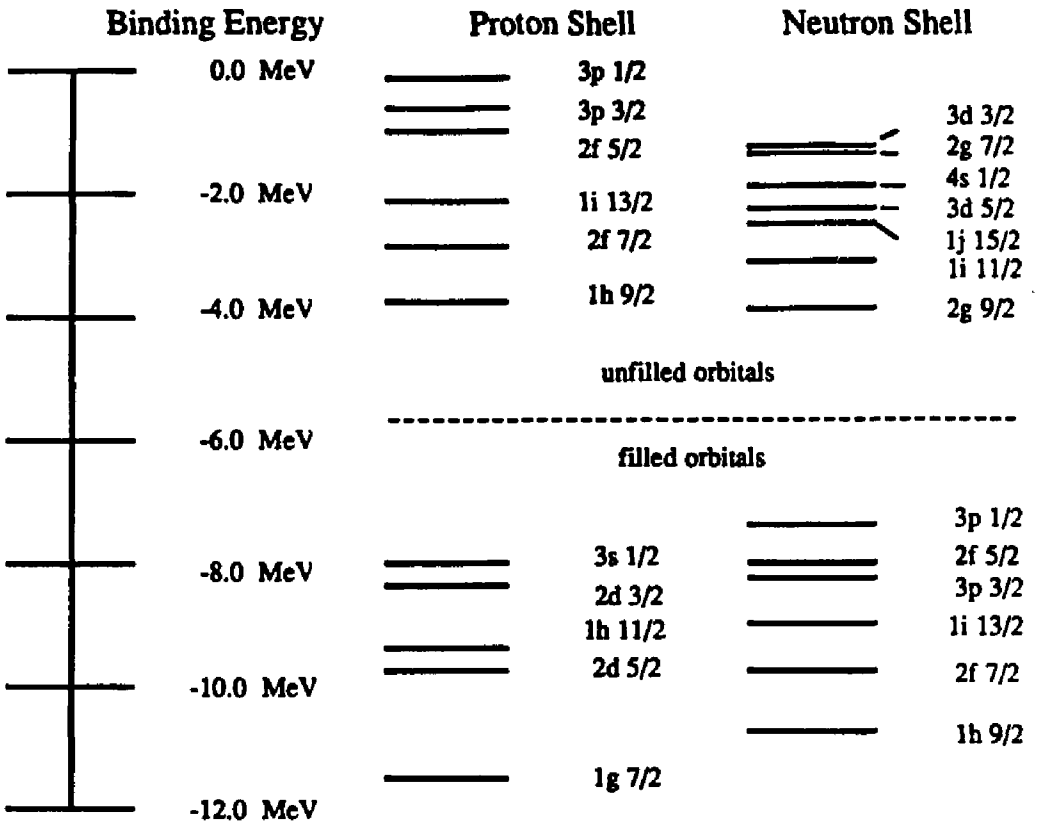

Fig.4.1 Mean field single particle levels near Fermi level for ^{208}Pb

region where $r < R_0$. Thus, Woods–Saxon wave functions may be expected to more accurately predict the energy level scheme of heavy spherical nuclei than wave functions derived from a Harmonic Oscillator potential which has an unrealistic asymptotic behavior. Still, the q–dependence of form factors generated is influenced by the choice of r_0, so their use in the analysis is restricted to cases where the value of r_0 has been determined with reasonable accuracy. A discussion of the use of Woods–Saxon wave functions in our DWBA analysis is given in Section 2.5.

Single particle wave functions may also be calculated using Hartree–Fock self consistent potentials. Many references exist on the application of Hartree–Fock theory to the derivations of nuclear wave functions and we refer the reader to

the text by DeShalit and Feshbach[42] for a thorough review of the subject. The problem addressed by the Hartree–Fock method is to derive a self-consistent single particle potential out the sum of two body interactions,

$$V(1...A) = \sum_{i<j=1}^{A} V(i,j) \sim \sum_{i<j}^{A} V(i) \tag{4.2}$$

Several forms of the two–body interaction have been derived. In practical applications, the two–body interaction is a phenomenologically parametized function of the relative and center–of–mass single particle coordinates and may be both non–local and density dependent.

The Density Matrix Expansion (DME) interaction of Negele and Vautherin[43] was used in this work to calculate HF wave functions. The DME calculates a low order expansion, up to second derivatives, of the nuclear density matrix in terms of the relative and center–of–mass coordinates of the interacting nucleons. The basic interaction is derived from a finite nuclear G–matrix calculation using a Reid soft core potential and the local density approximation. The DME interaction have been successful in predicting nuclear moments, rms radii and binding energies of spherical nuclei in addition to a reasonable value of the nuclear compressibility. All HF wave functions used in this work come from the DME codes used by Negele and expanded into Harmonic Oscillator wave functions with a radial parameter of $b = 2.44$.

Both Woods–Saxon and Hartree–Fock potentials have been used in this work to generate form factors for comparison to the experimental results. The particle–hole energies used in all calculations were determined from single particle energies shown in Table 4.1 and were those tabulated by Rinker and Speth[38]

Proton particle		Proton hole		Neutron particle		Neutron hole	
n l j	energy	n l j	energy	n l j	energy	n l j	energy
$1h_{9/2}$	−3.802	$3s_{1/2}$	−8.034	$2g_{9/2}$	−3.943	$3p_{1/2}$	−7.377
$2f_{7/2}$	−2.905	$2d_{3/2}$	−8.385	$1i_{11/2}$	−3.165	$2f_{5/2}$	−7.947
$1i_{13/2}$	−2.193	$1h_{11/2}$	−9.375	$1j_{15/2}$	−2.521	$3p_{3/2}$	−8.275
$2f_{5/2}$	−0.980	$2d_{5/2}$	−9.708	$3d_{5/2}$	−2.377	$1i_{13/2}$	−9.010
$3p_{3/2}$	−0.686	$1g_{7/2}$	−11.508	$4s_{1/2}$	−1.911	$2f_{7/2}$	−9.717
$3p_{1/2}$	−0.162			$2g_{7/2}$	−1.450	$1h_{9/2}$	−10.786
				$3d_{3/2}$	−1.404		
$1i_{11/2}$	3.3	$1g_{9/2}$	−14.4	$2h_{11/2}$	3.3	$1h_{11/2}$	−14.9
$2g_{9/2}$	4.1	$2p_{1/2}$	−15.7	$3f_{7/2}$	3.3	$3s_{1/2}$	−15.1
$3d_{5/2}$	6.3	$2p_{3/2}$	−16.4	$4p_{3/2}$	3.4	$2d_{3/2}$	−15.4
$2g_{7/2}$	6.3	$1f_{5/2}$	−18.5	$4p_{1/2}$	3.9	$2d_{5/2}$	−16.8
$1j_{15/2}$	6.4	$1f_{7/2}$	−20.7	$3f_{5/2}$	4.4	$1g_{7/2}$	−17.9
$4s_{1/2}$	7.0	$2s_{1/2}$	−22.7	$2h_{9/2}$	5.4	$1g_{9/2}$	−21.0
$3d_{3/2}$	7.1	$1d_{3/2}$	−24.6	$1j_{13/2}$	5.5	$2p_{1/2}$	−22.6
$2h_{11/2}$	11.0	$1d_{5/2}$	−25.5	$1k_{17/2}$	6.3	$2p_{3/2}$	−23.4
$1j_{13/2}$	11.7			$2i_{13/2}$	9.1	$1f_{5/2}$	−24.7
$4p_{3/2}$	12.0			$3g_{9/2}$	9.4	$1f_{7/2}$	−26.7
$3f_{7/2}$	12.0			$4d_{5/2}$	9.6		
$4p_{1/2}$	12.5			$5s_{1/2}$	10.2		
$3f_{5/2}$	12.9			$4d_{3/2}$	10.4		
$2h_{9/2}$	13.2			$3g_{7/2}$	10.4		
$1k_{17/2}$	14.0			$2i_{11/2}$	11.6		
				$1k_{15/2}$	13.4		

Table 4.1 Single particle energies (MeV) tabulated by Rinker and Speth[38] .

4.2 Tamm–Dancoff Approximation

In the IPM, the ground state occupation is filled precisely to the fermi level (Figure 4.1). In ^{208}Pb the gap to the unoccupied energy levels is rather large, 3.8 MeV for protons and 3.4 Mev for neutrons. The signature of this shell closure is seen in the relatively high excitation energy of the first excited state in ^{208}Pb of 2.615 MeV for the collective electric octopole vibration. In microscopic mean field theories, a ground state with a sharp cutoff at the fermi level is termed an *uncorrelated ground state*, $|0\rangle$, and is regarded as the vacuum in particle–hole space. *Particle states* are defined as the unoccupied ground state levels above the fermi level, while *hole states* are those states below the fermi level. An excitation from the i^{th} hole state to the j^{th} particle state may be written in terms of creation and annihilation operators in particle–hole space,

$$p_j h_i^{-1} |0\rangle \tag{4.3}$$

It is reasonable to suppose in the case of a doubly closed nucleus such as ^{208}Pb, where we assume the uncorrelated ground state to be a reasonable first order approximation of the true nuclear gound state, that excitations occur primarily through 1p-1h excitations . The essence of the Tamm-Dancoff Approximation (TDA) is to truncate the Hilbert space basis to include only 1p–1h excitations from an uncorrelated Hartree–Fock ground state,

$$|\nu\rangle = \sum_{ab} X^{\nu}_{ab}\ \mathrm{p_a h_b^{-1}}\ |0\rangle \tag{4.4}$$

where the excited state is expanded in a basis set composed of 1p–1h excitations.

Diagonalization of the Hamiltonian in this basis yields the coefficients X^{ν}_{i}. Besides the HF mean field Hamiltonian, $\mathbf{H_0}$, the T-D Hamiltonian includes a residual interaction which mixes 1p–1h excitations. The residual interaction is a

two body operator,

$$V_{res} = V_{\mu\nu,\mu'\nu'}\, a^{\dagger}_{\mu} a^{\dagger}_{\nu} a_{\nu} a_{\mu} \tag{4.5}$$

The calculation reduces to finding the matrix elements,

$$\langle p_m h_i | V_{res} | p_n h_j \rangle = \sum_{\mu\nu\mu'\nu'} V_{\mu\nu\mu'\nu'} \langle 0 | h_i p_m^{-1}\, a^{\dagger}_{\mu} a^{\dagger}_{\nu} a_{\nu} a_{\mu}\, p_n h_j^{-1} | 0 \rangle \tag{4.6}$$

Due to the absence of ground state correlations, the TDA has a limited usefulness in realistic calculations. However, in the case of ^{208}Pb, a large doubly closed nucleus, one would expect ground state correlations to be at a minimum. In TDA calculations with a particle–hole space truncated to on $1\hbar\omega$ configurations, qualitative agreement with experimental energies of collective negative parity states are seen in the spectrum of ^{208}Pb[39][40] . Calculations predict the lowest electric octopole state to be greatly reduced in energy from any single HF 1p-1h excitation which can couple to 3^-. This reduction in energy is characteristic of collective states in general, since the residual interaction is attractive and strong for natural parity states and in fact induces the collectivity seen in natural parity states. The residual interaction becomes weakly repulsive for unnatural parity transitions, raising the energy of these transitions from the IPM prediction.

4.3 Random Phase Approximation

The introduction of a residual interaction to the IPM permits not only configuration mixing in the transition to excited states, but also the possiblity of ground state correlations. Discrepencies between the calculated and experimental ground state charge densities reflects the ground states occupation of energy levels above the fermi level. These correlations must be included in any realistic nuclear structure calculation. The work by Pandharipande *et al.* suggests that a reduction in the occupation probability of levels just below the fermi surface by 30% is needed to correctly predict the quenching seen in the transitions to the high spin

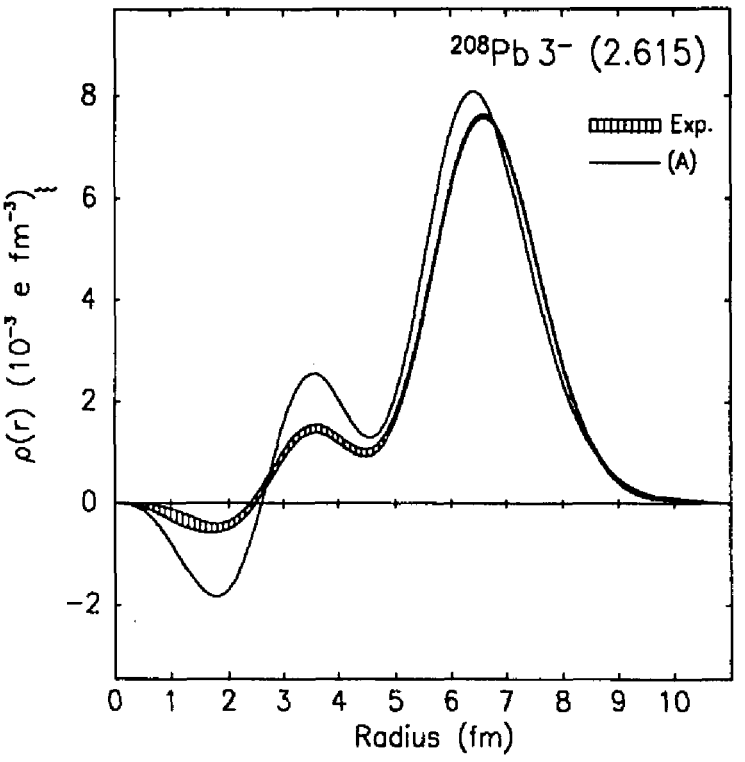

Fig.4.2 Transition charge density from the 2.615 MeV state by Goutte *et al.*[8] . Curve is from an RPA calculation using a Migdal interaction by Heisenberg and Krewald[10] .

states in ^{208}Pb[44] . Evidence for ground state correlations has also been seen in a comparison of ground state charge densities for nuclei in the lead region[46][47] .

The Random Phase Approximation (RPA) is a purely dynamical model of nuclear excitations based upon the equation of motion method[41] . The basic RPA assumption incorporates ground state correlations but does not specify the microscopic structure of these correlations. The 2p–2h terms of the Hamiltonian are linearized by summing over a certain class of correlations. In general, RPA calculations include only long range correlations from collective modes. The inclusion of ground state correlations permits the introduction of backward going hole-particle excitations, i.e. excitations which involve moving a particle from above the fermi level to a vacancy below the fermi level. The n^{th} excited state

may be described by the creation operator $\Omega_n^\dagger$ operating on the correlated ground state $|\tilde{0}\rangle$,

$$|n\rangle = \Omega_n^\dagger |\tilde{0}\rangle = \sum_{ph} (X_{ph} a_p^\dagger a_h + Y_{ph} a_h^\dagger a_p |\tilde{0}\rangle \qquad (4.7)$$

RPA is solved formally by an equation of motion operator method which spans in theory the complete set of particle–hole and hole–particle operators. The coefficients X_{ph} and Y_{ph} are obtained through the solution of a system of matrix equations dependent opon the commutator of the Hamiltonian with the quasi-particle operators ph^{-1} and hp^{-1}.

Several RPA calculations have been performed on ^{208}Pb with a variety of interactions and configuration spaces. Gillet *et al.*[39] obtained reasonable excitation energies for low-lying negative parity states with using a gaussian shaped central force and permitting only $1\hbar\omega$ 1p-1h transitions. The limited configuration space resulted in too much interior structure predicted for the first electric octupole state and poor agreement with experimental energies of positive parity states. By increasing the configuration space to allow 1p–1h transitions from $2\hbar\omega$ above and below the fermi level, Ring and Speth[7] , using a zero range density dependent Migdal interaction, were able to obtain much closer predictions for the positive parity collective states.

Heisenberg and Krewald[10] , using the same interaction as Ring and Speth, showed that increasing the configuration space up to $14\hbar\omega$ significantly effects the interior structure of the 2.615 MeV 3^- transition charge density. In Figure 4.2, the results of this calculation is compared to the experimental transition charge density from Goutte *et al.*[8] .

One of the most advanced RPA calculations on the microscopic structure of ^{208}Pb has been performed by Dechargé and Gogny[9] using the D3 force in a fully self consistent calculation using a large ph space. The D3 force is a finite range density dependent effective interaction which is used both to calculate the Hartree–Fock wave functions and the residual interaction used in the RPA calculation.

Recently, formalism has been developed to incorporate 2p–2h configurations explicitly in both the ground state and excitations by Takayanagi *et al.* through a modifed ph response function in second RPA theory which includes all second–order effects that can be obtained in RPA theory. No calculations have been published to date.

4.4 Tamm–Dancoff Approximation from a Correlated Ground State

The theoretical calculations presented in this work are from preliminary results by Heisenberg[11] using the TDA method outlined in Section 4.2 except that ground state correlations are calculated explicitly. In this formalism, particle–hole excitations are given by,

$$p_j h_i^{-1} \left|\tilde{0}\right\rangle \tag{4.8}$$

where,

$$\left|\tilde{0}\right\rangle = \left(1 \; + \; Z_{p_1,p_2,h_1,h_2} \;\; p_1 p_2 h_2^{-1} h_1^{-1}\right) \left|0\right\rangle \tag{4.9}$$

gives the correlations to the ground state from 2p–2h configurations. The interaction, which is phenomenologically adjusted to give the correct excitation energies for many of the well known levels in ^{208}Pb, is used for both the calculation of the ground state correlations and as the perturbing interaction in the conventional TDA calculation. The p–h configuration basis spans 100 single particle orbitals which are calculated with DME Hartree–Fock codes. To zeroth order, the 2p–2h amplitudes Z_{p_1,p_2,h_1,h_2} in the ground state correlation calculation are given by,

$$Z_{p_1,p_2,h_1,h_2} \approx \frac{-\left\langle p_1 h_1^{-1} \middle| V \middle| h_2 p_2^{-1} \right\rangle}{\varepsilon_{p_1 h_1} \; + \; \varepsilon_{p_2 h_2}} \; + \; \ldots \tag{4.10}$$

The preliminary results show that the interaction used was not correct. The calculated excitation energy of the first octupole state is several MeV too low, indicating too much collectivity is present in the calculations. The calculated excitation energies for other states in ^{208}Pb between 3.0 MeV and 7.5 MeV

are quite close to the experimental energies. As the collectivity decreases, the calculation does a much better job in predicting the strengths and shapes of transition densities. In particular, for magnetic and high spin states where the residual interaction is weak, the calculation shows some quenching from the 1p–1h densities. For states above 5.0 MeV, we will compare experimental results with the predictions from this preliminary calculation.

Chapter 5

Results

5.1 Introduction

^{208}Pb has been a focus of electron scattering experiments since the late 1960's. Beginning with the measurement of the elastic form factor at Darmstadt[49] and Stanford[50] , information from the ground state charge density and several strongly excited inelastic levels have attained a high degree of accuracy. For the purpose of this work, form factors calculated from the Fourier–Bessel coefficients determined by these well known levels have been used as a self–consistency check and to provide an over–all normalization.

Measurements on the elastic, octupole and 5^- states, as well as the four positive parity levels below 4.7 MeV have been discussed in an article by Heisenberg *et.al.*[30] . A forward angle energy loss spectrum at $q = 1.254\ fm^{-1}$ showing the states in this region is presented in Figure 5.1. A Distorted Wave Born Approximation (DWBA) analysis, including the data used in Heisenberg *et al.*[30] , has been performed on the inelastic transitions which were not used in the normalization to incorporate any new information from this experiment and to reduce the uncertainties in the transition densities.

The analyses from over fifty excitations are presented in this work, although this does not exhaust the information availiable in the data. The presentation and organization of the numerous excitations is in itself a difficulty. In general, excitations have been grouped together by excitation energy regimes and by multiplets stemming from a particular single particle–hole configuration. After a review of electron scattering results from the very well known low–lying collective excitations in Section 5.2, the negative parity states arising from $1\hbar\omega$ transitions are discussed in Section 5.3. High spin positive parity excitations near 5.0 MeV excitation energy are presented in Section 5.4. Results from the DWBA analyses

of low multipolarity electric excitations between 4.8 MeV and 6.0 MeV, for which the spin and parity are well established, are presented with little discussion in Section 5.5. Above 6.0 MeV excitation energy, although many levels with well defined form factors were observed, only the analyses of relatively high spin states are discussed. In Section 5.6, the results from transitions with $7 \geq J \geq 10$ are given, including the assignments of J^{π} to several levels not previously reported. Excitations believed to be purely single particle–hole states (*ie.* 12^{-}, 14^{-}) are discussed in detail in Section 5.7.

Table 5.1 lists the excitations for which analyses are presented with a comparison to excitation energies and spins reported by several experimental studies of ^{208}Pb and Nuclear Data Sheets[11] .

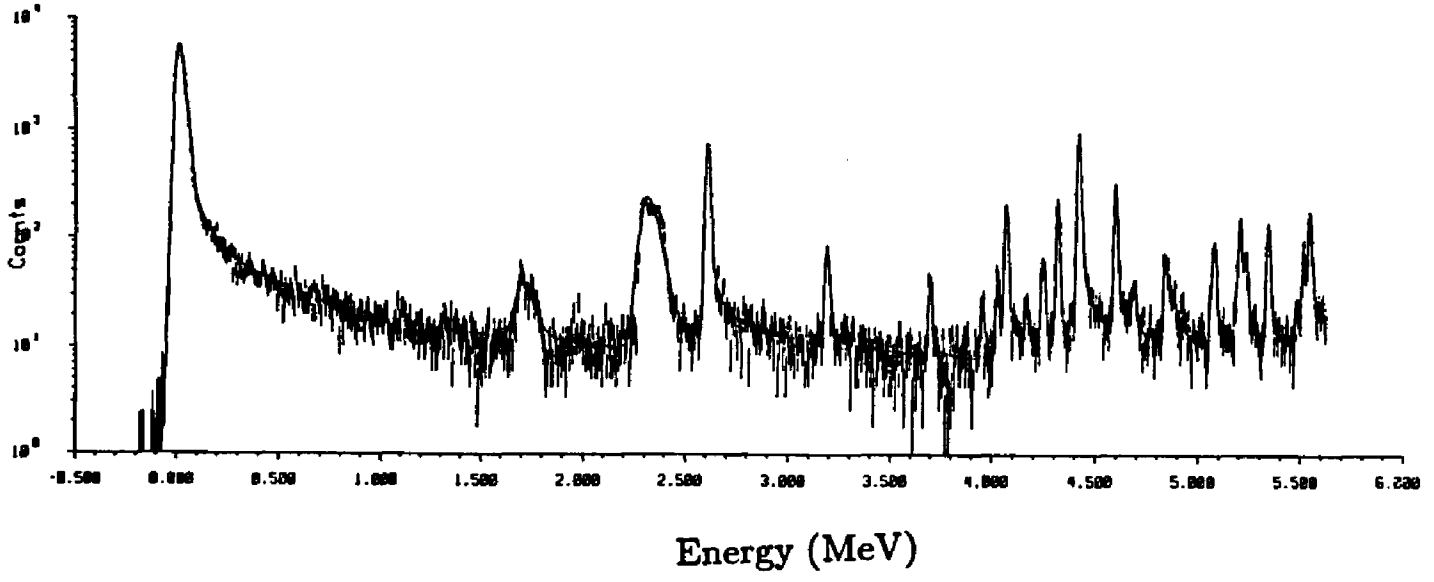

Fig 5.1 Low-lying inelastic levels in energy loss spectrum at a momentum transfer of 1.254 fm^{-1}. The density of levels increases dramatically above 5.0 MeV excitation energy.

This work (e,e')		Lichtenstadt[6] (e,e')		Vold *et al.*[53] $^{207}Pb(d,p)^{208}Pb$		Grabmayr *et al.*[61] $^{209}Bi(d,^3He)^{208}Pb$		Wagner *et al.*[60] (p,p')		Nuclear Data[1] Sheets (1986)	
Energy	J^π	Energy	J^π	Energy	J^π	Energy	J^π	Energy	J^π	Energy	J^π
2.615	3^-	2.615	3^-	2.615	3^-	2.607	3^-	2.6146	3^-	2.6146	3^-
3.198	5^-	3.198	5^-	3.198	5^-	3.197	5^-	3.1978	5^-	3.1977	5^-
3.709	5^-	3.709	5^-	3.708	5^-	3.710	5^-	3.7087	5^-	3.7084	5^-
3.946	4^-					3.948	4^-	3.946	4^-	3.9464	$(4)^-$
3.961	5^-	3.961	5^-			3.963	5^-	3.961	(5)	3.9609	5^-
4.037	7^-	4.037	7^-					4.037	(7)	4.037	7^-
4.085	2^+	4.085	2^+			4.084	2^+	4.0855	2	4.0854	2^+
4.124	5^-			4.120		4.125	4^-	4.125	4^-	4.1253	$(4,5)^-$
4.180	5^-			4.175	$5^-,6^-$	4.180	5^-	4.181	(5)	4.1804	5^-
4.210	6^-			4.200	$5^-,6^-$	4.210	6^-	4.206	6^-	4.2054	$(6)^-$
4.251	3^-			4.250	$(2^-,3^-)$	4.251	$4^-,(5^-)$	4.256		4.2535	(3^-)
4.262	4^-					4.262	$3^-,5^-$			4.2624	$(5)^-$
4.298	5^-			4.290	$3^-,4^-,5^-$	4.298	5^-	4.296	5	4.2962	5^-
4.323	4^+	4.324	4^+			4.325	4^+	4.323	4	4.3232	4^+
4.358	4^-			4.350	$4^-,5^-$	4.359	4^-	4.357	4^-	4.3585	$(4)^-$
4.383	6^-					4.384	6^-	4.385	6^-	4.3829	6^-
4.424	6^+	4.424	6^+			4.421	6^+	4.4235	6	4.422	6^+

Table 5.1 Energies(MeV), spins and parities for states analyzed in this work.

This work (e,e')		Lichtenstadt[6] (e,e')		Vold *et al.*[53] $^{207}Pb(d,p)^{208}Pb$		Grabmayr *et al.*[61] $^{209}Bi(d,^3He)^{208}Pb$		Wagner *et al.*[60] (p,p')		Nuclear Data[1] Sheets (1986)	
Energy	J^π	Energy	J^π	Energy	J^π	Energy	J^π	Energy	J^π	Energy	J^π
4.481	6^-					4.481	6^-	4.480	6^-	4.4805	6^-
4.610	8^+	4.610	8^+	4.605	$7^+,8^+$	4.610	8^+	4.610	8^+	4.610	8^+
4.691	3^-			4.698	3^-	4.691	3^-	4.698		4.691	3^-
4.707	5^-					4.707	3^-	4.711		4.711	
4.841	1^-			4.840				4.841	1^-	4.8421	1^-
4.862	8^+			4.865	$(8)^+$	4.860	$7^+,8^+$	4.863		4.865	$(7)^+$
4.895	10^+	4.89	10^+			4.894	10^+	4.895	(10)	4.895	10^+
5.010	9^+	5.01	9^+					5.010	(9)	5.010	(9^+)
5.068	10^+	5.07	10^+			5.067	10^+	5.072	(9)	5.0723	10^+
5.084	(8^+)			5.080		5.097	$(8)^+$	5.087	3	5.087	3^-
5.213	5^-			5.215	$2^-,3^-$	5.210	$(5)^+$	5.214		5.214	(5^-)
5.242	3^-			5.245	$2^-,3^-$			5.242		5.2446	3^-
5.260	9^+										
5.291	11^+	5.27	11^+	5.292	$0^-,1^-$			5.291	1^-	5.27	(11^+)
5.346	3^-			5.350	$0^-,1^-$	5.352	6^+	5.345	3	5.3478	3^-
5.481	5^-					5.487	$(6)^-$	5.483	5	5.483	5^-
5.514	3^-			5.515	$3^-,4^-$			5.514	3	5.5168	3^-
5.656	5^-					5.665	$(5)^-$	5.658	5	5.658	5^-

Table 5.1 (continued)

This work (e,e')		Lichtenstadt[6] (e,e')		Vold *et al.*[53] $^{207}Pb(d,p)^{208}Pb$		Grabmayr *et al.*[61] $^{209}Bi(d,^3He)^{208}Pb$		Wagner *et al.*[60] (p,p')		Nuclear Data[1] Sheets (1986)	
Energy	J^π	Energy	J^π	Energy	J^π	Energy	J^π	Energy	J^π	Energy	J^π
5.685	4^+					5.688	4^+	5.689	4	5.690	4^+
5.715	2^+					5.710	$(6)^+$	5.720	(7)	5.712	(2^+)
5.813	3^-					5.821	$(4)^+$	5.813	3	5.813	3^-
5.860	(11^+)										
5.928	10^+	5.92	10^+			5.922	10^+			5.920	10^+
5.954	9^+							5.966	(9)	5.966	(9)
5.997	6^+					5.996	4^-	5.993	6	5.993	6^+
6.089	(8^+)										
6.110	12^+	6.10	12^+					6.099		6.097	12^+
6.283	(10^-)										
6.437	12^-	6.45	12^-					6.745		6.738	12^-
6.745	14^-	6.74	14^-					6.745		6.738	14^-
6.833	(8^-)									6.833	8^-
6.859	9^-							6.862		6.843	(8^+)
6.879	7^-							6.876		6.876	
6.884	10^-							6.876		6.865	10^-
7.068	12^-	7.06	12^-					7.061		7.053	12^-

Table 5.1 (continued)

5.2 Elastic, Octupole and Collective Low-Lying Positive Parity States

The states discussed in this section are those for which well determined electron scattering form factors have been obtained from previous (e, e') experiments, and were used to establish the normalization of our data. These levels were not re-analyzed in in this work and are included here for the sake of completeness. A comparison of our data to the calculated form factors is given in Chapter 3.9. The densities presented in this section are from Goutte *et al.*[8] and Heisenberg *et al.*[30].

Elastic electron scattering measurements from ^{208}Pb have been instrumental in determining the ground state charge distribution to a high degree of accuracy. Low momentum transfer electron scattering data[49] coupled with data from the transition energies of muonic ^{208}Pb atoms[51] determined the r.m.s. radius of the ground state. Improved experimental accuracy and extension of the data to higher momentum transfer[50][52] indicated the existence of a central depression in the ^{208}Pb ground state charge density $\sim 7\%$ of the surface density. The strength of the central depression and the inablility of mean field independent particle models to predict this feature, suggested that ground state correlations were not being included properly in the calculation of the ground state charge distribution.

High momentum transfer data from Saclay[2], which include measurements up to $q = 3.7\ fm^{-1}$, determined the charge density to an accuracy of $\pm 1\%$ in the nuclear interior. Comparison of the experimental charge density with finite range density dependent Hartree-Fock calculations by Gogny[35] and Negele[53] show an over-prediction of charge in the region $0 \leq r \leq 5fm$. The amount of structure, as measured by oscillations within the nuclear interior, was also much smaller than predicted.

Indications of ground state correlations have been seen in a number of experiments. Exclusive electron scattering experiments (e, e', p) performed at NIKHEF have measured a depletion of the $3s_{1/2}$ proton orbit by approximately 20% from an uncorrelated mean field prediction. A recent precision NIKHEF experiment designed to re-measure the (e, e') absolute elastic cross sections in the region of

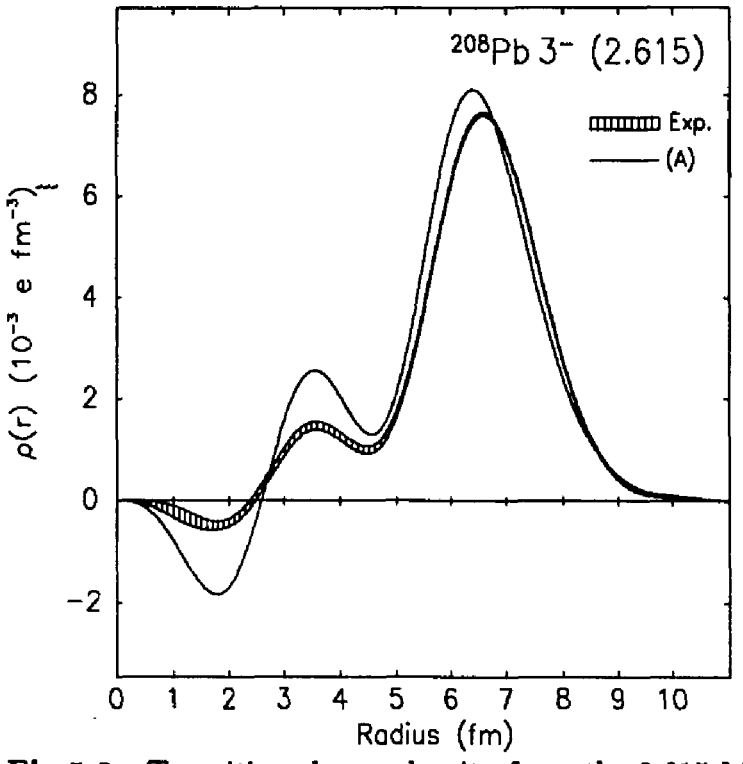

Fig.5.2 Transition charge density from the 2.615 MeV state by Goutte *et al.*[3] . Curve is from an RPA calculation using a Migdal interaction.

the form factor minima, should decrease the uncertainties in the charge density where oscillations may be present.

Just as the elastic level has provided an excellent laboratory for the testing of mean field predictions of the nuclear ground state, the study of the octopule level at 2.615 MeV has provided insight into nuclear dynamics. The importance of this level was recognized quite early and has been the subject of numerous experimental and theoretical investigations[3][4][7][25][34][35] . In particular, the work by Goutte *et.al.*[3] , which extended the data set to 3.4 fm^{-1} and incorporated most of the previous electron scattering measurements on this state, determined the transition charge density with a degree of accuracy unprecedented for an inelastic transition (Figure 5.2).

The 3^- level has been shown to be strongly collective and almost purely longitudinal. The interior of the transition charge density is approximately a factor of two smaller than predicted by RPA calulations [8] [56] [57] . The negative lobe in the interior of the transition charge density is dominated by the $\pi(2f_{7/2}, 3s_{1/2}^{-1})$ and the $\pi(3p, 2d^{-1})$ particle– hole components. As noted above, the analysis of both exlusive and inclusive electron scattering data from the ground state charge density has suggested a strong depletion of the proton $3s$ and $3d$ orbits, resulting in the reduction of the amplitudes for these particle–hole configurations contributing to the 3^- state and a reduction of the transition charge density in the interior.

Four positive parity states have been identified between 4.0 and 4.7 MeV [4] [6] . The 2^+ (4.085 MeV), 4^+ (4.323 MeV), 6^+ (4.424 MeV), and 8^+ (4.610 MeV) are collective states and display the strong surface peaked charge densities associated with collectivity (Figure 5.3). As noted by Lichtenstadt [6] , these levels are almost purely longitudinal except for a small transverse component due to the intrinsic convection current $J_{\lambda,\lambda-1}$.

Theoretical RPA calculations by Weber *et.al.* [58] indicate that the 2^+, 4^+, 6^+, 8^+ and possibly the 10^+ level at 5.068 MeV may represent a quasi–rotational band. The excitation energies of these states approximately obey the $J(J+1)$ rule, indicative of rotational behavior. The large amount of collectivity in these states lowers the excitation energy far below the single particle–hole energy of the first available mean field configurations which can couple to positive parity transitions. Although one would expect the collectivity to decrease with increasing multipolarity, the absence of any measurable transverse strength in the 8^+ state at 4.610 MeV indicates that a large amount of the available 8^+ sum rule strength is found in this state.

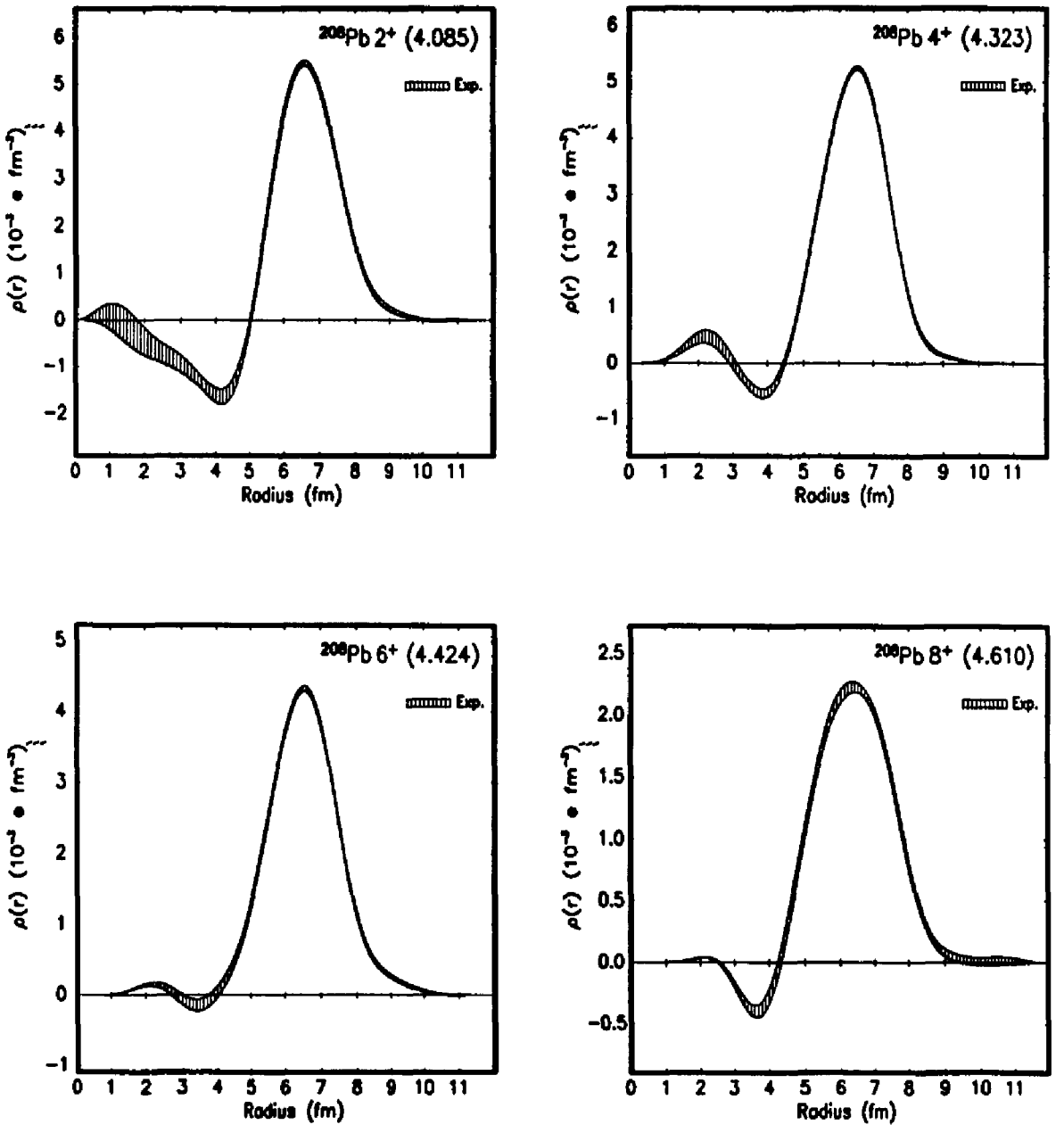

Fig.5.3 Transition charge densities from the DWBA analysis of 2^+ (4.085 MeV), 4^+ (4.323 MeV), 6^+ (4.424 MeV), and 8^+ (4.610 MeV) states.

5.3 Negative Parity States below 4.7 MeV

All of the levels seen in the energy level spectrum in ^{208}Pb below 4.7 MeV excitation energy have negative parity except for the very collective positive parity 2^+, 4^+, 6^+ and 8^+ states discussed above. States built upon $1\hbar\omega$ transitions typically have negative parity. In Figure 5.4, low-lying negative parity mean field transitions are shown. Table 5.2 lists the available 1p–1h transitions, single particle–hole energies and possible multipolarities. The single particle (SP) energies are based upon results from proton and neutron transfer reactions from neighboring nuclei. It should be noted that the effective SP energy for proton configurations is approximately 400 keV lower than the energies listed due to the effect of the Coulomb attraction.

In the lowest natural parity state of a given multipolarity, collectivity tends to build, enhancing the transition charge density at the surface and generally decreasing the transition current density. A large portion of the available strength for a given multipolarity is depleted in the lowest energy transition, as is the case for the electric octupole state at 2.615 MeV. The four experimentally observed 3^- states between 2.7 and 4.7 MeV seen in transfer and proton scattering experiments are orders of magnitude weaker than the 2.615 MeV level. Only two of these, the 4.251 MeV and 4.691 MeV 3^- levels were strong enough to be seen in this experiment. Although the 3^- case is the most extreme example, the phenomenon of collectivity building in the lowest energetic state leaving the higher states to be dominated by one or two 1p–1h configurations characterizes the natural parity transitions discussed in this section.

Magnetic states behave much differently. For unnatural parity transitions, the residual interaction which mixes 1p–1h configurations is weak and slightly repulsive. Although some configuration mixing is expected, especially between 1p–1h configurations which are energetically close, the collectivity seen in natural parity states does not occur in unnatural parity transitions.

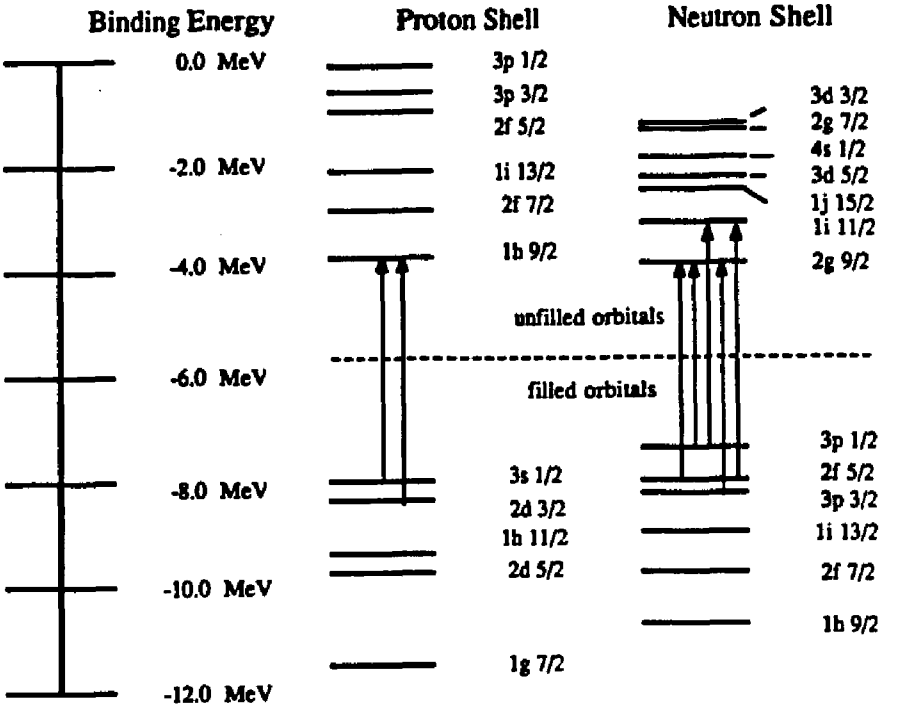

Fig 5.4 Mean field single particle configurations near Fermi level. Arrows indicate transitions that couple to negative parity with particle–hole energy below 4.8 MeV

SP Configurations	SP Energy	Electric	Magnetic
$\nu(2g_{9/2}, 3p_{1/2}^{-1})$	3.434 MeV	5^-	4^-
$\nu(2g_{9/2}, 2f_{5/2}^{-1})$	4.004 MeV	$3^-,5^-,7^-$	$2^-,4^-,6^-$
$\nu(1i_{11/2}, 3p_{1/2}^{-1})$	4.212 MeV	5^-	6^-
$\pi(1h_{9/2}, 3s_{1/2}^{-1})$	4.232 MeV	5^-	4^-
$\nu(2g_{9/2}, 3p_{3/2}^{-1})$	4.332 MeV	$3^-,5^-$	$4^-,6^-$
$\pi(1h_{9/2}, 2d_{3/2}^{-1})$	4.583 MeV	$3^-,5^-$	$4^-,6^-$
$\nu(1i_{11/2}, 2f_{5/2}^{-1})$	4.782 MeV	$3^-,5^-,7^-$	$4^-,6^-,8^-$

Table 5.2 Single particle configurations below 4.8 MeV which couple to negative parity states.

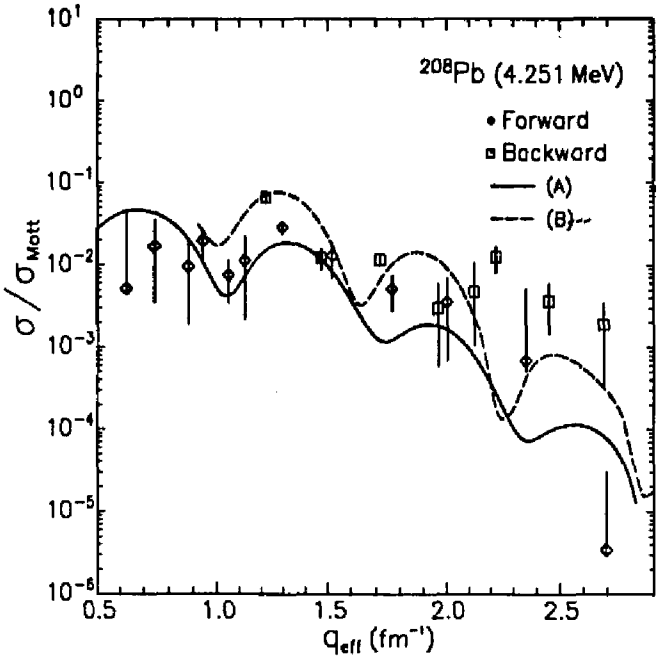

Fig.5.5 Form factor with the fitted curves for the 4.251 MeV 3^- state.

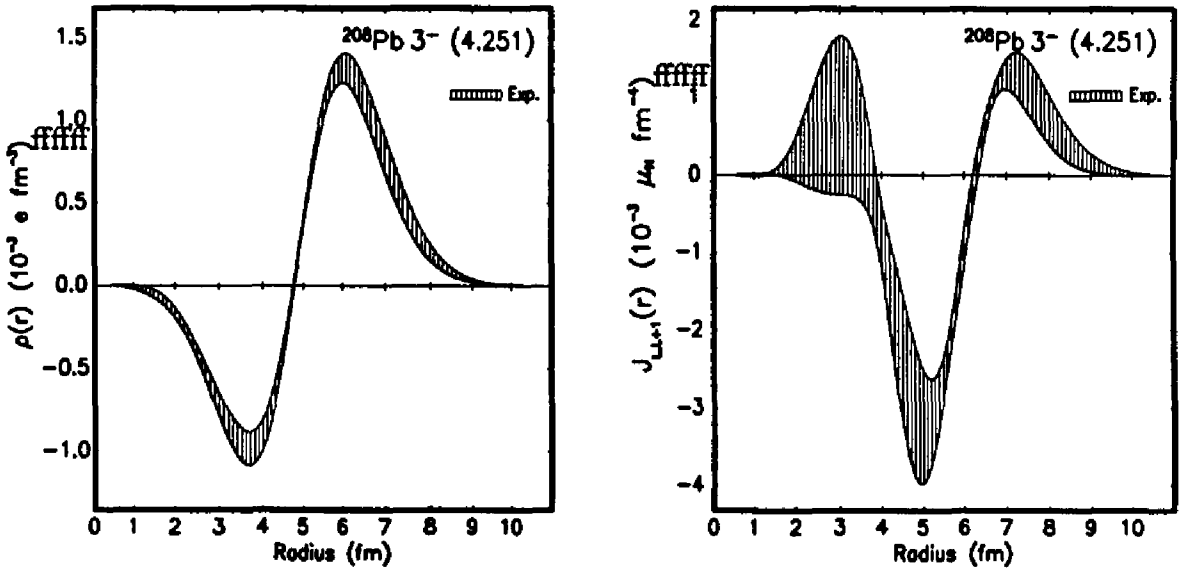

Fig.5.6 Transition charge and current densities from the 4.251 MeV 3^- state.

3^- States

Although several 3^- levels have been experimentally observed by transfer reactions and (p,p') experiments in the energy region below 4.7 MeV, only two other electric octupole states besides the 2.615 MeV 3^- are seen clearly in electron scattering. Both of these states, one at 4.251 MeV and the other at 4.691 MeV, are quite close in excitation energy to other levels and are still not unambiguously resolved even with 20 keV energy resolution.

4.251 MeV 3^- State

A possible multiplet of levels seen at 4.25 MeV excitation energy observed in proton scattering were suspected by Heussler and Brentano[59] to comprise a triplet with $J^\pi = 3^-,\ 4^-,\ 5^-$. In the case of the natural parity 3^- and 5^- transitions, some longitudinal strength would be apparent in the forward angle data. However, only one peak at 4.251 MeV is observed in our forward angle data, implying that either the 3^- and 5^- states are too close in energy to be resolved or that we are observing only one natural parity state at this energy. The number of 5^- states that we measure in this region (including the 4.124 MeV 5^- level, which was thought to be a 4^- transition by Heussler and Brentano) equal the number of available configurations which can couple to 5^-, and an additional 5^- level would mean that particle–hole configurations with SP energies above 5.0 MeV would be strongly mixed to configurations 500 keV lower. Assuming this possiblity to be unlikely, we analyzed the 4.251 MeV cross sections as a 3^- transition. In the 155° data, an additional level at 4.262 MeV was required to obtain a good fit to the data. Since this level appears purely transverse, an assumption of $J^\pi = 4^-$ was made based upon the work by Heussler and Brentano.

In the DWBA analysis of the 4.251 MeV level, three Woods–Saxon configurations were used, the $\pi(1h_{9/2}, 2d_{3/2}^{-1})$, $\nu(2g_{9/2}, 2f_{5/2}^{-1})$ and $\nu(2g_{9/2}, 3p_{3/2}^{-1})$ as well as a core polarization amplitude with scaled Fourier–Bessel coefficients taken from the 2.615 MeV octupole state. The results, shown in Table 5.3 and Figure 5.5 indicate that the transition charge density is very well described by the $\pi(1h_{9/2}, 2d_{3/2}^{-1})$ configuration with very little core polarization needed. The tran-

sition current density is dominated by a mixture of the proton configuration and the $\nu(2g_{9/2}, 2f_{5/2}^{-1})$ configuration. The χ^2 from the fit is small, which strengthens the assumption of a pure 3^- level at 4.251 MeV.

	4.251 MeV	4.691 MeV
$\nu(2g_{9/2}, 2f_{5/2}^{-1})_{3^-}$	-0.236 ± 0.070	
$\pi(1h_{9/2}, 2d_{3/2}^{-1})_{3^-}$	0.488 ± 0.043	-0.054 ± 0.149
$\nu(2g_{9/2}, 3p_{3/2}^{-1})_{3^-}$	0.061 ± 0.200	
$\nu(3d_{5/2}, 3p_{1/2}^{-1})_{3^-}$		0.357 ± 0.118
$\nu(1i_{11/2}, 2f_{5/2}^{-1})_{3^-}$		-0.695 ± 0.279
core pol ($\times$ 3_1^-)	-0.006 ± 0.022	-0.175 ± 0.041

Table 5.3 Woods–Saxon amplitudes obtained in DWBA fit to the 4.251 MeV and 4.691 MeV 3^- levels. Core polarization amplitude represents a scaling of the 2.615 MeV transition charge density to the data.

4.691 MeV 3^- State

The doublet at 4.7 MeV are the natural parity states with strong components of $\nu(1i_{11/2}, 2f_{5/2}^{-1})$ and $\pi(1h_{9/2}, 2d_{3/2}^{-1})_{3^-,5^-}$ configurations. These states are quite close in energy, 4.691 MeV for the 3^- and 4.707 MeV for the 5^-, and have not been resolved in previous electron scattering experiments. Figure 5.7 shows a spectrum taken at 280 MeV at 40° scattering angle displaying the degree of separation obtained between these states. Even with an energy resolution of 15 kev, it is still very difficult to separate these two states. The 4.691 MeV level generally appears as a shoulder on the low energy side of the relatively stronger 4.707 MeV 5^- level. For this reason, the experimental cross sections extracted

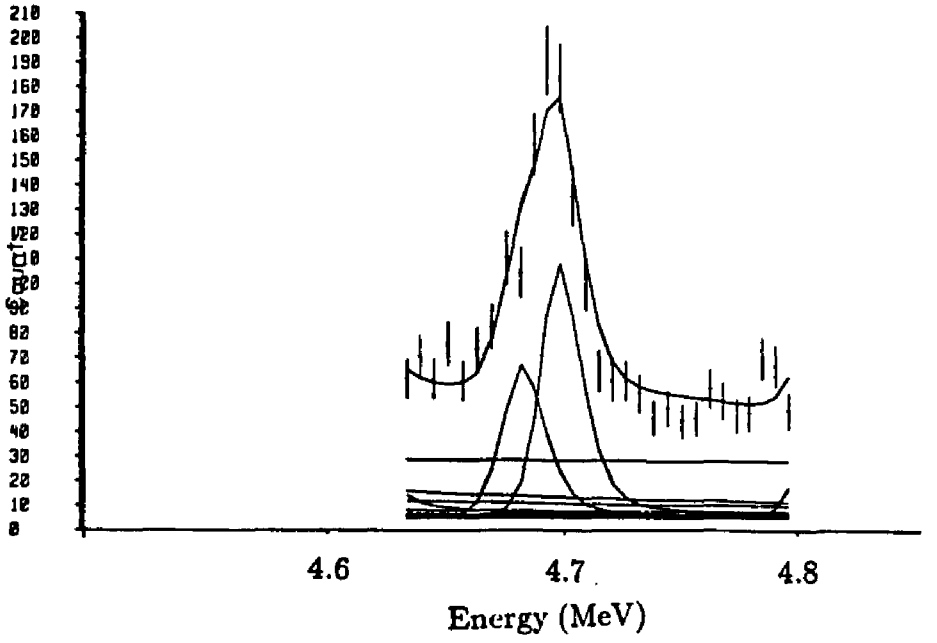

Fig 5.7 Spectrum (E_i = 280 MeV, θ =40°) in the energy region 4.6 to 4.8 MeV. The 4.691 MeV 3^- level appears as a shoulder on the lower energy side of the 4.707 MeV 5^- state.

for the 3^- level should not be regarded as reliable as the measurements obtained on the neighboring 5^- level.

The 4.691 MeV state has been identifed as a 3^- transition by the high resolution low energy proton scattering experiment by Wagner *et al*[60] . This assignment was also made by Grabmayr *et al.*[61] in a proton pickup reaction, observing a component of the $\pi(1h_{9/2}, 2d_{3/2}^{-1})$ configuration in the transition.

The DWBA analysis was performed by simultaneously fitting the amplitudes of the $\pi(1h_{9/2}, 2d_{3/2}^{-1})$, $\nu(3d_{5/2}, 3p_{1/2}^{-1})$ and $\nu(1i_{11/2}, 2f_{5/2}^{-1})$ Woods-Saxon configurations to both the transition charge and current densities, and by scaling the Fourier-Bessel coefficients from the 2.615 MeV 3^- state to the transition charge density. The longitudinal component was dominated by this scaled amplitude, which was only 3.1% of the strength seen in the first octupole state. The am-

plitude of the $\pi(1h_{9/2}, 2d_{3/2}^{-1})$ was small (-0.054), but this configuration is also a strong component of the 2.615 MeV state and therefore counted in the core polarization amplitude.

The transverse form factor was fitted with amplitudes of 0.357 ± 0.118 for the $\nu(3d_{5/2}, 3p_{1/2}^{-1})$ configuration and -0.695 ± 0.279 for the $\nu(1i_{11/2}, 2f_{5/2}^{-1})$ configuration. However, the sensitivity of the data to configuration mixing in 3^- states is suspect due to the lack of low-q data ($\leq 1.0\ fm^{-1}$) at 155° scattering angle. The fit to the forward and backward angle data is shown in Figure 5.8 and the resulting transition densities in Figure 5.9.

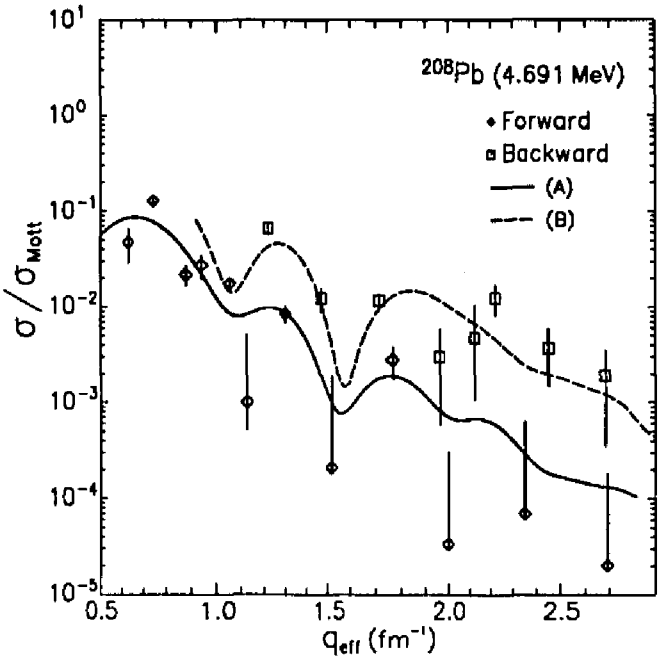

Fig.5.8 Form factor with the fitted curves for the 4.691 MeV 3^- state.

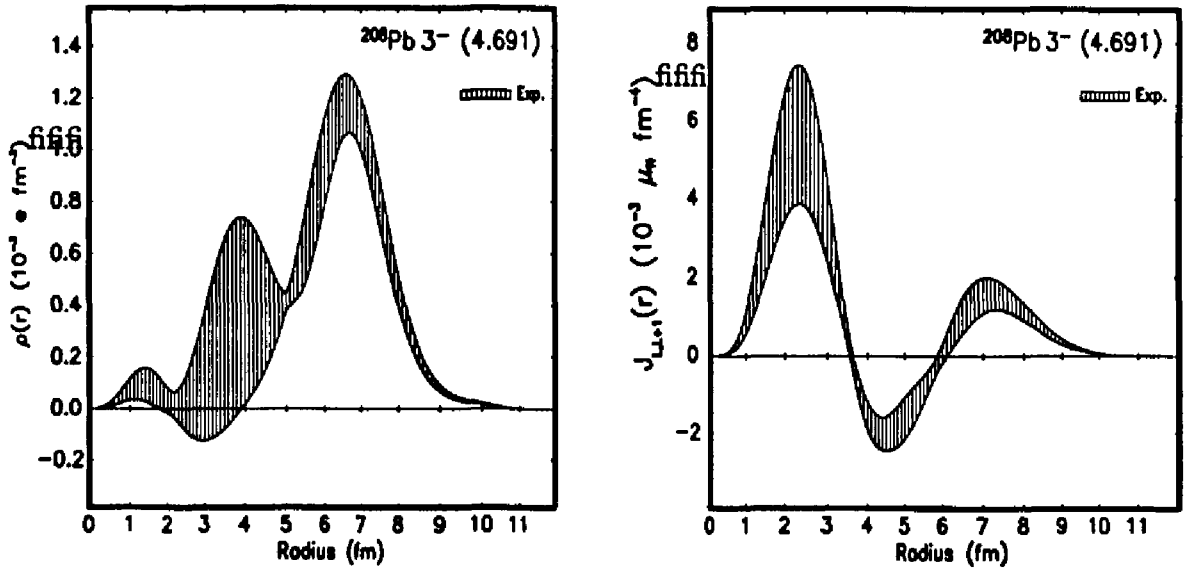

Fig.5.9 Transition charge and current densities from the 4.691 MeV 3^- state.

5^- states

The number of configurations within $1\hbar\omega$ of the fermi level which can couple to 5^- is rather large. The residual interaction, which for natural parity transitions is strongly attractive, will mix these configurations and to a lesser degree those configurations with a higher particle–hole energy. The energetically lowest configurations are given in Table 5.4 with a comparison to the energies of the observed 5^- below 4.71 MeV seen in this experiment. Effective SP energies for proton configurations should be lowered by approximately 400 keV due to the effect of the Coulomb attraction.

Particle–hole Configurations		Observed 5^- energies
$\nu(2g_{9/2}, 3p^{-1}_{1/2})_{5^-}$	3.434 MeV	3.198 ± 0.001 MeV
$\nu(2g_{9/2}, 2f^{-1}_{5/2})_{5^-}$	4.004 MeV	3.709 ± 0.001 MeV
$\nu(1i_{11/2}, 3p^{-1}_{1/2})_{5^-}$	4.212 MeV	3.961 ± 0.004 MeV
$\pi(1h_{9/2}, 3s^{-1}_{1/2})_{5^-}$	4.232 MeV	4.124 ± 0.003 MeV
$\nu(2g_{9/2}, 3p^{-1}_{3/2})_{5^-}$	4.332 MeV	4.180 ± 0.004 MeV
$\pi(1h_{9/2}, 2d^{-1}_{3/2})_{5^-}$	4.523 MeV	4.298 ± 0.003 MeV
$\nu(1i_{11/2}, 2f^{-1}_{5/2})_{5^-}$	4.782 MeV	4.707 ± 0.004 MeV

Table 5.4 Single particle–hole energies for low–lying configurations which can couple to 5^- and a listing of low–lying 5^- states observed in this experiment.

The first three 5^- states at 3.198, 3.709 and 3.961 MeV have been measured with (e, e') by Friedrich[4] and Heisenberg *et al.*[80] In the present analysis, the electron scattering data from Heisenberg *et al.* were included with our data in the DWBA analysis. The states at 4.124, 4.180, 4.298 and 4.707 MeV have been identified in transfer reactions[58][61] and proton scattering experiments[59][60], but

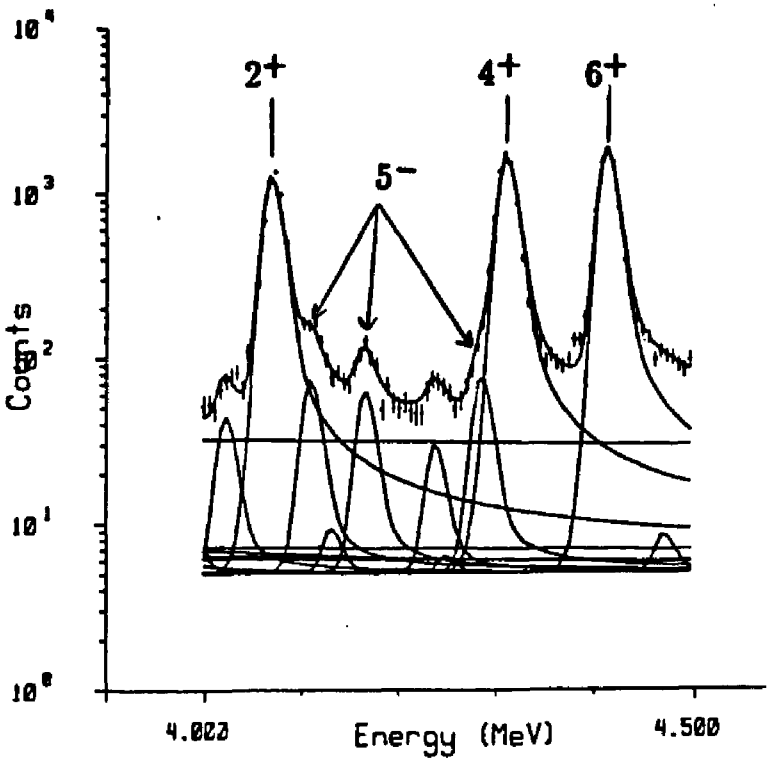

Fig.5.10 Energy spectrum ($q = 1.014\ fm^{-1}$) in the region between 4.0 and 4.5 MeV.

have been overwhelmed in electron scattering experiments by the much stronger positive parity states in this region. The presence of several low multipolarity magnetic transitions has also interfered with a precise measurement of the electromagnetic form factor for these states.

The increased energy resolution of the present experiment was sufficient to allow an unambiguous measurement of both the longitudinal and transverse form factors for the 4.124, 4.180 and 4.298 MeV 5^- states. Figure 5.10 shows a spectrum in the excitation region between 4.0 and 4.5 MeV measured at an effective momentum transfer of 1.014 fm^{-1}. The 5^- states are clearly distinguishable from the more strongly excited 2^+ (4.085 MeV) and 4^+ (4.343 MeV) states.

By measuring the transition charge density, electron scattering is sensitive to the proton components involved in the transition. The collectivity one expects in states where mixing is strong will be reflected in transition charge densities which are surface peaked due to the contribution of a large number of small amplitude

proton configurations. Interior structure in transition charge densities may be seen if one or more proton configurations dominant the transition.

Transition current densities for the 5^- states, which are sensitive to both neutron and proton contributions, can provide information on the dominant configurations participating in the transition. Currents arising from small amplitude configurations tend to cancel and only the remnants of large amplitude configurations will contribute.

3.198 MeV 5^- State

The 5^- state at 3.198 MeV exhibits a behavior which is quite different from that of the first octupole state. While the 3^- state displays a negligible transverse component, the DWBA analysis of electron scattering data by Lichtenstadt *et al.*[6] for the 3.198 MeV state has shown a significant transition current.

The 3.198 MeV level has been studied by stripping reactions[33] [34] and (p,p')[59] as well as electron scattering experiments[4][30] . While the state has been shown to be quite collective, as seen in the surface–peaked character of the charge density, the $\nu(2g_{9/2}, 3p_{1/2}^{-1})$ configuration appears to dominate the current density. Inclusion of the cross sections obtained from the present experiment with those used by Heisenberg *et.al.*[30] permitted a more precise measurement of the current density by increasing the number of data points, especially at higher momentum transfer. A DWBA analysis was performed on the entire data set, fitting the longitudinal component by a Fourier–Bessel expansion of the transition charge density and by use of Woods–Saxon wavefunctions to model the transverse piece. The particle–hole configurations used in the fit were the same used by Heisenberg *et.al.* which allowed for all the ph configurations listed in the wave function of Heusler and Brentano[59] .

A comparison of the transition current density for the 3.198 MeV state measured by Heisenberg *et.al.*[30] to that obtained by including the data from this work is shown in Figure 5.12. While the overall shape of the density remains unchanged, the interior negative lobe has been enhanced, due primarily to an

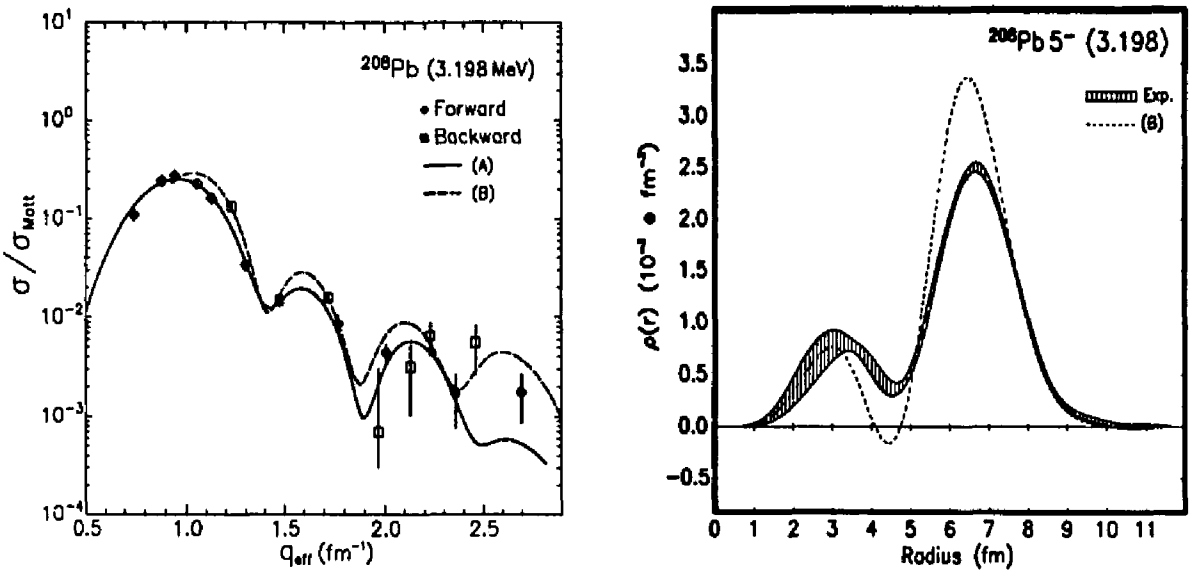

Fig.5.11 3.198 MeV form factor (left) and transition charge density (right).

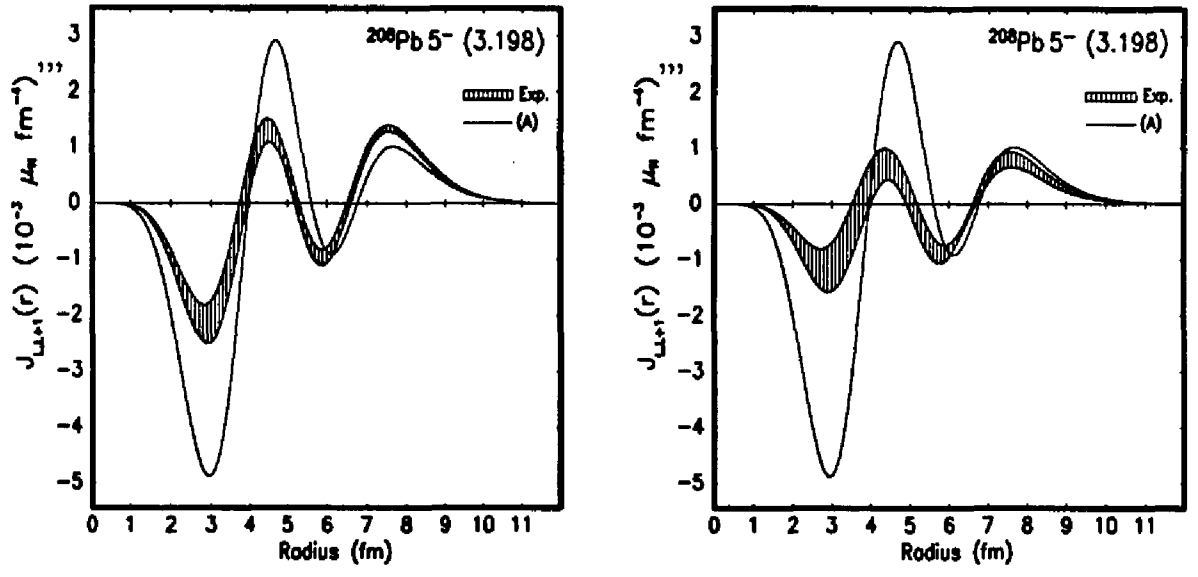

Fig.5.12 Transition current densities for the 3.198 MeV level from a microscopic DWBA analysis using Woods-Saxon wave functions. Density from a combined analysis of our data with Lichtenstadt's[6] (left). Density from Heisenberg *et.al.*[30] (right). Solid curve is from an RPA calculation from Heisenberg and Krewald[10]

increased amplitude of the $\nu(2g_{9/2}, 3p_{1/2}^{-1})$ configuration in the DWBA fit. The theoretical curves are from an RPA calculation by Heisenberg and Krewald[10] using a zero-range density dependent interaction.

3.709 MeV and 3.961 MeV 5^- States

The second and third 5^- states have been studied with electron scattering by Friedrich[4] and Heisenberg *et al.*[30] . The 3.709 MeV state is over 200 kev from the nearest observed excitation and has been reliably measured in past (e, e') experiments. This is not the case for the state at 3.961 MeV, which is less than 20 kev from the excitation at 3.946 MeV. In the high resolution proton pickup experiment by Grabmayr *et al.*[61] , a state identified as a 4^- transition at 3.946 MeV was resolved from the 5^- state, observed in that experiment at 3.963 MeV.

The 3.946 MeV state is a magnetic transition and purely transverse, therefore the best chance of observing cross section from this state is at backward scattering angles. Figure 5.17 shows a spectrum taken at 150 MeV and 155° scattering angle in the region between 3.7 and 4.2 MeV. The 4^- state is clearly differentiated from the 5^- state. The energies which gave the best fit to the data were 3.946 ± 0.005 MeV and 3.961 ± 0.004 MeV respectively.

The analysis of the 3.946 MeV state was performed first, assuming $J^\pi = 4^-$. Since this state was unresolved in the Heisenberg *et al.* experiment, the cross section from the 4^- was included in the analysis of the 3.961 MeV transition. To incorporate the previous data in our analysis of the 5^- state, a subtraction was performed on Heisenberg's data using the Fourier-Bessel coefficients from our DWBA analysis of the 4^- state.

The 5^- states at 3.709 and 3.961 MeV arise to lowest order from the constructive and destructive interference of the $\nu(2g_{9/2}, 2f_{5/2}^{-1})$ and the $\pi(1h_{9/2}, 3s_{1/2}^{-1})$ configurations. Strong components for both of these particle-hole excitations have been seen in stripping reactions[84][88] , as well as inferred by a model-dependent analysis of electron scattering data[80] .

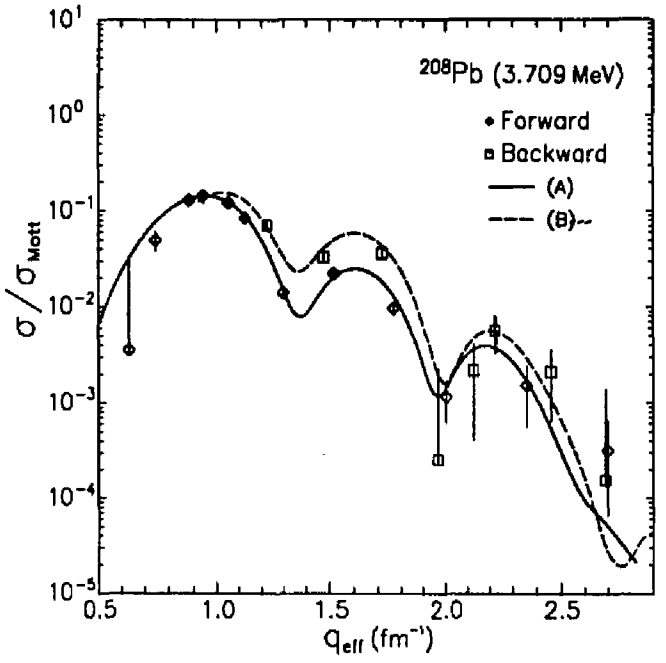

Fig.5.13 Form factor with the fitted curves for the 3.709 MeV 5^- state.

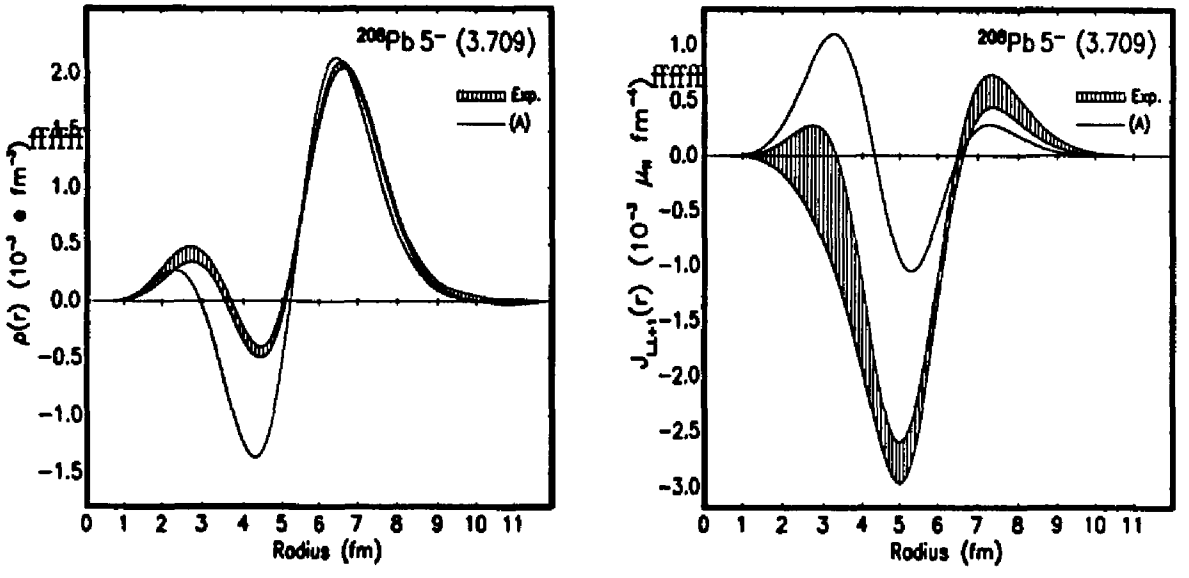

Fig.5.14 Transition charge and current densities from the 3.709 MeV 5^- level. Solid curve is from an RPA calculation from Heisenberg and Krewald[10] .

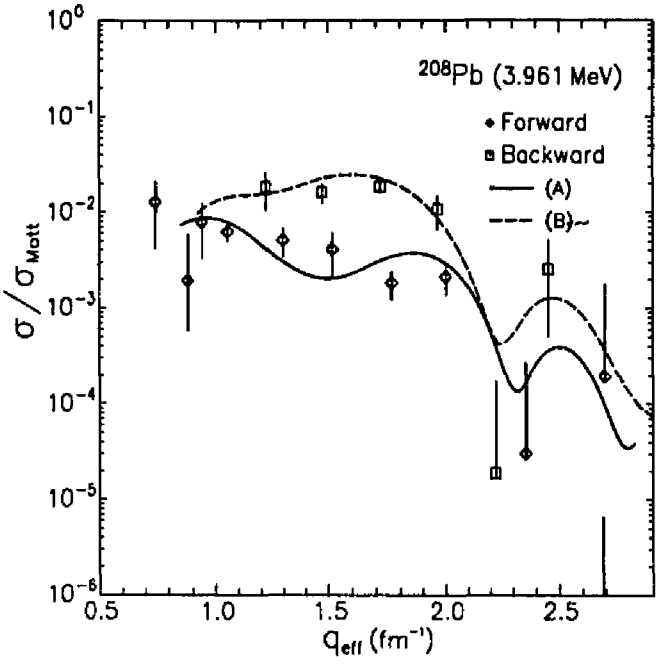

Fig.5.15 Form factor with the fitted curves for the 3.691 MeV 5^- state.

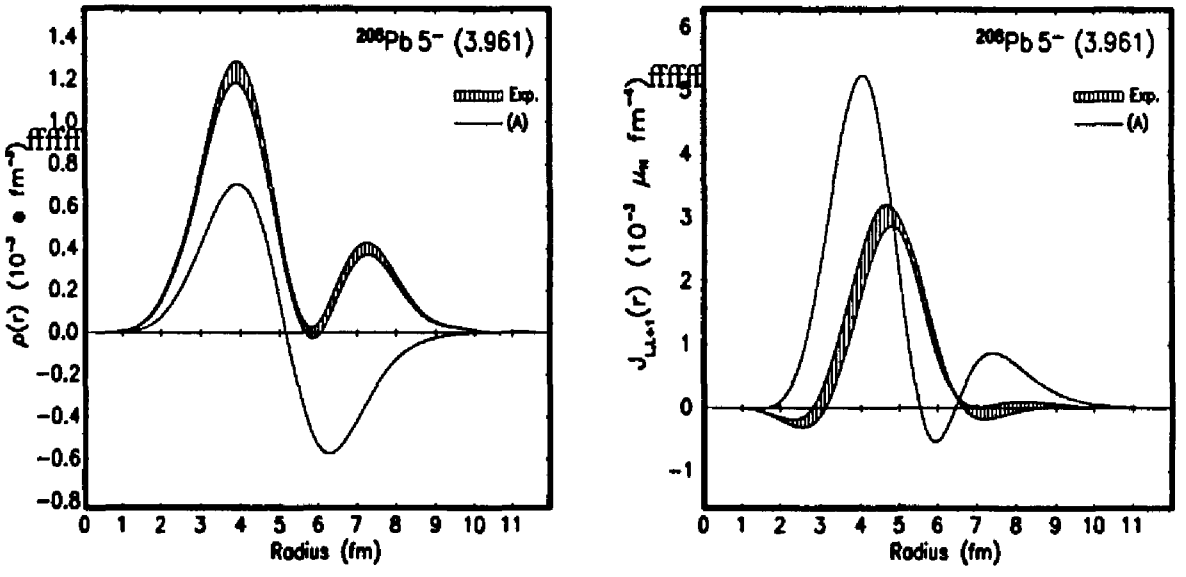

Fig.5.16 Transition charge and current densities from the 3.691 MeV 5^- level. Solid curve is from an RPA calculation from Heisenberg and Krewald[10] .

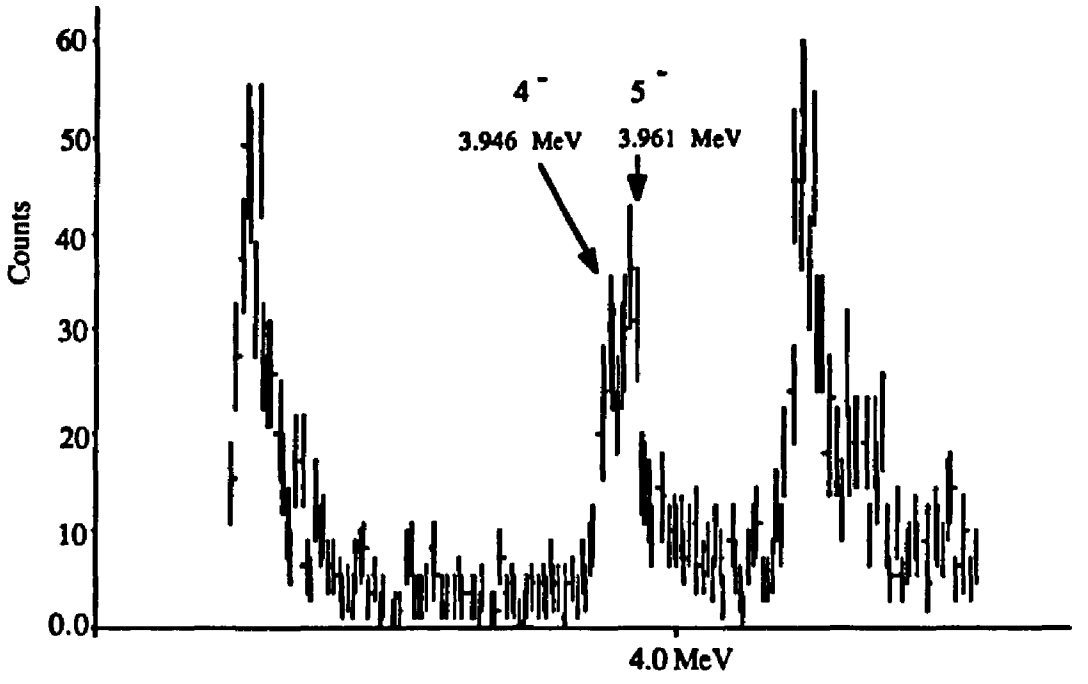

Fig.5.17 Energy spectrum ($E = 150$ MeV, θ =155°) in the region between 3.7 and 4.2 MeV.

Particle–hole Configurations	Amplitude
$\nu(1i_{11/2}, 3p^{-1}_{1/2})_{5^-}$	-0.4266 ± 0.1134
$\pi(1h_{9/2}, 3s^{-1}_{1/2})_{5^-}$	0.6358 ± 0.0373
	$f_m = 0.4188 \pm 0.0328$
	$f_c = 0.9770 \pm 0.0499$

Table 5.5 Results from a DWBA analysis for the 3.961 MeV 5^- state. Amplitudes to Woods–Saxon particle–hole configurations were adjusted as well as the magnetic quenching, f_m and the quenching of the convection current, f_c.

The charge density (Figure 5.14) of the 3.709 state is produced by the proton valence component and the polarization of the proton core by the valence neutron transition. The density is surface peaked, although a significant interior lobe is seen. The large surface component of the transition charge density is due to the proton valence configuration and the proton core polarization induced by the neutron valence transitions adding constructively.

The transition densities obtained from the third 5^- level at 3.961 MeV are shown in Figure 5.16. The $\nu(2g_{9/2}, 2f_{5/2}^{-1})$ and the $\pi(1h_{9/2}, 3s_{1/2}^{-1})$ configurations add destructively, leading to an enhancement of the interior lobe of the transition charge density and a decrease of charge at the surface.

The current density is dominated by the $\pi(1h_{9/2}, 3s_{1/2}^{-1})$ configuration. Thus, the current is due in large part by the convection current from this proton. Current quenching, seen in transition currents produced by the magnetic moment of the nucleon, may in the case of the 3.961 MeV state be compared with any quenching which arises from the convection current. In our DWBA analysis, the amplitudes of the the particle–hole configurations and the quenching factors for the magnetic and convection current were fit simultaneously to the current density. The results are summarized in Table 5.5.

Within the errors given, the quenching factors resulting from our analysis are identical to those quoted by Heisenberg *et al.* ($f_m = 0.43 \pm 0.015$, $f_c = 0.97 \pm 0.055$), reaffirming the conclusion reached in that work that only the magnetization current is quenched in the 3.961 MeV transition, while the convection current appears to remain unquenched.

4.124 MeV, 4.180 MeV and 4.298 MeV 5^- States

The excitations at 4.124, 4.180 and 4.298 MeV have been observed in proton scattering experiments[59][60] and transfer reactions[58][61] . The energies and multipolarities observed are given in Table 5.6.

The assignment of $J^\pi = 5^-$ to the excitation at 4.124 MeV has only been made tentatively by Vold *et al.* in a study of neutron particle–hole states in ^{208}Pb, observing contributions from both the $\nu(2g_{9/2}, 3p_{1/2}^{-1})$ and $\nu(1i_{11/2}, 3p_{1/2}^{-1})$ configurations. Proton scattering[60][59] and proton pickup reactions[61] made an assignment of $J^\pi = 4^-$ to this state. In our measurements, the presence of a strong longitudinal component (Figure 5.18) indicates that the state must have natural parity. Based upon the likely particle–hole configurations given by both neutron and proton transfer reactions, we analyzed the state as $J^\pi = 5^-$. From a DWBA analysis using Woods–Saxon single–particle wave functions to fit both charge and current densities, we observed strong components of the $\pi(1h_{9/2}, 2d_{3/2}^{-1})$ and $\nu(1i_{11/2}, 3p_{3/2}^{-1})$ configurations.

This work (e,e')		Vold *et al.*[58] $^{207}Pb(d,p)^{208}Pb$		Grabmayr *et al.*[61] $^{209}Bi(d,^3He)^{208}Pb$		Wagner *et al.*[60] (p,p')		Heussler *et al.*[59] (p,p')	
J^π	MeV	J^π	MeV	J^π	MeV	J^π	MeV	J^π	MeV
5^-	4.124 ± 0.003	5^-	4.120	4^-	4.126 ± 0.002	4^-	4.125 ± 0.001	4^-	4.126
5^-	4.180 ± 0.004	5^-	4.175	5^-	4.181 ± 0.003	5^-	4.181 ± 0.001	5^-	4.180
5^-	4.298 ± 0.003	5^-	4.290	5^-	4.298 ± 0.003	5^-	4.296 ± 0.002	5^-	4.296

Table 5.6 Energies and multipolarites observed from this work, transfer reactions and proton scattering experiments for the states at 4.12, 4.18 and 4.29 MeV.

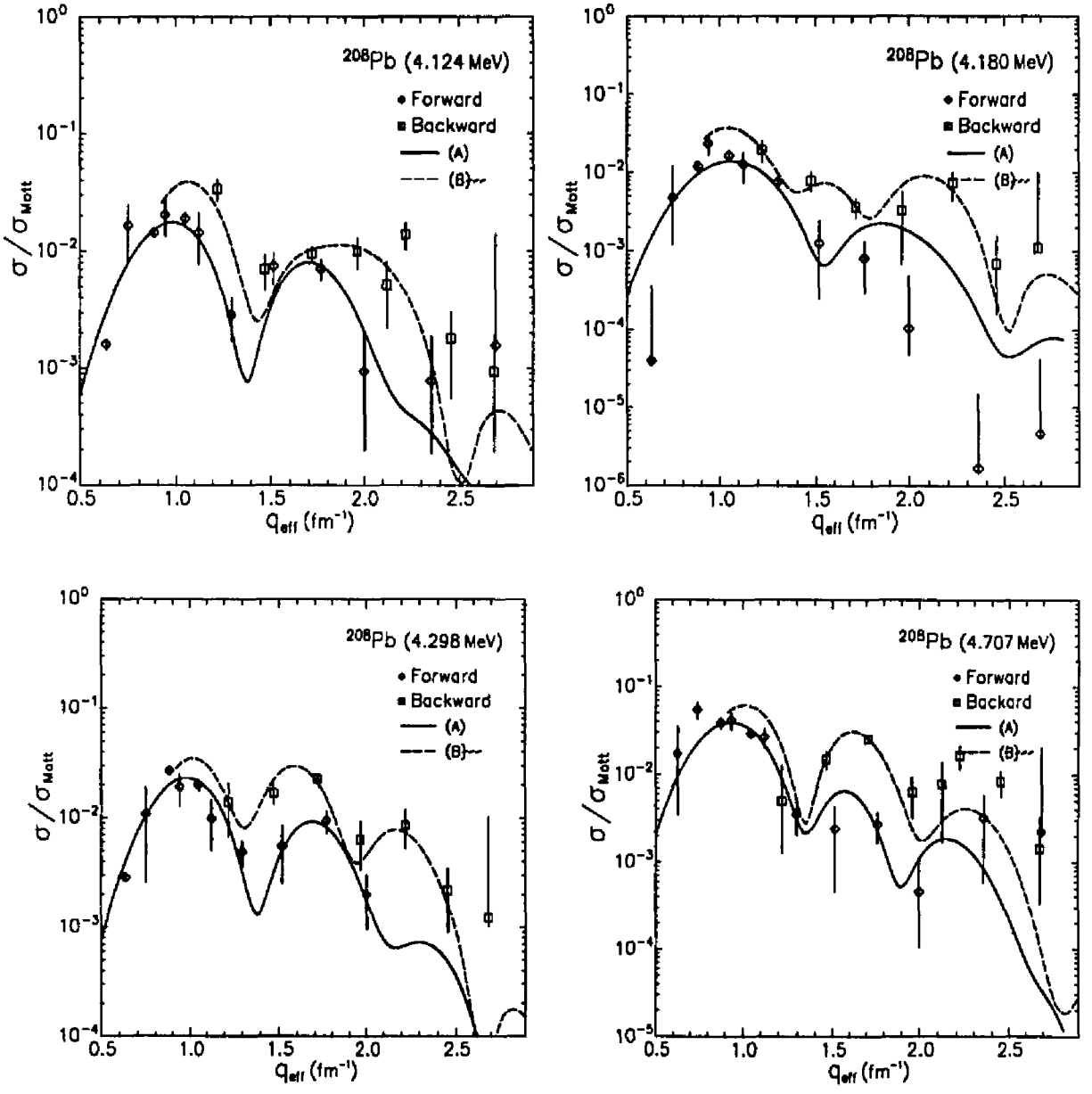

Fig.5.18 DWBA form factor fits to the 4.124, 4.180, 4.298 and 4.707 MeV 5^- states.

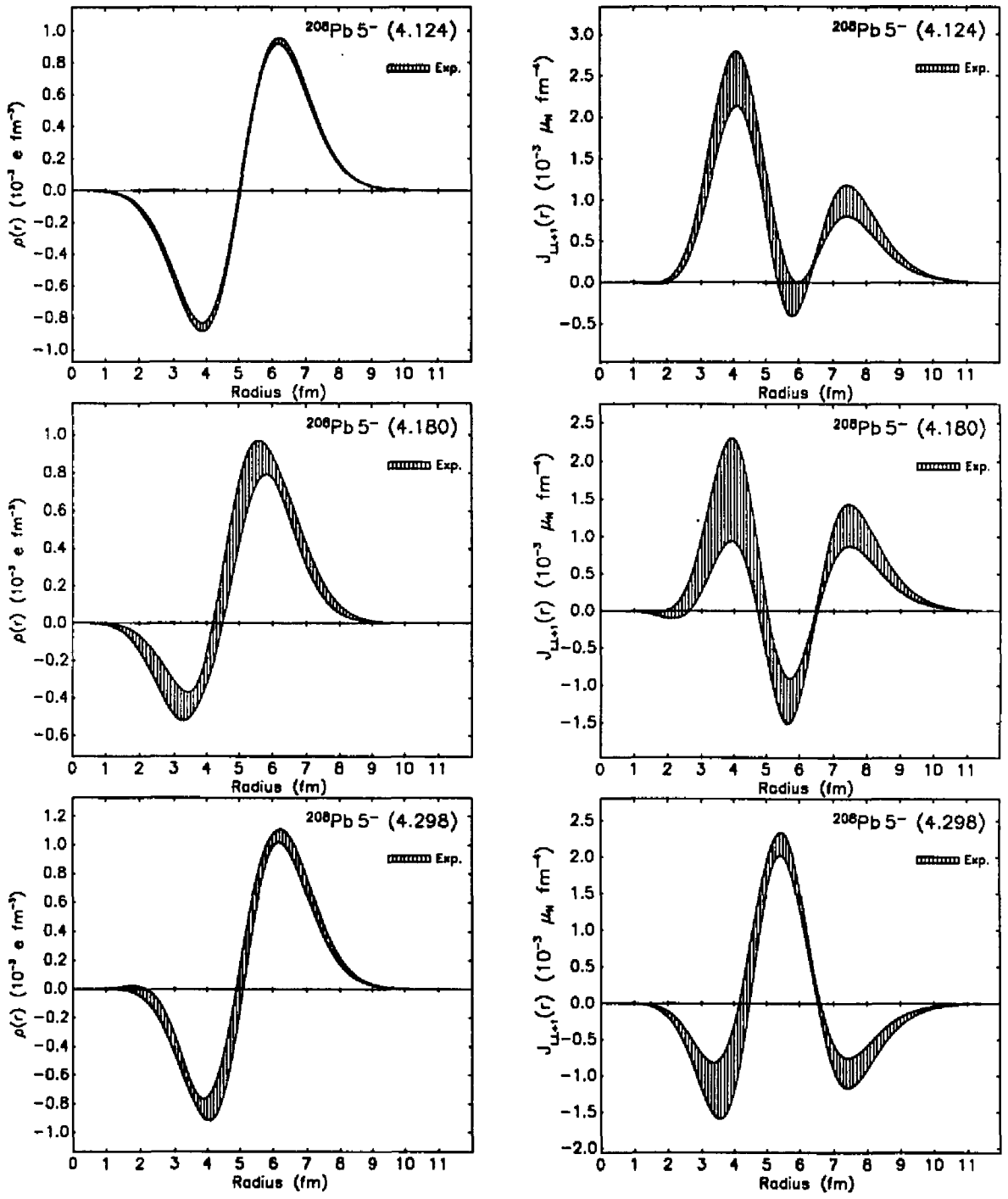

Fig.5.19 Transition charge and current densities from the 4.124, 4.180 and 4.298 MeV 5^- states.

There is general agreement that the state at 4.180 and 4.298 MeV are 5^- transitions. The charge densities are a mixture of the $\pi(1h_{9/2}, 2d_{3/2}^{-1})$ and the $\pi(1h_{9/2}, 3s_{1/2}^{-1})$ configurations. The current densities which, in addition to the convection current of the protons, are sensitive to the spin convection current of the neutrons. The 4.124 MeV state appears to have a strong component of the $\nu(1i_{11/2}, 3p_{3/2}^{-1})$ configuration while the 4.298 MeV state is dominated by the $\nu(2g_{9/2}, 3p_{3/2}^{-1})$ configuration. In the 4.180 MeV state approximately equal admixtures of these two neutron configurations contributed.

4.707 MeV 5^- State

The 4.707 MeV level is a member of a 3^-, 5^- doublet seen at 4.691 MeV and 4.707 MeV. As mentioned in the discussion of the 4.691 MeV 3^- state, the 5^- level is the more strongly excited of the two and hence cross sections could be extracted more reliably. Grabmayr *et al.* observed these levels in a proton pickup reaction with $l = 2$ ($\pi(1h_{9/2}, 2d_{3/2}^{-1})$) and assumed a 3^- assignment for both states based an exhaustation of the 4^-, 5^- and 6^- sum rule strength. However, a large amount of the 5^- spectroscopic strength was believed to be in the level at 4.26 MeV. No evidence for a 5^- state was seen in our experiment at 4.26 MeV, and if this were the case considerable 5^- strength would then be available for the level at 4.707 MeV.

Our assignment of 5^- was based upon the probability of a 5^- transition in this region from the $\nu(1i_{11/2}, 2f_{5/2}^{-1})$ configuration which has a SP energy of 4.780 MeV. The fit to the data was performed using Woods–Saxon wave functions representing this neutron transition and the $\pi(1h_{9/2}, 2d_{3/2}^{-1})$ configuration with a core polarization represented by scaled Fourier–Bessel coefficients from the 3.198 MeV 5^- state (Figure 5.20). The transition current density was dominated by the neutron configuration which reinforces our assignment of 5^- to this state. The transition densities are given in Figure 5.20.

7^- State

Electron scattering results from the 7^- state at 4.037 MeV have been reported by Heisenberg *et al*[30] . With the improved energy resolution in this experiment,

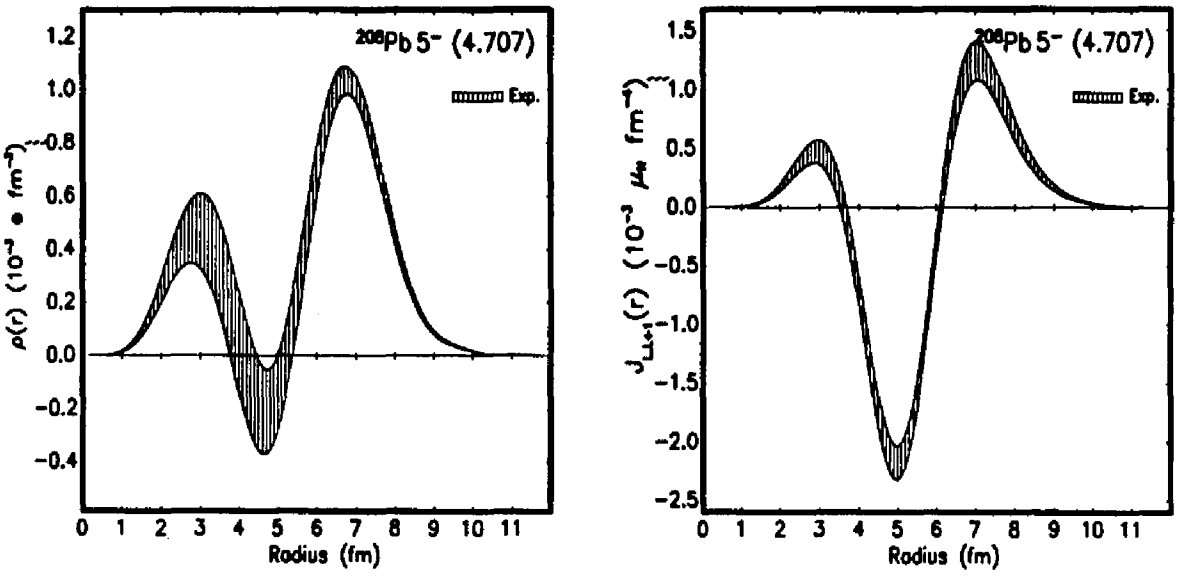

Fig.5.20 Transition charge and current densities from the 4.707 MeV 5^- state.

it was hoped that a more accurate separation of the 7^- level from the strong 2^+ state at 4.085 MeV could be accomplished.

The longitudinal component of the form factor was fit with Fourier–Bessel coefficients describing the first 7^- state in ^{206}Pb scaled to the data. The transverse currents were described by the Woods–Saxon $\nu(2g_{9/2}, 2f_{5/2}^{-1})$ configuration, adjusting the amplitude only. This model, the same used by Heisenberg *et al.*, gave a reasonable fit to the data (Figure 5.21). The resulting transition densities are given in Figure 5.22.

The current originates from the motion of the neutron spin. Thus, the amplitude of the fitted $\nu(2g_{9/2}, 2f_{5/2}^{-1})$ configuration corresponds to the quenching of magnetization current. The amount of quenching seen $f_m = 0.3056 \pm 0.051$ is substantially less than the $f_m = 0.505$ reported by Heisenberg *et al.*

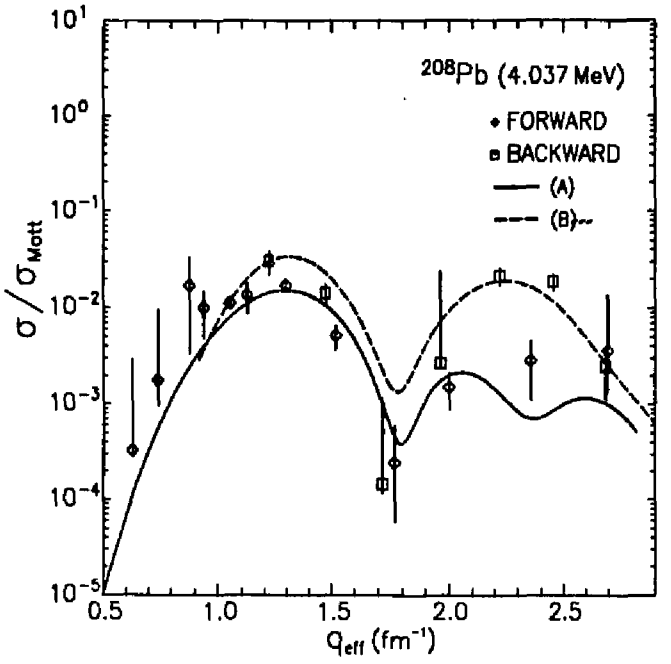

Fig.5.21 Form factor with the fitted curves for the 4.037 MeV 7^- state.

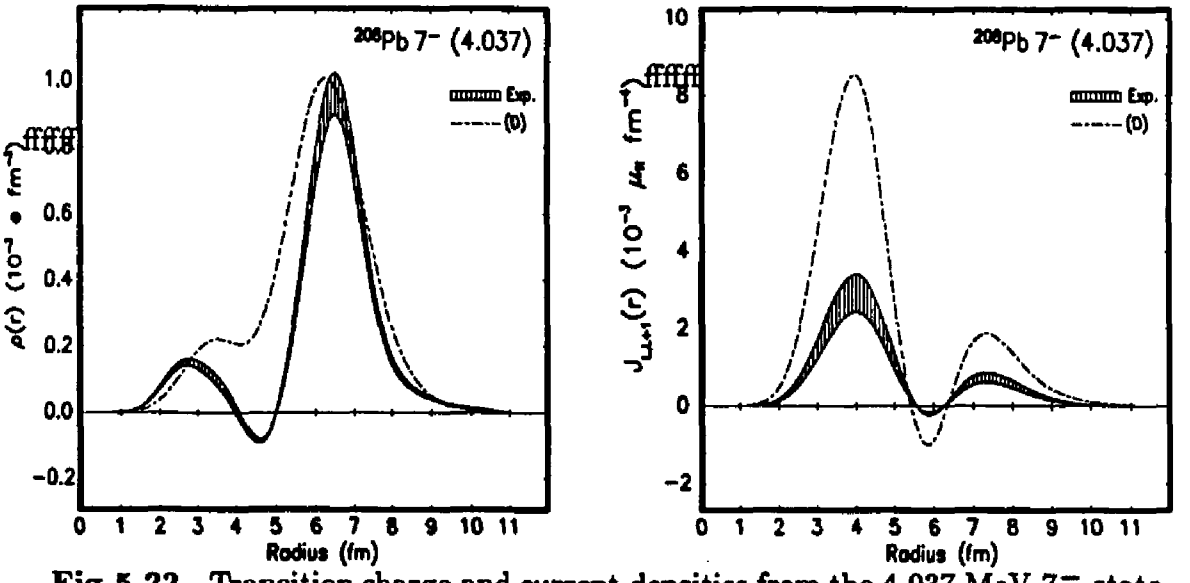

Fig.5.22 Transition charge and current densities from the 4.037 MeV 7^- state. Theoretical curves are RPA predictions from Heisenberg and Krewald[10] .

4^- and 6^- States

Many negative parity magnetic states with multipolarites $J = 4, 6$ have been observed below 4.7 MeV excitation energy in ^{208}Pb. The residual interaction, which for unnatural parity transitions is weakly repulsive, may still induce configuration mixing due to the number of single particle configurations within 500 kev of each other. In electron scattering, these states, which are far from being collective, result from the magnetization density of the neutron and proton spins. Since the number of particles which contribute is small relative to magnetic states with very high spins (*eg.* $J^\pi = 14^-$), one expects these lower multipolarity states to be weakly excited in (e, e') experiments. With the level of statistics at backward scattering angle in this experiment, only those transitions with a significant proton component, and hence a convective current, were observed. For example, the 2^- level at 4.230 MeV, which arises primarily from a single neutron configuration $\nu(2g_{9/2}, 2f_{5/2}^{-1})$, was unseen in our measurements.

Table 5.7 lists the available single particle configuratons with a SP energy below 4.7 MeV and the excitation energies of 4^- and 6^- states observed in a proton pickup experiment by Grabmayr *et al.*[61] and a proton scattering experiment by Wagner *et al.*[60] . The levels seen in this work are noted by an asterisk. Effective SP energies from proton configurations are approximately 400 keV lower than those listed due to the effect of the Coulomb attraction between protons. Table 5.7 excludes the reported 4^- state at 4.124 MeV since this assignment is inconsistent with our measurement of a strong longitudinal form factor.

3.946 MeV 4^- State

The 3.946 MeV 4^- level is within 20 kev of the 5^- level at 3.961 MeV and has been unresolved in previous (e, e') experiments. In the proton pickup experiment by Grabmayr *et al.*, a state at 3.948 ± 0.002 MeV was resolved from the 5^- state and shown to be dominantly a l=0 transfer with an admixture of l=2,

Particle-hole Configurations		Observed Energies
	4^-	
$\nu(2g_{9/2}, 3p^{-1}_{1/2})_{4^-}$	3.434 MeV	3.475 ± 0.002 MeV †‡
$\nu(2g_{9/2}, 2f^{-1}_{5/2})_{4^-}$	4.004 MeV	3.919 ± 0.001 MeV ‡
$\pi(1h_{9/2}, 3s^{-1}_{1/2})_{4^-}$	4.232 MeV	3.946 ± 0.002 MeV *†
$\nu(2g_{9/2}, 3p^{-1}_{3/2})_{4^-}$	4.332 MeV	4.262 ± 0.007 MeV *†‡
$\pi(1h_{9/2}, 2d^{-1}_{3/2})_{4^-}$	4.523 MeV	4.358 ± 0.003 MeV *†‡
	6^-	
$\nu(2g_{9/2}, 2f^{-1}_{5/2})_{6^-}$	4.004 MeV	3.997 ± 0.004 MeV †‡
$\nu(1i_{11/2}, 3p^{-1}_{1/2})_{6^-}$	4.212 MeV	4.210 ± 0.003 MeV *†‡
$\nu(2g_{9/2}, 3p^{-1}_{3/2})_{6^-}$	4.332 MeV	4.383 ± 0.002 MeV *†‡
$\pi(1h_{9/2}, 2d^{-1}_{3/2})_{6^-}$	4.523 MeV	4.481 ± 0.001 MeV *†‡

(*–this experiment, †– Grabmayr *et al.*[61] , ‡– Wagner *et al.*[60])

Table 5.7 Single particle–hole energies for low-lying configurations which can couple to 4^- and 6^-. Observed experimental energies from this experiment, proton pickup reaction[61] , and proton scattering experiment[60] are given.

indicating that the proton component is a mixture of the $\pi(1h_{9/2}, 3s^{-1}_{1/2})$ and the $\pi(1h_{9/2}, 2d^{-1}_{3/2})$ configurations. While this state has not been resolved in neutron pickup reactions, the proximity in energy of the neutron configurations which can couple to 4^- increases the likelihood that these configurations also play a role.

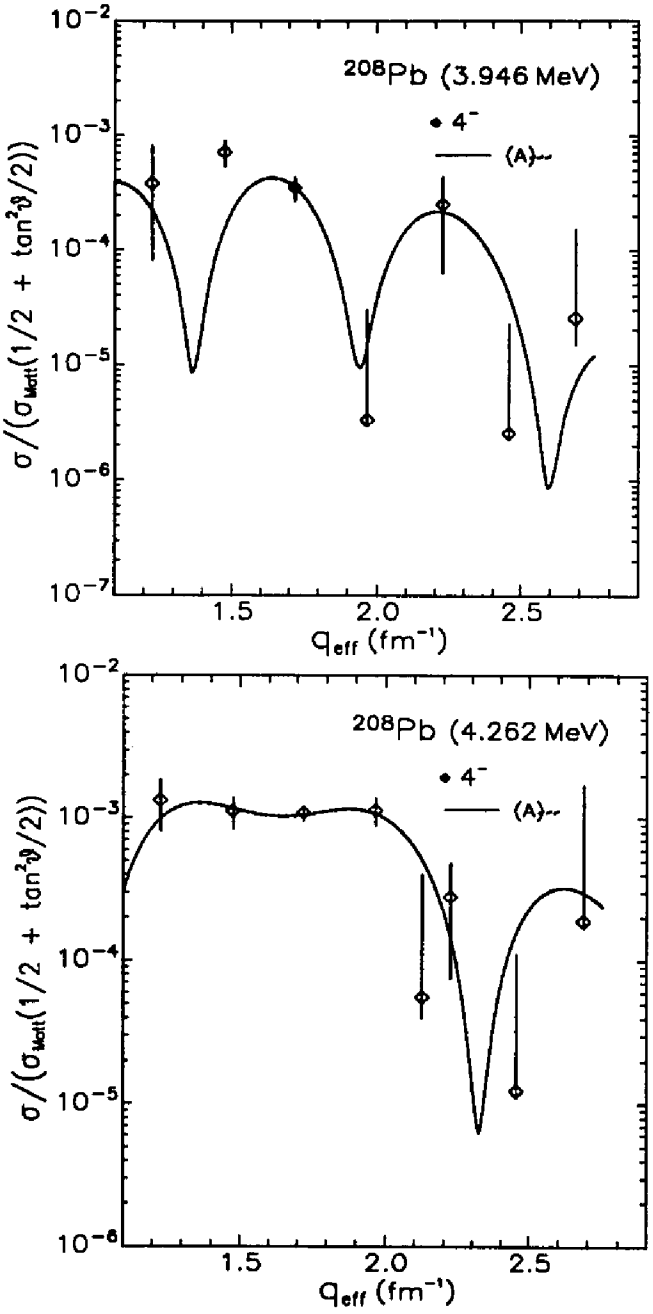

Fig.5.23 Form factors with the fitted curves for the 3.946 MeV and 4.262 MeV 4^- states.

4.262 MeV 4^- State

Evidence of a 4^- state in a proton transfer reaction has been reported by Grabmayr *et al.*[61] in the suspected 3^-, 4^- and 5^- multiplet of levels seen near 4.26 MeV. As noted in our discussion of the 4.251 MeV 3^- level, no clear indication was seen in the forward angle data for a 5^- state in this region. At 155° however, we do see some transverse strength in a peak at 4.262 MeV distinct from the level at 4.251 MeV. Based upon the purely transverse character of this state and the spin and parity assignment of Grabmayr, this level was analyzed as a 4^- transition.

Since this state is the weaker member of a doublet separated by only 11 keV, it seems likely that some strength from the 4.251 MeV state, which has a significant transverse component, is contaminating the 4^- cross section. While we do obtain an excellent fit to the data (Figure 5.23), the single-particle amplitudes obtained in the DWBA analysis are unrealistically large (Table 5.8), suggesting that this doublet has not been adequately resolved.

4.358 MeV 4^- State

The 4^- level at 4.358 MeV has been identified in both neutron[33] and proton[61] transfer reactions. The neutron $\nu(2g_{9/2}, 3p_{1/2}^{-1})$ configuration was determined by Vold *et al.* to be a constituent of the transition in a neutron transfer experiment based upon the l=4 signature of the angular distribution. However, the SP energy of this configuration is 3.434 MeV is low compared to th SP energy of 4.332 MeV for the $\nu(2g_{9/2}, 3p_{3/2}^{-1})$ configuration. Since there is very little sensitivity in the electromagnetic form factor to differentiate between these two configurations, we chose the latter configuration to be included in our DWBA fit. The proton pickup experiment by Grabmayr *et al.* observed an l=2 angular distribution indicating a $\pi(1h_{9/2}, 2d_{3/2}^{-1})$ component in this transition.

In the DWBA analysis, Woods-Saxon wave functions were fit to the 3.946 MeV backward angle data (the state was not observed at forward angles) and

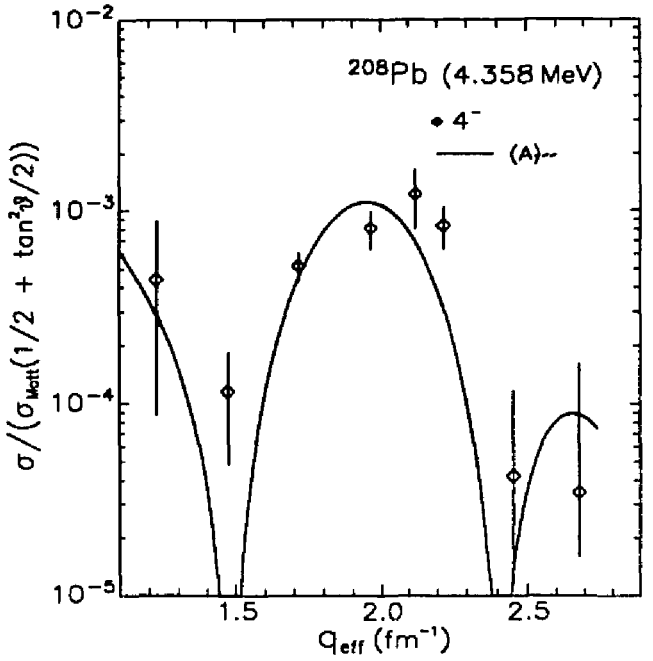

Fig.5.24 Form factor with the fitted curve for the 4.358 MeV 4^- state.

	3.946 MeV	4.262 MeV	4.358 MeV
$\nu(2g_{9/2}, 2f_{5/2}^{-1})_{4^-}$	0.353 ± 0.105		
$\pi(1h_{9/2}, 3s_{1/2}^{-1})_{4^-}$	0.466 ± 0.377	1.121 ± 0.136	
$\nu(2g_{9/2}, 3p_{3/2}^{-1})_{4^-}$		1.274 ± 0.169	0.617 ± 0.0592
$\pi(1h_{9/2}, 2d_{3/2}^{-1})_{4^-}$	-0.434 ± 0.377	-0.883 ± 0.157	0.337 ± 0.059

Table 5.8 Woods-Saxon amplitudes obtained in DWBA fit to the 3.946 MeV, 4.262 MeV and 4.358 MeV 4^- levels.

the 4.358 MeV data by adjusting the amplitudes only. The Woods-Saxon radii were those determined from the fits to the 14^- state and the 12^- state at 7.064 MeV for the neutron and proton single particle levels respectively. The fits to the form factors, shown in Figure 5.23, were given by the amplitudes and config-

urations listed in Table 5.8. Roughly equal admixtures of the $\pi(1h_{9/2}, 3s_{1/2}^{-1})$, $\pi(1h_{9/2}, 2d_{3/2}^{-1})$ and $\nu(2g_{9/2}, 2f_{5/2}^{-1})$ configurations were fit to the 4^- state at 3.946 MeV. The level at 4.358 MeV was fit best by a dominant $\nu(2g_{9/2}, 3p_{3/2}^{-1})$ configuration with a smaller contribution from the $\pi(1h_{9/2}, 3s_{1/2}^{-1})$ configuration.

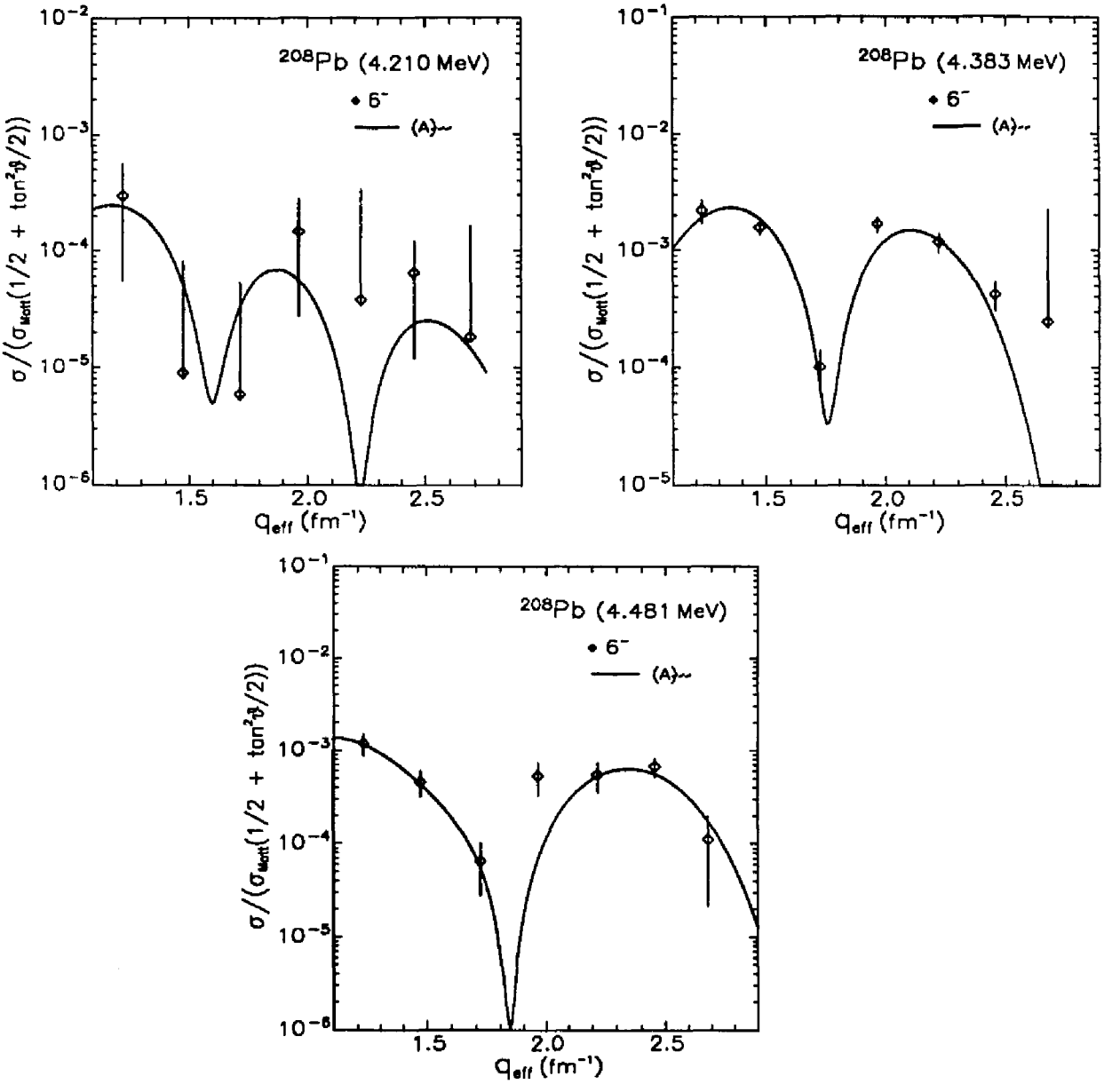

Fig.5.25 Form factors with the fitted curves for the 4.210 MeV, 4.383 MeV and 4.481 MeV 6^- states.

4.210 MeV 6^- State

This level is weakly excited in electron scattering and except for data taken at a momentum transfer where the form factor has maxima, we can only establish upper bounds on the cross section. The analysis was performed adjusting the amplitudes of two neutron Woods–Saxon configurations, the $\nu(1i_{11/2}, 3p^{-1}_{1/2})$ and $\nu(2g_{9/2}, 2f^{-1}_{5/2})$. Heussler and Brentano[59] predict the 4.210 MeV state to be primarily a $\nu(1i_{11/2}, 3p^{-1}_{1/2})$ transition mixed with small amplitudes of neighboring configurations. The fit to the 155° data (Figure 5.25) is well described by a dominant $\nu(1i_{11/2}, 3p^{-1}_{1/2})$ configuration although only 11.1% of the SP strength contributes (Table 5.8)

4.383 MeV 6^- State

The 4.383 MeV 6^- state has been observed in both proton scattering[60] and proton transfer reactions[34] [61] . In the $^{209}Bi(d,^3He)^{208}Pb$ experiment by Grabmayr *et al.* this state was found to exhaust 95% of the 6^- sum rule strength for the $\pi(1h_{9/2}, 2d^{-1}_{3/2})$ transition.

This level was seen with appreciable strength in both forward and backward angle spectra, although the forward angle data were not included in the analysis due to the large uncertainties and the completely transverse character of unnatural transitions. A good fit to the data was obtained assuming the state to be a pure 1p–1h transition from the $\pi(1h_{9/2}, 2d^{-1}_{3/2})$ configuration based upon the strong spectroscopic factor reported by Grabmayr and the lack of evidence for a state at this energy in neutron transfer reactions[33] . The DWBA analysis, in which both the Woods–Saxon radii (1.304 ± 0.018) and the SP amplitude was allowed to vary, reproduced 31.2% of the single–particle strength.

4.481 MeV 6^- State

The 4.481 MeV 6^- state is a well separated level observed in the 155° scattering data only. The data were analyzed using mixtures of the four single–particle configurations in this energy region that can couple to 6^- (Table 5.7), allowing only the amplitudes of the Woods–Saxon configurations to vary. The fit (Figure

5.25) was dominated by the $\nu(2g_{9/2}, 2f_{5/2}^{-1})$ transition with small admixtures of $\pi(1h_{9/2}, 2d_{3/2}^{-1})$ and $\nu(1i_{11/2}, 3p_{1/2}^{-1})$ (Table 5.9).

	4.210 MeV	4.383 MeV	4.481 MeV
$\nu(2g_{9/2}, 2f_{5/2}^{-1})_{6^-}$			0.096 ± 0.065
$\nu(1i_{11/2}, 3p_{1/2}^{-1})_{6^-}$	0.318 ± 0.116		-0.241 ± 0.110
$\nu(2g_{9/2}, 3p_{3/2}^{-1})_{6^-}$		0.402 ± 0.076	
$\pi(1h_{9/2}, 2d_{3/2}^{-1})_{6^-}$		0.559 ± 0.029	0.221 ± 0.034

Table 5.9 Woods–Saxon amplitudes obtained in DWBA fit to the 4.210 MeV, 4.383 MeV and 4.481 MeV 6^- levels.

Summary

Although the negative parity excitations discussed in this section have been measured with several reactions, only the first three 5^- levels and the 7^- level have been studied in previous electron scattering experiments. This energy regime is quite interesting as it encompasses most of the excitations which arise due to 1p–1h transitions from just below to just above the fermi level. Transition densities have been obtained for a majority of the negative parity states observed by other reactions. In this regime, a nearly complete set of electron scattering data have been measured. Transition charge, current and magnetization densities from these levels offer severe constraints to nuclear structure calculations in order to successfully predict both transition denity shapes and amplitudes.

In Figure 5.26, a comparison is made between the observed excitation energies and the p–h energies of $1\hbar\omega$ configurations which are expected to dominate in this energy regime. Although configuration mixing and the coupling to small

amplitude 1p–1h transitions tend to lower the excitation energy, in general there is a good one–to–one agreement between single particle–hole energies and the experimental levels. Predictions from a TDA calculation using a correlated ground state are also given.

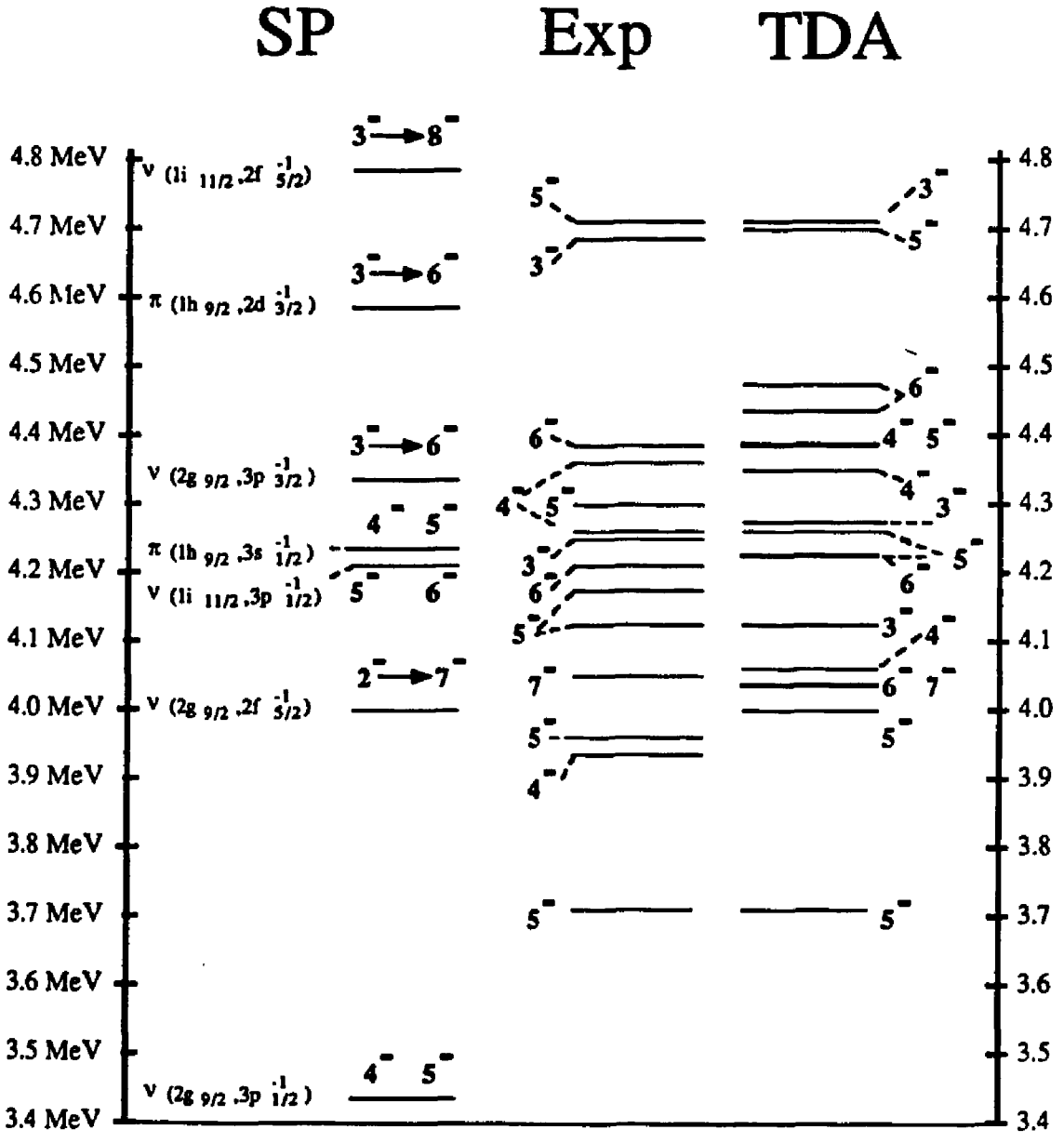

Fig.5.26 Comparison of the experimental energies, relevant single particle–hole energies and TDA predictions for negative parity excitations between 3.0 MeV and 4.8 MeV.

5.4 Positive Parity States between 4.8 MeV and 5.3 MeV

In the Independent Particle Model picture of the nucleus, the energetically lowest positive parity transitions result from intruder one–body levels of higher lying harmonic oscillator shells being lowered in energy by the spin–orbit coupling to shells with opposite parity. For example, in the proton level scheme in ^{208}Pb the intruder level of $\pi 1h_{11/2}$ $(5\hbar\omega, \pi = -)$ is lowered into the $4\hbar\omega$ $(\pi = +)$ shell, which is filled, and becomes available for positive parity transitions into the remaining $5\hbar\omega$ hole states. In the neutron shells, the $\nu 1j_{15/2}$ $(7\hbar\omega \rightarrow 6\hbar\omega)$ and the $\nu 1i_{13/2}$ $(6\hbar\omega \rightarrow 5\hbar\omega)$ both act as intruder levels and give rise to positive parity neutron transitions.

SP Configurations	SP Energy	Electric	Magnetic
$\nu(1j_{15/2}, 3p_{1/2}^{-1})$	4.856 MeV	8^+	7^+
$\nu(2g_{9/2}, 1i_{13/2}^{-1})$	5.067 MeV	$2^+,4^+,6^+,8^+,10^+$	$3^+,5^+,7^+,9^+,11^+$
$\pi(1h_{9/2}, 1h_{11/2}^{-1})$	5.573* MeV	$2^+,4^+,6^+,8^+,10^+$	$1^+,3^+,5^+,7^+,9^+$

* effective SP energy for proton configuration should be lowered by ~400 keV due to Coulomb interaction

Table 5.10 Single particle configurations between which couple to positive parity states observed in the excitation energy region between 4.8 MeV and 5.3 MeV.

Three configurations with an effective SP energy between 4.8 MeV and 5.3 MeV are available for positive parity transitions and are shown in Table 5.10. Possible transition spins range from 1^+ to 11^+. Of these, we see evidence for states with multipolarity $J \geq 8$ in this energy region. Lower multipolarity natural parity transitions will mix strongly with higher lying configurations, raising the observed experimental energy. Lower multipolarity unnatural states are relatively weaker and generally peak at a lower momentum transfer than sampled at 155° in

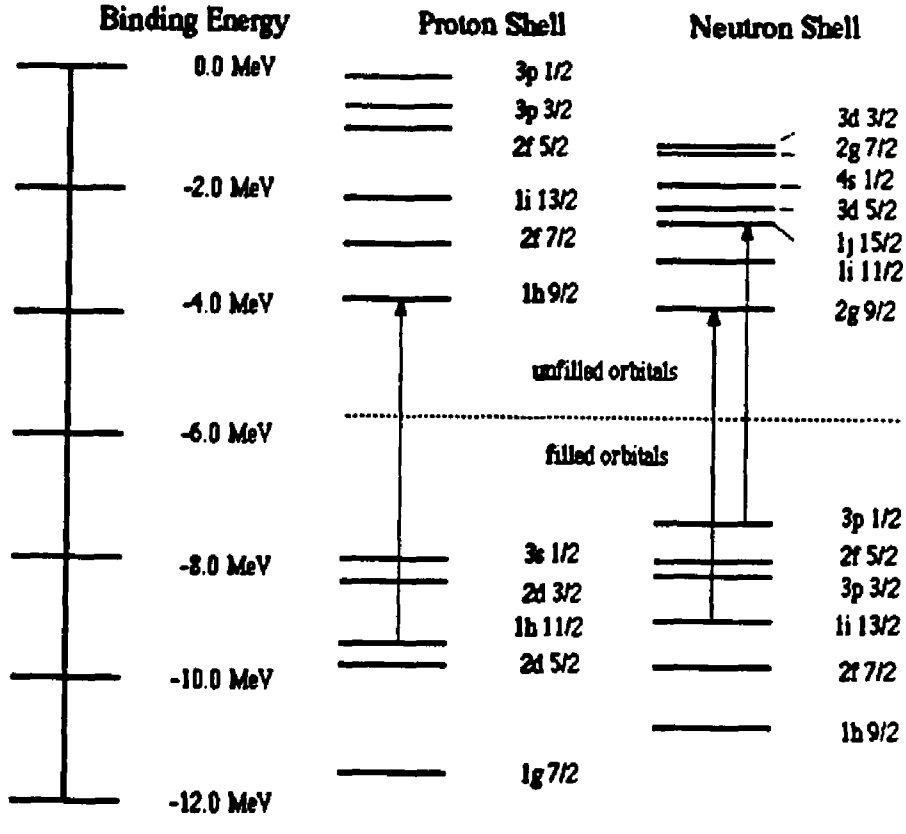

Fig 5.27 Mean field single particle configurations near Fermi level. Arrows indicate transitions coupling to positive parity that participate strongly in levels observed between 4.8 MeV and 5.3 MeV

this experiment. For example, the M1 states resulting from strong configuration mixing between the $\pi(1h_{9/2}, 1h_{11/2}^{-1})$ and $\nu(1i_{11/2}, 1i_{13/2}^{-1})$ spin–flip transitions, observed at 5.85 MeV and 6.24 MeV in polarized photon scattering[62] , are not seen in our backward angle scattering data.

This work (e,e')		Lichtenstadt (e,e')		Vold *et al.* $^{207}Pb(d,p)^{208}Pb$		Grabmayr *et al.* $^{209}Bi(d,^3He)^{208}Pb$		Wagner *et al.* (p,p')	
J^π	MeV	J^π	MeV	J^π	MeV	J^π	MeV	J^π	MeV
8^+	4.862 ± 0.003			$7^+,8^+$	4.865	$7^+,8^+$	4.860		4.863
10^+	4.895 ± 0.002	10^+	4.89			10^+	4.894	10	4.895
9^+	5.010 ± 0.003	9^+	5.01					9	5.010
10^+	5.068 ± 0.004	10^+	5.07			10^+	5.067	(9)	5.072
8^+	5.084 ± 0.006					3^-	5.084	3	5.087
9^+	5.260 ± 0.005	11^+	5.27						
11^+	5.291 ± 0.006	11^+	5.27						

Table 5.11 Energies and multipolarites observed from (e,e'), transfer reactions and proton scattering experiments for the high spin positive parity states between 4.8 MeV and 5.3 MeV.

In an electron scattering experiment at MIT–Bates, Lichtenstadt[6] assigned spins and parities of 9^+, 10^+ and 11^+ to states in the region near 5.0 MeV excitation energy. Proton scattering[60] and transfer reactions[58][61] have also reported states with $J \geq 8$ and positive parity transitions in this region. In Table 5.11 a comparison is made between J^π assignments from other experiments and those used or determined from this experiment.

Several levels listed form doublets (4.862 and 4.895 MeV, 5.068 and 5.084 MeV) and were not resolved with the 40 to 60 keV resolution in the (e, e') experiment by Lichtenstadt. Our data confirm the 10^+ assignments made by Lichtenstadt to the states at 4.89 MeV and 5.07 MeV, but in addition two levels for which we give $J^\pi = 8^+$ are seen at 4.862 MeV and 5.084 MeV. Lichtenstadt also reported an 11^+ state at 5.27 MeV. In this region, two high spin magnetic states are observed in this experiment, 9^+ (5.260 MeV) and 11^+ (5.291 MeV). Figure 5.28 shows a spectrum at 155° with the 8^+, 10^+ doublets clearly resolved.

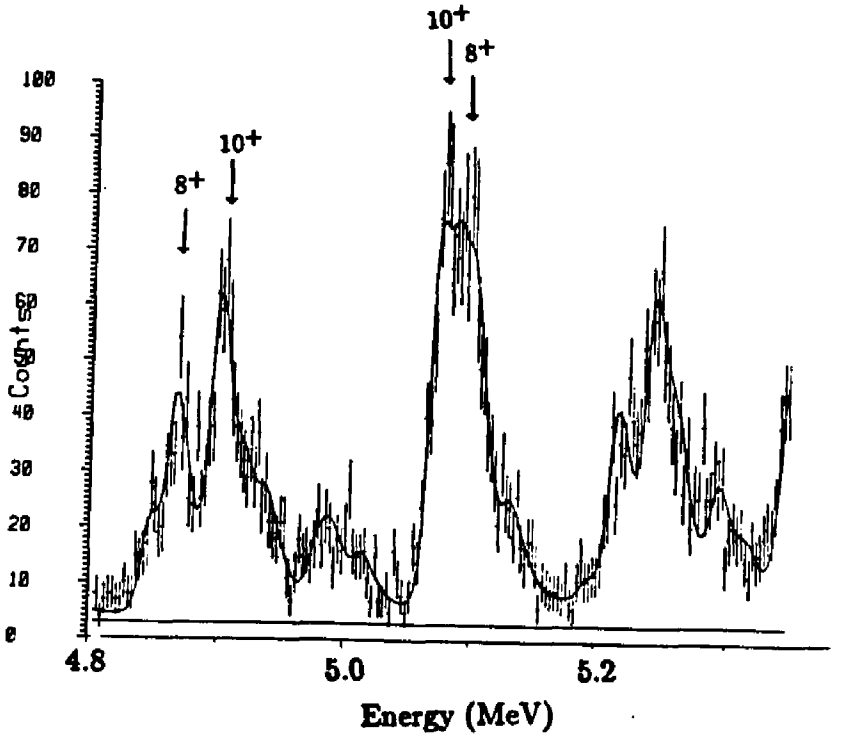

Fig 5.28 Spectrum (E_i = 150 MeV, θ =155° in the energy region 4.8 to 5.3 MeV.

8^+ and 10^+ States (4.8 MeV - 5.3 MeV)

Nuclear structure calculations using TDA from a correlated ground state[11] predict three 8^+ states and two 10^+ states near 5.0 MeV. E10 states have been reported in (e, e') and proton transfer reactions (Table 5.11) at 4.895 MeV and

5.068 MeV. A possible 7^+, 8^+ candidate was observed at 4.860 MeV in the proton transfer experiment by Grabmayr *et al*[61] with a small spectroscopic strength from the $\pi(1h_{9/2}, 1h^{-1}_{11/2})$ configuration.

	4.862 MeV	5.084 MeV
$\nu(1j_{15/2}, 3p^{-1}_{1/2})_{8+}$	-0.2023 ± 0.035	-0.3418 ± 0.149
$\pi(1h_{9/2}, 1h^{-1}_{11/2})_{8+}$	0.1976 ± 0.001	0.2163 ± 0.048
$\nu(2g_{9/2}, 1i^{-1}_{13/2})_{8+}$	0.1010 ± 0.211	
core pol ($\times$ 8^+_1)	-0.2287 ± 0.023	-0.4400 ± 0.048

Table 5.12 Woods–Saxon amplitudes obtained in DWBA fit to the 4.862 MeV and 5.084 MeV 8^+ levels. Core polarization amplitude represents a scaling of the 8^+ 4.610 MeV transition charge density to the data.

Assignments of 8^+ were made to the 4.862 MeV and 5.084 MeV levels based upon the strength of the longitudinal form factor, which would not be measured if the state were 7^+ or any other magnetic transition, and the shape of the form factor and excitation energy compared to nuclear structure calculations. The DWBA analysis on both states was performed using Woods–Saxon wave functions to model the densities with a core polarization amplitude represented by a scaling of the Fourier–Bessel coefficients from the 4.610 collective 8^+ state. The fits to the data are shown in Figure 5.29 and the resulting transition densities with theoretical calculations by Heisenberg[11] using TDA from a correlated ground state in Figure 5.30. Amplitudes to the Woods–Saxon configurations and core polarization are given in Table 5.12.

The 10^+ states at 4.895 MeV and 5.068 MeV were first identified by Wagner*et al.*[60] and also observed in a proton scattering experiment by Adams *et al.*[37]

and in electron scattering by Lichtenstadt[6] . In the work by Lichtenstadt on electron scattering data, the analysis of the 10^+ levels at 4.895 MeV and 5.068 MeV was performed in conjuction with the analysis of the 10^+ states he identified at 5.54 MeV and 5.92 MeV. In his analysis, using the four available Woods–Saxon configurations below 7.0 MeV that couple to 10^+, Lichtenstadt introduced an orthogonality constraint and allowed a parameter representing the overall effective charge to vary. The results are quite reasonable and show a strong mixing between the $\pi(1h_{9/2}, 1h^{-1}_{11/2})$ and $\nu(2g_{9/2}, 1i^{-1}_{13/2})$ configurations for the 4.895 MeV and 5.068 MeV states with little mixing from the higher configurations. For this reason, we used only the lower Woods–Saxon particle–hole configurations in our fit to these states and did not impose an orthogonality condition. The parameters representing the effective charge and quenching of the magnetic current were determined by Lichtenstadt to 0.92 and 0.65 respectively. These parameters were held constant in the present analysis and only the amplitudes of the Woods–Saxon configurations were allowed to vary. The amplitudes from the fit to the data and a comparison to Lichtenstadt's results are given in Table 5.13.

The amplitude of the proton configuration is well determined from our analysis since only the $\pi(1h_{9/2}, 1h^{-1}_{11/2})$ can contribute to the transition charge density. The strength of the proton transition is split nearly equally between the 4.895 MeV state and the 5.068 MeV state. To determine the neutron strength more precisely an analysis similar to Lichtenstadt's would have to be performed, considering all available configurations and constraining the four 10^+ states below 7.0 MeV to be orthogonal.

The transition charge and current densities for the 4.895 MeV and 5.068 MeV states are shown in Figure 5.31 with theoretical curves from Heisenberg's TDA calculation. The curves have the correct shape but over–predict the strength of the 4.895 MeV state and under–predict the strength of the 5.068 MeV state.

This work		
	4.895 MeV 10^+	**5.068 MeV 10^+**
$\nu(2g_{9/2}, 1i^{-1}_{13/2})_{10+}$	-0.975 ± 0.858	-0.912 ± 0.725
$\pi(1h_{9/2}, 1h^{-1}_{11/2})_{10+}$	-0.478 ± 0.023	0.552 ± 0.022
Lichtenstadt		
	4.89 MeV 10^+	**5.07 MeV 10^+**
$\nu(2g_{9/2}, 1i^{-1}_{13/2})_{10+}$	0.647	0.730
$\nu(1j_{15/2}, 2f^{-1}_{5/2})_{10+}$	−0.679	0.683
$\nu(1j_{15/2}, 1i^{-1}_{13/2})_{11+}$	0.304	−0.016
$\nu(1i_{11/2}, 1i^{-1}_{13/2})_{11+}$	−0.167	0.025

Table 5.13 Woods–Saxon amplitudes obtained in DWBA fit to the 4.895 MeV, and 5.068 MeV 10^+ levels and those reported by Lichtenstadt [6] .

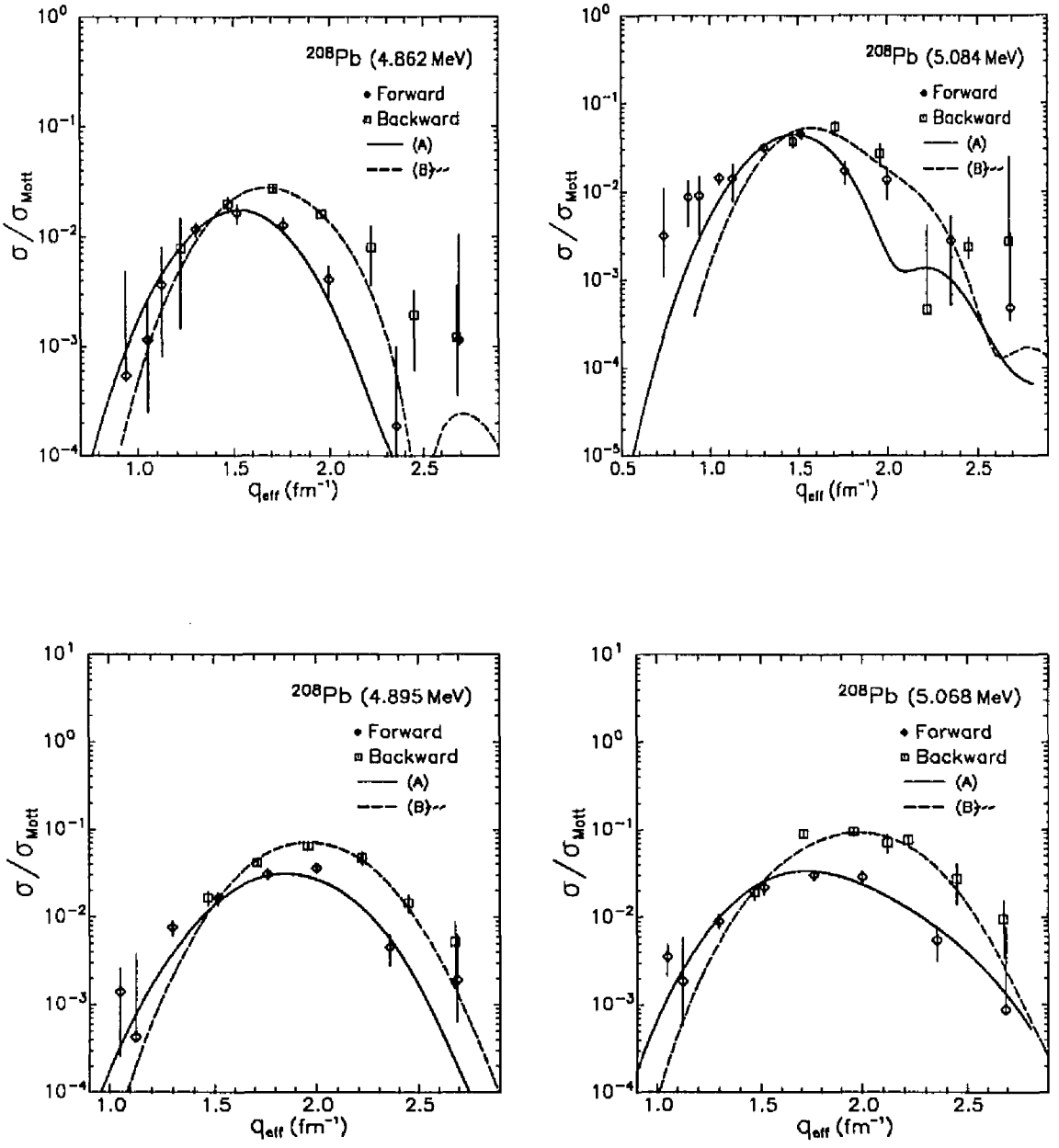

Fig.5.29 Form factors with the fitted curves for the 4.862 MeV (8^+), 5.084 MeV (8^+), 4.895 MeV (10^+), and 5.068 MeV (10^+) states.

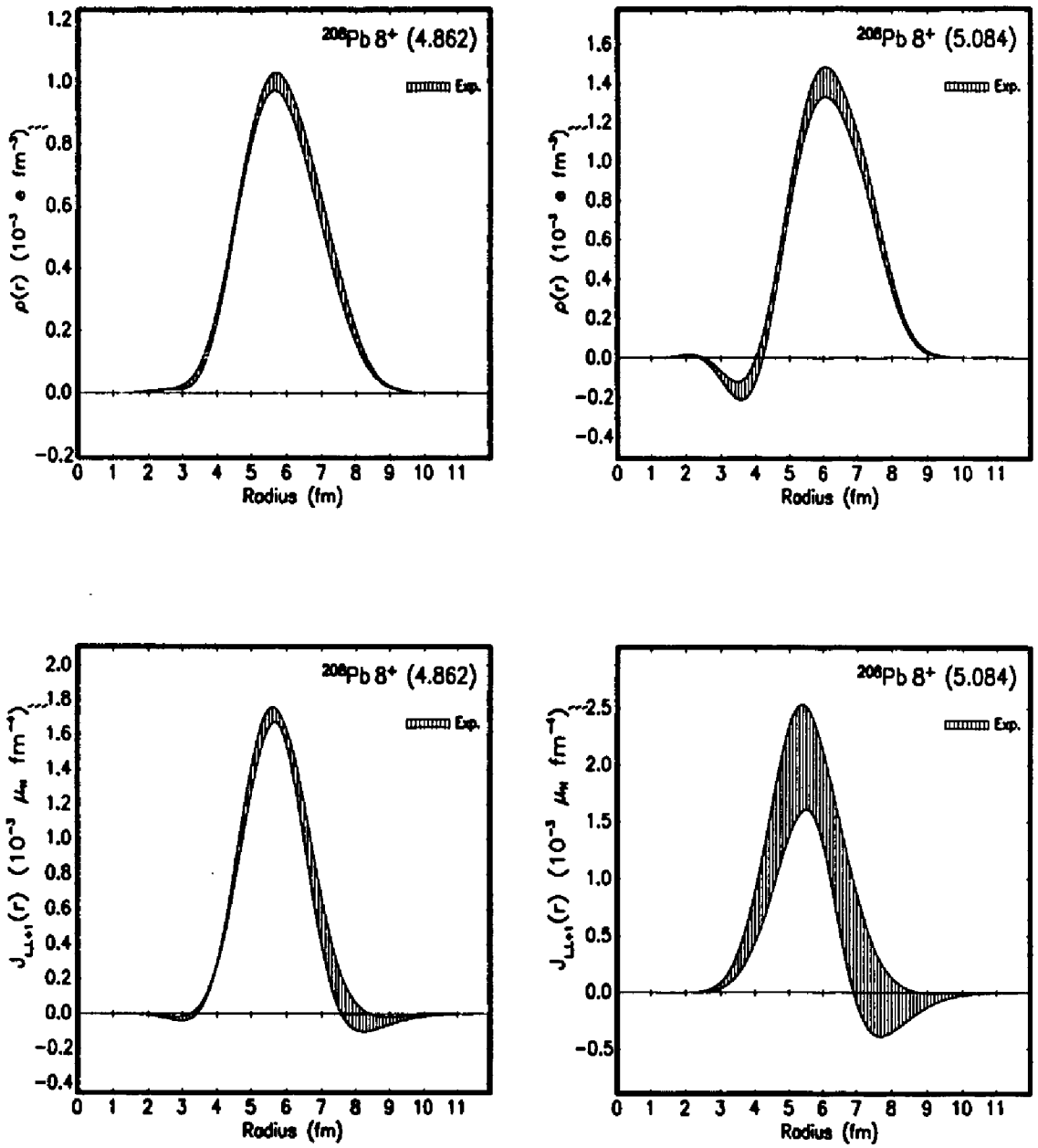

Fig.5.30 Transition densities from the 4.862 MeV and 5.084 MeV 8^+ states.

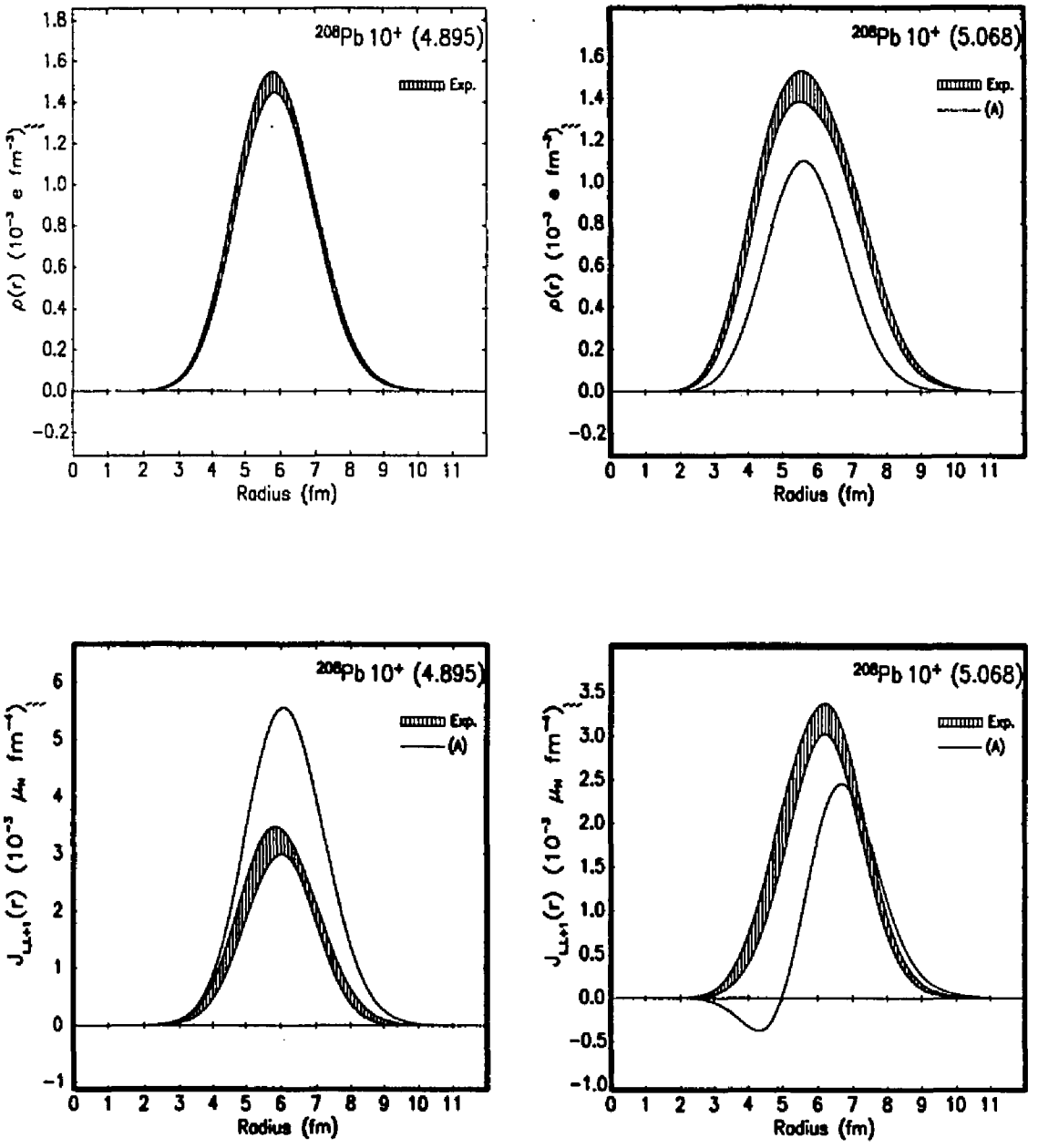

Fig.5.31 Transition densities from the 4.895 MeV (10^+) and 5.068 MeV (10^+) states.

9^+ and 11^+ States (4.8 MeV - 5.3 MeV)

The residual interaction that mixes 1p–1h configurations in magnetic transitions is weak, leading to the expectation that high multipolarity magnetic states will be dominated by a single particle–hole configuration. In the case of $J^\pi = 11^+$, this is a moot point since only the $\nu(2g_{9/2}, 1i^{-1}_{13/2})$ configuration can couple to this spin in the energy region near 5.0 MeV. However, there are five configurations with a SP energy between 5.0 MeV and 6.0 MeV that can couple to 9^+, and for configurations whose SP energy are quite close the mixing may be significant.

TDA calculations from a correlated ground state by Heisenberg[11] predict very little mixing between the the $\pi(1h_{9/2}, 1h^{-1}_{11/2})$ and $\nu(2g_{9/2}, 1i^{-1}_{13/2})$ transitions which dominate the two lowest 9^+ states. Lichtenstadt, in his analysis[6] of the first 9^+ state, which he identified at 5.01 MeV, reports an almost pure $\nu(2g_{9/2}, 1i^{-1}_{13/2})$ transition quenched by 50.0% with a small amplitude of the $\nu(1j_{15/2}, 2f^{-1}_{5/2})$ (SP energy of 5.436 MeV) also fitted. Unfortunately, the analysis did not include the proton spin–flip configuration which has an effective SP energy of $\sim$ 5.1 MeV, and the degree of mixing between the two most relevant configurations was not determined.

Besides the 5.010 MeV 9^+ level, our data also indicate the presence of two high multipolarity transverse states at 5.260 MeV and 5.291 MeV. We make assignments of 9^+ and 11^+ to these levels respectively. The assignments were made based upon the proximity of the excitation energies to the SP energies of the 1p–1h configurations given in Table 5.10, the absence of any measurable longitudinal form factor, and q-dependence of the transverse form factor. Although 9^+ and 11^+ transitions both peak above 1.5 fm^{-1}, the shapes predicted by calculations are entirely different. The configuration producing the 11^+ state which leads to a form factor shape characterized by a broad peak in momentum space. The second 9^+ state, conversely, is believed to be dominated by the $\pi(1h_{9/2}, 1h^{-1}_{11/2})$

This work			
	5.010 MeV 9^+	**5.260 MeV 9^+**	**5.291 MeV 11^+**
$\nu(2g_{9/2}, 1i^{-1}_{13/2})_{9+,11+}$	0.735 ± 0.028		0.617 ± 0.0592
$\pi(1h_{9/2}, 1h^{-1}_{11/2})_{9+}$	-0.027 ± 0.027	0.726 ± 0.074	
$\nu(1j_{15/2}, 2f^{-1}_{5/2})_{9+}$		-0.039 ± 0.122	
Lichtenstadt			
	5.01 MeV 9^+		**5.27 MeV 11^+**
$\nu(2g_{9/2}, 1i^{-1}_{13/2})_{9+,11+}$	0.96		0.83
$\nu(1j_{15/2}, 2f^{-1}_{5/2})_{9+}$	-0.27		
$\nu(1j_{15/2}, 1i^{-1}_{13/2})_{11+}$			0.55
f_m	$50.0 \pm 7.0\%$		$35.0 \pm 5.0\%$

Table 5.14 Woods–Saxon amplitudes from the DWBA fits to the 5.010 MeV, 5.260 MeV and 5.291 MeV 9^+ and 11^+ levels from our analysis and those reported by Lichtenstadt [6] . The magnetization quenching used in the analysis by Lichtenstadt is given by $g_{eff} = f_m^2 \times g_{free}$.

transition which has a minimum at 2.0 fm^{-1}. The levels at 5.291 MeV and 5.260 follow the form factor shapes predicted by this simple shell model picture.

The fits to the data for the 5.010 MeV, 5.260 MeV and 5.291 MeV states are shown in Figure 5.32. The analysis was performed adjusting only the amplitudes of the Woods–Saxon configurations. The resulting amplitudes and a comparison with those obtained by Lichtenstadt are given in Table 5.14.

In both 9^+ states and the 11^+ dominant single particle–hole transitions give excellent fits to the data. All three states see a reduction from the calculated 1p–1h strength, to 50.0% in the 5.010 MeV 9^+ and 5.291 MeV 11^+ states, and to 38.1% of the calculated strength in the 5.260 MeV 9^+ state. Comparisons of

the extracted transition magnetization densities to TDA calculations are shown in Figure 5.33. The theoretical curves give the correct shape for the densities and very good agreement for the strength for the 9^+ states. The signature of the 1p–1h character of the 9^+ states is seen in the node of the 5.010 transition density which is typical of transitions like $\nu(2g_{9/2}, 1i^{-1}_{13/2})$, where the radial quantum number changes from $n = 1 \rightarrow n = 2$. This same configuration is responsible for the 5.291 MeV 11^+ state and a similar node is seen. The 5.260 MeV transition density displays the single peak shape associated with transitions where $n = 1 \rightarrow n = 1$.

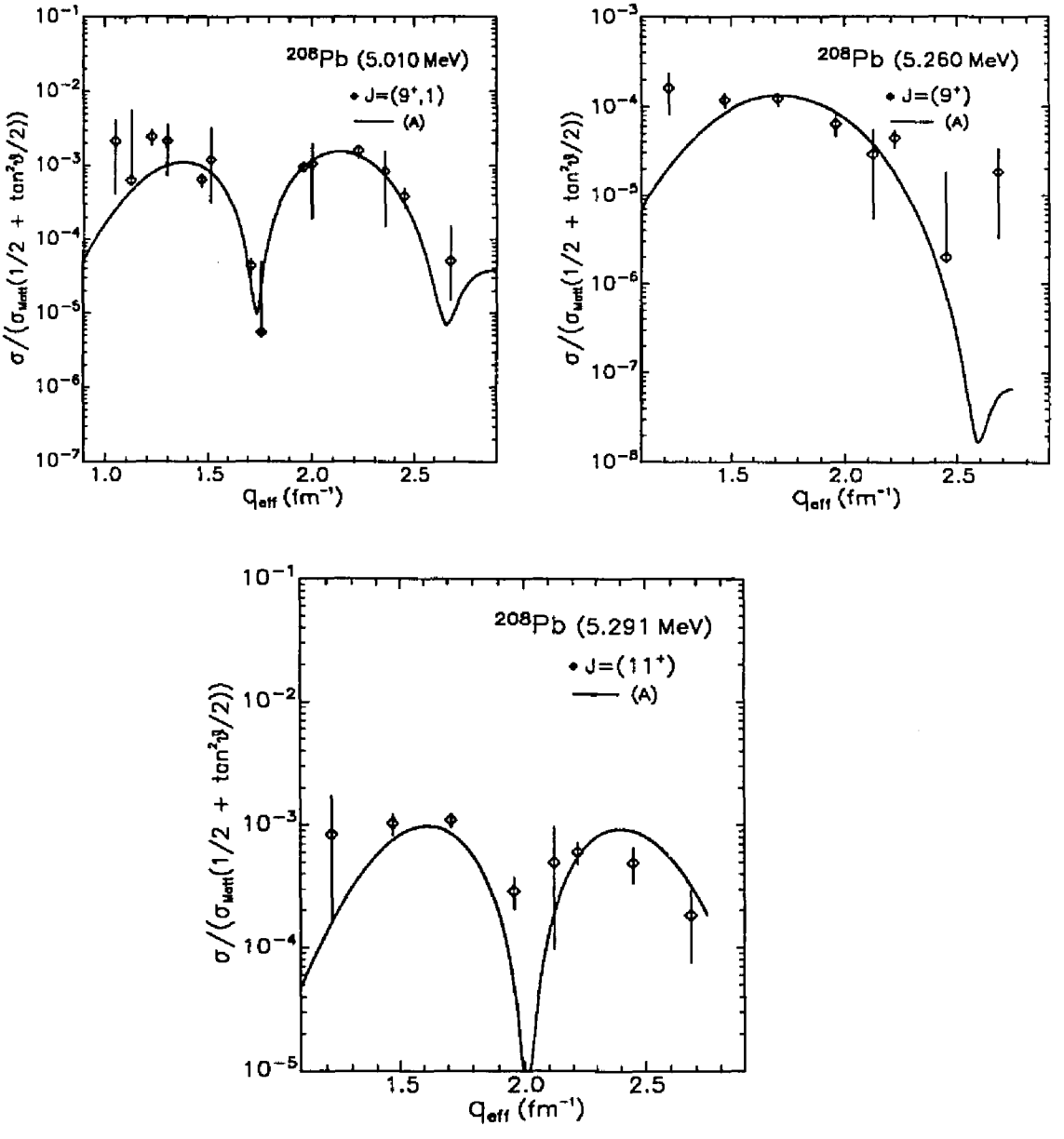

Fig.5.32 Form factors with the fitted curves for the 5.010 MeV (9^+), 5.260 MeV (9^+) and 5.291 MeV (11^+) states.

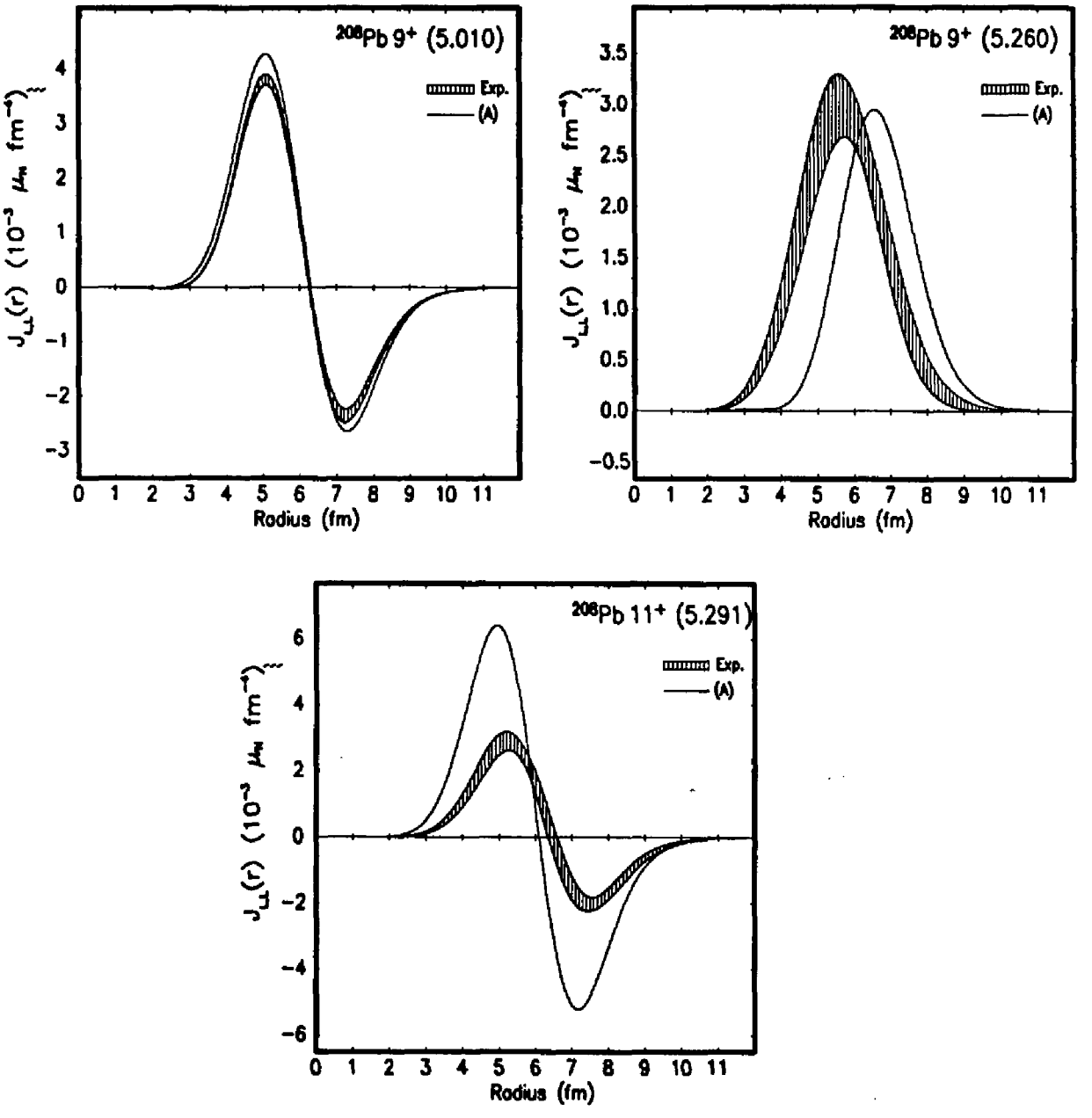

Fig.5.33 Transition magnetization densities from the 5.010 MeV (9^+), 5.260 MeV (9^+) and 5.291 MeV (11^+) states.

Summary

High spin positive parity excitations near 5.0 MeV excitation energy have been investigated in this section. The dominant configurations with single particle–hole energies between 4.8 MeV and 5.6 MeV that couple to positive parity are the $\pi(1h_{9/2}, 1h^{-1}_{11/2})$, $\nu(2g_{9/2}, 1i^{-1}_{13/2})$, $\nu(1j_{15/2}, 2f^{-1}_{5/2})$ and $\nu(1j_{15/2}, 1i^{-1}_{13/2})$ configurations. In Figure 5.34, energies of the single particle–hole configurations are compared to the observed experimental energies and TDA predictions.

In addition to the known 4.895 MeV $(10^+), 5.010 MeV(9^+)$ and 5.068 MeV (10^+) excitations, we assign spins and parities to the 4.862 MeV (8^+), 5.084 MeV (8^+), 5.260 MeV (9^+) and 5.291 MeV (11^+) levels. The reported 11^+ excitation by Lichtenstadt at 5.27 MeV was found to be a doublet containing high spin magnetic transitions (9^+, 11^+).

The electric excitations display strong transverse components and significant longitudinal strengths. Comparisons of TDA predictions to the transition charge and current densities show the correct shapes but generally over–predict the strengths by 50% to 100%. The exception is the 5.068 MeV 10^+ level which was under–predicted by 50% in both the charge and current densities.

DWBA analyses of the magnetic transitions using Woods–Saxon wave functions shown these states to be almost pure 1p–1h transitions. The 9^+ excitations were quenched from the single particle hole strength by 50%, and the 11^+ level was quenched by 40%. TDA predictions show the right amount of quenching for the 9^+ excitations but over predict the 11^+ state by a factor of three.

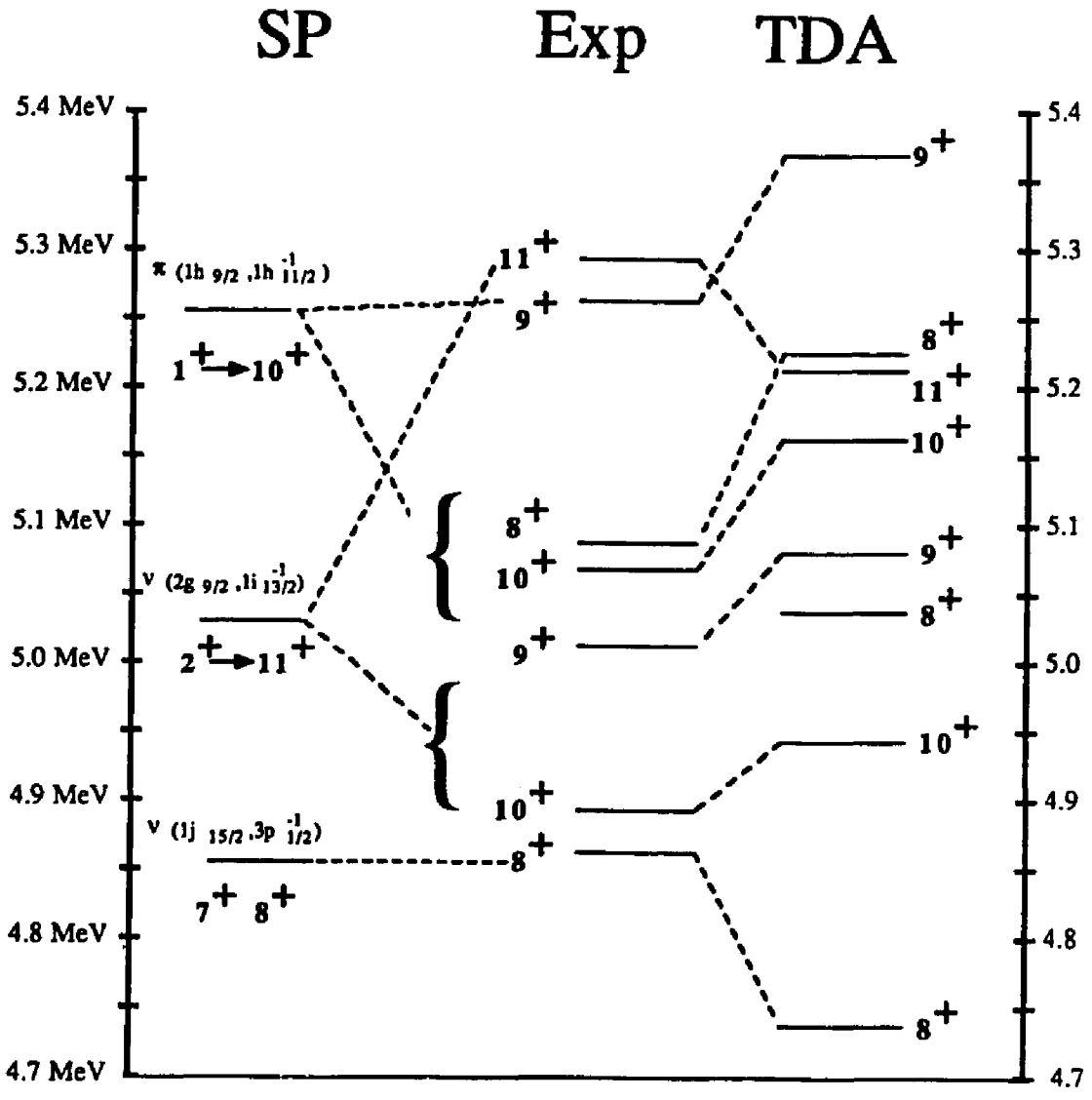

Fig.5.34 Comparison of the experimental energies, relevant single particle–hole energies and TDA predictions for positive parity excitations between 4.8 MeV and 5.3 MeV.

5.5 Low Multipolarity Electric Excitations (4.8 MeV – 6.0 MeV)

The forward scattering angle excitation energy spectrum of ^{208}Pb between 4.8 MeV and 6.0 MeV is highly populated by strong electric states with multipolarity $J \leq 6$. In this section, those levels with a strong longitudinal component to the form factor are presented. All of these states have been assigned spins and parity by previous experiments and we assumed those listed in Nuclear Data Sheets (1986). As seen in Figure 5.35, these levels dominate the low-q forward scattering angle spectra. Only a cursory discussion is offered here.

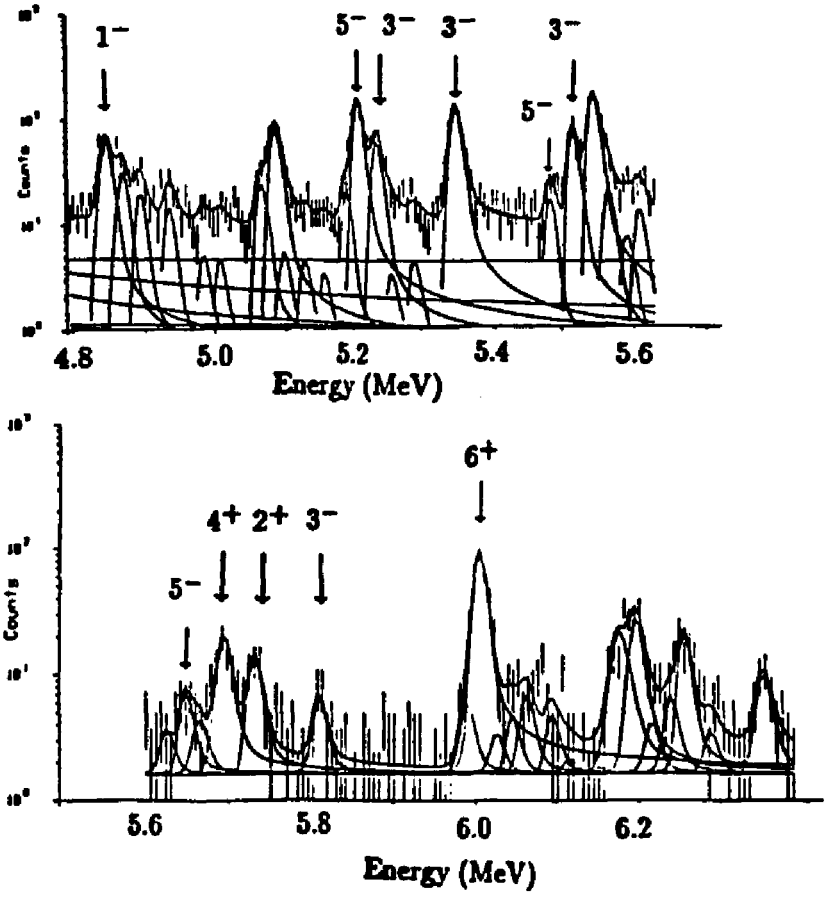

Fig.5.35 Energy spectrum (E_i = 280 MeV, θ =40°) in the region between 4.8 and 5.6 MeV and (E_i = 300 MeV, θ =40°) in the region between 5.6 and 6.3 MeV.

Summary

The experimental transition densities presented in this section are compared to predictions from correlated ground state TDA calculations by Heisenberg[11] . Predicted energies from this calculation and the experimental energies observed from this work are presented in Figure 5.36.

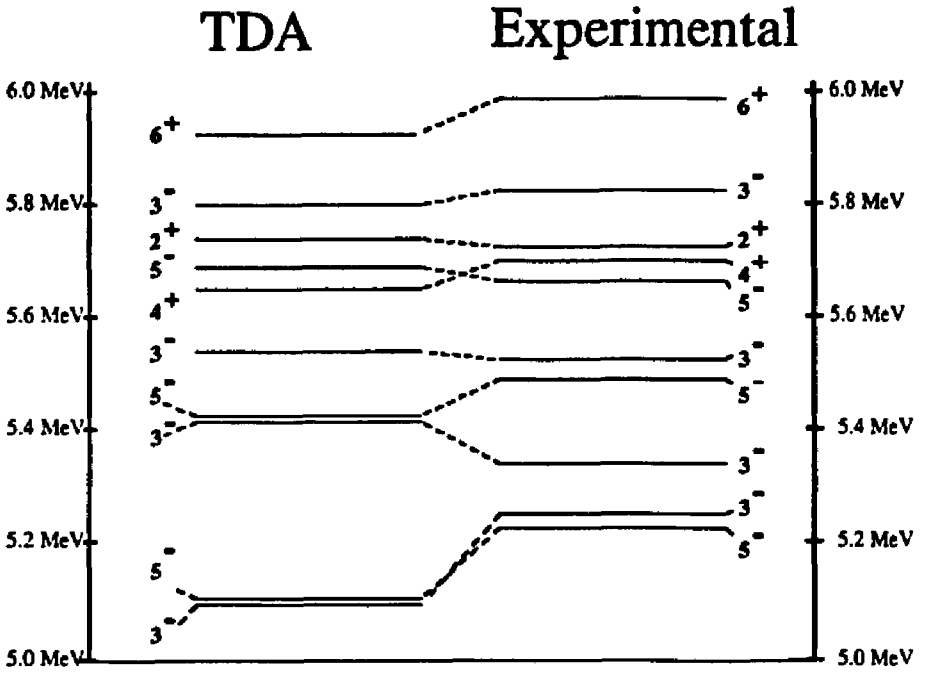

Fig 5.36 Comparison of experimental energies to predicted energies from a correlated ground state TDA calculation for low multipolarity natural parity transitions between 5.0 and 6.0 MeV[11]

The DWBA analysis was performed using a Fourier-Bessel expansion to model both the transition charge and current densities, except for the 5.997 MeV 6^+ excitation where a gaussian times a series of polynomials was fit to both longitudinal and transverse componenets, as outlined in Chapter 3. The resulting

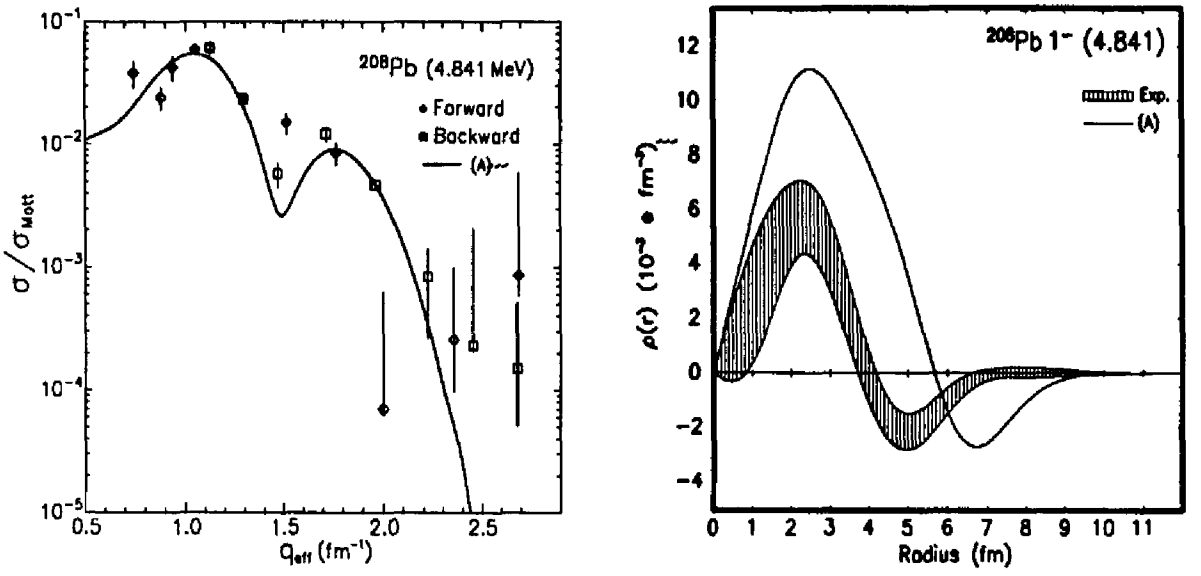

Fig.5.37 Transition charge density (right) from the 4.481 MeV electric dipole state. Fit (left) was obtained assuming a purely longitudinal form factor. Theoretical curve from TDA calculation by Heisenberg.

Fourier–Bessel coefficients with uncertainties and expansion radii are given in Tables 5.15, 5.16, 5.17, 5.18 and 5.19.

Configuration mixing is expected to play a major role in the structure of natural parity transitions where several single particle–hole transitions have energies which are close to the experimental excitation energies. All of the transition densities shown display interior structure and generally little collectivity. The exceptions are the 5.685 MeV 4^+ and 5.997 MeV 6^+ excitations. In these cases, the transition charge densities display large surface peaked lobes which are signatures of collectivity in the transition.

A precise knowledge of the residual interaction is necessary in order to perform reliable nuclear structure calculations for the natural parity states in this energy region. While the TDA calculations predict the excitation energies fairly well,

the calculated transition densities do not agree with the experimental densities. The TDA calculation does a better job predicting the shapes of the transition current densities than the transition charge densities. The currents are more sensitive to the valence transitions than the transition charge densities, so that better qualitative agreement is seen. Clearly, the residual interaction used in the calculation is not correct. At the time of this writing, work is in progress on improving the form of the interaction.

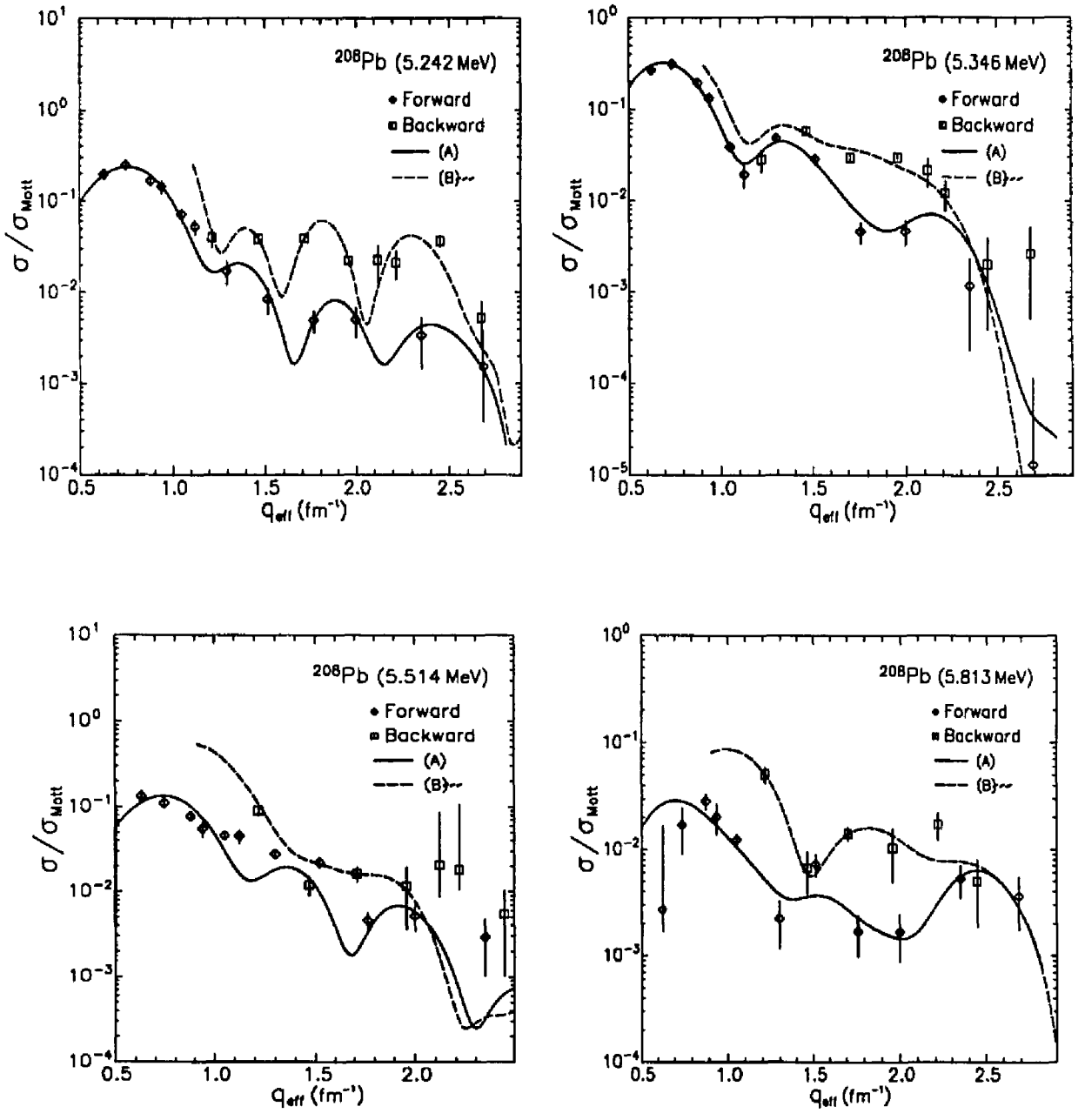

Fig.5.38 Form factors with the fitted curves for the 5.242 MeV, 5.346 MeV, 5.514 MeV and 5.813 MeV 3^- states.

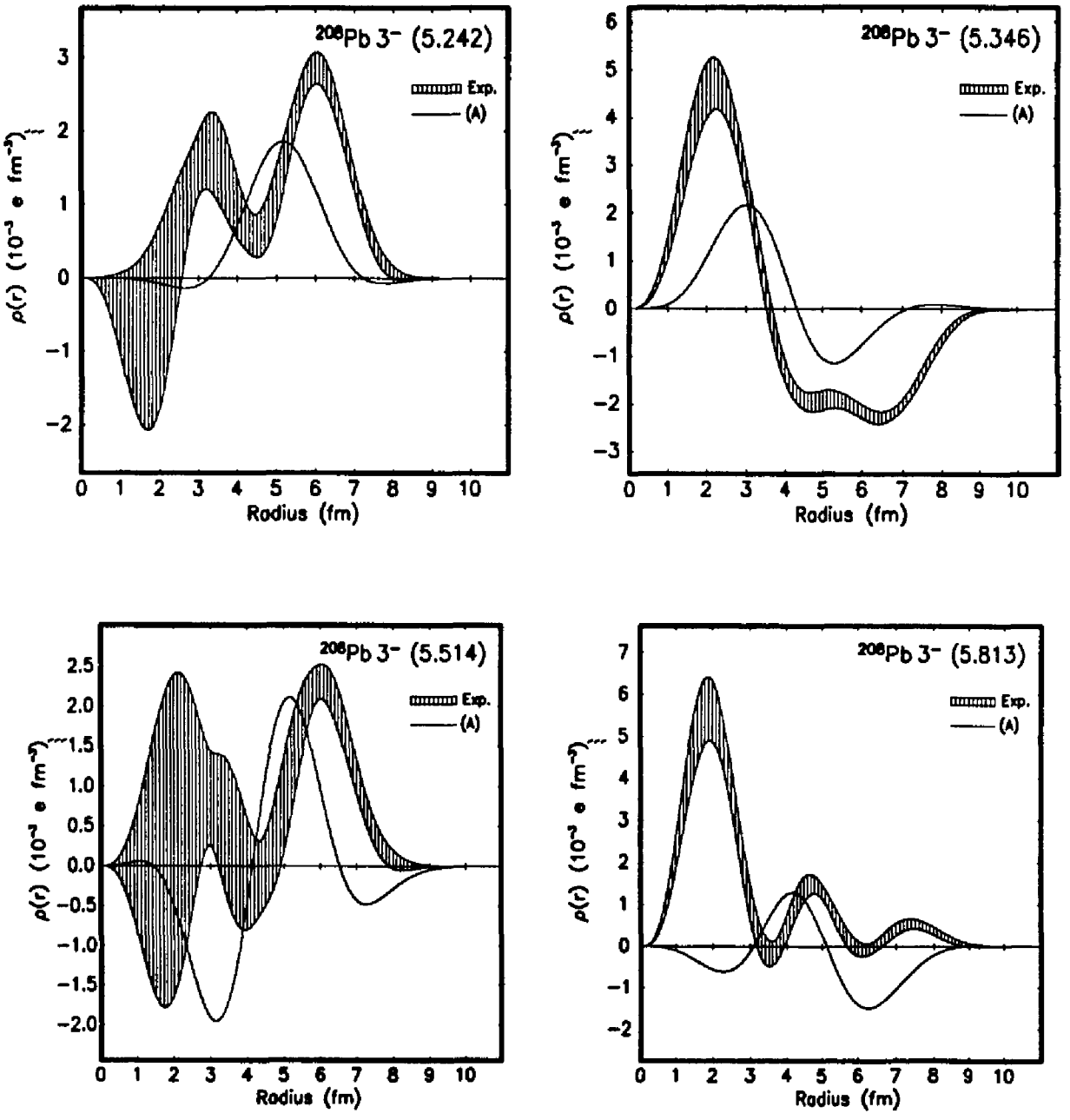

Fig.5.39 Transition charge densities for the 5.242 MeV, 5.346 MeV, 5.514 MeV and 5.813 MeV 3^- states with theoretical densities from correlated ground state TDA calculation.

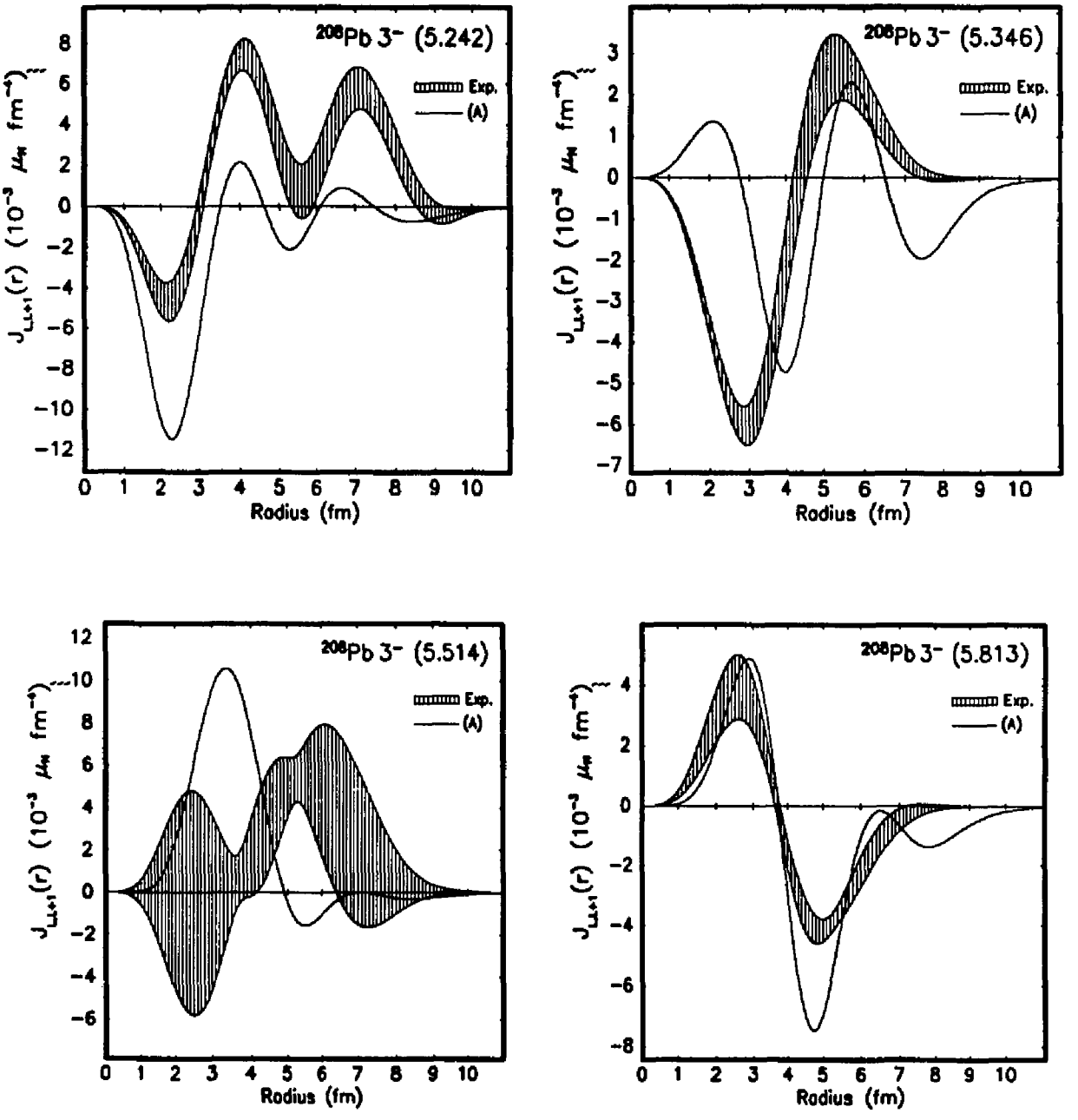

Fig.5.40 Transition current densities for the 5.242 MeV, 5.346 MeV, 5.514 MeV and 5.813 MeV 3^- states with theoretical densities from correlated ground state TDA calculation.

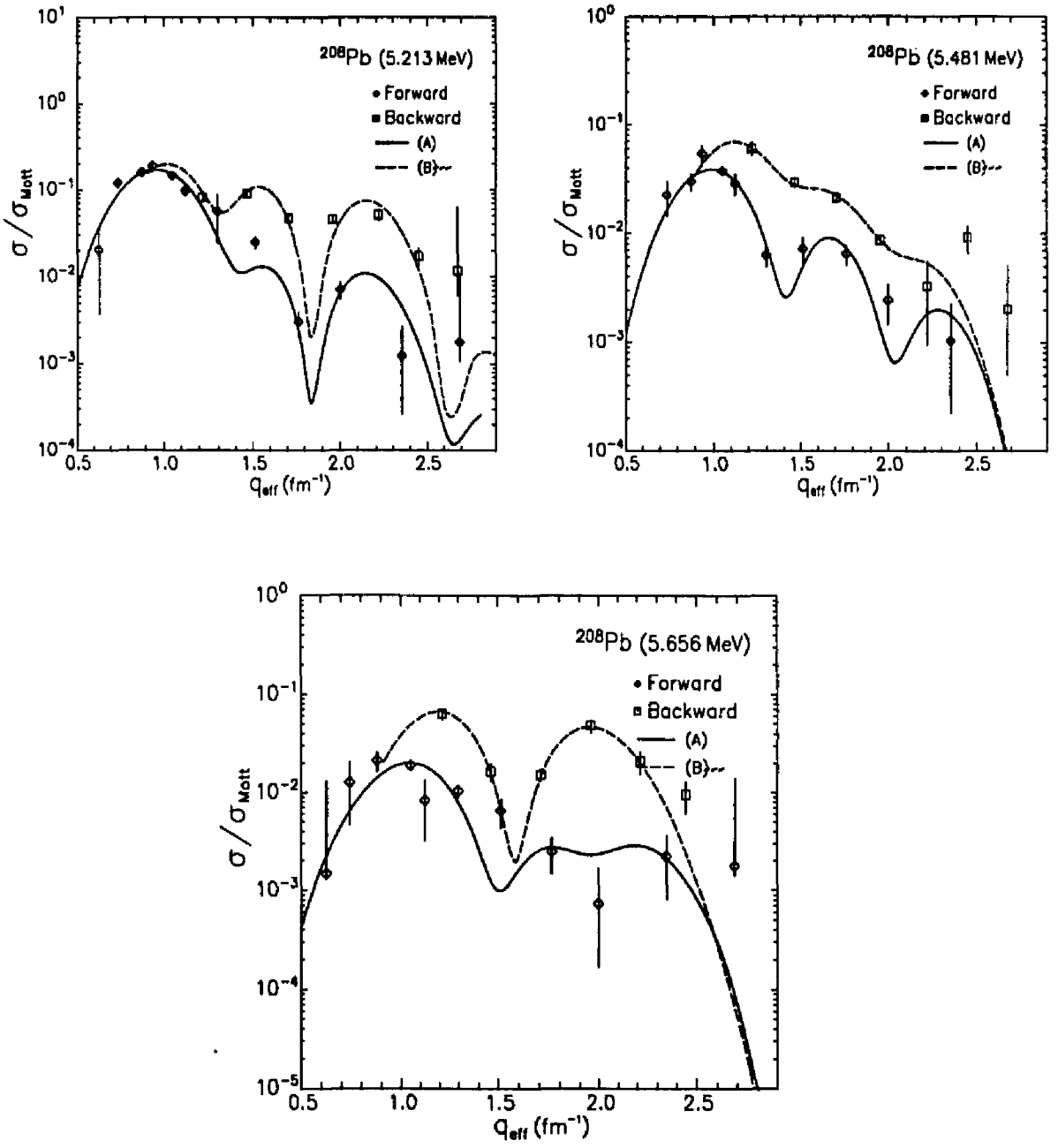

Fig.5.41 Form factors with the fitted curves for the 5.213 MeV, 5.656 MeV and 5.481 MeV 5^- states.

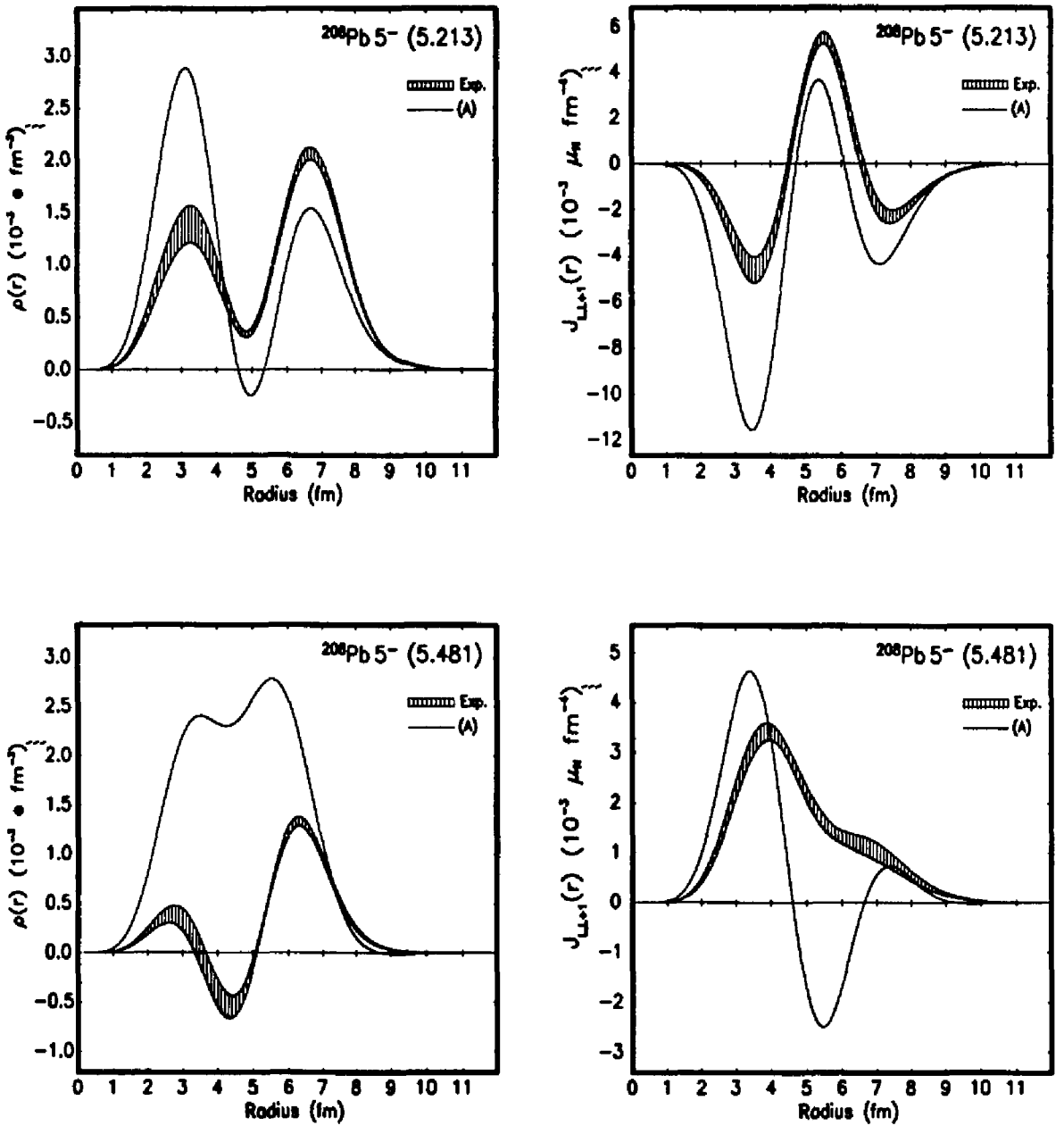

Fig.5.42 Transition charge (left) and current (right) densities for the 5.213 MeV and 5.481 MeV 5^- states with theoretical densities from correlated ground state TDA calculation.

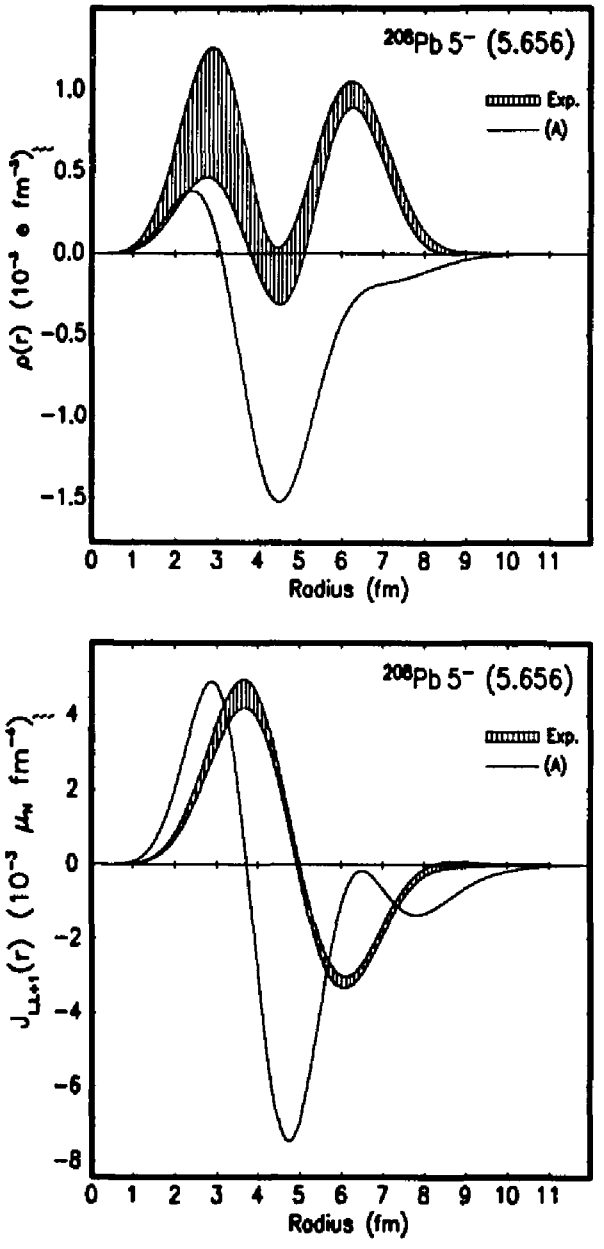

Fig.5.43 Transition charge (left) and current (right) densities 5.656 MeV 5^- state with theoretical densities from correlated ground state TDA calculation.

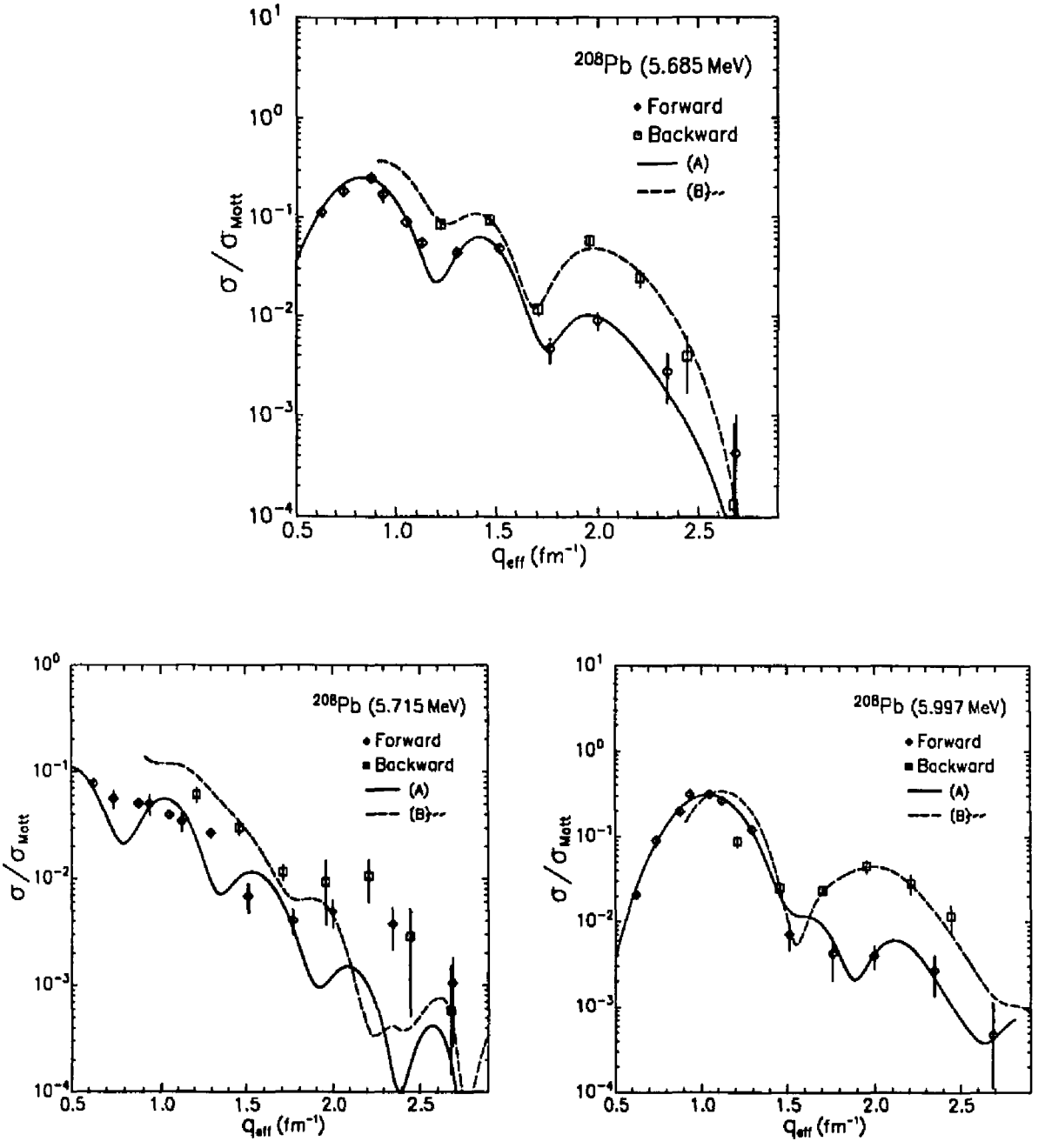

Fig.5.44 Form factors with the fitted curves for the 5.685 MeV (4^+), 5.715 MeV (2^+) and 5.997 MeV 6^+ states.

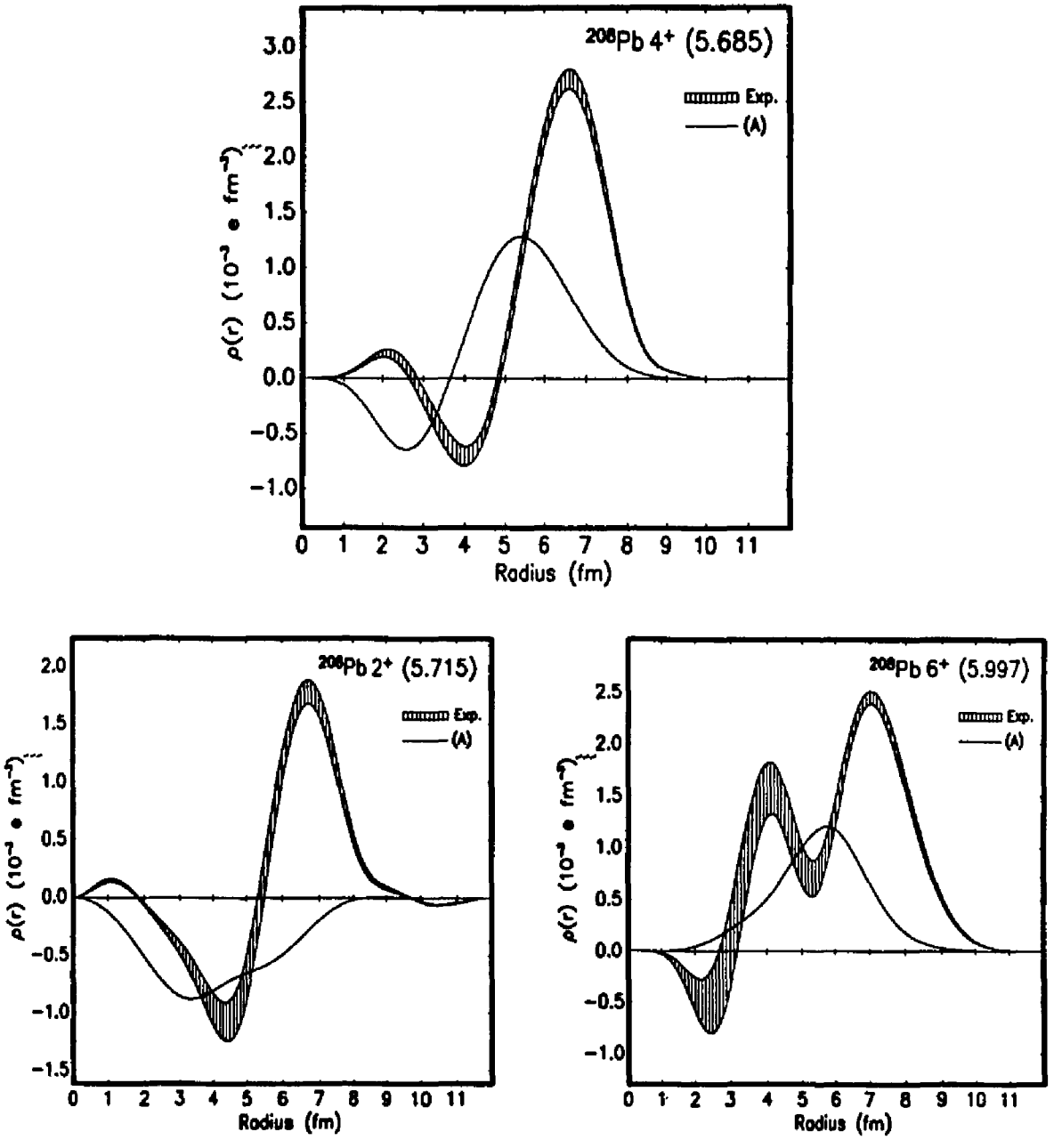

Fig.5.45 Transition charge densities for the 5.685 MeV (4^+), 5.715 MeV (2^+) and 5.997 MeV 6^+ states with theoretical densities from correlated ground state TDA calculation.

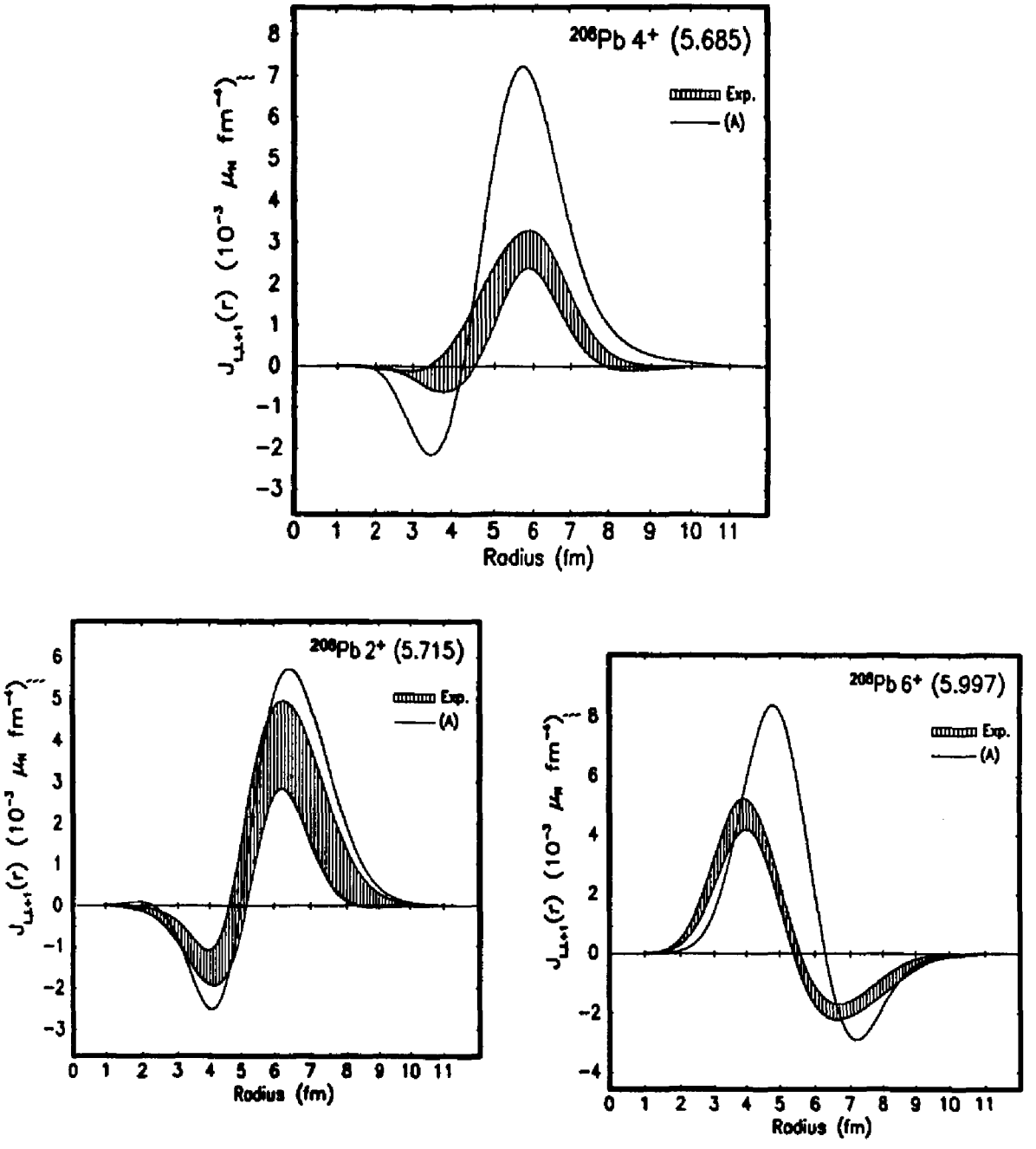

Fig.5.46 Transition current densities for the 5.685 MeV (4^+), 5.715 MeV (2^+) and 5.997 MeV 6^+ states with theoretical densities from correlated ground state TDA calculation.

Transition Charge and Current Density Parameters

Fourier–Bessel Expansion $R_0 = 12.0\,fm$

	4.841 MeV 1^-		5.715 MeV 2^+	
N	charge	charge	current	current
1	2.420 ± 1.137	0.000 ± 0.000	2.375 ± 0.142	2.394 ± 0.935
2	2.429 ± 1.310	0.000 ± 0.000	2.595 ± 0.276	6.451 ± 1.836
3	3.457 ± 0.894	0.000 ± 0.000	-3.025 ± 0.375	0.312 ± 2.546
4	7.919 ± 0.547	0.000 ± 0.000	-3.024 ± 0.221	-8.822 ± 2.763
5	2.458 ± 0.755	0.000 ± 0.000	1.838 ± 0.271	-3.616 ± 3.311
6	3.942 ± 0.855	0.000 ± 0.000	1.813 ± 0.152	5.610 ± 2.354
7	0.611 ± 0.582	0.000 ± 0.000	-0.776 ± 0.138	3.599 ± 2.148
8	2.773 ± 0.773	0.000 ± 0.000	-0.761 ± 0.064	-2.044 ± 1.416
9	2.518 ± 1.476	0.000 ± 0.000	0.485 ± 0.068	-1.815 ± 0.800
10	3.565 ± 1.794	0.000 ± 0.000	0.126 ± 0.012	0.514 ± 0.556
11	0.153 ± 1.361	0.000 ± 0.000	-0.058 ± 0.011	0.574 ± 0.202
12	0.577 ± 1.041	0.000 ± 0.000	0.073 ± 0.008	-0.142 ± 0.135
13	0.296 ± 0.768	0.000 ± 0.000	-0.018 ± 0.001	-0.131 ± 0.050
14	0.078 ± 0.560	0.000 ± 0.000	-0.015 ± 0.001	0.052 ± 0.022
15	0.133 ± 0.285	0.000 ± 0.000	0.019 ± 0.001	0.023 ± 0.014

Table 5.15 Fourier–Bessel density expansion coefficients for 4.841 MeV 1^- and 5.715 MeV 2^+ states. The 1^- state was assumed to be purely longitudinal. The coefficients A_n have all been multiplied by a factor of 1000.

Transition Charge and Current Density Parameters

Fourier–Bessel Expansion $R_0 = 11.0\,fm$

	5.242 MeV 3^-		5.346 MeV 3^-	
N	charge	current	charge	current
1	3.861 ± 0.224	7.301 ± 2.919	-5.260 ± 0.218	-1.138 ± 0.515
2	7.136 ± 0.305	17.173 ± 4.279	-7.471 ± 0.198	-3.751 ± 1.864
3	1.779 ± 0.300	1.341 ± 1.459	0.666 ± 0.308	-0.997 ± 2.418
4	-2.543 ± 0.387	2.739 ± 1.166	4.183 ± 0.327	9.143 ± 1.391
5	0.962 ± 0.511	15.650 ± 1.648	2.255 ± 0.424	14.342 ± 0.771
6	2.231 ± 0.633	-13.949 ± 2.392	3.231 ± 0.448	8.894 ± 0.762
7	-1.101 ± 1.068	-21.311 ± 2.630	2.760 ± 0.527	2.276 ± 0.304
8	-1.820 ± 0.905	-3.537 ± 0.804	0.476 ± 0.397	0.141 ± 0.034
9	-0.261 ± 0.329	0.119 ± 0.134	-0.068 ± 0.115	-0.001 ± 0.002
10	0.116 ± 0.215	-0.016 ± 0.092	0.035 ± 0.048	0.000 ± 0.000
11	-0.052 ± 0.146	-0.002 ± 0.059	-0.012 ± 0.024	0.000 ± 0.000
12	0.009 ± 0.097	0.005 ± 0.037	0.002 ± 0.020	-0.000 ± 0.000
13	0.005 ± 0.061	-0.004 ± 0.022	-0.001 ± 0.007	0.000 ± 0.000
14	-0.007 ± 0.035	0.002 ± 0.012	0.000 ± 0.003	0.000 ± 0.000
15	0.004 ± 0.022	0.003 ± 0.017	-0.000 ± 0.003	0.000 ± 0.000

Table 5.16 Fourier–Bessel density expansion coefficients for the 5.242 MeV 3^- and 5.346 MeV 3^- states. The coefficients A_n have all been multiplied by a factor of 1000.

Transition Charge and Current Density Parameters

Fourier–Bessel Expansion $R_0 = 11.0\,fm$

	5.514 MeV 3^-		5.813 MeV 3^-	
N	charge	current	charge	current
1	3.021 ± 0.330	4.446 ± 5.222	1.576 ± 0.223	-1.699 ± 0.492
2	5.227 ± 0.498	13.592 ± 9.885	2.296 ± 0.192	-6.761 ± 1.168
3	0.441 ± 0.582	9.487 ± 3.402	1.380 ± 0.238	-7.544 ± 0.857
4	-2.799 ± 0.434	-4.619 ± 7.243	1.888 ± 0.294	1.539 ± 1.281
5	0.794 ± 0.820	-7.220 ± 7.671	1.368 ± 0.326	10.220 ± 1.482
6	2.428 ± 1.058	-0.810 ± 13.512	1.013 ± 0.578	9.354 ± 2.731
7	-0.082 ± 1.787	1.660 ± 10.247	3.132 ± 0.530	3.912 ± 1.715
8	-0.972 ± 1.226	0.476 ± 3.350	3.272 ± 0.630	0.728 ± 0.461
9	-0.131 ± 0.308	-0.078 ± 0.583	1.075 ± 0.462	0.035 ± 0.039
10	0.068 ± 0.161	0.034 ± 0.312	0.029 ± 0.072	-0.000 ± 0.001
11	-0.033 ± 0.091	-0.008 ± 0.190	0.002 ± 0.033	-0.000 ± 0.000
12	0.004 ± 0.060	0.001 ± 0.121	-0.001 ± 0.018	0.000 ± 0.000
13	0.003 ± 0.034	0.000 ± 0.062	0.000 ± 0.010	-0.000 ± 0.000
14	-0.003 ± 0.018	-0.001 ± 0.035	-0.000 ± 0.007	0.000 ± 0.000
15	0.002 ± 0.008	0.000 ± 0.078	0.001 ± 0.005	0.000 ± 0.000

Table 5.17 Fourier–Bessel density expansion coefficients for the 5.514 MeV 3^- and 5.813 MeV 3^- states. The coefficients A_n have all been multiplied by a factor of 1000.

Transition Charge and Current Density Parameters

Fourier–Bessel Expansion $R_0 = 12.0\,fm$

	5.213 MeV 5^-		5.481 MeV 5^-		5.656 MeV 5^-	
N	charge	current	charge	current	charge	current
1	-2.999 ± 0.087	2.453 ± 0.364	-1.267 ± 0.052	1.542 ± 0.215	0.769 ± 0.069	-1.374 ± 0.189
2	-6.162 ± 0.178	2.250 ± 1.062	-2.948 ± 0.101	5.080 ± 0.555	2.059 ± 0.105	-5.696 ± 0.423
3	-3.040 ± 0.096	-9.707 ± 0.820	-1.621 ± 0.056	6.597 ± 0.450	1.619 ± 0.174	-6.282 ± 0.429
4	1.239 ± 0.117	-11.941 ± 0.900	1.372 ± 0.143	6.304 ± 0.575	-0.347 ± 0.269	4.142 ± 0.491
5	-0.006 ± 0.161	9.143 ± 1.317	1.587 ± 0.216	6.727 ± 0.321	-0.692 ± 0.321	15.034 ± 0.828
6	-2.194 ± 0.181	22.765 ± 1.774	-0.389 ± 0.132	6.071 ± 0.636	0.705 ± 0.476	12.886 ± 1.275
7	-1.314 ± 0.124	11.335 ± 1.312	-1.173 ± 0.056	3.322 ± 0.543	1.226 ± 0.412	4.294 ± 0.841
8	-0.012 ± 0.032	-2.896 ± 0.435	-0.463 ± 0.034	0.739 ± 0.184	0.527 ± 0.189	0.334 ± 0.147
9	0.097 ± 0.013	-4.166 ± 0.210	0.109 ± 0.007	-0.273 ± 0.138	0.019 ± 0.041	-0.008 ± 0.018
10	0.009 ± 0.006	-0.406 ± 0.060	0.096 ± 0.007	-0.256 ± 0.051	-0.012 ± 0.026	0.000 ± 0.010
11	-0.013 ± 0.000	0.566 ± 0.032	-0.007 ± 0.000	-0.034 ± 0.013	0.007 ± 0.014	0.000 ± 0.004
12	-0.049 ± 0.002	-0.016 ± 0.010	-0.007 ± 0.001	0.042 ± 0.007	-0.003 ± 0.010	0.000 ± 0.002
13	0.004 ± 0.000	-0.112 ± 0.006	0.003 ± 0.000	0.008 ± 0.003	-0.000 ± 0.006	0.000 ± 0.000
14	-0.002 ± 0.000	0.019 ± 0.002	0.002 ± 0.000	-0.012 ± 0.001	0.000 ± 0.003	-0.000 ± 0.000
15	0.013 ± 0.000	0.017 ± 0.001	-0.001 ± 0.000	-0.001 ± 0.000	-0.000 ± 0.001	-0.000 ± 0.001

Table 5.18 Fourier–Bessel density expansion coefficients for 5.213 MeV 5^-, 5.481 MeV 5^- and 5.656 MeV 5^- states. The coefficients A_n have all been multiplied by a factor of 1000.

Transition Charge and Current Density Parameters

Fourier–Bessel Expansion $R_0 = 12.0\,fm$

	5.685 MeV 4^+		5.997 MeV 6^+	
N	charge	current	charge	current
1	-3.300 ± 0.125	-1.001 ± 0.133	4.681 ± 0.074	1.165 ± 0.810
2	-7.114 ± 0.107	-4.935 ± 0.476	8.557 ± 0.120	-0.153 ± 1.461
3	-1.190 ± 0.153	-8.227 ± 0.655	3.082 ± 0.220	-5.492 ± 0.662
4	4.532 ± 0.173	-2.587 ± 0.683	-1.333 ± 0.297	0.153 ± 1.358
5	0.712 ± 0.546	10.553 ± 0.767	0.586 ± 0.433	14.147 ± 1.557
6	-1.956 ± 0.383	18.074 ± 1.347	0.082 ± 0.627	13.503 ± 1.726
7	-1.451 ± 1.029	13.312 ± 1.580	-1.568 ± 0.480	2.464 ± 2.810
8	-0.722 ± 0.843	4.200 ± 1.544	-0.210 ± 0.400	-1.179 ± 1.588
9	-0.092 ± 0.182	-0.175 ± 0.960	0.629 ± 0.336	-0.134 ± 0.229
10	0.004 ± 0.035	-0.110 ± 0.541	0.039 ± 0.154	0.008 ± 0.062
11	-0.000 ± 0.021	0.243 ± 0.432	-0.068 ± 0.102	-0.001 ± 0.031
12	0.000 ± 0.012	-0.063 ± 0.340	0.036 ± 0.060	0.000 ± 0.017
13	0.000 ± 0.007	-0.108 ± 0.250	-0.011 ± 0.037	0.000 ± 0.013
14	-0.000 ± 0.004	0.056 ± 0.206	0.000 ± 0.021	-0.000 ± 0.007
15	0.000 ± 0.005	0.052 ± 0.105	0.001 ± 0.014	-0.000 ± 0.003

Table 5.19 Fourier–Bessel density expansion coefficients for the 5.485 MeV 4^+ and 5.997 MeV 6^+ states. The coefficients A_n have all been multiplied by a factor of 1000.

5.6 High Spin States Dominated by a Single Mean Field Configuration

In the excitation energy region between 6.0 MeV and 7.1 MeV, the spectra taken at a momentum transfer above 1.5 fm^{-1} show a large number of strong levels. Although the level density is very high in this regime, an interpretation based upon the mean field picture of the nucleus permits a grouping of levels as members of a single particle–hole transition. In particular, three mean field configurations, $\nu(1i_{11/2}, 1i^{-1}_{13/2})$ (SP energy, 5.845 MeV), $\nu(1j_{15/2}, 1i^{-1}_{13/2})$ (SP energy, 6.489 MeV) and $\pi(1i_{13/2}, 1h^{-1}_{11/2})$ (SP energy, 7.182 MeV) can couple to high spin states and have single particle–hole energies in this excitation energy region.

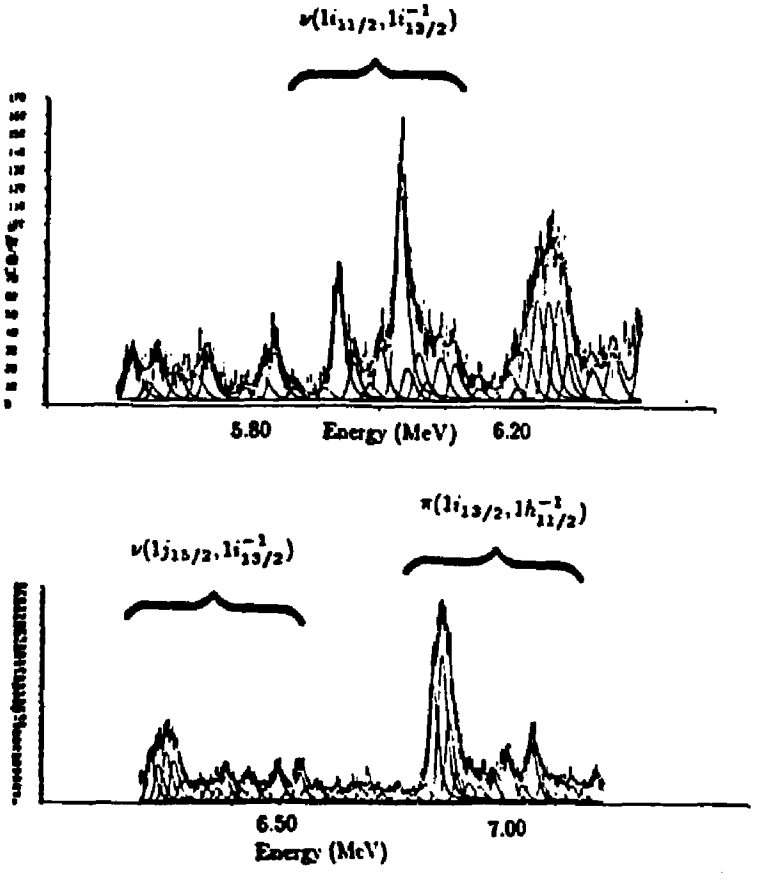

Fig.5.47 Spectrum ($q_{eff} \sim 2.0\ fm^{-1}$) taken at 150 MeV at 155° scattering angle (a) region between 5.7 and 6.3 MeV, and (b) region between 6.2 and 7.2 MeV.

Figure 5.47 shows backward angle spectra taken at a momentum transfer

of $q_{eff} \sim 2.0\ fm^{-1}$. Several multiplets of states are apparent, with braces encompasing the energy region where the mean field configurations listed above are expected to be dominant. Table 5.20 lists the high spin states available from these mean field configurations.

SP Configurations	SP Energy	Electric	Magnetic
$\nu(1i_{11/2}, 1i^{-1}_{13/2})$	5.845 MeV	8^+,10^+,12^+	9^+,11^+
$\nu(1j_{15/2}, 1i^{-1}_{13/2})$	6.489 MeV	7^-,9^-,11^-, 13^-	8^-,10^-,12^-,14^-
$\pi(1i_{13/2}, 1h^{-1}_{11/2})$	7.182* MeV	7^-,9^-,11^-,	8^-,10^-,12^-

* effective SP energy for proton configuration should be lowered by ~400 keV due to Coulomb interaction

Table 5.20 Single particle configurations which couple to high spin states observed in the excitation energy region between 5.8 MeV and 7.2 MeV.

The highest multipolarity members of each multiplet, the 12^+, 12^-_1, 12^-_2 and 14^- transitions are worthy of special attention since these configurations are unique in their ability to couple to these very high spins. These levels, which have been the subject of much theoretical and experimental interest, will discussed in detail in the next section.

$\nu(1i_{11/2}, 1i^{-1}_{13/2})$ Transitions

Of the positive parity states which arise from the neutron $\nu(1i_{11/2}, 1i^{-1}_{13/2})$ configuration, only the 12^+ at 6.110 MeV and the 10^+ 5.928 MeV were reported

in the electron scattering experiment by Lichtenstadt[6] . To three other states at 5.860 MeV, 5.954 MeV and 6.089 MeV we assign spins and parity of 11^+, 9^+ and 8^+ respectively. These assignments were based upon the proximity of the experimental energies to the $\nu(1i_{11/2}, 1i^{-1}_{13/2})$ single particle–hole energy of 5.845 MeV, comparisons to the calculated SP form factors and obtaining a reasonable Woods–Saxon amplitude from the DWBA analysis.

The 8^+ assignment is the weakest of the three since considerable mixing with other 8^+ configurations is expected. The 6.089 MeV state is clearly an electric transition with a substantial longitudinal cross section (Figure 5.48). A comparison was made with predicted form factors from a TDA calculation and the assignment was made on that basis. The longitudinal form factor was well described by theoretical calculation, which at this energy was dominated by the $\pi(2f_{7/2}, 1h^{-1}_{11/2})$ configuration. The mixing of neutron transitions considered in the analysis, $\nu(1i_{11/2}, 1i^{-1}_{13/2})$ and $\nu(3d_{5/2}, 1i^{-1}_{13/2})$ cannot be reliably extracted, due to the uncertainty in the high–q backward angle cross sections from contamination from the nearby 12^+ state. These configurations served merely to model the transition current density. The fits to the data and the resulting transition charge and current densities are shown in Figure 5.48. Theoretical densites from a predicted TDA 8^+ state at 6.049 MeV are also shown. The calculation does a good job in predicting the transition charge density but is quite far off in the transition current density. The uncertainty in the backward angle data at high–q for this level makes a convincing comparison difficult.

The 10^+ state at 5.928 MeV was identified in the electron scattering experiment by Lichtenstadt[6] . In his work, the four 10^+ states observed below 7.0 MeV were analyzed with the constraint of orthogonality applied to the resultant mixtures of Woods–Saxon configurations. The 5.928 MeV state was reported to be dominantly due to the $\nu(1i_{11/2}, 1i^{-1}_{13/2})$ configuration with small admixtures of the $\nu(2g_{9/2}, 1i^{-1}_{13/2})$, $\pi(1h_{9/2}, 1h^{-1}_{11/2})$ and $\nu(1j_{15/2}, 2f^{-1}_{5/2})$ configurations.

Our analysis used the same Woods–Saxon configurations to model the transition densities but without the orthogonality constraint. A comparison of the

Woods–Saxon amplitudes from Lichtenstadt's work and this experiment is made in Table 5.21. The radial parameters were held constant at 1.258 fm for the neutron orbitals and 1.288 fm for the proton orbitals.

	This experiment	Lichtenstadt
$\nu(2g_{9/2}, 1i^{-1}_{13/2})_{10+}$	−0.111	0.116
$\pi(1h_{9/2}, 1h^{-1}_{11/2})_{10+}$	−0.263	−0.162
$\nu(1j_{15/2}, 1i^{-1}_{13/2})_{11+}$	0.169	−0.071
$\nu(1i_{11/2}, 1i^{-1}_{13/2})_{11+}$	0.439	0.977

Table 5.21 Woods–Saxon amplitudes obtained in DWBA fit to the 5.928 MeV 10^+ level and those reported by Lichtenstadt[6] .

While the results essentially agree that the $\nu(1i_{11/2}, 1i^{-1}_{13/2})$ configuration dominates this state, our analysis shows much more configuration mixing, particularly from the proton transition. A comparison between the transition densities and TDA predictions in Figure 5.49 show that the transition charge density is under–predicted by nearly a factor of two.

The states at 5.954 MeV and 5.860 MeV, to which we assign $J^\pi = 9^+, 11^+$ respectively, were analyzed assuming a pure $\nu(1i_{11/2}, 1i^{-1}_{13/2})$ transition for the 11^+ state and a combination of the $\nu(1i_{11/2}, 1i^{-1}_{13/2})$ and $\pi(2f_{7/2}, 1h^{-1}_{11/2})$ configurations for the 9^+ state. The assumption of a single particle–hole configuration for the 11^+ level is justified since the next nearest 1p–1h transition that can couple to 11^+ has a SP energy of 5.067 MeV. The Woods–Saxon orbital radii were held constant at the same values used in the analysis of the 10^+ states and only the amplitudes of the configurations adjusted. The fits and extracted transition magnetization densites are shown in Figure 5.50.

The fit to the 5.860 MeV 11^+ state shows a reduction of of the cross section to 60.5% of the pure 1p–1h cross section from the $\nu(1i_{11/2}, 1i^{-1}_{13/2})$ transition. Quenching from the single–particle hole strengths has also been observed in the 12^+, 12^- and 14^- single particle states discussed in Section 5.7.

The analysis of the 5.954 MeV 9^+ state gave amplitudes of 0.7079 ± 0.094 from the $\nu(1i_{11/2}, 1i^{-1}_{13/2})$ configuration and 0.4406 ± 0.053 from the $\pi(2f_{7/2}, 1h^{-1}_{11/2})$ configuration. Predicted densities from a correlate ground state TDA calculation by Heisenberg (Figure 5.50) is in good agreement with the experimental densites.

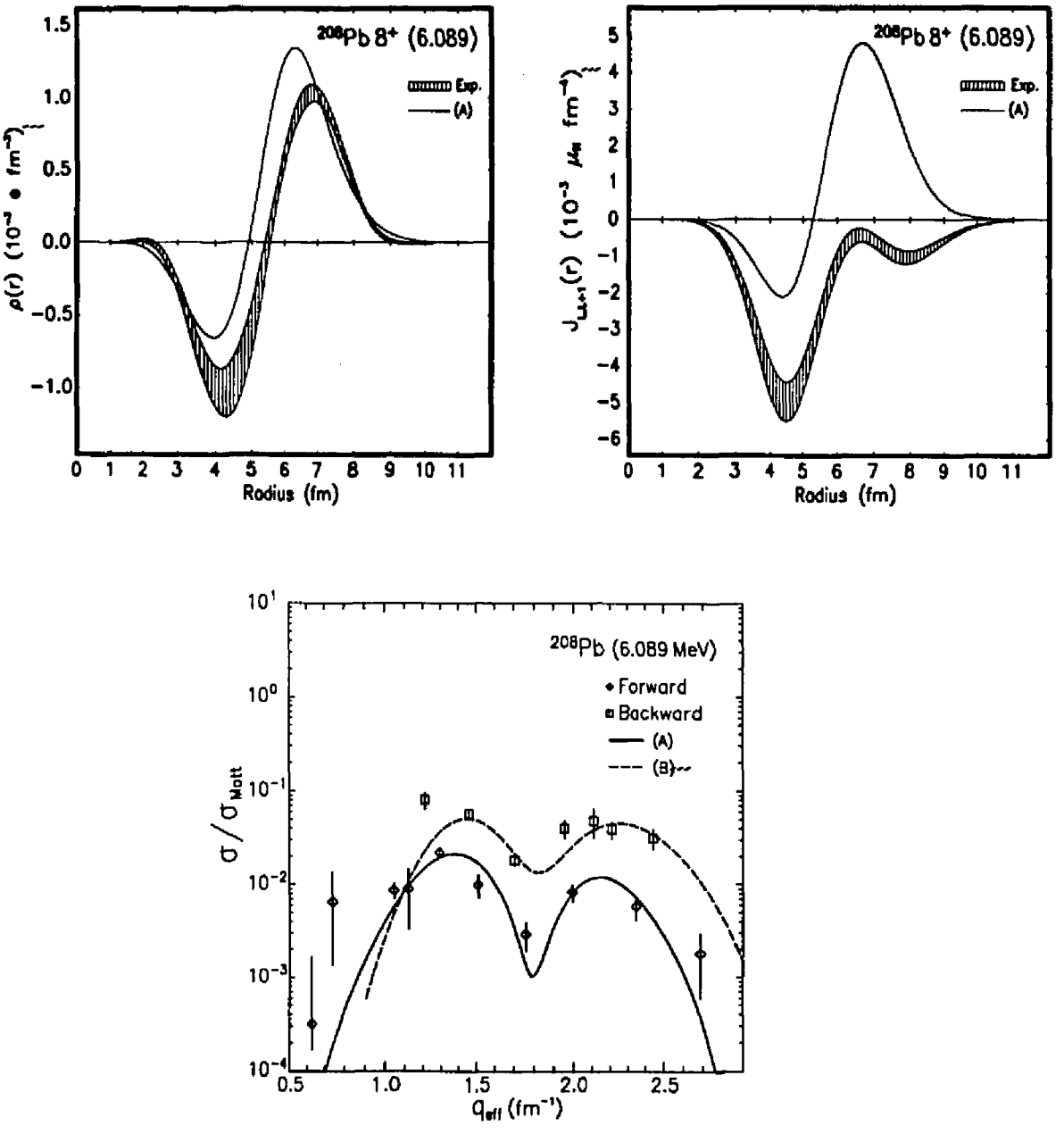

Fig.5.48 DWBA fits to the data and transition charge and current densities for the 6.089 MeV 8^+ state.

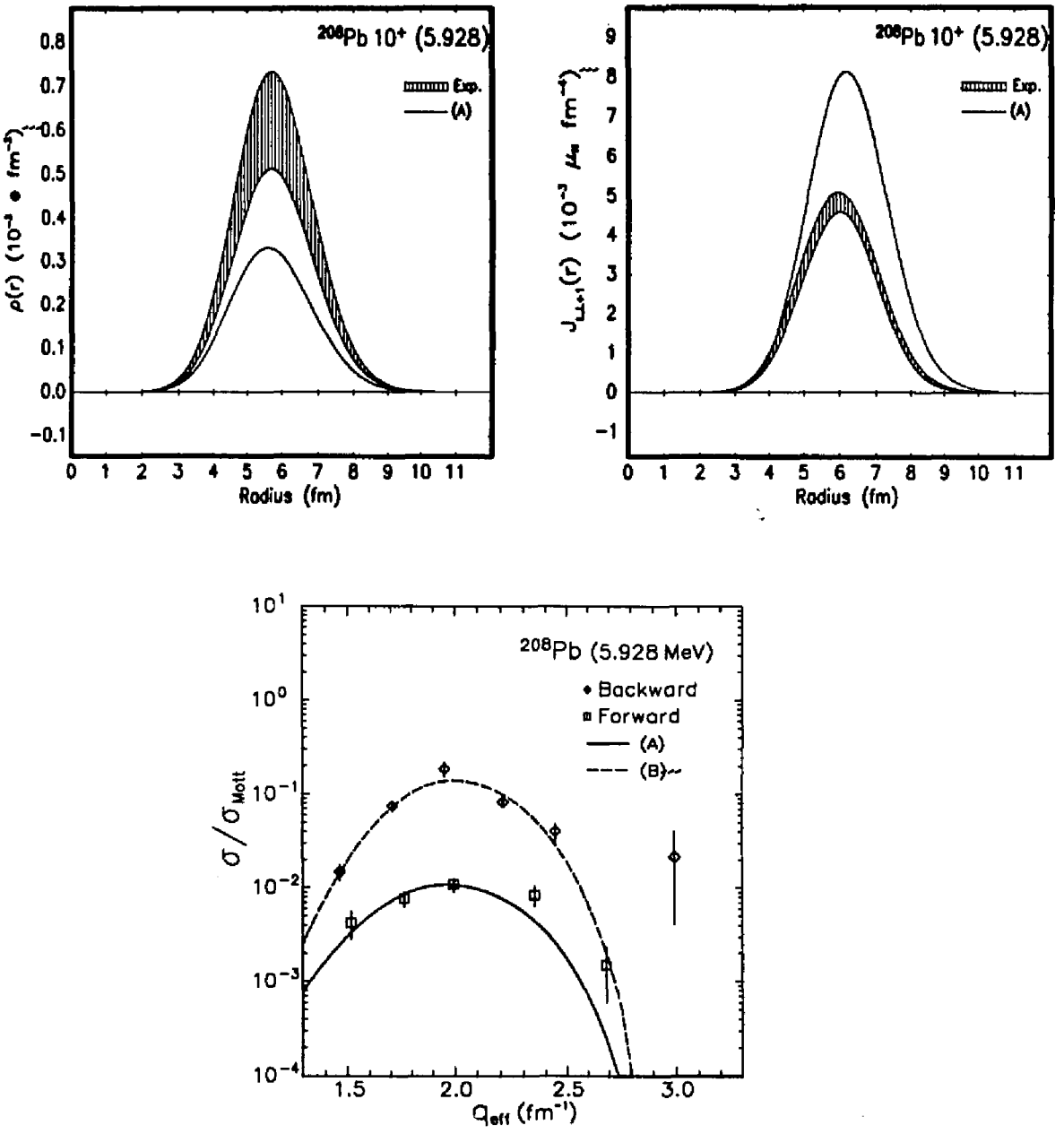

Fig.5.49 DWBA fits to the data and transition charge and current densities for the 5.928 MeV 10^+ state.

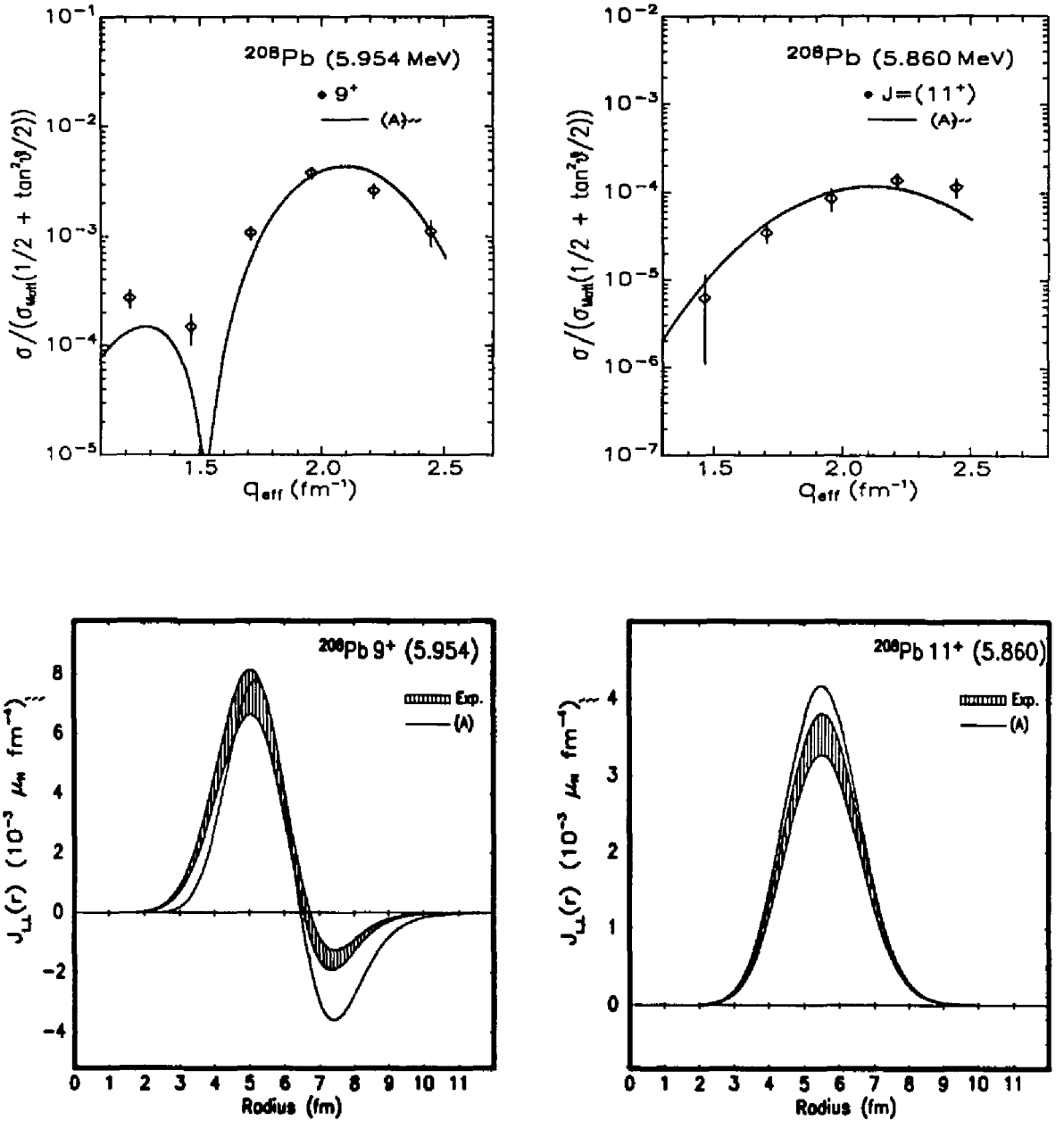

Fig.5.50 DWBA fits to the data and transition magnetization densities for the 5.954 MeV 9^+ and 5.860 MeV 11^+ states. Theoretical curves from TDA calculation.

$\nu(1j_{15/2}, 1i^{-1}_{13/2})$ Transitions

Previous electron scattering[12] and proton scattering experiments[13] have identified a 12^- excitation at 6.437 MeV. A combined analysis of both electron and proton scattering data[14] has shown this level to result from the $\nu(1j_{13/2}, 1i^{-1}_{13/2})$ configuration. A search was made in our data for the lower multipolarity members of this configuration. A group of closely spaced levels are observed near 6.2 MeV excitation energy which are believed to be a multiplet based upon the $\nu(1j_{15/2}, 1i^{-1}_{13/2})$ configuration. Several negative parity states (3^-, 5^-, 7^-) have been reported in this region[1] .

As shown in Figure 5.47, the level density is very high in this energy region. Only one form factor has been reliably extracted from this multiplet; an excitation at 6.283 MeV which peaks at higher momentum transfer than other levels seen in this region. No strength was observed for the 6.283 MeV level in the forward angle data indicating the excitation to be purely transverse.

Calculations show that the electromagnetic cross section from the 9^-, 11^- and 13^- members of the $\nu(1j_{15/2}, 1i^{-1}_{13/2})$ multiplet to be only a few percent of the 12^- cross section and unmeasurable in this experiment. An assignment of 10^- was made to the 6.283 MeV excitation based upon the shape of the form factor and the strength of the excitation. The predicted form factor shape of the 8^- transition from this configuration peaks at 1.2 fm^{-1} and gave a poor fit to the data.

In the DWBA analysis, two 1p–1h Woods–Saxon configurations were assumed, the $\nu(1j_{15/2}, 1i^{-1}_{13/2})$ and $\pi(1i_{13/2}, 1h^{-1}_{11/2})$ using the radial parameters obtained from the analysis of the 12^- level at 6.437 MeV. The fit to the data and the transition magnetization density are shown in Figure 5.51. The best fit was obtained with an amplitude of 0.7987 for the $\nu(1j_{15/2}, 1i^{-1}_{13/2})$ configuration and 0.134 for the $\pi(1i_{13/2}, 1h^{-1}_{11/2})$ configuration. The TDA calculation by Heisenberg[11] gives good qualitative agreement with the transition density but over–predicts the strength by 40%.

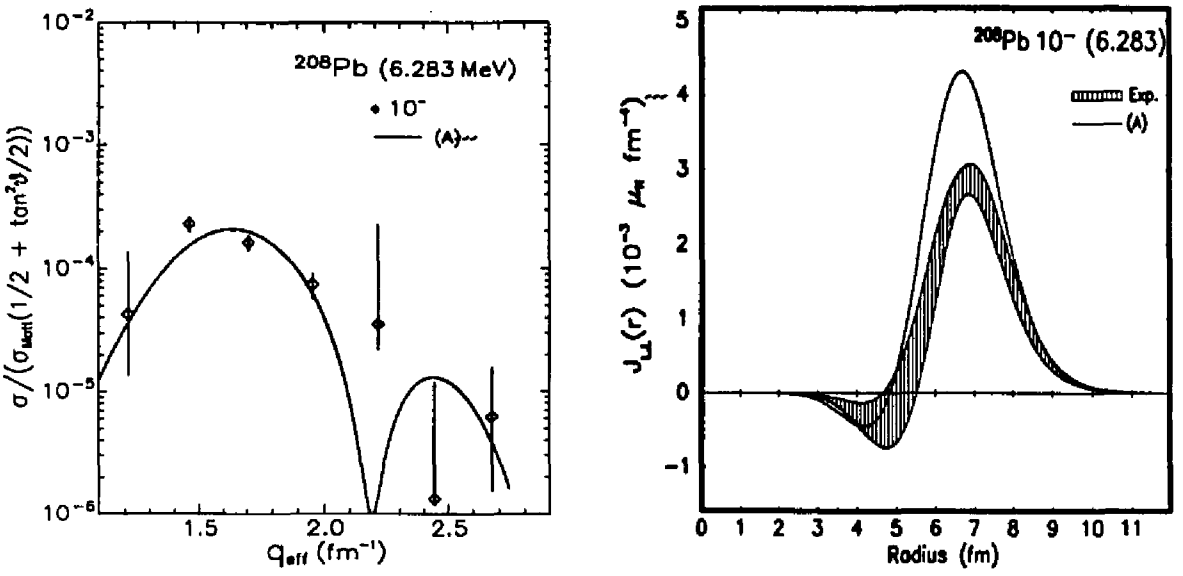

Fig.5.51 DWBA fit to the data and transition magnetization density for the 6.283 MeV 10^- excitation. Theoretical curve from TDA calculation.

$\pi(1i_{13/2}, 1h^{-1}_{11/2})$ Transitions

The multiplet of states near 6.85 MeV display large cross sections in the momentum transfer region between 1.2 fm^{-1} and 2.0 fm^{-1} in both the forward and backward angle data. These levels are quite close to the effective single particle-hole energy of the $\pi(1i_{13/2}, 1h^{-1}_{11/2})$ configuration at ~6.75 MeV (including the lowering of the energy due to the Coulomb attraction of the protons). It was suspected that several magnetic high spin transitions was included in this mulitplet.

The energy proximity of the states are so close that even with a resolution of 20 keV a separation of the levels is quite difficult. In order to determine the energies and extract cross sections for these states, the following method was employed. First, energies of the forward angle peaks were determined since the magnetic states contribute much less and the resolution of the forward angle data

was generally better than the 155° data. Next, the backward angle data was fit, determining the energies of peaks at the momentum transfer where each level was at a maximum. The entire data set was then refit, using a consistent minimum set of energies required to give a good χ^2. This method is crucially dependent upon using a precise channel to energy calibration in the peak fitting routine. Consistency was therefore required in the energies of well separated levels such as the 14^- at 6.737 MeV and the 6^+ at 5.997 MeV. In Figure 5.52, several backward angle spectra are displayed, showing the overall consistency of the peak fits in the excitation energy region near 6.8 MeV.

Two strong states at 6.859 MeV and 6.879 MeV were seen in the forward angle spectra with apparently strong longitudinal components. A comparison of the form factor shapes with TDA predictions showed a strong similarity to a predicted 9^- transition at 7.089 MeV to the 6.859 MeV level, and a predicted 7^- transition at 6.966 MeV to the 6.879 MeV level. The calculated states primarily resulted from the $\pi(1i_{13/2}, 1h^{-1}_{11/2})$ configuration. The calculation also indicated that both of these states have a very small transition current density. For this reason, the 6.879 MeV and 6.859 MeV levels were only fit in the forward angle data and analyzed assuming a purely longitudinal transition. The DWBA analysis was performed by simply scaling the predicted Fourier–Bessel coefficients from the TDA calculation. The fits to the data are given in Figure 5.53 with the resulting transition charge densities. The experimental charge density was found to contain only 38.3% of the predicted TDA strength for the 7^- state, and 67.1% of the predicted TDA strength for the 9^- state. The scaled Fourier–Bessel coefficients are given in Table 5.22.

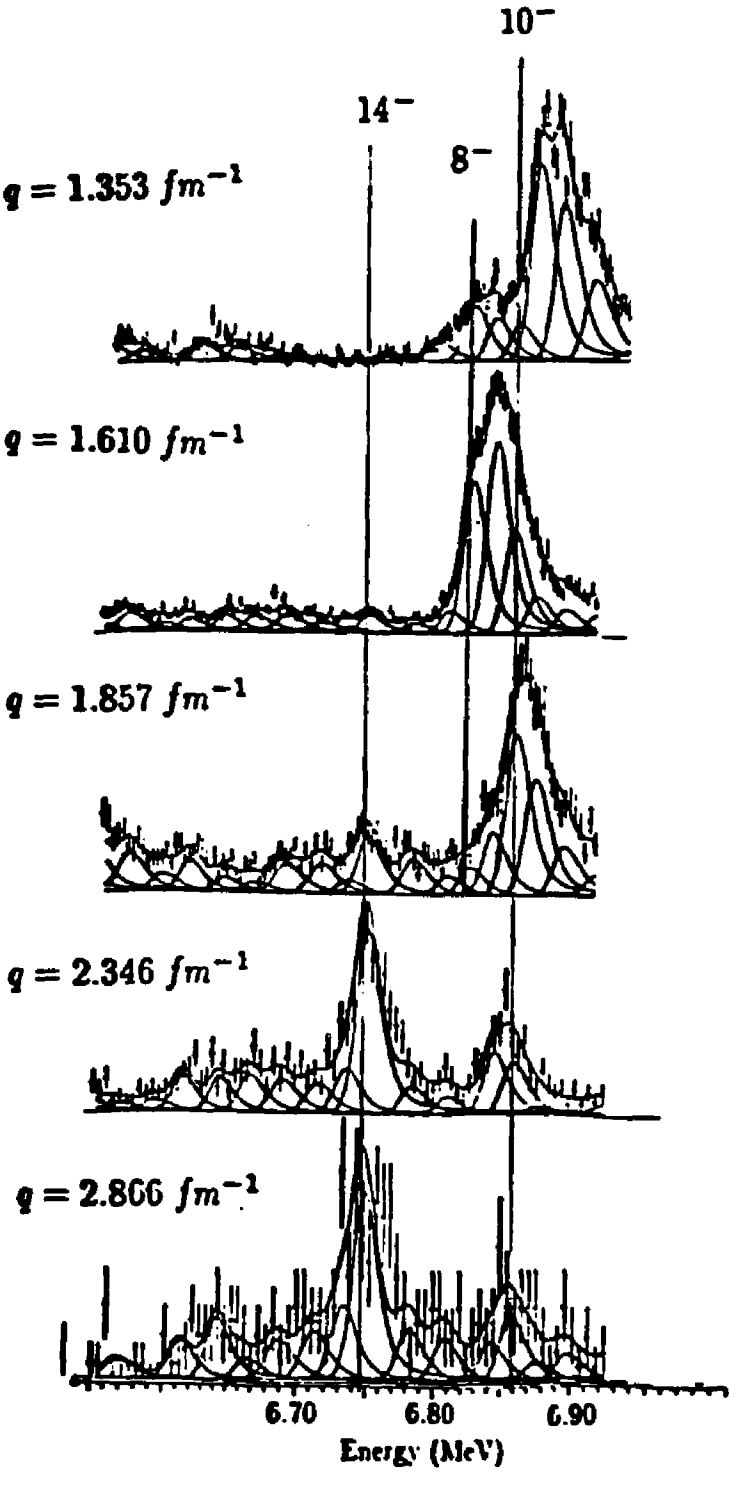

Fig.5.52 Backward scattering angle spectra in the region near 6.8 MeV. The lines indicate the consistency of the fits.

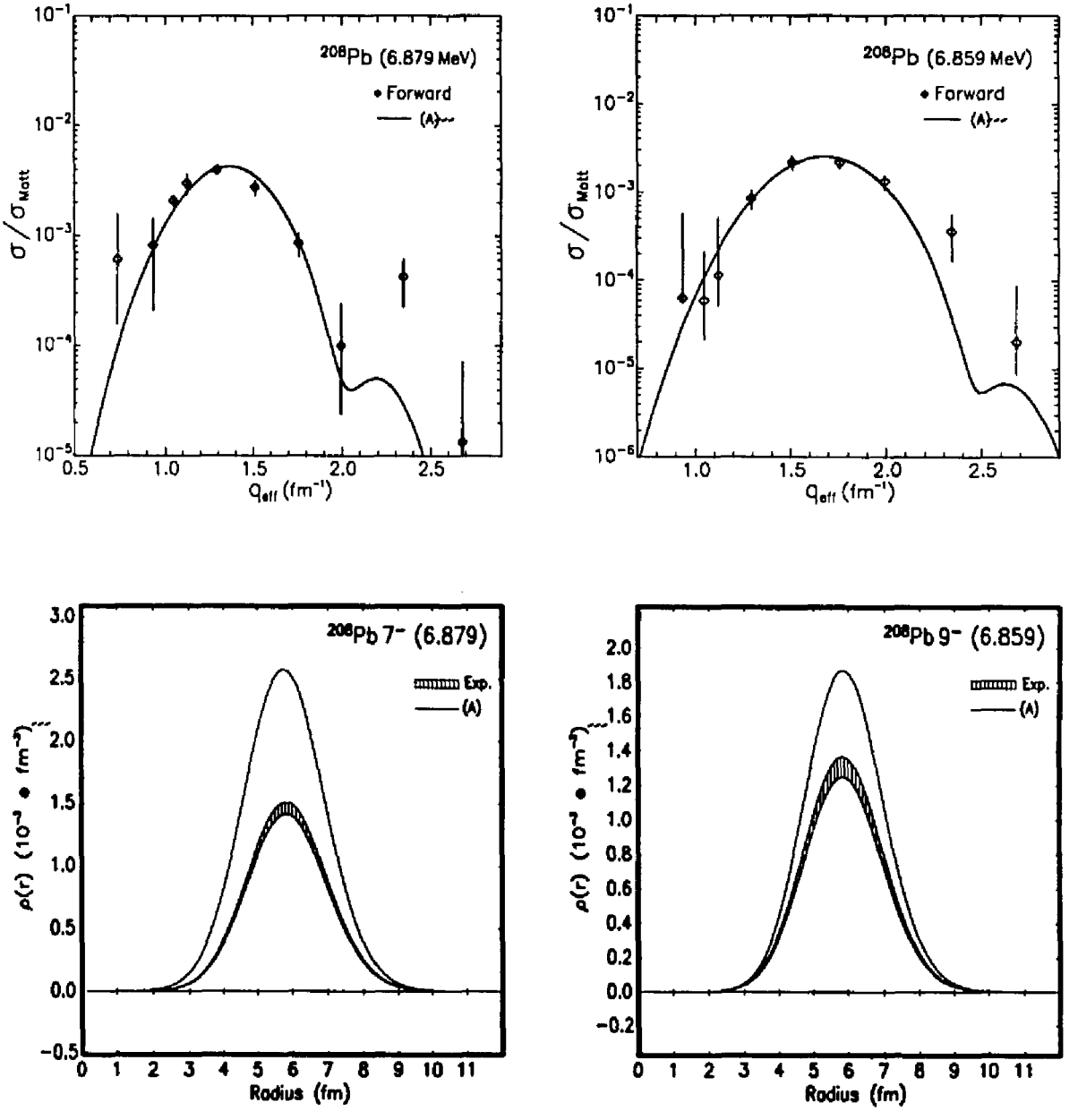

Fig.5.53 DWBA fits to the data and transition charge densities for the 6.879 MeV 7^- and 6.859 MeV 9^- states. Theoretical curves from TDA calculation.

Transition Charge Density Parameters

Fourier–Bessel Expansion $R_0 = 12.0\,fm$

	6.879	6.859
N	7^-	9^-
1	0.975 ± 0.031	0.604 ± 0.026
2	3.011 ± 0.096	2.134 ± 0.094
3	3.668 ± 0.117	3.194 ± 0.141
4	1.884 ± 0.060	2.435 ± 0.107
5	-0.006 ± 0.000	0.832 ± 0.036
6	-0.397 ± 0.012	-0.057 ± 0.002
7	-0.077 ± 0.002	-0.126 ± 0.005
8	0.057 ± 0.001	-0.012 ± 0.000
9	0.018 ± 0.000	0.013 ± 0.000
10	-0.006 ± 0.000	0.002 ± 0.000
11	-0.002 ± 0.000	-0.001 ± 0.000
12	0.000 ± 0.000	-0.000 ± 0.000
13	0.000 ± 0.000	0.000 ± 0.000
14	0.000 ± 0.000	0.000 ± 0.000
15	0.000 ± 0.000	0.000 ± 0.000

Table 5.22 Fourier–Bessel density expansion coefficients for the 6.879 MeV 7^- and 6.859 MeV 9^- states. The coefficients A_n have all been multiplied by a factor of 1000.

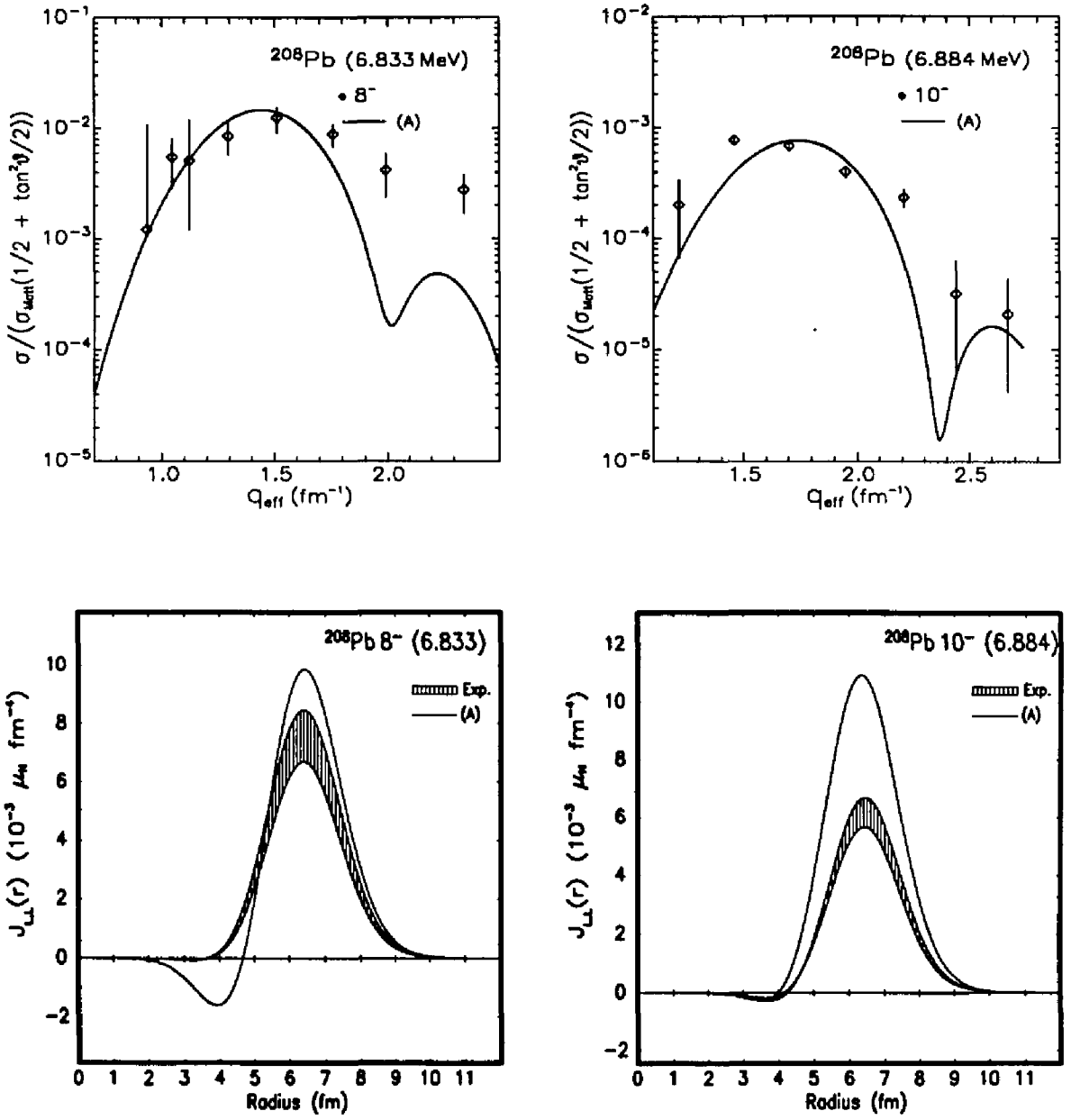

Fig.5.54 DWBA fits to the data and transition magnetization densities for the 6.833 MeV 8^- and 6.884 MeV 10^- states. Theoretical curves from TDA calculation.

In the search for magnetic transitions in the 6.85 MeV multiplet, only two states fulfilled the criteria established to justify an assignment of spin and parity, an 8^- state at 6.833 MeV and a 10^- state at 6.884 MeV. The extraction of cross sections for the 6.884 MeV level was based upon the assumption that the 6.879 MeV 7^- state was purely longitudinal.

The DWBA analysis of the 6.833 MeV 8^- state was performed using a pure $\pi(1i_{13/2}, 1h_{11/2}^{-1})$ Woods–Saxon configuration, adjusting the amplitudes only with the orbital radius fixed to the value obtained in the analysis of the 7.064 MeV 12^- state. The form factor fits and transition magnetization densities are shown in Figure 5.54. The fitted amplitudes show a reduction in the experimental cross section to 55.7% of the 1p–1h strength for the 8^- state.

The analysis of the 6.884 MeV 10^- state used two Woods–Saxon configurations, the $\pi(1i_{13/2}, 1h_{11/2}^{-1})$ and the $\nu(1i_{11/2}, 1h_{9/2}^{-1})$ configuration, which has a single particle–hole energy of 7.621 MeV. The amplitude for the proton configuration was -0.9118 and the amplitude of the neutron configuration was 0.1480, with an overall scaling of the magnetization current by 0.6196.

Summary

The excitation energy region in ^{208}Pb above 5.9 MeV at high momentum transfer is dominated by the multiplet of levels due to the $\nu(1i_{11/2}, 1i^{-1}_{13/2})$, $\pi(1i_{13/2}, 1h^{-1}_{11/2})$ and $\nu(1j_{15/2}, 1i^{-1}_{13/2})$ configurations. While the highest multipolarity states from each multiplet have been identifed and studied in earlier experiments, the lower high spin members, except for the 10^+ excitation at 5.928 MeV, have not been previously identified. In this section, assignments of J^π have been made to several electric and magnetic excitations. The magnetic states have been analyzed in terms of a single particle–hole configuration. Reductions of 40% to 50% from calculated single particle–hole strengths are seen in the 9^+, 10^- and 11^+ excitations.

The electric states resulting from the $\nu(1i_{11/2}, 1i^{-1}_{13/2})$ transition, the 8^+ level at 6.089 MeV and the 10^+ level at 5.928 MeV are strongly transverse but have measurable transition charge densities due to core polarization. The 5.954 MeV and 5.860 MeV levels are identifed as the 9^+ and 11^+ members of this configuration.

Although a number of closely spaced levels near 6.2 MeV are suspected as members of the $\nu(1j_{15/2}, 1i^{-1}_{13/2})$ configuration, only the 6.283 MeV excitation was unambiguously measured and identified as $J^\pi = 10^-$. The analysis showed that only 50% of the single particle–hole strength is seen.

Four levels in the 6.8 MeV multiplet were identifed as belonging to the $\pi(1i_{13/2}, 1h^{-1}_{11/2})$ configuration. Two electric states, the 7^- level at 6.879 MeV and the 9^- level at 6.859 MeV are strongly excited in the forward angle data and are seen to be almost entirely longitudinal. The excitations at 6.833 MeV and 6.884 MeV were identified as 8^- and 10^- states respectively. Both levels show a reduction of approximately 50% from the single particle–hole strengths.

Figure 5.55 shows the experimental energies compared to single particle–hole energies and TDA predictions for the excitations discussed in this section.

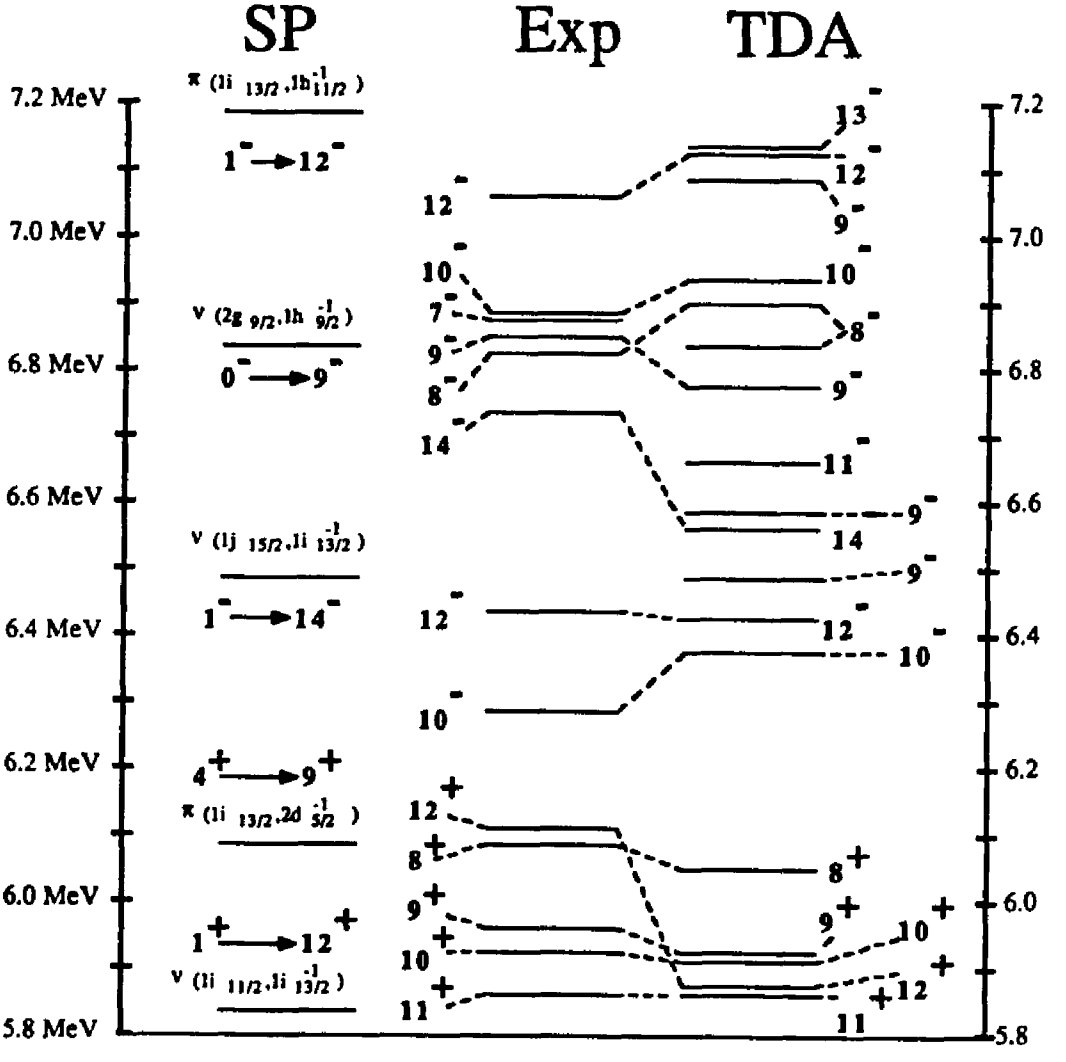

Fig 5.55 Comparison of experimental energies to predicted energies from a correlated ground state TDA calculation for high spin excitations between 5.8 and 7.2 MeV[11]

5.7 Single Particle–Hole States

High spin states in ^{208}Pb ($J \geq 12$) are an important source of nuclear structure information since the number of configurations which can contribute are constrained by the selection rules governing angular momentum coupling. In the basis set of levels near the fermi surface, the 12^+ and 14^- transitions have unique particle–hole configurations and only two configurations which couple to 12^{-1}. These transitions are termed single particle–hole transitions (SPH) and provide a crucial test for mean–field predictions.

J^π	Particle–hole Configurations	S–P Energy	Expt Energy
14^{-1}	$\nu(1j_{15/2}, 1i^{-1}_{13/2})$	6.489 MeV	6.745 MeV
12^{-1}	$\nu(1j_{15/2}, 1i^{-1}_{13/2})$	6.489 MeV	6.437 MeV
12^{-1}	$\pi(1i_{13/2}, 1h^{-1}_{11/2})$	7.182 MeV	7.064 MeV
12^{+1}	$\nu(1i_{11/2}, 1i^{-1}_{13/2})$	5.875 MeV	6.110 MeV

Table 5.23 High spin single states dominated by a single mean field configuration. Effective proton SP energies should be lowered approxiamately 400 keV due to Coulomb interation between protons.

The high spin states listed Table 5.23 have been identified in both (e, e')[12][36] and (p, p')[18][37][14] experiments. An important result from all of these analyses is the quenching of the single particle–hole strengths. The observed cross sections from these states in $(e, e')$and (p, p')experiments are reported to be less than 50% of the single particle–hole strengths. However, discrepencies have been observed between (e, e') and (p, p')in the degree of quenching, particularly for the 12^- transitions. As reported by Lichtenstadt *et al.*[12] , the quenching of the 14^- and 12^- form factors is approximately 50% in all three cases. Bacher *et al.*[18] , in the analysis of the scattering of 135 MeV protons from these excitations report

that the magnitudes of the theoretical form factors are too large by factors of ~ 2 (14^-), ~ 1.2 (12_1^-) and ~ 5 (12_2^-).

Several theoretical mechanisms have been suggested to explain the source of this quenching. Core polarization contributions through a δ residual interaction have been investigated by Hamamoto *et al.*[15] and by Suzuki *et al*[16] using a G matrix interaction. These approaches predict a q–dependence of the quenching and applies only to magnetic transitions. It has also been suggested that reduction of the single–particle strength may be due to coupling to the octupole vibrational state[15][16] . Krewald and Speth[17] have shown that inclusion of 2p–2h contributions fragments the single–particle strength, which would effect natural and unnatural parity transitions alike. An analysis of not only the very high spin states considered in this section, but of states with a lower multipolarity but still dominantly single particle in character, is neccesary in the evaluation of the contributions from these various models.

The criterion used in the assignment of the spins and parity to candidates for high spins states by Lichtenstadt *et al.*[12] was threefold; 1.) the matching of the q–dependence of the form factor to that given by either Woods–Saxon(WS) or Hartree–Fock(HF) single particle predictions, 2.) whether the observed experimental excitation energies are close to the particle–hole energies, and 3.) the absence of the longitudinal component to the form factor for magnetic or purely neutron transitions.

The improved energy resolution from this experiment provides a more precise determination of the excitation energy for these states, which has ranged from $\pm$ 10 to 15 kev[86] . We are also better able to separate nearby contaminant states which may also have a substantial cross section at high momentum transfer. A DWBA analysis was performed using Woods–Saxon wave functions to model the transition density by adjusting the overall amplitude of the particle–hole configuration and the radial parameter.

<u>14^- State at 6.745 MeV</u>

In the mean field approach to the nuclear structure of ^{208}Pb, only one config-

uration with a particle hole energy below 8.0 MeV can produce a 14^- magnetic transition. This is the neutron $\nu(1j_{15/2}, 1i^{-1}_{13/2})$ configuration which has a single particle–hole energy of 6.489 MeV[7] .

The 14^- state was identifed at 6.74 ± 0.01 kev using the criteria listed above in an (e, e')experiment by Lichtenstadt *et al.*[12] . The identification was made using Hartree–Fock wave functions, which have no adjustable radial parameters, to ascertain the correct q–dependence, and then analyzed with Woods–Saxon wave functions adjusting both the amplitude and the well size. The form factors were shown to contain no measurable longitudinal component through the combined analysis of forward and backward angle scattering data. A quenching of the single particle–hole strength was observed to be $\sim$ 50%.

The 14^- state has been seen using the (p, p') reaction at approximately the same excitation energy by Bacher *et al.*[13] (6.72 MeV) and Cook *et al.*[14] (6.74 MeV). Since only the spin density contributes to the calculated 14^- cross section for both the electron and proton probes, the nuclear structure sampled in both cases is very similar. Both analyses fitted the data in the Distorted Wave Impulse Approximation (DWIA) using optical model parameters and either harmonic oscillator[13] or Woods–Saxon[14] single particle wave functions. A quenching of the single p–h amplitude observed in the previous (e, e') experiment was also reported in their analyses.

We observed the 14^- state at 6.745 ± 0.007 MeV. This state dominants the very high q backward angle spectra ($q \geq 2.0$ MeV) and displays no longitudinal component of the form factor. This aspect is displayed graphically in Figure 5.56 by plotting the cross section divided by $\sigma_{Mott}(1/2 + tan^2(\theta/2))$ versus q_{eff}. Any longitudinal component would enhance the forward angle data in this representation. The DWBA fit was performed using Woods–Saxon wave functions. The well radii of the Woods–Saxon single–particle wave functions and the amplitude of the configuration were adjusted. We observed $51.7 \pm 4.2\%$ of the calculated single–particle strength, which is only slightly greater than the quenching factors reported by Lichtenstadt or Bacher*et al.*[13] . The fitted well radius,

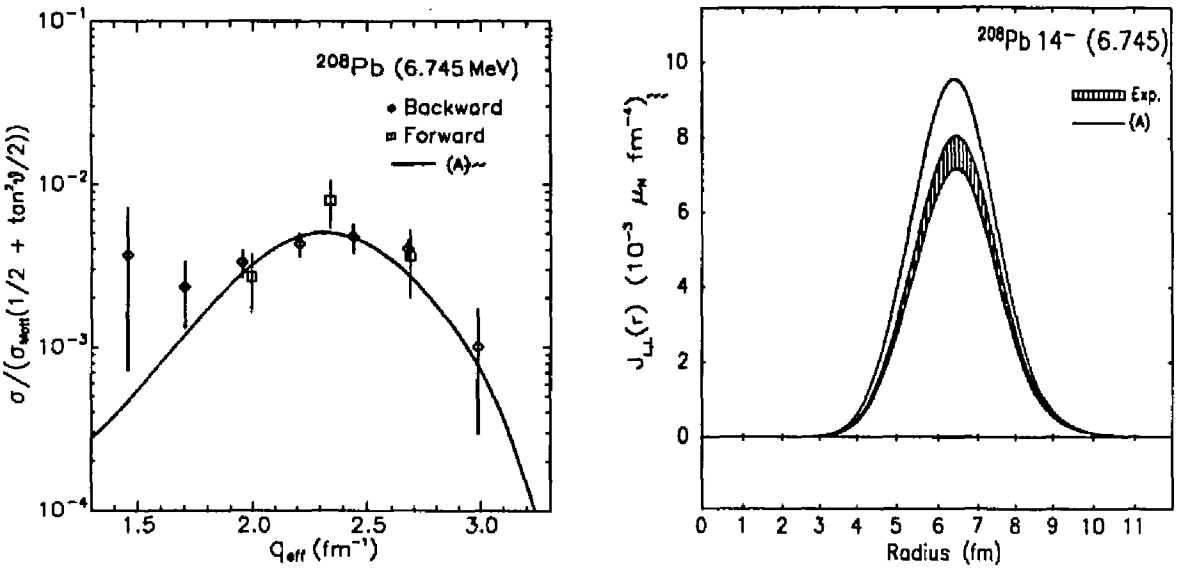

Fig.5.56 Form factor (left) from the 14^- state with DWBA fit using Woods–Saxon single particle wave functions. Magnetization density (right) compared with TDA prediction.

which also gave the best fit in the analysis of the 12^- state at 6.437 MeV, was $1.225 \pm 0.007\ fm$. This value is lower than the value reported by Lichtenstadt ($1.255 \pm 0.003\ fm$) but closer to the well radius of 1.200 fm reported by Cook *et al.*[14] in a combined analysis of electron and proton scattering data.

12^- States at 6.437 and 7.064 MeV

Two 12^- states have been observed in ^{208}Pb at 6.43 MeV and 7.06 MeV[12][13] . The lower level arises primarily from the neutron configuration $\nu(1j_{15/2}, 1i^{-1}_{13/2})$ with a single particle–hole energy of 6.489 MeV. The second state was reported by Lichtenstadt *et al.*[12] to result from the proton $\pi(1i_{13/2}, 1h^{-1}_{11/2})$ with a single particle–hole energy of 7.20 MeV.

A great deal of interest has been generated by the comparison of electron and proton scattering results for the 12^- states. In the previous (e, e') experiment by Lichtenstadt, the overall strength of the 12^- form factors was reported to be

only 50% of the predicted single particle strength. This is the same quenching observed in both (e,e') and (p,p') analyses of the 14^- state and is consistent with a pure configuration treatment of the 12^- states.

Proton scattering experiments have reported much different reductions of the cross sections from the single particle predictions as calculated in the Distorted Wave Impulse Approximation (DWIA). Bacher *et al.*[13] , in an analysis of 135 MeV (p,p')data have observed cross sections to be 80% of the calculated cross section for the 6.43 MeV state and cross sections for the 7.06 MeV state which were quenched to 20% of the calculated cross section. Cook *et al.*[14] in an analysis of 318 MeV proton scattering data report a similar quenching of the 6.43 MeV state and a reduction in the 7.06 MeV state to 38.9% the single particle prediction. Cook's work was a combined analysis of proton scattering data with Lichtenstadt's electron scattering data which included a small amount of mixing between the proton and neutron configurations. Small amounts of configuration mixing was shown to have a significant effect on the amount of quenching seen in (e,e') data while having no effect on the q-dependence of the electromagnetic form factor for these states. Using this method, Cook obtained quenching factors for Lichtenstadt's (e,e') cross sections of 45.3% and 39.9% for the 6.43 MeV and 7.06 MeV levels respectively.

In this experiment we have identified the 12^- states at 6.437 ± 0.006 MeV and 7.064 ± 0.004 MeV for the neutron and proton transitions respectively. The greater resolution of this experiment allowed us to differentiate the 12^- states from neighboring levels which were unseen in the previous (e,e') experiment, particularly in the case of the 7.064 MeV state.

Figure 5.57 displays the excitation energy region between 6.9 and 7.3 MeV (E_i=200 MeV, θ=155°). A strong level at 7.086 MeV is observed close to the 12^- at 7.064 MeV. This level, which appears to be transverse and peaks at a momentum transfer of q= 2.1 $fm-1$, was unresolved in Lichtenstadt's experiment. In Figure 5.58(a) a comparison is made between the backward angle cross sections for the 7.064 MeV 12^- state and the 7.086 MeV level. The form factors are nearly

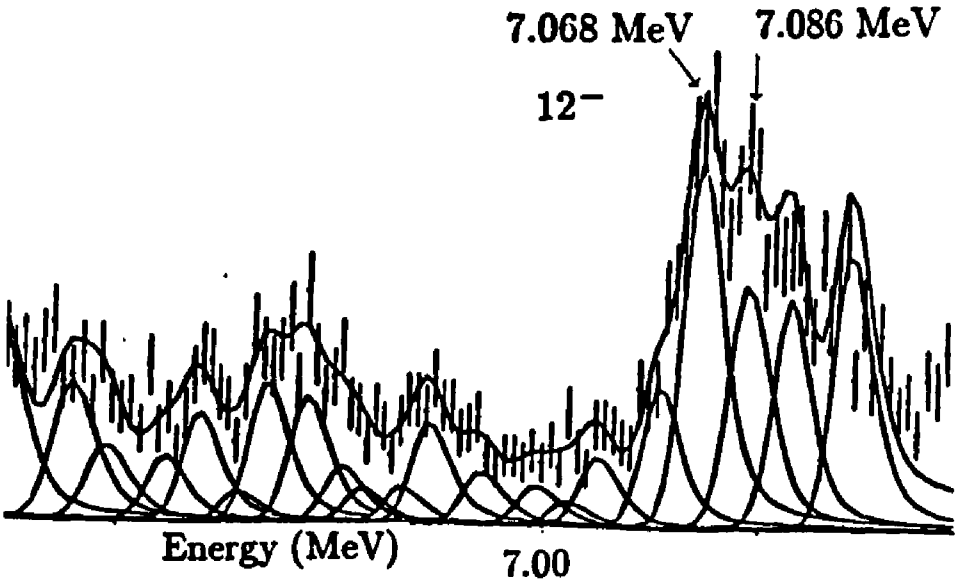

Fig.5.57 Spectrum ($q_{eff} \sim 2.0\ fm^{-1}$) taken at 200 MeV at 155° scattering angle, excitation region between 6.9 and 7.3 MeV.

identical in shape although the level at 7.086 MeV displays less strength than the 7.064 MeV state.

In Figure 5.58 (b), Lichtenstadt's data for the 7.06 MeV state is compared with the sum of our data for the 7.064 MeV and 7.086 MeV levels, recalulated to 335 MeV, with the DWBA fit obtained by Lichtenstadt. The sum reproduces the cross section reported by Lichtenstadt, suggesting that both states were included in the previous (e, e') analysis of the 12^- state at 7.06 MeV. The similarity between the shapes of the form factors for these two levels, and the lack of longitudinal strength in both cases renders these states very difficult to resolve for energy resolutions greater than 25 kev.

An attempt was made to fit the 7.086 MeV form factor as a 10^- state. How-

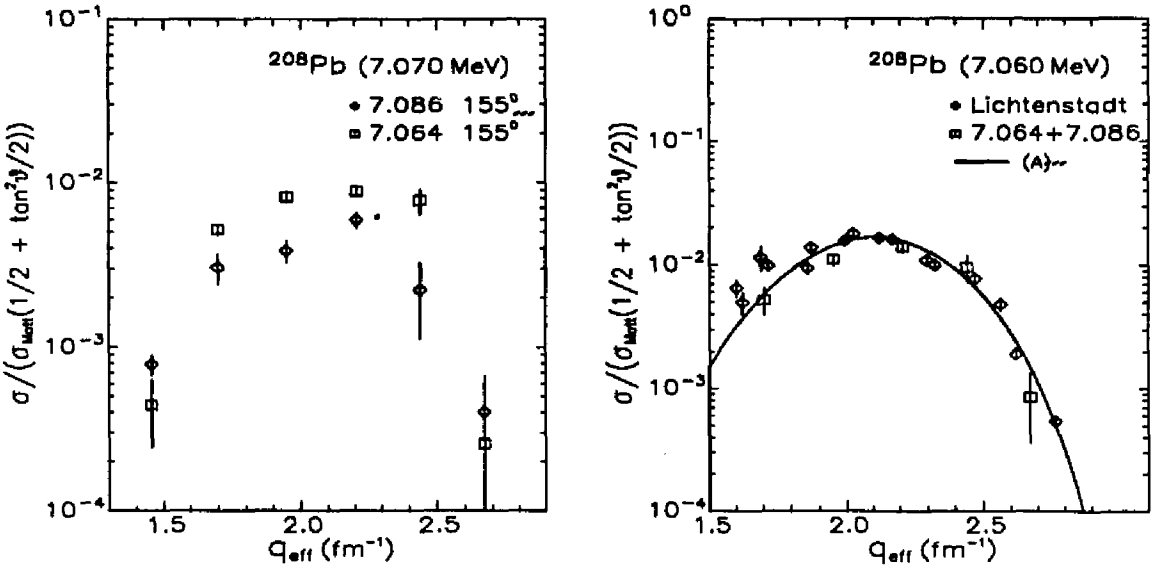

Fig.5.58 (a) Backward angle data from the present experiment from the 7.064 MeV 12^- level and the neighboring 7.086 MeV level; (b) comparison to Lichtenstadt's data at 7.06 MeV with the sum of the 7.064 MeV and 7.086 MeV cross sections reported in this experiment. DWBA fit is from Lichtenstadt. Cross sections are recalculated to 335 MeV.

ever, the only configuration which provided enough strength at large momentum transfer to give a reasonable χ^2 was the $\nu(1i_{11/2}, 1h_{9/2}^{-1})$ which has a single particle–hole energy of 7.621 MeV. It is unlikely that the experimental energy would be lowered by almost 600 kev unless strong mixing occured, which is not expected for magnetic transitions. A more likely possibility is the fragmentation of the 12^- strength through mixing with the $2p-2h$ excitation $(3^- \otimes 10^+)_{12^-}$.

The analysis was performed on the 12^- states assuming no mixing between the proton and neutron configurations. The results from the proton scattering experiments indicate small amounts of configuration mixing may be present; however, due to the similarity between the shape of the calculated neutron and proton configuration form factors, permitting amplitudes from both configurations to vary freely would have given unreliable results. In the DWBA analysis of the 6.437 MeV and 7.064 MeV states, the $\nu(1j_{15/2}, 1i_{13/2}^{-1})$ and $\pi(1i_{13/2}, 1h_{11/2}^{-1})$

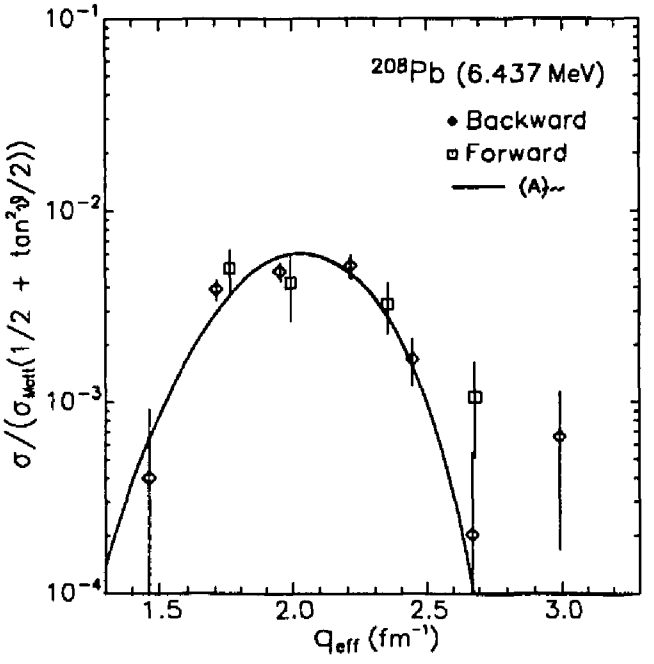

Fig.5.59 DWBA analysis of the 12^- state at 6.437 MeV with Woods-Saxon single particle configuration $\nu(1j_{15/2}, 1i^{-1}_{13/2})$.

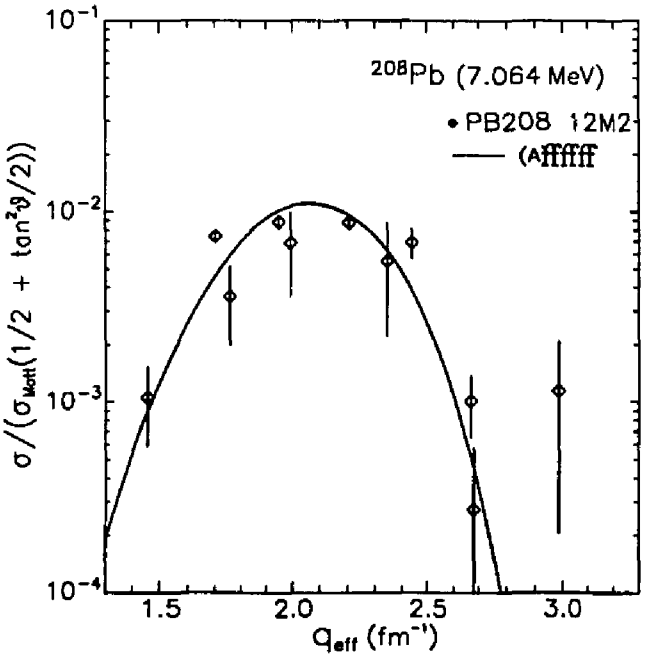

Fig.5.60 DWBA analysis of the 12^- state at 7.064 MeV with Woods-Saxon single particle configuration $\pi(1i_{13/2}, 1h^{-1}_{11/2})$.

Woods-Saxon configurations were fitted, respectively, allowing the amplitudes to vary. The radius for the neutron transition was taken from the fitted radius from the fit of the same configuration in the analysis of the 14^- state (1.225 fm^{-1}), while the radius of the proton configuration was permitted to vary. The amplitude of the neutron 6.437 MeV neutron transition was $45.6 \pm 7.0\%$ of the calculated single particle cross section. This amplitude, while slightly smaller than the quenching reported by Lichtenstadt, is within the calculated error essentially the same. The quenching of the proton 12^- transition at 7.064 MeV came to only $31.7 \pm 5.0\%$ of the calculated single particle cross section with a fitted single particle radius was 1.288 ± 0.007 fm. If indeed the strength of the proton 12^- is fragmented between two levels, the total strength reported by Lichtenstadt is recovered and the quenching of 50% is valid for the total 12^- cross section from the proton configuration. Figure 5.59 (6.437 MeV) and 5.60 (7.064 MeV) show the fitted curves to the data, plotting cross section divided by $\sigma_{Mott}(1/2 + tan^2(\theta/2))$ versus q_{eff}.

12^+ State at 6.110 MeV

The 12^+ state was observed at 6.110 ± 0.006 MeV, 10 kev higher than reported by Lichtenstadt[36] or the proton scattering experiments by Adams *et al.*[37] and Cook *et al.*[14] ; 250 kev higher than the single particle energy of 5.86 MeV. This transition, due primarily to the $\nu(1i_{11/2}, 1i^{-1}_{13/2})$ configuration has natural parity and is therefore electric in character.

Electron scattering is sensitive only to the currents produced by the spins of the participating neutrons, and by the effective charge of the neutron. The effective charge, which is produced by high lying proton particle–hole components which can couple to 12^+ or $2p-2h$ effects, has been calculated to be very small. A Rosenbluth separation in our data confirms Lichtenstadt's conclusion that no measurable longitudinal strength to the cross section was observed.

The Woods-Saxon configuration $\nu(1i_{11/2}, 1i^{-1}_{13/2})$ was used to model the transition current and charge densities. The fit to the data, shown in Figure 5.61,

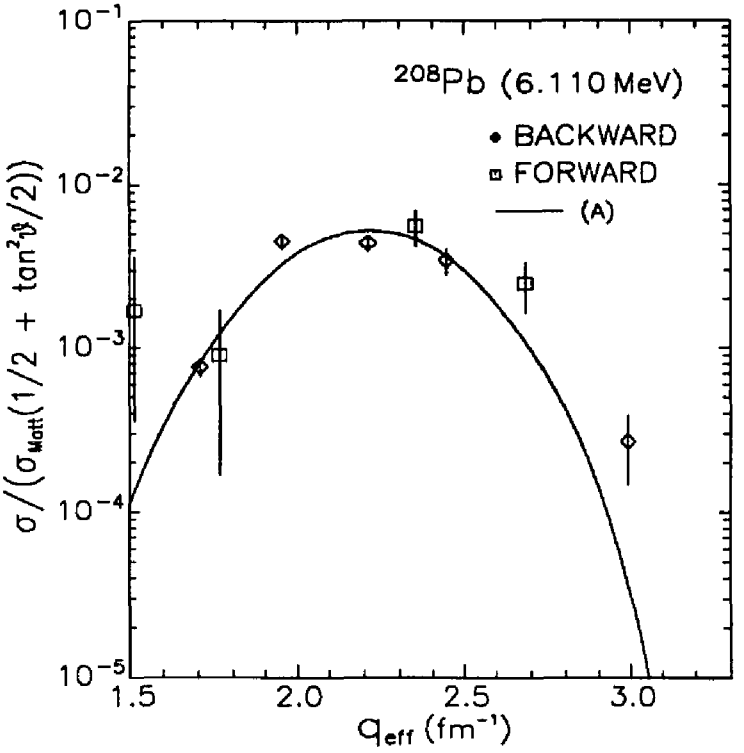

Fig.5.61 DWBA analysis of the 12^+ state at 6.110 MeV with Woods–Saxon single particle configuration $\nu(1i_{11/2}, 1i^{-1}_{13/2})$.

was performed allowing both the radii and amplitude of the transition to vary. An effective magnetic moment of $g_{eff} = 0.627 \times g_{free}$ was observed producing a reduction to $39.3 \pm 6.0\%$ of the single particle–hole strength. The Woods–Saxon radius was 1.274 ± 0.03 fm. This reduction is slightly lower than the $42.0 \pm 2.5\%$ quenching reported by Lichtenstadt, but the values are the same within the errors quoted.

Summary

The 14^- (6.745 MeV), 12_1^- (6.437 MeV), 12_2^- (7.068 MeV) and 12^+ (6.110 MeV) may be considered as pure single particle–hole transitions. Lichtenstadt *et al.*[12] reported a quenching of 50% from the SP strength for the magnetic excitations and 42% for the 12^+ level in a previous electron scattering experiment. The results from the present experiment agree with these conclusions, except for the 7.068 MeV 12^- level where the observed strength was only $31.7 \pm 5.0\%$ of the single particle–hole strength. A nearby level at 7.086 MeV, unresolved in the Lichtenstadt experiment, was seen. This excitation appears to be transverse and to peak at $\sim 2.0\ fm{-}1$. Although the 7.086 MeV level is well described as a 10^- transition based upon the $\nu(1i_{11/2}, 1h_{9/2}^{-1})$, this level could also be seen as another 12^- state from a 2p–2h transition which fragments the single particle strength.

Chapter 6

Conclusion

Inclusive electron scattering cross sections have been measured from over 120 levels below 7.3 MeV excitation energy with energy resolution better than 22 keV. Form factors from fifty excitations have been analyzed within the framework of the Distorted Wave Born Approximation and transition charge, current and magnetization densites have been measured.

The excitations below 4.7 MeV, which are dominated by $1\hbar\omega$ transitions, have been sufficiently resolved to permit electromagnetic form factors to be measured for both electric and magnetic states with $J^\pi = 3^-$, 4^-, 5^-, 6^-. The data set in this energy regime may be considered nearly complete in the sense that a large majority of the transitions predicted by RPA or TDA calculations have been identified in low excitation energy ^{208}Pb spectra. A rigorous comparison of the transition densites from the excitations in this region with theoretical densities from nuclear structure calculations would provide a information on the strength of residual interaction as a function of multipolarity and (un)natural parity.

A multiplet of positive parity excitations were observed near 5.0 MeV. These transitions result from intruder orbitals from higher or lower harmonic oscillator shells coupling to orbitals near the fermi level. Results from several high spin states (8^+, 9^+, 10^+, 11^+) were presented. Assignments of J^π have been made to the 4.862 MeV (8^+), 5.084 MeV (8^+), 5.260 MeV (9^+) and 5.291 MeV (11^+) levels. The 11^+ excitation was analyzed as a pure 1p-1h transition from the $\nu(2g_{9/2}, 1i^{-1}_{13/2})$ configuration. Only 40% of the particle-hole strength was observed.

The energy regime between 4.8 MeV and 6.0 MeV is populated by a large number of low spin electric excitations. Transition charge and current densities were measured for states with known spin and parity (1^-, 2^+, 3^-, 4^+, 5^-, 6^+) and comparisons made with TDA predictions. Only the well defined excitations

were analyzed so the investigation in this regime is not as complete as in the 3.8 MeV to 4.7 MeV region.

A search was made for high spin members of the multiplets due to the configurations $\nu(1i_{11/2}, 1i^{-1}_{13/2})$, $\pi(1i_{13/2}, 1h^{-1}_{11/2})$ and $\nu(1j_{15/2}, 1i^{-1}_{13/2})$. The highest multipolarities of each configuration (14^-, 6.745 MeV; 12^-_1, 6.437 MeV; 12^-_2, 7.068; 12^+, 6.110 MeV) were reported by Lichtenstadt *et al.* to be quenched from the calculated 1p–1h strength by 50%. Our results agree with Lichtenstadt's except for the 12^-_2 level which was reduced to 32% of the single particle–hole strength. A neighboring level at 7.086 MeV was unresolved by Lichtenstadt and may be a 2p–2h 12^- transition which fragments the strength of the 1p–1h excitation.

States dominated by the $\nu(1i_{11/2}, 1i^{-1}_{13/2})$ configuration were identified at 6.089 MeV (8^+), 5.954 MeV (9^+) and 5.860 MeV (11^+) in addition to the previously known 10^+ excitation at 5.298 MeV. Besides the 12^-_1 state, only the 10^- member of the $\nu(1j_{15/2}, 1i^{-1}_{13/2})$ multiplet was observed at 6.283 MeV. Assuming this state to be a pure 1p–1h transition, we observe the same quenching factor of 50% seen in the 12^-_1 state.

Assignments of J^π were made to the 7^- level at 6.879 MeV, 8^- level at 6.833 MeV, 9^- level at 6.879 MeV and 10^- level at 6.884 MeV resulting from the $\pi(1i_{13/2}, 1h^{-1}_{11/2})$ configuration. The electric states are predicted by TDA to be mainly longitudinal and this assumption was built into our extraction of the transverse cross sections for the neighboring levels. The magnetic states were quenched to 40% to 50% of the single particle–hole strength.

The discrete levels reported in this work by no means exhausts the information garnered by this experiment. The analysis, which has been slowed somewhat by the composition of this dissertation, is continuing. In particular, a search for lower spin magnetic excitations may prove fruitful and provide a more complete picture of nuclear structure of ^{208}Pb.

Bibliography

1. *Nuclear Data Sheets* **47** (1986) 797.
2. B. Frois, J. Bellicard, J. Cavedon, M. Huet, P. Leconte, P. Ludeau, I. Sick, A. Nakada and X. H. Phan, *Phys. Rev. Let* **38** (1977) 152.
3. D. Goutte, J. B. Bellicard, J. M. Cavedon, B. Frois, M. Huet, P. Leconte, Phan Xuan Ho, S. K. Platchkov, J. Heisenberg, J. Lichtenstadt, C. N. Papanicolas, and I. Sick, *Phys. Rev. Let.* **45** (1980) 1618.
4. J. Friedrich, *Nucl. Phys.* **A191** (1972) 118.
5. J. Friedrich, N. Voegler and H. Euteneuer,, *Phys. Let.* **64B** (1976) 269.
6. J. Lichtenstadt, Ph. D. Thesis, MIT 1979 (unpublished).
7. P. Ring and J. Speth, *Nucl. Phys.* **A235** (1974) 315.
8. W. Knüpfer and M. G. Huber, *Phys. Rev.* **C14** (1976) 2254
9. J. Dechargé and D. Gogny, *Phys. Rev. C* **21** (1980) 1568.
10. J. H. Heisenberg and S. Krewald (unpublished).
11. J. H. Heisenberg, *Univeristy of New Hampshire* preliminary results
12. J. Lichtenstadt, J. Heisenberg, C. Papanicolas, C. Sargent, A. Courtemanche and J. S. McCarthy, *Phys. Rev. C* **20** (1979) 497.
13. A. D. Bacher, G. T. Emery, W. P. Jones, D. W. Miller, G. S. Adams, F. Petrovich and W. G. Love, *Phys. Let.* **97B** (1980) 58.
14. D. Cook, N. M. Hintz, M. M. Gazzaly, G. Pauletta, R. W. Fergerson, G. W. Hoffman, J. B. McClelland and K. W. Jones, *Phys. Rev. C* **35** (1987) 456.
15. I. Hamamoto, J. Lichtenstadt and G. F. Bertsch, *Phys. Lett.* **93B** (1980) 213.

16. T. Suzuki, M. Oka, H. Hyuga and A. Arima, *Phys. Rev. C* **26** (1982) 750.

17. S. Krewald and J. Speth, *Phys. Rev. Lett* **45** (1980) 417.

18. T. deForest and J. D. Walecka, 'Electron Scattering and Nuclear Structure',, *Adv. in Phys.* **15** (1966) 1.

19. H. Überall, *Electron Scattering from Complex Nuclei*, (Academic, New York, 1971).

20. J. D. Walecka, *Electron Scattering – Lectures given at Argonne National Laboratory*, NTIS Report ANL-83-50 (1983).

21. H. C. Lee, Atomic Energy of Canada, Report AECL-4839, Chalk River, Ontario (1975).

22. J. Heisenberg, "Nuclear Transition Density Determintation from Inelastic Electron Scattering", Adv. Nucl. Phys., **12** (1981) 61.

23. L. Maximon, MIT 1967 Summer Study: Medium Energy Nuclear Physics with Electron Linear Accelerators, (1967) 249.

24. S. T. Tuan, L. E. Wright, D. S. Onley, *Nucl. Instrum. and Meth.* **60** (1968) 70.

25. H. Rothhaas, J. Friedrich, K. Merle and B. Dreher, *Phys. Let.* **51B** (1974) 23.

26. G. G. Simon, Ch. Schmitt, F. Borkowski, and V. H. Walther, *Nucl. Phys.* **A173** (1971) 32.

27. W. Bertozzi, M. V. Hynes, C. P. Sargent, W. Turchinetz, and C. Williamson, *Nucl. Instrum. Methods* **162** (1979) 211.

28. W. Bertozzi, M. V. Hynes, C. P. Sargent, C. Cresswell, P. C. Dunn, A. Hirsh, M. Seitch, B. Norum, F. N. Rad, T. Sasanuma, *Nucl. Instrum. Methods* **141** (1977) 457.

29. T. E. Milliman, Ph. D. Thesis, UNH 1987 (unpublished).

30. J. Heisenberg, J. Lichtenstadt, C. N. Papanicolas, and J. S. McCarthy, *Phys. Rev. C* **25** (1982) 2292.

31. R. Frey, A. Richter, A. Schwierczinski, E. Spamer, O. Titze and W. Knüpfer, *Phys. Lett.* **74B** (1978) 45.

32. S. Muller, A. Richter, E. Spamer, W. Knüpfer and B. C. Metsch, *Phys. Lett.* **120B** (1983) 305.

33. P.B. Vold, J. O. Andreassen, J. R. Lien and A. Graue, *Nucl. Phys.* **A215** (1973) 61.

34. E. A. McClatchie, C. Glashausser and D. L. Hendrie, *Phys. Rev. C* **1** (1970) 1828.

35. D. Gogny, *Nuclear Self-Consistent Fields*, ed. by G. Ripka and M. Porneuf (North-Holland, Amsterdam, 1975)

36. J. Lichtenstadt,.C. N. Papanicolas, C. Sargent, J. Heisenberg, and J. McCarthy, *Phys. Rev. Let.* **44** (1980) 858.

37. G. S. Adams, A. D. Bacher, G. T. Emery, W. P. Jones, D. W. Miller, F. Petrovich and W. G. Love, *Phys. Let.* **91B** (1980) 23.

38. G. A. Rinker and J. Speth, *Nucl. Phys.* **A306** (1978) 360.

39. V. Gillet, A. M. Green and E. A. Sanderson, *Phys. Lett.* **11** (1964) 44.

40. L. E. LeTourneux and J. M. Eisenberg, *Nucl. Phys.* **85** (1966) 119.

41. D. J. Rowe, *Phys. Rev.* **175** (1968) 1283.

42. A. deShalit and H. Feshbach *Theoretical Nuclear Physics*, Vol.1 (J. Wiley and Sons Inc., New York, 1974)

43. J. W. Negele and D. Vauthérin, *Phys.Rev. C* **5** (1972) 1472.

44. V. R. Pandharipande, C. N. Papanicolas and J. Wambach, *Phys. Rev. Let.* **53** (1984) 1133.

45. H. Euteneuer, J. Friedrich, and N. Voegler, *Phys. Rev. Let* **36** (1976) 129.

46. J. Cavedon, B. Frois, D. Goutte, M. Huet, P. Leconte, X. Phan, S. Platchkov, C. N. Papanicolas, S. E. Williamson, W. Boeglin, I. Sick and J. Heisenberg, *Phys. Rev. Let.* **58** (1987) 195.

47. B. Frois, J. M. Cavedon, D. Goutte, M. Huet, Ph. Leconte, C. Papanicolas, X.-H. Phan, S. K. Platchkov, S. E. Williamson, *Nucl. Phys.* **A396** (1983) 409.

48. K. Takayanagi, K. Shimizu and A. Arima, *Nucl. Phys.* **A477** (1988) 205.

49. G. J. C. Van Niftrik, *Nucl. Phys.* **A131** (1969) 574.

50. J. Heisenberg, R. Hofstadter, J. S. McCarthy, I. Sick, B. C. Clark, R. Herman and D. G. Ravenhall, *Phys. Rev. Let.* **23** (1969) 1402.

51. H. L. Acker, G. Backenstoss, C. Daum, J. C. Sens and S. A. de Wit, *Nucl. Phys.* **87** (1966) 1.

52. J. B. Bellicard and K. J. van Oostrum, *Phys. Rev. Let.* **19** (1967) 242.

53. J. L. Friar and J. W. Negele, *Nucl. Phys.* **A212** (1973) 93.

54. J. Heisenberg and I. Sick, *Phys. Let.* **32B** (1970) 249.

55. J. F. Ziegler and G. A. Peterson, *Phys. Rev.* **165** (1968) 1337.

56. D. Gogny, in *Proceedings of the Conference on Nuclear Physics with Electromagnetic Interactions, Mainz, 1979*, edited by H. Arenhövel and D. Dreschel (Springer–Verlag, New York, 1979)

57. I. Hamamoto, *Phys. Let.* **66B** (1977) 410.

58. E. Weber, W. Knüpfer, E. Grecksch and M. G. Huber, *Phys. Let.* **22** (1966) 189.

59. A. Heussler and P. von Brentano, *Ann. Phys.(NY)* **75** (1973) 381.

60. W. T. Wagner, G. M. Crawley, G. R. Hammerstein and H. McManus, *Phys. Rev. C* **12** (1975) 757.

61. P. Grabmayr, G. Mairle, U. Schmidt–Rohr, G. P. A. Berg, J. Meissburger, P. Von Rossen and J. L. Tain, *Nucl. Phys.* **A469** (1987) 285.

62. R. M. Laszewski, R. Alarcon, D. S. Dale and S. D. Hoblit *The Distribution of M1 Transitions in* ^{208}Pb University of Illinois, Internal Report (1988)

Appendix A

Tables of Cross Sections

from States Analyzed in Chapter 5

Cross sections of excitations analyzed in this dissertation are tabulated in Appendix A. The solid angles, calibrated energies and effective momenta transfer are given in Table A.1.

E_{inc} (MeV)	θ_{lab} (degrees)	q_{eff} (fm^{-1})	ρ_A (mg/cm^2)	$\delta\theta$ (degrees)	$\delta\phi$
149.967 ± 0.4	42.00	0.591	2.5	0.377	1.455
187.54 ± 0.8	40.00	0.750	2.5	0.753	5.84
224.468 ± 0.3	41.00	0.844	2.5	0.572	1.695
247.735 ± 0.1	40.00	0.903	2.5	0.376	3.65
279.670 ± 0.95	40.00	1.014	2.5	1.505	7.299
300.632 ± 0.53	40.00	1.086	2.5	0.376	6.204
279.670 ± 0.95	50.00	1.245	2.5	1.505	7.299
300.632 ± 0.53	55.00	1.467	2.5	1.505	6.201
300.632 ± 0.53	65.00	1.706	2.5	1.505	7.299
300.632 ± 0.53	75.00	1.933	2.5	1.505	7.299
279.670 ± 0.95	100.00	2.272	2.5	1.505	7.299
300.632 ± 0.53	110.00	2.601	2.5	1.505	7.299
100.3 ± 1.5	155.00	1.105	4.0	1.501	7.279
125.4 ± 0.7	155.00	1.353	2.5	1.502	5.095
149.967 ± 0.4	155.00	1.610	2.5	1.425	7.279
175.043 ± 1.9	155.00	1.857	2.5	1.425	7.279
200.992 ± 2.3	155.00	2.114	2.5	1.425	7.279
224.468 ± 0.3	155.00	2.346	2.5	1.425	7.279
247.735 ± 0.1	155.00	2.659	2.5	1.425	7.279
279.670 ± 0.95	155.00	2.866	2.5	1.425	7.279

Table A.1 The data set from this experiment.

Normalized Cross Sections in mb/sr

		0.000	2.615	3.198	3.709
Energy	**Angle**	0^+	3^-	5^-	5^-
150 MeV	42°	$4.173E+00 \pm 9.03E-03$	$3.802E-02 \pm 7.81E-04$	$3.179E-06 \pm 3.18E-05$	$3.209E-06 \pm 3.21E-04$
187 MeV	40°	$1.632E+00 \pm 1.73E-02$	$2.562E-02 \pm 4.84E-04$	$9.375E-04 \pm 1.21E-04$	$4.164E-04 \pm 9.20E-05$
225 MeV	41°	$5.554E-01 \pm 1.84E-03$	$8.034E-03 \pm 1.19E-04$	$1.430E-03 \pm 5.57E-05$	$7.531E-04 \pm 4.64E-05$
250 MeV	40°	$3.256E-01 \pm 9.74E-03$	$3.802E-03 \pm 1.53E-04$	$1.494E-03 \pm 2.21E-04$	$7.778E-04 \pm 1.21E-04$
280 MeV	40°	$8.456E-02 \pm 1.42E-03$	$1.374E-03 \pm 3.09E-05$	$9.713E-04 \pm 2.91E-05$	$5.231E-04 \pm 1.82E-05$
300 MeV	40°	$3.197E-02 \pm 4.02E-04$	$1.325E-03 \pm 6.57E-05$	$5.935E-04 \pm 5.03E-05$	$3.096E-04 \pm 3.54E-05$
280 MeV	50°	$9.432E-03 \pm 8.84E-05$	$6.231E-04 \pm 1.20E-05$	$5.965E-05 \pm 3.89E-06$	$2.443E-05 \pm 2.67E-06$
300 MeV	55°	$1.550E-03 \pm 2.24E-05$	$4.261E-05 \pm 3.17E-06$		$2.191E-05 \pm 2.85E-06$
300 MeV	65°	$1.794E-04 \pm 4.36E-06$	$2.963E-05 \pm 1.39E-06$	$4.246E-06 \pm 9.68E-07$	$4.684E-06 \pm 7.15E-07$
300 MeV	75°	$3.035E-05 \pm 1.17E-06$	$1.961E-06 \pm 3.07E-07$	$1.181E-06 \pm 2.70E-07$	$3.084E-07 \pm 1.39E-07$
280 MeV	100°	$2.217E-06 \pm 2.67E-07$	$6.226E-07 \pm 1.42E-07$	$1.379E-07 \pm 7.51E-08$	$1.234E-07 \pm 7.79E-08$
300 MeV	110°	$3.750E-08 \pm 2.06E-08$	$1.274E-09 \pm 1.27E-08$	$7.375E-08 \pm 3.74E-08$	$1.322E-08 \pm 1.44E-08$
100 MeV	155°		$1.818E-05 \pm 4.99E-07$	$3.563E-06 \pm 2.64E-07$	$1.887E-06 \pm 2.19E-07$
125 MeV	155°		$1.890E-06 \pm 8.14E-08$	$2.535E-07 \pm 3.75E-08$	$5.578E-07 \pm 4.86E-08$
150 MeV	155°	$6.981E-06 \pm 1.39E-07$	$1.393E-06 \pm 4.54E-08$	$1.879E-07 \pm 1.85E-08$	$4.248E-07 \pm 2.78E-08$
175 MeV	155°	$7.457E-07 \pm 4.09E-08$	$7.994E-08 \pm 2.79E-08$	$6.051E-09 \pm 2.07E-08$	$8.217E-10 \pm 1.91E-08$
200 MeV	155°	$1.643E-07 \pm 2.84E-08$	$5.003E-08 \pm 2.02E-08$	$4.295E-08 \pm 1.50E-08$	$3.743E-08 \pm 1.53E-08$
225 MeV	155°	$2.941E-08 \pm 1.31E-08$	$8.041E-09 \pm 9.17E-09$	$2.950E-08 \pm 1.53E-08$	$1.127E-08 \pm 7.88E-09$
250 MeV	155°	$1.940E-09 \pm 1.68E-09$	$8.093E-10 \pm 1.46E-09$	$3.419E-12 \pm 3.42E-11$	$1.087E-10 \pm 5.94E-09$

Table A.2 Normalised cross sections in mb/sr for the elastic, 2.615 MeV, 3.198 MeV and 3.709 MeV levels.

Normalized Cross Sections in mb/sr

		3.946	3.961	4.037	4.085
Energy	**Angle**	4^-	5^-	7^-	2^+
150 MeV	42°			$2.568E-05 \pm 1.18E-06$	$1.166E-02 \pm 4.70E-04$
187 MeV	40°		$1.077E-04 \pm 7.21E-05$	$1.301E-04 \pm 4.23E-06$	$4.332E-03 \pm 2.84E-04$
225 MeV	41°		$1.124E-05 \pm 2.34E-05$	$8.089E-05 \pm 2.40E-06$	$1.246E-03 \pm 5.24E-05$
250 MeV	40°		$4.254E-05 \pm 2.46E-05$	$2.151E-05 \pm 7.57E-07$	$1.481E-03 \pm 2.19E-04$
280 MeV	40°		$2.675E-05 \pm 5.50E-06$	$4.930E-05 \pm 1.60E-06$	$1.492E-03 \pm 4.18E-05$
300 MeV	40°			$6.290E-05 \pm 6.16E-06$	$1.171E-03 \pm 7.88E-05$
280 MeV	50°		$1.246E-05 \pm 2.15E-06$	$2.916E-05 \pm 2.87E-06$	$1.291E-04 \pm 5.58E-06$
300 MeV	55°		$4.471E-06 \pm 1.40E-06$	$6.562E-06 \pm 2.04E-07$	$4.329E-05 \pm 4.60E-06$
300 MeV	65°		$8.839E-07 \pm 2.86E-07$	$2.061E-07 \pm 1.64E-08$	$7.512E-06 \pm 1.03E-06$
300 MeV	75°		$5.647E-07 \pm 1.94E-07$	$3.736E-07 \pm 1.69E-08$	$7.749E-07 \pm 2.97E-07$
280 MeV	100°		$2.194E-10 \pm 2.19E-08$	$3.480E-07 \pm 2.15E-08$	$6.540E-11 \pm 6.54E-09$
300 MeV	110°		$7.326E-14 \pm 7.33E-11$	$1.546E-07 \pm 1.78E-08$	$2.475E-08 \pm 2.48E-07$
100 MeV	155°	$1.717E-07 \pm 1.98E-07$	$4.903E-07 \pm 2.05E-07$	$7.966E-07 \pm 2.12E-07$	$7.272E-06 \pm 3.25E-07$
125 MeV	155°	$2.597E-07 \pm 6.55E-08$	$2.752E-07 \pm 6.51E-08$	$2.407E-07 \pm 5.68E-08$	$1.113E-06 \pm 6.65E-08$
150 MeV	155°	$9.712E-08 \pm 2.22E-08$	$2.202E-07 \pm 2.65E-08$	$1.717E-09 \pm 1.22E-08$	$4.179E-07 \pm 2.88E-08$
175 MeV	155°	$4.931E-11 \pm 4.93E-09$	$9.403E-08 \pm 3.56E-08$	$2.076E-10 \pm 2.08E-07$	$5.008E-08 \pm 2.31E-08$
200 MeV	155°	$3.074E-08 \pm 2.30E-08$	$1.117E-11 \pm 1.12E-09$	$1.414E-07 \pm 2.77E-08$	$8.323E-08 \pm 2.55E-08$
225 MeV	155°	$2.153E-10 \pm 2.15E-09$	$1.334E-08 \pm 1.37E-08$	$9.895E-08 \pm 1.97E-08$	$9.945E-10 \pm 6.27E-09$
250 MeV	155°	$2.369E-09 \pm 1.14E-08$	$2.855E-13 \pm 2.85E-11$	$1.078E-08 \pm 5.87E-09$	$5.736E-09 \pm 3.54E-09$

Table A.3 Normalised cross sections in mb/sr for the 3.946 MeV, 3.961 MeV, 4.037 MeV and 4.085 MeV levels.

Normalized Cross Sections in mb/sr

		4.124	4.180	4.210	4.251
Energy	Angle	5^-	5^-	6^-	3^-
150 MeV	42°	$1.969E-05 \pm 1.97E-05$	$3.972E-07 \pm 3.97E-06$		$1.856E-05 \pm 5.48E-04$
187 MeV	40°	$1.515E-04 \pm 7.96E-05$	$4.370E-05 \pm 6.79E-05$		$1.537E-04 \pm 1.67E-04$
225 MeV	41°	$8.599E-05 \pm 3.48E-06$	$7.193E-05 \pm 5.18E-06$		$5.726E-05 \pm 5.88E-05$
250 MeV	40°	$1.112E-04 \pm 3.72E-05$	$1.273E-04 \pm 3.48E-05$		$1.068E-04 \pm 4.10E-05$
280 MeV	40°	$8.139E-05 \pm 9.40E-06$	$7.011E-05 \pm 7.42E-06$		$3.212E-05 \pm 1.71E-05$
300 MeV	40°	$5.335E-05 \pm 2.42E-05$	$4.692E-05 \pm 1.90E-05$		$4.169E-05 \pm 4.08E-05$
280 MeV	50°	$4.931E-06 \pm 2.00E-06$	$1.266E-05 \pm 2.26E-06$		$4.844E-05 \pm 7.57E-06$
300 MeV	55°	$7.397E-06 \pm 2.28E-06$	$1.251E-06 \pm 1.21E-06$		$1.275E-05 \pm 5.74E-06$
300 MeV	65°	$3.444E-06 \pm 6.78E-07$	$3.968E-07 \pm 2.52E-07$		$2.500E-06 \pm 1.14E-06$
300 MeV	75°	$2.492E-07 \pm 2.75E-07$	$2.724E-08 \pm 9.92E-08$		$9.308E-07 \pm 8.95E-07$
280 MeV	100°	$6.183E-08 \pm 8.77E-08$	$1.090E-10 \pm 1.09E-06$		$5.456E-08 \pm 3.55E-07$
300 MeV	110°	$5.915E-11 \pm 5.92E-07$	$6.030E-11 \pm 1.69E-07$		$1.187E-10 \pm 1.19E-06$
100 MeV	155°	$8.974E-07 \pm 1.86E-07$	$5.175E-07 \pm 1.60E-07$	$1.791E-07 \pm 1.59E-07$	$1.673E-06 \pm 3.18E-07$
125 MeV	155°	$1.193E-07 \pm 3.99E-08$	$1.342E-07 \pm 3.76E-08$	$1.797E-11 \pm 4.05E-08$	$4.550E-07 \pm 9.12E-08$
150 MeV	155°	$1.127E-07 \pm 1.67E-08$	$4.357E-08 \pm 1.23E-08$	$3.479E-10 \pm 1.12E-08$	$6.970E-08 \pm 2.57E-08$
175 MeV	155°	$8.724E-08 \pm 2.59E-08$	$2.864E-08 \pm 2.26E-08$	$2.746E-08 \pm 2.49E-08$	$8.168E-08 \pm 4.92E-08$
200 MeV	155°	$3.170E-08 \pm 5.30E-08$	$4.866E-08 \pm 1.92E-08$	$3.067E-09 \pm 1.99E-08$	$9.205E-09 \pm 3.36E-08$
225 MeV	155°	$9.561E-09 \pm 9.63E-09$	$3.712E-09 \pm 4.77E-09$	$6.969E-09 \pm 6.17E-09$	$1.155E-08 \pm 1.40E-08$
250 MeV	155°	$4.081E-09 \pm 4.30E-09$	$2.232E-09 \pm 4.12E-08$	$1.563E-09 \pm 1.34E-07$	

Table A.4 Normalized cross sections in mb/sr for the 4.124 MeV, 4.180 MeV, 4.210 MeV and 4.251 MeV levels.

Normalized Cross Sections in mb/sr

		4.262	4.298	4.323	4.358
Energy	**Angle**	4^-	5^-	4^+	4^-
150 MeV	42°		$3.503E-05 \pm 2.03E-05$	$5.746E-03 \pm 3.61E-04$	
187 MeV	40°		$9.875E-05 \pm 7.50E-05$	$7.038E-03 \pm 2.34E-04$	
225 MeV	41°		$1.614E-04 \pm 3.51E-05$	$5.927E-03 \pm 1.03E-04$	
250 MeV	40°		$1.036E-04 \pm 3.41E-05$	$5.188E-03 \pm 1.94E-04$	
280 MeV	40°		$8.598E-05 \pm 9.60E-06$	$1.999E-03 \pm 4.16E-05$	
300 MeV	40°		$3.644E-05 \pm 1.76E-05$	$8.288E-04 \pm 5.49E-05$	
280 MeV	50°		$8.288E-06 \pm 2.25E-06$	$1.430E-04 \pm 5.74E-06$	
300 MeV	55°		$5.472E-06 \pm 2.94E-06$	$1.580E-04 \pm 6.73E-06$	
300 MeV	65°		$4.619E-06 \pm 1.04E-06$	$5.211E-06 \pm 7.38E-07$	
300 MeV	75°		$5.235E-07 \pm 2.70E-07$	$5.449E-06 \pm 5.85E-07$	
280 MeV	100°		$1.141E-10 \pm 1.14E-06$	$4.434E-08 \pm 1.81E-07$	
300 MeV	110°		$6.057E-11 \pm 6.06E-07$	$2.256E-07 \pm 5.06E-07$	
100 MeV	155°	$7.354E-07 \pm 2.86E-07$	$3.684E-07 \pm 1.92E-07$	$2.407E-06 \pm 2.34E-07$	$1.687E-07 \pm 1.71E-07$
125 MeV	155°	$3.489E-07 \pm 8.56E-08$	$2.869E-07 \pm 6.10E-08$	$3.176E-06 \pm 1.12E-07$	$1.628E-07 \pm 9.42E-08$
150 MeV	155°	$2.605E-07 \pm 3.01E-08$	$2.704E-07 \pm 2.49E-08$	$4.290E-07 \pm 2.78E-08$	$1.133E-07 \pm 1.87E-08$
175 MeV	155°	$2.257E-07 \pm 4.90E-08$	$5.523E-08 \pm 2.58E-08$	$1.094E-07 \pm 2.63E-08$	$1.544E-07 \pm 3.26E-08$
200 MeV	155°	$4.000E-08 \pm 2.90E-08$	$5.656E-08 \pm 2.14E-08$	$4.437E-08 \pm 2.39E-08$	$1.172E-07 \pm 2.77E-08$
225 MeV	155°	$3.327E-11 \pm 1.20E-08$	$1.151E-08 \pm 6.74E-09$	$3.989E-09 \pm 1.05E-08$	$3.019E-09 \pm 5.47E-09$
250 MeV	155°	$1.548E-11 \pm 1.55E-07$	$5.334E-09 \pm 3.93E-07$	$8.607E-10 \pm 8.61E-09$	$3.139E-09 \pm 1.15E-06$

Table A.5 Normalised cross sections in mb/sr for the 4.262 MeV, 4.298 MeV, 4.323 MeV and 4.358 MeV levels.

Normalized Cross Sections in mb/sr

		4.383	4.424	4.481	4.610
Energy	Angle	6^-	6^+	6^-	8^+
150 MeV	42°		$2.535E-05 \pm 2.33E-04$		$8.424E-06 \pm 8.42E-05$
187 MeV	40°		$4.485E-04 \pm 8.83E-05$		$1.424E-05 \pm 6.46E-05$
225 MeV	41°		$1.279E-03 \pm 5.51E-05$		
250 MeV	40°		$2.081E-03 \pm 1.04E-04$	$1.813E-07 \pm 2.41E-05$	$4.776E-05 \pm 2.75E-05$
280 MeV	40°	$2.657E-06 \pm 7.26E-06$	$2.098E-03 \pm 4.45E-05$	$4.314E-06 \pm 7.58E-06$	$1.556E-04 \pm 9.50E-06$
300 MeV	40°	$1.702E-05 \pm 1.90E-05$	$2.077E-03 \pm 8.96E-05$	$5.547E-06 \pm 1.94E-05$	$1.352E-04 \pm 2.55E-05$
280 MeV	50°	$1.272E-06 \pm 1.84E-06$	$6.263E-04 \pm 1.31E-05$	$4.250E-08 \pm 2.64E-06$	$1.824E-04 \pm 6.44E-06$
300 MeV	55°	$1.691E-06 \pm 1.84E-06$	$4.427E-05 \pm 3.71E-06$	$2.422E-11 \pm 2.42E-07$	$1.347E-04 \pm 5.76E-06$
300 MeV	65°	$7.191E-07 \pm 3.62E-07$	$1.560E-05 \pm 1.13E-06$	$1.506E-07 \pm 3.15E-07$	$1.157E-05 \pm 9.77E-07$
300 MeV	75°	$1.045E-06 \pm 3.53E-07$	$4.948E-06 \pm 6.74E-07$	$4.722E-11 \pm 1.12E-07$	$7.996E-07 \pm 2.44E-07$
280 MeV	100°	$3.617E-07 \pm 2.51E-07$	$3.090E-07 \pm 1.57E-07$	$1.784E-09 \pm 1.63E-07$	$1.181E-07 \pm 1.12E-07$
300 MeV	110°		$1.557E-08 \pm 6.97E-08$	$1.041E-07 \pm 1.88E-07$	$3.496E-12 \pm 3.50E-11$
100 MeV	155°	$9.462E-07 \pm 2.08E-07$	$1.275E-05 \pm 4.55E-07$	$7.592E-07 \pm 1.97E-07$	$1.290E-06 \pm 2.19E-07$
125 MeV	155°	$6.442E-07 \pm 6.57E-08$	$2.298E-06 \pm 1.01E-07$	$1.697E-07 \pm 5.08E-08$	$2.413E-06 \pm 1.11E-07$
150 MeV	155°	$3.999E-08 \pm 1.45E-08$	$2.672E-07 \pm 2.23E-08$	$2.116E-08 \pm 1.19E-08$	$9.984E-07 \pm 4.41E-08$
175 MeV	155°	$2.989E-07 \pm 3.83E-08$	$2.579E-07 \pm 3.50E-08$	$7.274E-08 \pm 2.75E-08$	$1.648E-08 \pm 2.22E-08$
200 MeV	155°	$1.649E-07 \pm 2.98E-08$	$2.419E-08 \pm 3.25E-08$	$7.663E-08 \pm 2.66E-08$	$2.935E-08 \pm 2.28E-08$
225 MeV	155°	$4.375E-08 \pm 1.15E-08$	$1.157E-08 \pm 2.50E-08$	$7.583E-08 \pm 1.70E-08$	$7.892E-09 \pm 1.13E-08$
250 MeV	155°	$2.620E-09 \pm 2.21E-07$	$3.248E-09 \pm 8.39E-09$	$1.000E-08 \pm 7.92E-09$	$1.338E-09 \pm 3.11E-09$

Table A.6 Normalised cross sections in mb/sr for the 4.383 MeV, 4.424 MeV, 4.481 MeV and 4.610 MeV levels.

Normalized Cross Sections in mb/sr

		4.691	4.707	4.841	4.862
Energy	Angle	3^-	5^-	1^-	8^+
150 MeV	42°	$5.768E-04 \pm 2.24E-04$	$2.101E-04 \pm 8.10E-04$	$8.431E-07 \pm 3.76E-04$	$1.983E-05 \pm 2.27E-04$
187 MeV	40°	$1.179E-03 \pm 1.32E-04$	$5.000E-04 \pm 9.06E-04$	$3.378E-04 \pm 8.09E-05$	$1.158E-04 \pm 6.92E-04$
225 MeV	41°	$1.309E-04 \pm 2.99E-05$	$2.325E-04 \pm 1.01E-05$	$1.368E-04 \pm 2.88E-05$	$3.783E-05 \pm 5.60E-05$
250 MeV	40°	$1.487E-04 \pm 3.99E-05$	$2.258E-04 \pm 4.99E-05$	$2.262E-04 \pm 4.74E-05$	$3.489E-07 \pm 2.65E-05$
280 MeV	40°	$7.482E-05 \pm 9.45E-06$	$1.248E-04 \pm 1.03E-05$	$2.540E-04 \pm 1.21E-05$	$4.912E-06 \pm 6.17E-06$
300 MeV	40°	$3.694E-06 \pm 1.55E-05$	$9.883E-05 \pm 2.43E-05$	$2.250E-04 \pm 2.85E-05$	$1.347E-05 \pm 2.67E-05$
280 MeV	50°	$1.447E-05 \pm 2.79E-06$	$5.971E-06 \pm 2.44E-06$	$4.202E-05 \pm 3.63E-06$	$2.003E-05 \pm 3.00E-06$
300 MeV	55°	$1.187E-08 \pm 1.84E-06$	$2.390E-06 \pm 1.94E-06$	$1.492E-05 \pm 2.82E-06$	$1.628E-05 \pm 3.13E-06$
300 MeV	65°	$1.360E-06 \pm 5.08E-07$	$1.330E-06 \pm 5.09E-07$	$4.141E-06 \pm 8.01E-07$	$6.204E-06 \pm 1.06E-06$
300 MeV	75°	$4.868E-11 \pm 7.90E-08$	$1.201E-07 \pm 1.57E-07$	$1.830E-08 \pm 1.47E-07$	$1.077E-06 \pm 3.40E-07$
280 MeV	100°	$1.124E-11 \pm 5.00E-08$	$2.559E-07 \pm 8.11E-07$	$2.398E-08 \pm 6.82E-08$	$1.490E-08 \pm 6.44E-08$
300 MeV	110°	$6.881E-11 \pm 7.57E-09$	$3.674E-08 \pm 8.07E-07$	$3.544E-08 \pm 2.09E-07$	$4.352E-11 \pm 4.35E-07$
100 MeV	155°	$1.753E-06 \pm 2.39E-07$	$1.331E-07 \pm 2.06E-07$	$1.677E-06 \pm 2.20E-07$	$2.074E-07 \pm 1.84E-07$
125 MeV	155°	$2.083E-07 \pm 5.88E-08$	$2.537E-07 \pm 5.97E-08$	$1.984E-07 \pm 4.49E-08$	$3.359E-07 \pm 5.19E-08$
150 MeV	155°	$1.384E-07 \pm 2.13E-08$	$3.001E-07 \pm 2.65E-08$	$1.575E-07 \pm 1.96E-08$	$3.258E-07 \pm 2.70E-08$
175 MeV	155°	$2.588E-08 \pm 2.59E-08$	$5.498E-08 \pm 2.70E-08$	$1.790E-08 \pm 4.18E-10$	$1.393E-07 \pm 3.34E-09$
200 MeV	155°	$8.212E-08 \pm 2.84E-08$	$1.089E-07 \pm 3.30E-08$	$2.908E-08 \pm 1.96E-08$	$5.300E-08 \pm 2.91E-08$
225 MeV	155°	$1.946E-08 \pm 1.16E-08$	$4.473E-08 \pm 1.46E-08$	$1.650E-11 \pm 5.43E-09$	$1.021E-08 \pm 6.97E-09$
250 MeV	155°	$8.256E-09 \pm 7.13E-09$	$6.213E-09 \pm 8.23E-09$	$4.302E-09 \pm 1.09E-08$	$5.280E-09 \pm 1.04E-08$

Table A.7 Normalised cross sections in mb/sr for the 4.691 MeV, 4.707 MeV, 4.841 MeV and 4.862 MeV levels.

Normalized Cross Sections in mb/sr

		4.895	5.010	5.068	5.084
Energy	**Angle**	10^+	9^+	10^+	8^+
150 MeV	42°				$9.222E-09 \pm 9.22E-03$
187 MeV	40°				$2.889E-05 \pm 7.12E-05$
225 MeV	41°				$5.221E-05 \pm 2.76E-05$
250 MeV	40°				$4.908E-05 \pm 3.13E-05$
280 MeV	40°	$6.012E-06 \pm 5.08E-06$	$5.823E-06 \pm 5.36E-06$	$1.512E-05 \pm 5.88E-06$	$6.082E-05 \pm 8.16E-06$
300 MeV	40°	$4.343E-07 \pm 1.38E-05$	$3.471E-07 \pm 1.30E-05$	$6.855E-06 \pm 1.48E-05$	$5.195E-05 \pm 2.27E-05$
280 MeV	50°	$1.298E-05 \pm 2.46E-06$	$2.620E-06 \pm 1.73E-06$	$1.541E-05 \pm 2.66E-06$	$5.318E-05 \pm 4.85E-06$
300 MeV	55°	$1.629E-05 \pm 2.71E-06$	$8.999E-07 \pm 1.49E-06$	$2.182E-05 \pm 3.69E-06$	$4.456E-05 \pm 5.42E-06$
300 MeV	65°	$1.507E-05 \pm 1.85E-06$	$2.572E-12 \pm 2.20E-08$	$1.484E-05 \pm 1.85E-06$	$8.359E-06 \pm 2.33E-06$
300 MeV	75°	$9.487E-06 \pm 1.12E-06$	$2.991E-07 \pm 2.61E-07$	$7.556E-06 \pm 1.28E-06$	$3.552E-06 \pm 1.39E-06$
280 MeV	100°	$3.616E-07 \pm 1.39E-07$	$1.278E-07 \pm 1.07E-07$	$4.372E-07 \pm 1.83E-07$	$2.222E-07 \pm 1.92E-07$
300 MeV	110°	$7.933E-08 \pm 1.87E-07$	$4.340E-11 \pm 4.34E-07$	$3.423E-08 \pm 2.97E-07$	$2.014E-08 \pm 1.25E-07$
100 MeV	155°		$8.454E-07 \pm 1.90E-07$		$6.399E-08 \pm 2.36E-06$
125 MeV	155°	$2.824E-07 \pm 4.93E-08$	$2.641E-07 \pm 4.90E-08$	$3.282E-07 \pm 6.12E-08$	$6.299E-07 \pm 8.68E-08$
150 MeV	155°	$4.930E-07 \pm 3.44E-08$	$6.803E-08 \pm 1.62E-08$	$1.074E-06 \pm 7.71E-08$	$6.357E-07 \pm 1.05E-07$
175 MeV	155°	$5.634E-07 \pm 4.91E-08$	$1.508E-07 \pm 3.88E-09$	$8.292E-07 \pm 6.91E-08$	$2.343E-07 \pm 6.42E-08$
200 MeV	155°	$3.115E-07 \pm 5.01E-08$	$2.272E-07 \pm 4.14E-08$	$5.057E-07 \pm 6.98E-08$	$1.287E-11 \pm 2.74E-08$
225 MeV	155°	$7.765E-08 \pm 1.66E-08$	$4.526E-08 \pm 1.30E-08$	$5.458E-08 \pm 2.02E-08$	$1.261E-07 \pm 3.26E-08$
250 MeV	155°	$2.274E-08 \pm 1.61E-08$	$4.238E-09 \pm 8.12E-09$	$4.132E-08 \pm 2.62E-08$	$7.655E-09 \pm 1.01E-07$

Table A.8 Normalised cross sections in mb/sr for the 4.895 MeV, 5.010 MeV, 5.068 MeV and 5.084 MeV levels.

Normalized Cross Sections in mb/sr

		5.213	5.242	5.260	5.291
Energy	**Angle**	5^-	3^-	9^+	11^+
150 MeV	42°	$2.490E-04 \pm 2.08E-04$	$2.398E-03 \pm 2.73E-04$		
187 MeV	40°	$1.102E-03 \pm 1.20E-04$	$2.292E-03 \pm 1.87E-04$		
225 MeV	41°	$9.632E-04 \pm 5.16E-05$	$1.005E-03 \pm 5.76E-05$		
250 MeV	40°	$1.025E-03 \pm 1.56E-04$	$7.868E-04 \pm 1.27E-04$		
280 MeV	40°	$6.301E-04 \pm 2.14E-05$	$3.057E-04 \pm 1.37E-05$		
300 MeV	40°	$3.584E-04 \pm 4.09E-05$	$1.956E-04 \pm 3.62E-05$		
280 MeV	50°	$9.656E-05 \pm 5.44E-04$	$3.928E-05 \pm 3.74E-06$		
300 MeV	55°	$2.472E-05 \pm 3.63E-06$	$8.372E-06 \pm 2.60E-06$		
300 MeV	65°	$1.494E-06 \pm 4.86E-07$	$2.415E-06 \pm 6.59E-07$		
300 MeV	75°	$1.894E-06 \pm 4.33E-07$	$1.326E-06 \pm 4.74E-07$		
280 MeV	100°	$9.768E-08 \pm 1.14E-07$	$2.690E-07 \pm 1.51E-07$		
300 MeV	110°	$7.468E-08 \pm 3.81E-07$	$6.365E-08 \pm 9.78E-08$		
100 MeV	155°	$2.182E-06 \pm 2.75E-07$	$1.069E-06 \pm 2.43E-07$	$4.341E-07 \pm 2.08E-07$	$1.595E-07 \pm 1.71E-07$
125 MeV	155°	$1.528E-06 \pm 8.39E-08$	$6.633E-07 \pm 7.23E-08$	$3.332E-07 \pm 6.15E-08$	$2.630E-07 \pm 5.12E-08$
150 MeV	155°	$3.115E-07 \pm 2.70E-08$	$4.652E-07 \pm 3.57E-08$	$2.995E-07 \pm 4.62E-08$	$2.997E-07 \pm 3.85E-08$
175 MeV	155°	$4.622E-07 \pm 4.45E-08$	$1.947E-07 \pm 1.92E-08$	$1.241E-07 \pm 3.44E-08$	$1.003E-07 \pm 2.86E-08$
200 MeV	155°	$4.493E-07 \pm 5.56E-08$	$1.403E-07 \pm 4.83E-08$	$6.489E-08 \pm 1.33E-08$	$7.158E-08 \pm 1.48E-08$
225 MeV	155°	$8.099E-08 \pm 1.82E-08$	$1.943E-07 \pm 2.92E-08$	$2.918E-11 \pm 2.05E-08$	$5.483E-08 \pm 1.73E-08$
250 MeV	155°	$2.643E-08 \pm 1.21E-08$	$2.277E-08 \pm 1.22E-08$	$1.631E-08 \pm 1.37E-08$	$1.675E-08 \pm 9.74E-09$

Table A.9 Normalised cross sections in mb/sr for the 5.213 MeV, 5.242 MeV, 5.260 MeV and 5.291 MeV levels.

Normalized Cross Sections in mb/sr

		5.346	5.481	5.514	5.656
Energy	Angle	3^-	5^-	3^-	5^-
150 MeV	42°	$3.278E-03 \pm 2.98E-04$	$4.134E-08 \pm 4.13E-01$	$1.619E-03 \pm 2.54E-04$	$6.322E-06 \pm 1.55E-04$
187 MeV	40°	$2.853E-03 \pm 2.09E-04$	$2.040E-04 \pm 7.24E-05$	$1.015E-03 \pm 1.17E-04$	$1.162E-04 \pm 7.37E-05$
225 MeV	41°	$1.171E-03 \pm 5.75E-05$	$1.793E-04 \pm 3.06E-05$	$4.671E-04 \pm 3.92E-05$	$1.269E-04 \pm 2.79E-05$
250 MeV	40°	$7.209E-04 \pm 1.14E-04$	$2.943E-04 \pm 5.50E-05$	$3.011E-04 \pm 5.77E-05$	
280 MeV	40°	$1.652E-04 \pm 9.61E-06$	$1.599E-04 \pm 9.45E-06$	$1.953E-04 \pm 1.07E-05$	$8.050E-05 \pm 8.36E-06$
300 MeV	40°	$7.201E-05 \pm 2.04E-05$	$1.064E-04 \pm 2.27E-05$	$1.682E-04 \pm 2.90E-05$	$3.066E-05 \pm 1.89E-05$
280 MeV	50°	$8.223E-05 \pm 4.78E-06$	$1.070E-05 \pm 2.16E-06$	$4.760E-05 \pm 3.75E-06$	$1.766E-05 \pm 2.81E-06$
300 MeV	55°	$2.827E-05 \pm 3.69E-06$	$7.135E-06 \pm 1.90E-06$	$2.190E-05 \pm 3.22E-06$	$6.441E-06 \pm 2.09E-06$
300 MeV	65°	$2.267E-06 \pm 5.57E-07$	$3.178E-06 \pm 6.28E-07$	$2.252E-06 \pm 5.66E-07$	$1.211E-06 \pm 4.87E-07$
300 MeV	75°	$1.220E-06 \pm 3.43E-07$	$6.396E-07 \pm 2.52E-07$	$1.352E-06 \pm 4.47E-07$	$1.914E-07 \pm 2.51E-07$
280 MeV	100°	$9.373E-08 \pm 9.32E-08$	$8.211E-08 \pm 9.82E-08$	$2.312E-07 \pm 1.48E-07$	$1.779E-07 \pm 1.13E-07$
300 MeV	110°	$4.438E-11 \pm 4.44E-07$	$4.312E-11 \pm 4.31E-07$		$7.449E-08 \pm 5.15E-07$
100 MeV	155°	$7.462E-07 \pm 1.99E-07$	$1.616E-06 \pm 2.13E-07$	$2.408E-06 \pm 2.89E-07$	$1.676E-06 \pm 2.15E-07$
125 MeV	155°	$9.874E-07 \pm 7.05E-08$	$4.991E-07 \pm 5.49E-08$	$2.046E-07 \pm 4.91E-08$	$2.789E-07 \pm 5.56E-08$
150 MeV	155°	$3.554E-07 \pm 2.85E-08$	$2.517E-07 \pm 2.30E-08$	$1.938E-07 \pm 4.05E-08$	$1.799E-07 \pm 2.41E-08$
175 MeV	155°	$2.611E-07 \pm 1.30E-08$	$7.587E-08 \pm 3.56E-09$	$1.017E-07 \pm 7.02E-08$	$4.180E-07 \pm 6.14E-08$
200 MeV	155°	$8.045E-08 \pm 2.93E-08$	$2.168E-08 \pm 1.54E-08$	$2.197E-07 \pm 5.88E-06$	$1.378E-07 \pm 3.57E-08$
225 MeV	155°	$1.073E-08 \pm 1.03E-08$	$4.857E-08 \pm 1.35E-08$	$2.897E-08 \pm 2.59E-08$	$5.039E-08 \pm 1.77E-08$
250 MeV	155°	$1.163E-08 \pm 1.09E-08$	$8.882E-09 \pm 1.31E-08$	$4.148E-08 \pm 2.43E-08$	

Table A.10 Normalised cross sections in mb/sr for the 5.346 MeV, 5.481 MeV, 5.514 MeV and 5.656 MeV levels.

Normalized Cross Sections in mb/sr

Energy	Angle	5.685 4^+	5.715 2^+	5.813 3^-	5.860 11^+
150 MeV	42°	$1.370E-03 \pm 9.30E-05$	$9.504E-04 \pm 2.25E-05$	$3.293E-05 \pm 1.72E-04$	
187 MeV	40°	$1.685E-03 \pm 1.53E-04$	$5.136E-04 \pm 9.70E-05$	$1.558E-04 \pm 7.21E-05$	
225 MeV	41°	$1.515E-03 \pm 6.56E-05$	$3.027E-04 \pm 8.83E-06$	$1.714E-04 \pm 2.75E-05$	
250 MeV	40°	$9.218E-04 \pm 1.43E-04$	$2.725E-04 \pm 6.08E-05$	$1.112E-04 \pm 3.53E-05$	
280 MeV	40°	$3.807E-04 \pm 1.52E-05$	$1.691E-04 \pm 1.01E-05$	$5.285E-05 \pm 6.73E-06$	
300 MeV	40°	$2.028E-04 \pm 1.17E-05$	$1.264E-04 \pm 2.45E-05$	$4.224E-08 \pm 1.24E-05$	
280 MeV	50°	$7.466E-05 \pm 4.62E-06$	$4.543E-05 \pm 3.75E-06$	$3.784E-06 \pm 1.81E-06$	
300 MeV	55°	$4.766E-05 \pm 5.03E-06$	$6.794E-06 \pm 2.08E-06$	$7.201E-06 \pm 1.68E-06$	
300 MeV	65°	$2.298E-06 \pm 6.63E-07$	$1.972E-06 \pm 5.19E-07$	$8.273E-07 \pm 3.42E-07$	
300 MeV	75°	$2.371E-06 \pm 4.69E-07$	$1.281E-06 \pm 3.61E-07$	$4.378E-07 \pm 2.04E-07$	
280 MeV	100°	$2.218E-07 \pm 1.14E-07$	$2.971E-07 \pm 1.27E-07$	$4.202E-07 \pm 1.40E-07$	
300 MeV	110°	$1.777E-08 \pm 2.52E-08$	$4.359E-08 \pm 3.22E-08$	$1.511E-07 \pm 7.77E-08$	
100 MeV	155°	$2.252E-06 \pm 2.39E-07$	$1.636E-06 \pm 2.65E-07$	$1.348E-06 \pm 2.23E-07$	
125 MeV	155°	$1.600E-06 \pm 8.32E-08$	$5.123E-07 \pm 6.95E-08$	$1.131E-07 \pm 4.84E-08$	$1.165E-08 \pm 9.56E-09$
150 MeV	155°	$1.400E-07 \pm 1.93E-08$	$1.359E-07 \pm 2.19E-08$	$1.688E-07 \pm 2.29E-08$	$6.809E-08 \pm 1.52E-08$
175 MeV	155°	$5.056E-07 \pm 5.97E-08$	$8.075E-08 \pm 4.90E-08$	$9.031E-08 \pm 4.73E-08$	$1.486E-07 \pm 4.20E-08$
200 MeV	155°	$1.625E-07 \pm 3.24E-08$	$7.023E-08 \pm 3.01E-08$	$1.135E-07 \pm 3.14E-08$	$1.959E-07 \pm 3.23E-08$
225 MeV	155°	$2.107E-08 \pm 1.21E-08$	$1.509E-08 \pm 1.24E-08$	$2.641E-08 \pm 1.65E-08$	$1.287E-07 \pm 2.99E-08$
250 MeV	155°	$5.712E-10 \pm 3.08E-09$	$2.513E-09 \pm 3.97E-09$		

Table A.11 Normalised cross sections in mb/sr for the 5.685 MeV, 5.715 MeV, 5.813 MeV and 5.860 MeV levels.

Normalized Cross Sections in mb/sr

		5.928	5.954	5.997	6.089
Energy	**Angle**	10^+	9^+	6^+	8^+
150 MeV	42°			$2.536E-04 \pm 9.95E-06$	$3.872E-06 \pm 1.66E-04$
187 MeV	40°			$8.257E-04 \pm 1.21E-04$	$5.951E-05 \pm 6.61E-05$
225 MeV	41°			$1.180E-03 \pm 5.73E-05$	$4.102E-08 \pm 2.46E-05$
250 MeV	40°			$1.694E-03 \pm 2.54E-04$	$7.261E-09 \pm 4.84E-05$
280 MeV	40°			$1.330E-03 \pm 3.99E-05$	$3.678E-05 \pm 7.15E-06$
300 MeV	40°			$9.756E-04 \pm 7.43E-05$	$3.326E-05 \pm 2.07E-05$
280 MeV	50°			$2.051E-04 \pm 9.57E-06$	$3.737E-05 \pm 3.55E-06$
300 MeV	55°	$4.206E-06 \pm 1.35E-06$		$7.040E-06 \pm 2.43E-06$	$9.890E-06 \pm 2.68E-06$
300 MeV	65°	$3.760E-06 \pm 6.48E-07$		$2.080E-06 \pm 1.07E-06$	$1.423E-06 \pm 4.79E-07$
300 MeV	75°	$2.842E-06 \pm 4.70E-07$		$1.043E-06 \pm 3.09E-07$	$2.169E-06 \pm 4.47E-07$
280 MeV	100°	$6.656E-07 \pm 1.62E-07$		$2.137E-07 \pm 1.05E-07$	$4.612E-07 \pm 1.33E-07$
300 MeV	110°	$6.220E-08 \pm 3.71E-08$		$1.995E-08 \pm 2.81E-08$	$7.501E-08 \pm 5.02E-08$
100 MeV	155°		$1.175E-07 \pm 2.19E-08$	$7.307E-06 \pm 4.32E-06$	$2.149E-06 \pm 4.21E-06$
125 MeV	155°	$2.517E-07 \pm 4.95E-08$	$1.484E-07 \pm 4.49E-08$	$4.272E-07 \pm 6.35E-08$	$9.710E-07 \pm 8.66E-08$
150 MeV	155°	$8.865E-07 \pm 9.74E-08$	$1.832E-07 \pm 2.42E-08$	$2.704E-07 \pm 2.82E-08$	$2.163E-07 \pm 2.98E-08$
175 MeV	155°	$1.619E-06 \pm 2.87E-07$	$6.698E-07 \pm 7.64E-08$	$3.579E-07 \pm 6.82E-08$	$3.514E-07 \pm 7.36E-08$
200 MeV	155°	$5.496E-07 \pm 6.04E-08$	$3.707E-07 \pm 5.48E-08$	$1.708E-07 \pm 4.60E-08$	$2.586E-07 \pm 5.06E-08$
225 MeV	155°	$2.118E-07 \pm 4.33E-08$	$1.243E-07 \pm 3.22E-08$	$6.147E-08 \pm 2.20E-08$	$1.678E-07 \pm 4.08E-08$
250 MeV	155°			$2.271E-09 \pm 4.51E-09$	
280 MeV	155°	$7.341E-08 \pm 6.60E-08$		$8.042E-09 \pm 4.90E-09$	

Table A.12 Normalised cross sections in mb/sr for the 5.928 MeV, 5.954 MeV, 5.997 MeV and 6.089 MeV levels.

Normalized Cross Sections in mb/sr

Energy	Angle	6.110 12^+	6.283 10^-	6.437 12^-	6.745 14^-
150 MeV	42°				
187 MeV	40°				
225 MeV	41°				
250 MeV	40°				
280 MeV	40°				
300 MeV	40°				
280 MeV	50°				
300 MeV	55°	$1.302E-06 \pm 1.45E-06$			
300 MeV	65°	$3.974E-07 \pm 3.51E-07$			
300 MeV	75°				$7.731E-07 \pm 3.07E-07$
280 MeV	100°	$8.429E-07 \pm 2.06E-07$			$1.194E-06 \pm 3.88E-07$
300 MeV	110°	$2.636E-07 \pm 8.79E-08$			$3.856E-07 \pm 3.72E-07$
100 MeV	155°		$1.000E-07 \pm 2.22E-07$		
125 MeV	155°		$6.386E-07 \pm 8.35E-08$	$8.003E-12 \pm 3.50E-08$	$1.258E-07 \pm 1.07E-06$
150 MeV	155°	$1.885E-07 \pm 2.43E-08$	$4.232E-07 \pm 5.82E-08$	$4.418E-07 \pm 4.63E-08$	$3.918E-07 \pm 8.03E-06$
175 MeV	155°	$8.189E-07 \pm 7.88E-08$	$1.712E-07 \pm 3.73E-08$	$5.232E-07 \pm 5.00E-08$	$5.227E-07 \pm 9.54E-08$
200 MeV	155°	$6.036E-07 \pm 6.04E-08$	$4.589E-08 \pm 7.71E-08$	$4.353E-07 \pm 5.56E-08$	$8.076E-07 \pm 1.33E-07$
225 MeV	155°	$3.777E-07 \pm 6.76E-08$	$3.831E-11 \pm 1.29E-08$	$1.465E-07 \pm 3.47E-08$	$8.398E-07 \pm 1.69E-07$
250 MeV	155°	$4.951E-08 \pm 1.31E-08$	$5.718E-09 \pm 8.69E-09$	$5.596E-09 \pm 2.46E-08$	$5.898E-07 \pm 7.66E-08$
280 MeV	155°	$1.905E-08 \pm 8.53E-09$		$1.745E-08 \pm 1.62E-08$	$7.333E-08 \pm 5.15E-08$

Table A.13 Normalised cross sections in mb/sr for the 6.110 MeV, 6.283 MeV, 6.437 MeV and 6.745 MeV levels.

Normalized Cross Sections in mb/sr

Energy	Angle	6.833 8^-	6.859 9^-	6.879 7^-	6.884 10^-
150 MeV	42°				
187 MeV	40°			$4.836E-05 \pm 7.78E-05$	
225 MeV	41°				
250 MeV	40°	$8.107E-08 \pm 3.58E-05$	$3.123E-07 \pm 2.87E-05$	$4.284E-05 \pm 3.18E-05$	
280 MeV	40°	$1.487E-05 \pm 6.98E-06$	$2.535E-06 \pm 6.45E-06$	$8.817E-05 \pm 8.64E-06$	
300 MeV	40°	$1.203E-05 \pm 1.62E-05$	$4.283E-06 \pm 1.51E-05$	$1.116E-04 \pm 2.49E-05$	
280 MeV	50°	$1.043E-05 \pm 3.39E-06$	$1.424E-05 \pm 3.24E-06$	$6.721E-05 \pm 5.04E-06$	
300 MeV	55°	$9.461E-06 \pm 2.42E-06$	$2.158E-05 \pm 3.67E-06$	$2.716E-05 \pm 4.16E-06$	
300 MeV	65°	$3.936E-06 \pm 8.72E-07$	$1.057E-05 \pm 1.52E-06$	$4.182E-06 \pm 1.01E-06$	
300 MeV	75°	$1.247E-06 \pm 5.12E-07$	$3.462E-06 \pm 6.36E-07$	$2.684E-07 \pm 3.70E-07$	
280 MeV	100°	$4.240E-07 \pm 1.64E-07$	$2.828E-07 \pm 1.48E-07$	$3.362E-07 \pm 1.55E-07$	
300 MeV	110°		$8.444E-09 \pm 2.83E-08$	$5.698E-09 \pm 2.41E-08$	
100 MeV	155°				$4.307E-07 \pm 2.89E-07$
125 MeV	155°	$7.639E-07 \pm 1.01E-07$			$1.958E-06 \pm 1.51E-07$
150 MeV	155°	$5.678E-07 \pm 6.96E-08$			$1.656E-06 \pm 1.17E-07$
175 MeV	155°	$2.033E-07 \pm 5.01E-08$			$8.175E-07 \pm 9.04E-08$
200 MeV	155°	$3.435E-07 \pm 6.65E-08$			$3.771E-07 \pm 6.91E-08$
225 MeV	155°	$1.648E-08 \pm 2.75E-08$			$2.767E-08 \pm 2.77E-08$
250 MeV	155°	$5.738E-09 \pm 2.00E-08$			$1.885E-08 \pm 2.01E-08$

Table A.14 Normalised cross sections in mb/sr for the 6.833 MeV, 6.859 MeV, 6.879 MeV and 6.884 MeV levels.

Normalized Cross Sections in mb/sr

Energy	Angle	7.064 12^-	7.086 $(12^-),(10^-)$
300 MeV	65°	$1.590E-06 \pm 6.94E-07$	
300 MeV	75°	$1.963E-06 \pm 9.25E-07$	
280 MeV	100°	$8.544E-07 \pm 5.06E-07$	
300 MeV	110°	$2.934E-08 \pm 3.14E-08$	
125 MeV	155°	$1.569E-07 \pm 6.92E-08$	$2.795E-07 \pm 3.79E-08$
150 MeV	155°	$1.280E-06 \pm 8.20E-08$	$7.558E-07 \pm 1.56E-07$
175 MeV	155°	$1.489E-06 \pm 1.02E-07$	$6.996E-07 \pm 1.07E-07$
200 MeV	155°	$1.290E-06 \pm 8.71E-08$	$8.143E-07 \pm 8.87E-08$
225 MeV	155°	$8.600E-07 \pm 1.46E-07$	$2.455E-07 \pm 1.19E-07$
250 MeV	155°	$1.046E-07 \pm 3.66E-08$	$3.655E-08 \pm 2.40E-08$
280 MeV	155°	$5.757E-08 \pm 4.76E-08$	

Table A.15 Normalised cross sections in mb/sr for the 7.064 MeV and 7.086 MeV levels.

Appendix B

Tables of Cross Sections

Cross sections from excitations for which cross sections were measured but were not analyzed any further are given in this appendix. Assignments of spin and multipolarity are taken from Nuclear Data Sheets (1986)[1] .

Normalized Cross Sections in mb/sr

		3.997	4.230	4.447	4.738
Energy	Angle	$(5)^-$	2^-	(5^-)	
100 MeV	155°	$8.811E-08 \pm 1.36E-07$	$1.545E-07 \pm 1.80E-07$	$1.859E-07 \pm 4.63E-07$	$1.028E-07 \pm 1.60E-07$
125 MeV	155°	$4.709E-08 \pm 3.30E-08$	$1.795E-11 \pm 4.82E-08$	$1.798E-11 \pm 6.21E-08$	$6.191E-08 \pm 3.91E-08$
150 MeV	155°	$4.191E-08 \pm 1.28E-08$	$2.980E-08 \pm 1.37E-08$	$1.216E-08 \pm 1.39E-08$	$1.175E-07 \pm 2.77E-08$
175 MeV	155°	$2.271E-08 \pm 2.14E-08$	$2.807E-11 \pm 2.88E-08$	$1.236E-07 \pm 3.42E-08$	$3.113E-08 \pm 2.04E-08$
200 MeV	155°	$2.093E-08 \pm 1.49E-08$	$3.199E-08 \pm 2.31E-08$	$1.092E-07 \pm 5.85E-08$	$7.284E-08 \pm 2.35E-08$
225 MeV	155°	$5.416E-09 \pm 4.98E-09$	$2.799E-09 \pm 6.92E-09$	$1.747E-08 \pm 8.57E-09$	$3.914E-09 \pm 8.27E-09$
250 MeV	155°	$3.463E-09 \pm 5.63E-09$	$3.779E-10 \pm 3.78E-06$	$8.837E-10 \pm 1.70E-08$	$6.520E-09 \pm 1.05E-08$

Table B.1 Normalised cross sections in mb/sr for the 3.997 MeV, 4.230 MeV, 4.447 MeV and 4.738 MeV levels.

Normalized Cross Sections in mb/sr

Energy	Angle	4.762 (7^-)	4.918 $J > 6$	4.935 3^-	4.975
150 MeV	42°			$1.153E-06 \pm 3.14E-04$	$8.149E-07 \pm 3.85E-04$
187 MeV	40°			$1.325E-04 \pm 6.87E-05$	$2.206E-04 \pm 8.32E-05$
225 MeV	41°			$1.961E-05 \pm 2.35E-05$	$1.049E-04 \pm 3.04E-05$
250 MeV	40°			$1.109E-04 \pm 3.22E-05$	$1.090E-04 \pm 3.81E-05$
280 MeV	40°			$2.356E-05 \pm 5.57E-06$	$1.382E-05 \pm 6.72E-06$
300 MeV	40°			$3.273E-05 \pm 1.76E-05$	$3.017E-05 \pm 2.18E-05$
280 MeV	50°			$9.090E-06 \pm 2.16E-06$	$2.411E-10 \pm 2.41E-06$
300 MeV	55°			$2.167E-08 \pm 1.28E-06$	$1.874E-06 \pm 2.23E-06$
300 MeV	65°			$1.486E-06 \pm 5.11E-07$	$1.833E-07 \pm 4.54E-07$
300 MeV	75°			$6.666E-07 \pm 3.56E-07$	$4.713E-11 \pm 2.12E-07$
280 MeV	100°			$4.096E-07 \pm 1.52E-07$	$6.201E-08 \pm 1.28E-07$
300 MeV	110°			$3.726E-08 \pm 5.80E-08$	$1.334E-08 \pm 4.99E-07$
100 MeV	155°	$4.550E-07 \pm 1.69E-07$	$1.121E-06 \pm 2.47E-07$	$6.536E-07 \pm 2.20E-07$	$5.576E-07 \pm 2.49E-07$
125 MeV	155°	$1.673E-10 \pm 3.46E-08$	$1.373E-07 \pm 5.20E-08$	$4.849E-07 \pm 5.91E-08$	$2.452E-07 \pm 6.46E-08$
150 MeV	155°	$9.072E-08 \pm 2.40E-08$	$2.615E-07 \pm 4.79E-08$	$2.061E-07 \pm 3.92E-08$	$1.806E-07 \pm 4.06E-08$
175 MeV	155°	$9.268E-08 \pm 2.38E-08$	$1.190E-07 \pm 3.83E-08$	$1.575E-07 \pm 3.43E-08$	$6.968E-08 \pm 3.45E-08$
200 MeV	155°	$5.826E-08 \pm 2.01E-08$	$4.393E-08 \pm 3.45E-08$	$1.538E-07 \pm 3.44E-08$	$5.031E-08 \pm 3.31E-08$
225 MeV	155°	$1.388E-08 \pm 8.25E-09$	$8.063E-08 \pm 2.34E-08$	$1.975E-08 \pm 1.67E-08$	$2.091E-09 \pm 9.71E-09$
250 MeV	155°	$1.363E-09 \pm 8.07E-07$	$1.787E-08 \pm 1.95E-08$	$2.119E-08 \pm 2.08E-08$	$1.107E-08 \pm 1.12E-08$

Table B.2 Normalised cross sections in mb/sr for the 4.762 MeV, 4.918 MeV, 4.935 MeV and 4.975 MeV levels.

Normalized Cross Sections in mb/sr

Energy	Angle	4.987 $J > 8$	5.099	5.128 $(2, 3^-)$	5.190 (3^-)
150 MeV	42°		$2.454E-08 \pm 2.45E-08$	$2.445E-08 \pm 2.45E-08$	$9.204E-09 \pm 9.20E-09$
187 MeV	40°		$2.919E-04 \pm 8.34E-05$	$1.440E-04 \pm 7.12E-05$	$2.503E-04 \pm 7.52E-05$
225 MeV	41°		$1.641E-05 \pm 2.52E-05$	$5.721E-05 \pm 2.46E-05$	$3.504E-06 \pm 2.57E-05$
250 MeV	40°		$2.722E-05 \pm 2.65E-05$	$3.598E-05 \pm 2.42E-05$	$5.418E-10 \pm 2.21E-06$
280 MeV	40°		$2.822E-05 \pm 6.69E-06$	$1.239E-05 \pm 4.90E-06$	$5.244E-05 \pm 7.19E-06$
300 MeV	40°		$3.428E-05 \pm 2.14E-05$	$4.601E-08 \pm 1.70E-05$	$1.497E-06 \pm 1.72E-05$
280 MeV	50°		$3.105E-06 \pm 3.26E-06$	$2.547E-06 \pm 1.76E-06$	$1.284E-05 \pm 2.69E-06$
300 MeV	55°		$1.644E-06 \pm 2.21E-06$	$6.203E-07 \pm 1.45E-06$	$6.659E-06 \pm 2.14E-06$
300 MeV	65°		$3.649E-06 \pm 2.00E-06$	$1.021E-06 \pm 5.57E-07$	$5.832E-07 \pm 3.78E-07$
300 MeV	75°		$5.755E-10 \pm 6.75E-07$	$3.693E-07 \pm 3.01E-07$	$4.689E-11 \pm 1.06E-07$
280 MeV	100°		$4.772E-09 \pm 1.30E-07$	$3.458E-07 \pm 1.42E-07$	$3.002E-07 \pm 1.39E-07$
300 MeV	110°		$4.855E-08 \pm 1.76E-07$	$4.948E-08 \pm 9.98E-08$	$4.379E-11 \pm 4.38E-07$
100 MeV	155°	$1.227E-09 \pm 2.65E-07$	$2.845E-07 \pm 2.14E-07$	$3.508E-06 \pm 2.74E-07$	$7.272E-06 \pm 3.25E-07$
125 MeV	155°	$1.563E-11 \pm 6.05E-08$	$4.241E-07 \pm 7.11E-08$	$9.952E-08 \pm 4.46E-08$	$1.113E-06 \pm 6.65E-08$
150 MeV	155°	$1.414E-07 \pm 4.25E-08$	$5.373E-07 \pm 7.28E-08$	$6.990E-08 \pm 2.56E-08$	$4.179E-07 \pm 2.88E-08$
175 MeV	155°	$1.061E-07 \pm 3.77E-08$	$2.288E-07 \pm 4.90E-08$	$1.065E-07 \pm 2.77E-08$	$5.008E-08 \pm 2.31E-08$
200 MeV	155°	$3.755E-08 \pm 3.74E-08$	$1.989E-07 \pm 4.50E-08$	$1.788E-07 \pm 3.62E-08$	$8.323E-08 \pm 2.55E-08$
225 MeV	155°	$1.387E-08 \pm 1.26E-08$	$4.847E-09 \pm 2.14E-08$	$2.136E-08 \pm 1.18E-08$	$9.945E-10 \pm 6.27E-09$
250 MeV	155°	$1.677E-08 \pm 1.79E-08$	$1.064E-08 \pm 3.10E-08$	$5.381E-10 \pm 4.26E-08$	$5.736E-09 \pm 3.54E-09$

Table B.3 Normalised cross sections in mb/sr for the 4.987 MeV, 5.099 MeV, 5.128 MeV and 5.190 MeV levels.

Normalized Cross Sections in mb/sr

Energy	Angle	5.314 $(1,2^+)$	5.370 5^-	5.389 (2^-)	5.415 $(6^+,7^-)$
150 MeV	42°	$9.194E-09 \pm 9.19E-09$			
187 MeV	40°	$6.753E-05 \pm 6.98E-05$	$1.286E-04 \pm 7.87E-05$		
225 MeV	41°	$2.379E-05 \pm 2.51E-05$	$1.047E-04 \pm 3.10E-05$		
250 MeV	40°	$8.372E-06 \pm 2.62E-05$	$5.417E-10 \pm 3.01E-06$		
280 MeV	40°	$3.137E-05 \pm 6.19E-06$			
300 MeV	40°	$1.034E-08 \pm 1.49E-05$	$1.451E-05 \pm 1.51E-05$		
280 MeV	50°	$5.896E-09 \pm 1.78E-06$	$1.856E-06 \pm 1.62E-06$		
300 MeV	55°	$2.713E-06 \pm 1.77E-06$	$1.654E-06 \pm 1.75E-06$		
300 MeV	65°	$1.060E-06 \pm 4.79E-07$	$1.122E-06 \pm 4.42E-07$		
300 MeV	75°	$3.470E-08 \pm 2.08E-07$	$2.745E-08 \pm 2.32E-07$		
280 MeV	100°	$1.075E-07 \pm 9.63E-08$	$1.094E-10 \pm 7.77E-08$		
300 MeV	110°	$4.398E-11 \pm 4.40E-07$	$3.727E-08 \pm 1.02E-06$		
100 MeV	155°	$7.462E-07 \pm 1.99E-07$	$1.616E-06 \pm 2.13E-07$	$7.001E-07 \pm 2.04E-07$	$3.134E-07 \pm 1.70E-07$
125 MeV	155°	$9.874E-07 \pm 7.05E-08$	$4.991E-07 \pm 5.49E-08$	$9.455E-08 \pm 4.79E-08$	$2.228E-07 \pm 4.58E-08$
150 MeV	155°	$3.554E-07 \pm 2.85E-08$	$2.517E-07 \pm 2.30E-08$	$1.946E-07 \pm 3.60E-08$	$1.072E-07 \pm 2.71E-08$
175 MeV	155°	$2.611E-07 \pm 1.30E-08$	$7.587E-08 \pm 3.56E-09$	$1.271E-07 \pm 3.26E-08$	$6.921E-08 \pm 2.58E-08$
200 MeV	155°	$8.045E-08 \pm 2.93E-08$	$2.168E-08 \pm 1.54E-08$	$5.545E-08 \pm 2.38E-08$	$2.336E-08 \pm 1.69E-08$
225 MeV	155°	$1.073E-08 \pm 1.03E-08$	$4.857E-08 \pm 1.35E-08$	$9.292E-09 \pm 1.03E-08$	$1.616E-08 \pm 1.04E-08$
250 MeV	155°	$1.163E-08 \pm 1.09E-08$	$8.882E-09 \pm 1.31E-08$	$2.179E-09 \pm 1.46E-06$	$3.784E-11 \pm 3.78E-07$

Table B.4 Normalised cross sections in mb/sr for the 5.314 MeV, 5.370 MeV, 5.389 MeV and 5.415 MeV levels.

Normalized Cross Sections in mb/sr

		5.453	5.537	5.547	5.564
Energy	**Angle**	$J > 6$	10^+	7^-	$(3,4^-)$
150 MeV	42°		$3.633E-07 \pm 4.92E-04$		$1.770E-04 \pm 2.06E-04$
187 MeV	40°		$1.518E-04 \pm 1.50E-04$		$8.342E-04 \pm 1.06E-04$
225 MeV	41°		$1.272E-06 \pm 6.85E-05$		$4.166E-04 \pm 3.82E-05$
250 MeV	40°		$5.403E-10 \pm 5.40E-06$		$2.739E-04 \pm 5.58E-05$
280 MeV	40°		$2.578E-04 \pm 1.31E-05$		$1.354E-04 \pm 1.05E-05$
300 MeV	40°		$1.999E-04 \pm 3.30E-05$		$8.343E-05 \pm 2.53E-05$
280 MeV	50°		$1.100E-04 \pm 6.01E-06$		$1.290E-05 \pm 3.19E-06$
300 MeV	55°		$1.461E-05 \pm 2.81E-06$		$9.718E-07 \pm 1.61E-06$
300 MeV	65°		$4.336E-06 \pm 8.16E-07$		$1.031E-06 \pm 5.46E-07$
300 MeV	75°		$3.160E-06 \pm 1.95E-06$		$1.825E-06 \pm 5.85E-07$
280 MeV	100°		$2.419E-07 \pm 1.47E-07$		$4.320E-07 \pm 1.54E-07$
300 MeV	110°		$8.659E-08 \pm 3.08E-07$		$8.053E-08 \pm 1.32E-07$
100 MeV	155°	$9.620E-07 \pm 1.82E-07$	$3.320E-07 \pm 4.61E-07$	$2.433E-07 \pm 4.12E-07$	$4.548E-07 \pm 2.06E-07$
125 MeV	155°	$9.014E-11 \pm 3.72E-08$	$9.712E-07 \pm 1.09E-07$	$2.186E-07 \pm 1.39E-07$	$3.435E-07 \pm 9.42E-08$
150 MeV	155°	$3.425E-08 \pm 2.10E-08$	$1.467E-06 \pm 1.50E-07$	$2.734E-07 \pm 1.07E-07$	$1.649E-07 \pm 6.83E-08$
175 MeV	155°	$2.432E-08 \pm 2.06E-08$	$6.523E-07 \pm 1.13E-07$	$2.539E-07 \pm 3.98E-08$	$9.377E-08 \pm 5.82E-08$
200 MeV	155°	$1.970E-08 \pm 1.47E-08$	$4.176E-07 \pm 1.01E-07$	$4.813E-11 \pm 1.11E-07$	$1.213E-07 \pm 8.29E-08$
225 MeV	155°	$6.403E-12 \pm 9.51E-09$	$3.155E-07 \pm 5.52E-08$		$8.095E-08 \pm 4.62E-08$
250 MeV	155°	$2.102E-08 \pm 7.04E-08$	$2.056E-08 \pm 2.91E-08$	$3.488E-08 \pm 5.33E-08$	$2.257E-08 \pm 3.51E-08$

Table B.5 Normalised cross sections in mb/sr for the 5.453 MeV, 5.537 MeV, 5.547 MeV and 5.562 MeV levels.

Normalized Cross Sections in mb/sr

Energy	Angle	5.589 $0,1^-$	5.616 $J>6$	5.788 (2^+)	5.831 (1^+)
150 MeV	42°	$9.221E-09 \pm 9.22E-09$	$3.523E-06 \pm 1.84E-04$		
187 MeV	40°	$1.108E-04 \pm 7.28E-05$	$8.526E-05 \pm 6.76E-05$		
225 MeV	41°	$9.453E-07 \pm 2.86E-05$	$7.875E-05 \pm 2.27E-05$		
250 MeV	40°	$1.781E-09 \pm 6.59E-06$	$1.994E-09 \pm 1.99E-05$		
280 MeV	40°	$5.864E-06 \pm 6.17E-06$	$1.572E-05 \pm 5.44E-06$		
300 MeV	40°	$2.785E-05 \pm 1.88E-05$	$2.261E-05 \pm 1.38E-05$		
280 MeV	50°	$4.585E-06 \pm 2.20E-06$	$1.203E-05 \pm 2.24E-06$		
300 MeV	55°	$5.837E-08 \pm 1.49E-06$	$4.326E-06 \pm 1.40E-06$		
300 MeV	65°	$2.309E-07 \pm 3.79E-07$	$6.891E-07 \pm 3.25E-07$		
300 MeV	75°	$4.662E-11 \pm 2.18E-07$	$6.179E-07 \pm 2.40E-07$		
280 MeV	100°	$2.457E-09 \pm 1.34E-07$	$2.426E-07 \pm 1.24E-07$		
300 MeV	110°	$5.166E-08 \pm 8.81E-08$	$5.795E-10 \pm 8.15E-08$		
100 MeV	155°		$7.311E-07 \pm 1.70E-07$	$5.010E-07 \pm 5.01E-06$	$2.623E-07 \pm 2.02E-07$
125 MeV	155°		$3.084E-07 \pm 4.74E-08$	$2.209E-07 \pm 7.85E-08$	$5.753E-07 \pm 6.21E-08$
150 MeV	155°		$2.732E-07 \pm 2.37E-08$	$6.382E-08 \pm 1.42E-08$	$2.108E-07 \pm 2.46E-08$
175 MeV	155°		$4.212E-07 \pm 5.47E-08$	$9.542E-08 \pm 2.77E-08$	$2.114E-07 \pm 5.06E-08$
200 MeV	155°		$2.559E-07 \pm 3.50E-08$	$9.676E-08 \pm 2.58E-08$	$1.189E-07 \pm 3.13E-08$
225 MeV	155°		$2.581E-08 \pm 1.23E-08$	$1.895E-08 \pm 1.12E-08$	$1.762E-07 \pm 3.76E-08$

Table B.6 Normalised cross sections in mb/sr for the 5.589 MeV, 5.616 MeV, 5.788 MeV and 5.831 MeV levels.

Normalized Cross Sections in mb/sr

Energy	Angle	5.908	5.986	6.022 (3^-)	6.039
150 MeV	42°				$3.708E-06 \pm 1.52E-04$
187 MeV	40°			$18.082E \pm 057.31E$	$5.649E-05 \pm 7.12E-05$
225 MeV	41°			$4.711E-05 \pm 2.84E-05$	
250 MeV	40°			$1.264E-04 \pm 5.74E-05$	$2.339E-06 \pm 4.29E-05$
280 MeV	40°			$7.322E-07 \pm 1.29E-05$	$3.900E-05 \pm 1.02E-05$
300 MeV	40°			$1.900E-05 \pm 2.79E-05$	$3.189E-05 \pm 2.21E-05$
280 MeV	50°		$3.292E-05 \pm 5.13E-06$	$1.527E-05 \pm 3.93E-06$	$1.374E-05 \pm 3.23E-06$
300 MeV	55°		$5.502E-06 \pm 1.94E-06$	$1.251E-05 \pm 2.75E-06$	$1.046E-05 \pm 3.17E-06$
300 MeV	65°		$3.795E-06 \pm 1.02E-06$	$4.598E-06 \pm 9.33E-07$	$1.373E-06 \pm 6.97E-07$
300 MeV	75°			$2.125E-07 \pm 2.55E-07$	$7.823E-07 \pm 3.43E-07$
280 MeV	100°			$1.250E-07 \pm 1.11E-07$	$9.679E-08 \pm 1.05E-07$
300 MeV	110°			$1.413E-08 \pm 1.94E-07$	$1.648E-07 \pm 1.29E-07$
100 MeV	155°	$1.175E-06 \pm 2.04E-07$	$5.171E-06 \pm 3.68E-07$	$1.694E-06 \pm 3.44E-07$	$4.997E-07 \pm 3.78E-07$
125 MeV	155°	$1.660E-07 \pm 4.55E-08$	$3.218E-07 \pm 5.78E-08$	$1.387E-06 \pm 1.14E-07$	$1.192E-06 \pm 1.27E-07$
150 MeV	155°	$8.486E-08 \pm 1.80E-08$	$8.969E-08 \pm 2.32E-08$	$1.108E-06 \pm 6.89E-08$	$1.338E-07 \pm 5.73E-08$
175 MeV	155°	$2.122E-07 \pm 5.34E-08$	$1.703E-07 \pm 6.36E-08$	$4.200E-07 \pm 1.02E-07$	$7.459E-08 \pm 8.77E-08$
200 MeV	155°	$1.330E-07 \pm 3.13E-08$	$2.447E-07 \pm 6.08E-08$	$3.234E-07 \pm 7.71E-08$	$9.396E-08 \pm 5.51E-08$
225 MeV	155°	$3.467E-08 \pm 1.76E-08$	$5.358E-09 \pm 1.83E-08$	$1.753E-07 \pm 4.99E-08$	$8.814E-12 \pm 2.92E-08$

Table B.7 Normalised cross sections in mb/sr for the 5.908 MeV, 5.986 MeV, 6.022 MeV and 6.039 MeV levels.

Normalized Cross Sections in mb/sr

		6.057	6.070	6.146	6.191
Energy	**Angle**				3^-
150 MeV	42°	$6.344E-05 \pm 1.74E-04$			$1.523E-03 \pm 2.35E-04$
187 MeV	40°	$3.393E-04 \pm 8.29E-05$			$3.152E-04 \pm 8.50E-05$
225 MeV	41°	$7.910E-05 \pm 2.42E-05$			$8.888E-05 \pm 2.40E-05$
250 MeV	40°	$1.309E-04 \pm 4.37E-05$			$1.585E-05 \pm 2.97E-05$
280 MeV	40°	$2.472E-05 \pm 8.38E-06$			$1.791E-04 \pm 1.14E-05$
300 MeV	40°	$5.692E-05 \pm 2.33E-05$			$2.867E-04 \pm 4.12E-05$
280 MeV	50°	$2.845E-05 \pm 3.45E-06$			$2.515E-05 \pm 3.05E-06$
300 MeV	55°	$1.493E-05 \pm 4.17E-06$			$6.628E-06 \pm 1.86E-06$
300 MeV	65°	$1.546E-06 \pm 5.74E-07$			$9.461E-07 \pm 4.21E-07$
300 MeV	75°	$6.291E-07 \pm 3.30E-07$			$6.882E-07 \pm 2.87E-07$
280 MeV	100°	$2.106E-07 \pm 1.07E-07$			$1.180E-07 \pm 9.19E-08$
300 MeV	110°	$3.540E-08 \pm 5.17E-08$			$2.249E-10 \pm 2.37E-08$
100 MeV	155°	$1.401E-06 \pm 4.02E-07$	$3.054E-06 \pm 4.31E-07$	$5.563E-07 \pm 1.88E-07$	$2.777E-06 \pm 3.42E-07$
125 MeV	155°	$5.225E-07 \pm 1.10E-07$	$4.449E-07 \pm 9.90E-08$	$1.434E-07 \pm 4.78E-08$	$4.220E-08 \pm 5.46E-08$
150 MeV	155°	$2.517E-07 \pm 4.64E-08$	$9.502E-08 \pm 3.72E-08$	$6.475E-08 \pm 1.58E-08$	$1.228E-07 \pm 2.51E-08$
175 MeV	155°	$2.508E-07 \pm 1.21E-07$	$1.390E-08 \pm 1.20E-07$	$1.753E-07 \pm 4.95E-08$	$1.652E-07 \pm 6.40E-08$
200 MeV	155°	$2.628E-08 \pm 4.79E-08$	$1.080E-07 \pm 5.08E-08$	$2.682E-07 \pm 4.28E-08$	$3.148E-07 \pm 5.56E-08$
225 MeV	155°	$4.308E-08 \pm 2.80E-08$	$4.644E-09 \pm 2.42E-08$	$4.473E-08 \pm 2.12E-08$	$2.038E-08 \pm 2.13E-08$

Table B.8 Normalised cross sections in mb/sr for the 6.057 MeV, 6.070 MeV, 6.146 MeV and 6.191 MeV levels.

Normalized Cross Sections in mb/sr

Energy	Angle	6.216	6.233 ($2^+, 5^-$	6.250 (7^-)	6.266 1^-
187 MeV	40°	$3.629E-04 \pm 8.26E-05$	$1.382E-04 \pm 7.62E-05$	$2.613E-04 \pm 8.39E-05$	
250 MeV	40°	$1.098E-04 \pm 3.56E-05$	$2.109E-05 \pm 3.47E-05$	$3.533E-04 \pm 6.65E-05$	
280 MeV	40°	$1.407E-04 \pm 9.75E-06$	$1.517E-05 \pm 7.67E-06$	$3.486E-04 \pm 1.48E-05$	
300 MeV	40°	$1.952E-04 \pm 3.12E-05$	$5.349E-05 \pm 2.40E-05$	$2.248E-04 \pm 3.47E-05$	
280 MeV	50°	$1.754E-05 \pm 2.65E-06$	$1.079E-05 \pm 2.91E-06$	$7.581E-05 \pm 4.83E-06$	
300 MeV	55°	$5.177E-06 \pm 1.66E-06$	$1.244E-05 \pm 3.18E-06$	$4.103E-05 \pm 4.89E-06$	
300 MeV	65°	$3.066E-06 \pm 6.30E-07$	$4.951E-07 \pm 5.50E-07$	$6.148E-06 \pm 9.95E-07$	
300 MeV	75°	$1.831E-06 \pm 4.22E-07$	$3.292E-08 \pm 3.10E-07$	$5.377E-07 \pm 2.69E-07$	
280 MeV	100°	$1.723E-07 \pm 8.52E-08$	$1.623E-07 \pm 1.12E-07$	$3.633E-07 \pm 1.45E-07$	
300 MeV	110°	$2.671E-08 \pm 3.43E-08$	$1.089E-08 \pm 3.73E-08$	$5.287E-08 \pm 4.86E-08$	
100 MeV	155°	$1.777E-06 \pm 2.58E-07$	$2.740E-06 \pm 4.03E-07$	$2.216E-06 \pm 3.35E-07$	$2.529E-07 \pm 2.73E-07$
125 MeV	155°	$4.510E-07 \pm 6.48E-08$	$1.007E-06 \pm 1.07E-07$	$1.638E-06 \pm 1.23E-07$	$1.152E-06 \pm 1.17E-07$
150 MeV	155°	$8.501E-07 \pm 6.10E-08$	$5.206E-07 \pm 4.94E-08$	$9.733E-07 \pm 9.25E-08$	$9.418E-07 \pm 9.14E-08$
175 MeV	155°	$4.042E-07 \pm 4.89E-08$	$5.805E-07 \pm 1.03E-07$	$9.647E-08 \pm 5.28E-08$	$1.367E-07 \pm 4.95E-08$
200 MeV	155°	$2.561E-07 \pm 5.01E-08$	$4.763E-07 \pm 7.32E-08$	$6.062E-08 \pm 5.97E-08$	$1.675E-07 \pm 5.85E-08$
225 MeV	155°	$1.053E-07 \pm 2.80E-08$	$1.327E-07 \pm 4.02E-08$	$5.087E-08 \pm 3.05E-08$	$4.066E-08 \pm 2.38E-08$
250 MeV	155°	$2.557E-08 \pm 1.45E-08$		$5.272E-09 \pm 9.83E-09$	$6.350E-09 \pm 1.04E-08$
280 MeV	155°	$6.497E-09 \pm 8.21E-09$	$9.413E-08 \pm 7.50E-08$		

Table B.9 Normalised cross sections in mb/sr for the 6.216 MeV, 6.233 MeV, 6.250 MeV and 6.266 MeV levels.

Normalized Cross Sections in mb/sr

Energy	Angle	6.317 (3^-)	6.340 3^-	6.361 1^-	6.397 3^-
187 MeV	40°		$2.826E-04 \pm 7.65E-05$		$1.786E-04 \pm 7.27E-05$
250 MeV	40°		$6.783E-05 \pm 3.00E-05$		$1.229E-04 \pm 3.93E-05$
280 MeV	40°		$6.882E-05 \pm 7.41E-06$		$4.740E-05 \pm 7.34E-06$
300 MeV	40°		$9.447E-05 \pm 2.18E-05$		$5.744E-05 \pm 2.02E-05$
280 MeV	50°		$7.412E-06 \pm 2.11E-06$		$3.085E-07 \pm 1.62E-06$
300 MeV	55°		$5.678E-06 \pm 1.65E-06$		$4.614E-06 \pm 1.73E-06$
300 MeV	65°		$1.275E-06 \pm 4.09E-07$		$6.327E-07 \pm 3.85E-07$
300 MeV	75°		$1.030E-06 \pm 2.96E-07$		$5.738E-07 \pm 2.65E-07$
280 MeV	100°		$3.006E-07 \pm 1.18E-07$		$1.768E-07 \pm 1.11E-07$
300 MeV	110°		$9.202E-08 \pm 3.95E-08$		$4.831E-08 \pm 2.26E-08$
100 MeV	155°	$2.318E-07 \pm 1.89E-07$	$1.436E-06 \pm 2.46E-07$	$4.983E-07 \pm 2.45E-07$	$1.767E-07 \pm 2.28E-07$
125 MeV	155°	$8.785E-08 \pm 5.02E-08$	$3.293E-07 \pm 6.08E-08$	$2.081E-07 \pm 6.33E-08$	$9.254E-08 \pm 6.01E-08$
150 MeV	155°	$2.650E-07 \pm 3.98E-08$	$2.879E-07 \pm 4.30E-08$	$2.616E-07 \pm 4.66E-08$	$4.253E-07 \pm 5.68E-08$
175 MeV	155°	$1.049E-07 \pm 3.04E-08$	$4.664E-08 \pm 2.94E-08$	$5.165E-08 \pm 3.29E-08$	$8.031E-08 \pm 4.00E-08$
200 MeV	155°	$4.437E-08 \pm 7.06E-08$	$1.046E-07 \pm 3.77E-08$	$6.675E-08 \pm 3.81E-08$	$1.254E-07 \pm 4.34E-08$
225 MeV	155°	$2.354E-08 \pm 1.26E-08$	$3.021E-08 \pm 1.45E-08$	$2.060E-08 \pm 1.59E-08$	$3.350E-08 \pm 1.84E-08$
250 MeV	155°	$2.138E-08 \pm 1.32E-08$	$9.654E-13 \pm 6.13E-09$	$7.476E-09 \pm 1.24E-08$	$3.993E-09 \pm 1.85E-08$

Table B.10 Normalised cross sections in mb/sr for the 6.317 MeV, 6.340 MeV, 6.361 MeV and 6.397 MeV levels.

Normalized Cross Sections in mb/sr

Energy	Angle	6.415 (3^-)	6.462 ($1^-, 2^+$)	6.490 2^-	6.508
187 MeV	40°	$2.608E-04 \pm 7.81E-05$	$8.033E-05 \pm 6.60E-05$	$3.819E-05 \pm 6.27E-05$	
250 MeV	40°	$2.938E-06 \pm 3.40E-05$	$3.323E-05 \pm 3.14E-05$	$1.229E-06 \pm 2.93E-05$	
280 MeV	40°	$1.497E-05 \pm 6.96E-06$		$1.543E-05 \pm 7.48E-06$	
300 MeV	40°	$4.175E-05 \pm 1.87E-05$	$4.343E-05 \pm 1.96E-05$	$7.887E-05 \pm 2.29E-05$	
280 MeV	50°	$1.426E-06 \pm 1.72E-06$	$3.998E-07 \pm 1.76E-06$	$1.216E-05 \pm 2.33E-06$	
300 MeV	55°	$3.989E-06 \pm 1.79E-06$	$3.286E-07 \pm 1.19E-06$	$3.019E-06 \pm 1.33E-06$	
300 MeV	65°	$5.467E-07 \pm 3.93E-07$		$3.381E-06 \pm 7.01E-07$	
300 MeV	75°	$5.223E-07 \pm 2.92E-07$	$1.813E-06 \pm 4.30E-07$		
280 MeV	100°	$1.817E-07 \pm 1.12E-07$	$7.138E-08 \pm 1.07E-07$	$3.589E-07 \pm 1.32E-07$	
300 MeV	110°	$5.816E-08 \pm 4.13E-08$	$1.860E-07 \pm 6.69E-08$	$1.037E-07 \pm 5.51E-08$	
100 MeV	155°	$5.915E-07 \pm 2.23E-07$	$1.052E-06 \pm 2.14E-07$	$3.285E-07 \pm 2.07E-07$	$3.496E-07 \pm 2.07E-07$
125 MeV	155°	$6.187E-08 \pm 5.36E-08$	$6.127E-08 \pm 4.49E-08$	$1.750E-07 \pm 5.68E-08$	$5.115E-07 \pm 6.79E-08$
150 MeV	155°	$9.484E-08 \pm 4.22E-08$	$2.174E-07 \pm 3.76E-08$	$4.795E-07 \pm 5.08E-08$	$3.850E-07 \pm 4.99E-08$
175 MeV	155°	$2.508E-09 \pm 3.39E-08$	$2.327E-07 \pm 3.92E-08$	$1.143E-07 \pm 3.58E-08$	$9.973E-08 \pm 3.65E-08$
200 MeV	155°	$9.129E-08 \pm 4.37E-08$	$3.329E-07 \pm 5.12E-08$	$5.322E-08 \pm 4.24E-08$	$2.650E-07 \pm 5.05E-08$
225 MeV	155°	$6.590E-08 \pm 2.33E-08$	$6.495E-08 \pm 2.33E-08$	$6.027E-10 \pm 1.28E-08$	$3.343E-08 \pm 1.61E-08$
250 MeV	155°	$2.139E-12 \pm 2.14E-08$	$3.352E-12 \pm 7.62E-09$	$1.800E-09 \pm 6.17E-09$	$2.618E-08 \pm 1.64E-08$

Table B.11 Normalised cross sections in mb/sr for the 6.415 MeV, 6.462 MeV, 6.490 MeV and 6.508 MeV levels.

Normalized Cross Sections in mb/sr

Energy	Angle	6.535 (5^-)	6.547	6.578 (2^+)	6.602 (3^-)
187 MeV	40°	$7.507E-05 \pm 8.39E-05$	$2.568E-06 \pm 8.83E-05$		$1.222E-04 \pm 6.66E-05$
250 MeV	40°	$1.319E-04 \pm 4.84E-05$	$6.408E-06 \pm 4.37E-05$		$3.450E-05 \pm 3.15E-05$
280 MeV	40°	$1.082E-04 \pm 1.06E-05$	$1.376E-05 \pm 8.98E-06$		$6.251E-05 \pm 7.77E-06$
300 MeV	40°	$6.662E-05 \pm 2.53E-05$	$5.943E-05 \pm 2.47E-05$		$8.556E-05 \pm 2.24E-05$
280 MeV	50°	$7.074E-06 \pm 2.98E-06$	$4.889E-05 \pm 4.27E-06$		$1.551E-05 \pm 2.63E-06$
300 MeV	55°	$6.218E-06 \pm 2.63E-06$	$1.537E-05 \pm 3.12E-06$		$5.563E-06 \pm 1.90E-06$
300 MeV	65°	$2.416E-06 \pm 7.22E-07$	$1.356E-06 \pm 6.67E-07$		$2.149E-06 \pm 5.66E-07$
300 MeV	75°	$2.176E-06 \pm 5.32E-07$	$1.449E-07 \pm 3.71E-07$		$1.004E-06 \pm 3.07E-07$
280 MeV	100°	$1.457E-07 \pm 1.29E-07$	$2.921E-07 \pm 1.51E-07$		$1.846E-07 \pm 1.07E-07$
300 MeV	110°	$4.532E-07 \pm 1.20E-07$	$5.968E-09 \pm 7.64E-08$		$1.272E-07 \pm 5.90E-08$
100 MeV	155°	$1.087E-06 \pm 2.91E-07$	$1.238E-07 \pm 2.77E-07$	$9.214E-07 \pm 2.12E-07$	$4.978E-07 \pm 2.11E-07$
125 MeV	155°	$3.048E-11 \pm 7.06E-08$	$7.814E-07 \pm 8.44E-08$	$2.081E-07 \pm 5.48E-08$	$4.754E-13 \pm 4.75E-13$
150 MeV	155°	$1.853E-07 \pm 5.42E-08$	$6.205E-07 \pm 6.08E-08$	$2.727E-07 \pm 3.86E-08$	$1.416E-07 \pm 3.56E-08$
175 MeV	155°	$3.600E-07 \pm 6.23E-08$	$4.706E-07 \pm 6.49E-08$	$2.110E-07 \pm 3.88E-08$	$8.551E-08 \pm 3.51E-08$
200 MeV	155°	$2.196E-07 \pm 6.55E-08$	$3.424E-07 \pm 6.56E-08$	$2.201E-07 \pm 4.57E-08$	$7.997E-08 \pm 4.10E-08$
225 MeV	155°	$6.993E-08 \pm 3.02E-08$	$1.145E-07 \pm 3.48E-08$	$3.309E-08 \pm 1.78E-08$	$4.342E-08 \pm 1.92E-08$
250 MeV	155°	$2.225E-12 \pm 2.23E-08$	$3.233E-08 \pm 2.22E-08$	$2.726E-09 \pm 6.87E-09$	$1.118E-08 \pm 9.79E-09$

Table B.12 Normalised cross sections in mb/sr for the 6.535 MeV, 6.547 MeV, 6.578 MeV and 6.602 MeV levels.

Normalized Cross Sections in mb/sr

Energy	Angle	6.623	6.652 4^+	6.697 $(1^-,3^-)$	6.775
187 MeV	40°	$5.753E-04 \pm 9.55E-05$			
250 MeV	40°	$3.076E-04 \pm 5.96E-05$	$9.761E-06 \pm 2.72E-05$		$7.448E-05 \pm 3.78E-05$
280 MeV	40°	$9.095E-05 \pm 8.56E-06$	$7.968E-07 \pm 6.40E-06$		$6.499E-06 \pm 8.07E-06$
300 MeV	40°	$8.398E-05 \pm 2.23E-05$	$7.219E-06 \pm 1.83E-05$		$5.466E-05 \pm 2.43E-05$
280 MeV	50°	$3.474E-05 \pm 3.50E-06$	$1.660E-06 \pm 1.97E-06$		$1.274E-05 \pm 4.59E-06$
300 MeV	55°	$1.470E-05 \pm 2.63E-06$	$8.491E-06 \pm 2.01E-06$		$6.035E-06 \pm 2.34E-06$
300 MeV	65°	$5.952E-07 \pm 4.15E-07$	$3.390E-06 \pm 6.61E-07$		$5.507E-07 \pm 5.17E-07$
300 MeV	75°	$1.895E-07 \pm 1.84E-07$	$3.124E-07 \pm 1.77E-07$		$1.649E-06 \pm 4.61E-07$
280 MeV	100°	$5.414E-08 \pm 9.05E-08$	$5.497E-07 \pm 1.58E-07$		$2.786E-07 \pm 2.01E-07$
300 MeV	110°	$8.747E-08 \pm 5.33E-08$			
100 MeV	155°	$1.365E-07 \pm 1.92E-07$	$2.914E-07 \pm 1.91E-07$	$9.684E-08 \pm 1.96E-07$	
125 MeV	155°	$3.394E-07 \pm 5.72E-08$	$2.685E-07 \pm 5.57E-08$	$1.007E-08 \pm 4.55E-08$	
150 MeV	155°	$2.187E-07 \pm 3.52E-08$	$1.636E-07 \pm 3.35E-08$	$3.161E-07 \pm 4.03E-08$	
175 MeV	155°	$1.664E-07 \pm 3.58E-08$	$5.050E-08 \pm 2.90E-08$	$1.616E-07 \pm 3.49E-08$	
200 MeV	155°	$1.941E-07 \pm 4.34E-08$	$1.195E-07 \pm 3.87E-08$	$7.866E-08 \pm 3.96E-08$	
225 MeV	155°	$1.302E-07 \pm 3.13E-08$	$1.250E-07 \pm 3.19E-08$	$1.221E-07 \pm 3.32E-08$	
250 MeV	155°	$4.884E-08 \pm 2.49E-08$	$5.652E-08 \pm 2.85E-08$	$5.284E-08 \pm 2.77E-08$	

Table B.13 Normalised cross sections in mb/sr for the 6.623 MeV, 6.652 MeV, 6.697 MeV and 6.775 MeV levels.

Normalized Cross Sections in mb/sr

Energy	Angle	6.790 (3^+)	6.816 (2^+)	6.906	6.929 2^-
187 MeV	40°	$1.739E-04 \pm 5.07E-05$	$1.803E-05 \pm 8.45E-05$		
250 MeV	40°	$1.445E-04 \pm 4.48E-05$	$2.919E-05 \pm 3.40E-05$	$1.654E-05 \pm 2.90E-05$	
280 MeV	40°	$2.271E-04 \pm 1.26E-05$	$5.261E-06 \pm 7.48E-06$	$2.414E-07 \pm 6.50E-06$	
300 MeV	40°	$2.164E-04 \pm 3.44E-05$	$3.138E-05 \pm 2.07E-05$	$4.606E-05 \pm 1.95E-05$	
280 MeV	50°	$8.214E-05 \pm 5.92E-06$	$3.089E-05 \pm 4.08E-06$	$2.151E-05 \pm 3.40E-06$	
300 MeV	55°	$3.011E-06 \pm 2.04E-06$	$9.270E-08 \pm 1.69E-06$	$4.945E-06 \pm 2.19E-06$	
300 MeV	65°	$1.904E-06 \pm 6.09E-07$	$7.900E-07 \pm 5.35E-07$	$2.606E-06 \pm 7.57E-07$	
300 MeV	75°	$5.299E-07 \pm 3.99E-07$	$3.155E-06 \pm 6.50E-07$	$6.089E-07 \pm 2.87E-07$	
280 MeV	100°	$3.688E-07 \pm 1.84E-07$	$1.978E-07 \pm 1.36E-07$	$5.030E-07 \pm 1.71E-07$	
300 MeV	110°	$9.678E-08 \pm 4.91E-08$	$1.361E-07 \pm 5.41E-08$		
100 MeV	155°	$1.347E-06 \pm 2.28E-07$	$7.691E-07 \pm 2.52E-07$	$3.230E-06 \pm 2.49E-07$	$2.999E-06 \pm 2.46E-07$
125 MeV	155°	$3.658E-07 \pm 5.69E-08$	$9.715E-07 \pm 8.85E-08$	$1.413E-06 \pm 1.12E-07$	$1.835E-07 \pm 9.86E-08$
150 MeV	155°	$2.137E-07 \pm 3.34E-08$	$1.193E-07 \pm 3.86E-08$	$4.977E-07 \pm 6.99E-08$	$3.883E-07 \pm 7.11E-08$
175 MeV	155°	$1.898E-07 \pm 3.58E-08$	$9.751E-08 \pm 3.85E-08$	$3.056E-07 \pm 5.53E-08$	$1.148E-07 \pm 5.62E-08$
200 MeV	155°	$3.954E-07 \pm 5.45E-08$	$1.571E-07 \pm 5.50E-08$	$1.547E-07 \pm 5.22E-08$	$1.738E-07 \pm 6.42E-08$
225 MeV	155°	$9.980E-08 \pm 3.16E-08$	$6.511E-08 \pm 2.67E-08$	$1.635E-08 \pm 1.93E-08$	$3.900E-08 \pm 2.58E-08$
250 MeV	155°	$4.788E-08 \pm 2.60E-08$	$2.600E-08 \pm 2.03E-08$	$1.500E-08 \pm 1.55E-08$	$1.880E-08 \pm 1.82E-08$

Table B.14 Normalized cross sections in mb/sr for the 6.790 MeV, 6.816 MeV, 6.906 MeV and 6.929 MeV levels.

Normalized Cross Sections in mb/sr

Energy	Angle	6.942 3^-	6.951	6.988 (3^-)	7.006 (9^+)
187 MeV	40°		$9.408E-05 \pm 6.07E-05$	$7.518E-05 \pm 6.54E-05$	$3.313E-05 \pm 6.93E-05$
250 MeV	40°		$7.003E-06 \pm 2.62E-05$	$2.571E-06 \pm 3.07E-05$	$1.273E-05 \pm 4.25E-05$
280 MeV	40°		$7.925E-05 \pm 7.69E-06$	$2.435E-07 \pm 6.20E-06$	$1.274E-06 \pm 8.01E-06$
300 MeV	40°		$1.119E-04 \pm 2.30E-05$	$4.583E-05 \pm 2.18E-05$	$1.117E-05 \pm 2.86E-05$
280 MeV	50°		$3.707E-05 \pm 3.60E-06$	$6.115E-06 \pm 2.57E-06$	$2.226E-05 \pm 3.51E-06$
300 MeV	55°		$4.261E-06 \pm 1.56E-06$	$2.151E-05 \pm 3.60E-06$	$1.429E-05 \pm 4.35E-06$
300 MeV	65°		$5.432E-08 \pm 3.45E-07$	$1.169E-06 \pm 5.88E-07$	$4.316E-06 \pm 1.04E-06$
300 MeV	75°		$7.016E-07 \pm 2.63E-07$	$3.748E-07 \pm 3.46E-07$	$6.570E-07 \pm 7.74E-07$
280 MeV	100°		$3.631E-07 \pm 1.38E-07$	$7.284E-08 \pm 9.84E-08$	$1.023E-09 \pm 1.38E-07$
300 MeV	110°		$4.458E-08 \pm 3.06E-08$	$6.545E-08 \pm 4.20E-08$	$4.887E-09 \pm 5.25E-08$
100 MeV	155°	$6.681E-07 \pm 3.07E-07$	$4.992E-07 \pm 2.89E-07$	$2.058E-07 \pm 2.34E-07$	$4.096E-07 \pm 2.48E-07$
125 MeV	155°	$6.715E-08 \pm 1.11E-07$	$2.196E-06 \pm 1.25E-07$	$5.214E-07 \pm 8.74E-08$	$7.581E-08 \pm 8.25E-08$
150 MeV	155°	$1.202E-07 \pm 7.08E-08$	$3.940E-07 \pm 5.45E-08$	$4.423E-07 \pm 5.60E-08$	$6.462E-07 \pm 7.03E-08$
175 MeV	155°	$1.386E-07 \pm 5.97E-08$	$1.560E-07 \pm 4.39E-08$	$6.512E-08 \pm 3.66E-08$	$1.238E-07 \pm 4.32E-08$
200 MeV	155°	$2.223E-07 \pm 7.19E-08$	$1.106E-07 \pm 4.92E-08$	$9.539E-08 \pm 4.30E-08$	$1.148E-07 \pm 5.13E-08$
225 MeV	155°	$2.117E-08 \pm 2.73E-08$	$5.691E-08 \pm 2.36E-08$	$4.049E-08 \pm 2.12E-08$	$3.172E-08 \pm 2.37E-08$
250 MeV	155°	$1.245E-12 \pm 1.21E-08$	$1.901E-08 \pm 1.60E-08$	$2.946E-08 \pm 1.89E-08$	$2.147E-12 \pm 1.61E-08$

Table B.15 Normalised cross sections in mb/sr for the 6.942 MeV, 6.951 MeV, 6.988 MeV and 7.006 MeV levels.

Normalized Cross Sections in mb/sr

Energy	Angle	7.023 $(1^-, 3^-)$	7.044	7.103	7.129
187 MeV	40°	$1.826E-05 \pm 7.44E-05$			$3.367E-05 \pm 6.01E-05$
250 MeV	40°	$1.141E-06 \pm 3.93E-05$		$2.035E-06 \pm 3.09E-05$	$1.947E-06 \pm 2.92E-05$
280 MeV	40°	$1.470E-05 \pm 7.48E-06$	$1.107E-07 \pm 5.96E-06$	$1.940E-07 \pm 7.43E-06$	$1.957E-07 \pm 5.62E-06$
300 MeV	40°	$3.058E-05 \pm 2.84E-05$	$2.620E-05 \pm 1.57E-05$	$3.624E-06 \pm 2.05E-05$	$2.369E-05 \pm 1.49E-05$
280 MeV	50°	$9.298E-06 \pm 3.07E-06$	$3.880E-06 \pm 2.39E-06$	$8.933E-08 \pm 3.00E-06$	$1.083E-05 \pm 2.49E-06$
300 MeV	55°	$1.119E-05 \pm 3.43E-06$	$7.284E-07 \pm 1.92E-06$	$2.172E-06 \pm 2.10E-06$	$5.836E-06 \pm 1.91E-06$
300 MeV	65°	$1.075E-06 \pm 7.98E-07$	$1.586E-06 \pm 6.46E-07$	$1.173E-06 \pm 6.15E-07$	$1.702E-06 \pm 5.17E-07$
300 MeV	75°	$3.979E-07 \pm 9.02E-07$	$5.882E-06 \pm 8.57E-07$	$1.891E-06 \pm 6.55E-07$	$1.263E-06 \pm 5.04E-07$
280 MeV	100°	$2.519E-07 \pm 1.61E-07$	$3.267E-07 \pm 1.60E-07$	$6.547E-07 \pm 2.12E-07$	$3.186E-07 \pm 1.49E-07$
300 MeV	110°	$8.680E-08 \pm 6.32E-08$	$1.311E-09 \pm 5.15E-08$		$8.364E-08 \pm 4.16E-08$
100 MeV	155°	$6.287E-07 \pm 2.15E-07$	$1.168E-06 \pm 2.54E-07$	$7.693E-07 \pm 2.59E-07$	$3.450E-07 \pm 1.99E-07$
125 MeV	155°	$9.426E-07 \pm 9.24E-08$	$5.086E-07 \pm 8.12E-08$	$4.609E-08 \pm 6.64E-08$	$4.754E-07 \pm 6.74E-08$
150 MeV	155°	$4.291E-07 \pm 6.19E-08$	$2.742E-07 \pm 5.40E-08$	$2.761E-07 \pm 5.03E-08$	$2.682E-07 \pm 4.27E-08$
175 MeV	155°	$6.335E-08 \pm 3.98E-08$	$2.616E-07 \pm 5.04E-08$	$3.643E-07 \pm 6.10E-08$	$5.642E-07 \pm 5.85E-08$
200 MeV	155°	$1.627E-07 \pm 5.15E-08$	$3.407E-07 \pm 5.81E-08$	$7.141E-07 \pm 8.06E-08$	$6.739E-07 \pm 7.34E-08$
225 MeV	155°	$6.716E-08 \pm 2.63E-08$	$4.245E-09 \pm 3.20E-08$	$6.619E-08 \pm 3.46E-08$	$9.328E-08 \pm 2.99E-08$
250 MeV	155°	$1.449E-08 \pm 1.59E-08$	$2.676E-08 \pm 1.87E-08$	$1.422E-09 \pm 1.46E-08$	$2.148E-08 \pm 1.58E-08$

Table B.16 Normalised cross sections in mb/sr for the 7.023 MeV, 7.044 MeV, 7.103 MeV and 7.129 MeV levels.

Normalized Cross Sections in mb/sr

Energy	Angle	7.152 $(2^-, 3^+)$	7.180	7.205	7.237 (1^-)
100 MeV	155°	$1.336E-06 \pm 2.35E-07$	$1.817E-06 \pm 2.45E-07$	$1.177E-06 \pm 2.33E-07$	$2.124E-06 \pm 2.51E-07$
125 MeV	155°	$5.801E-07 \pm 7.01E-08$	$1.726E-07 \pm 5.62E-08$	$1.928E-07 \pm 5.60E-08$	$4.771E-07 \pm 6.29E-08$
150 MeV	155°	$2.985E-07 \pm 4.19E-08$	$1.960E-07 \pm 3.74E-08$	$4.126E-07 \pm 4.33E-08$	$6.237E-07 \pm 5.02E-08$
175 MeV	155°	$2.024E-07 \pm 4.45E-08$	$2.156E-07 \pm 4.11E-08$	$1.610E-07 \pm 3.70E-08$	$2.238E-07 \pm 3.79E-08$
200 MeV	155°	$2.699E-07 \pm 5.79E-08$	$3.550E-07 \pm 5.49E-08$	$2.925E-07 \pm 5.17E-08$	$2.390E-07 \pm 4.70E-08$
225 MeV	155°	$1.804E-11 \pm 1.71E-08$	$2.078E-10 \pm 1.62E-08$	$5.907E-08 \pm 2.08E-08$	$6.694E-08 \pm 2.15E-08$
250 MeV	155°	$5.786E-09 \pm 1.10E-08$	$2.867E-08 \pm 1.67E-08$	$6.321E-09 \pm 8.77E-09$	$7.510E-09 \pm 9.07E-09$

Energy	Angle	7.267 $(3^-, 4^-)$	7.283 $(1^+, 2^+)$
100 MeV	155°		$3.130E-06 \pm 2.79E-07$
125 MeV	155°	$7.578E-07 \pm 8.41E-08$	$6.172E-07 \pm 8.07E-08$
150 MeV	155°	$5.022E-07 \pm 5.56E-08$	$2.982E-07 \pm 4.87E-08$
175 MeV	155°	$1.410E-07 \pm 4.17E-08$	$3.183E-07 \pm 4.69E-08$
200 MeV	155°	$1.697E-07 \pm 5.27E-08$	$3.115E-07 \pm 5.75E-08$
225 MeV	155°	$1.081E-08 \pm 1.67E-08$	$2.619E-08 \pm 1.81E-08$
250 MeV	155°	$2.878E-09 \pm 9.04E-09$	$5.818E-09 \pm 8.83E-09$

Table B.17 Normalised cross sections in mb/sr for the 7.152 MeV, 7.180 MeV, 7.205 MeV, 7.237 MeV, 7.267 MeV and 7.283 MeV levels.